

MASTER OF SCIENCE THESIS

DBD Plasma Actuators for Karman Shedding Suppression

Investigation of Spanwise Modulated Configurations

Siddharth Ravichandran

October 2012

DBD Plasma Actuators for Karman Shedding Suppression

Investigation of Spanwise Modulated Configurations

Master of Science Thesis

For obtaining the degree of Master of Science in Aerospace
Engineering at Delft University of Technology

Siddharth Ravichandran

October 2012



Copyright © Aerospace Engineering, Delft University of Technology
All rights reserved.

DELFT UNIVERSITY OF TECHNOLOGY
FACULTY OF AEROSPACE ENGINEERING
DEPARTMENT OF AERODYNAMICS

DECLARATION

The undersigned hereby certify that they have read and recommend to the Faculty of Aerospace Engineering for acceptance a thesis entitled "**DBD Plasma Actuators for Karman Shedding Suppression**" by **Siddharth Ravichandran** in partial fulfilment of the requirements for the degree of **Master of Science**.



Dated: October 2012

Committee Members:

Prof.dr.ir. F. Scarano (Supervisor)

dr. ir. B. W van Oudheusden

dr.M. Kotsonis

Mr. S. Ghaemi

Preface

This Thesis report is a culmination of two years of intense study and research at the Aerodynamics department in the Aerospace Engineering faculty at TU Delft. I consider myself extremely lucky to have had the chance of travelling across the world to study at one of the finest universities in the world and work in a highly motivating environment with the brightest and the best in this field. I would therefore like to express my gratitude to those who helped me reach the fulfilment of my Masters' Thesis.

I would like to thank Prof. Fulvio Scarano for giving me the opportunity to work on the interesting and relevant research topic presented here. This Thesis study combined a healthy dose of theory with the use of advanced instruments and flow measurement techniques and some creative thinking and designing of experiments. In my opinion, it is an ideal way to end my Masters education. Prof. Scarano's guidance enabled me to keep challenging myself on improving the quality of the research and not losing sight of the larger goal of the Thesis. But it was the continuous mentoring that I received from Dr. Marios Kotsonis and Mr. Sina Ghaemi that enabled me to face the daily challenges involved with designing, scheduling, setting up and carrying out the experimental campaigns. The regular (scheduled as well as on the spot!) meetings that I had with them provided me with valuable insights regarding issues ranging from the underlying flow physics to tips on presenting my results. Marios, as an expert on all things plasma related, instilled within me the realisation that engineering is the practical art of arranging and making experiments work. Sina, as a PIV expert, was ever ready to help me understand and overcome the various issues that I faced during the PIV testing campaigns. I am grateful to them for the peek they gave me into the life of a researcher in Aerodynamics.

I thank the staff and students at the Aerodynamics department. The technical staff - Stefan, Nico, Frits, Eric, Leo and Peter were ever available to help with any technical issues that I had to face. My fellow master students and co-inhabitants of the 'basement' were always open for discussions (technical and otherwise!), debates, after-work events and sharing the temporary miseries that often accompany research!

I would like to thank my various friends from all over the world in Delft, for their company and the much-needed distractions that they offered, and for giving my life the international flavour that made study in a foreign country such a pleasure the past two years.

A lot of love and gratitude goes to my family - my dear parents and brother, for giving me their approval and support at every stage in my life, for always being there for me and reaching out and keeping me grounded at the moments when I needed it the most.

Abstract

Vortex shedding occurs from commonly encountered objects in flows such as blunt and divergent (truncated) airfoil trailing edges [12], landing gear of aircraft [37], etc. In addition to undesired aero-elastic effects such as vortex-induced vibration and fluctuating aerodynamic forces, tonal acoustic noise is emitted due to the regular and periodic nature of the shedding. With the aim of eliminating this emitted noise, an experimental study was carried out on a D-shaped bluff body model using appropriately designed and implemented plasma actuator configurations to achieve active three-dimensional vortex shedding suppression.

The work of Nati [27] in using spanwise uniform plasma actuation to generate opposing transverse jets from the upper and lower trailing edges to give rise to a streamwise jet was used as the starting base of the work here. Extending the limits of actuator effectiveness in shedding suppression seen in this work was one of the objectives of the present study. Insights obtained from experimental works such as the use of spanwise modulated distributed forcing [21], [22] and the use of plasma in streamwise vortex generation [20] were used to devise the spanwise modulated actuation schemes that were used.

Based on the direction of forcing with respect to the flow and the electrode layout over the upper and lower trailing edge surfaces of the model, the spanwise modulated actuation schemes (or 'modes') implemented were named the transverse opposing, transverse staggered and spanwise modes. For each of these modes, multiple 'configurations' were tested based on the spatial interval over which the actuation scheme was repeated over the model span. To have a benchmark to compare the spanwise modulated actuated results with, transverse actuation that was uniform over the span was also tested. Time-resolved two component particle image velocimetry (2C-PIV) was the flow measurement technique of choice, due to the high spatial and temporal resolution of the imaged wake velocity fields obtained. To take into account the fact that the expected flow behaviour across the span will be different at different positions in a spatial cycle of actuation, the flow at multiple spanwise planes was imaged and measured. Additionally, transverse planes were also imaged for representative configurations in each actuation mode to study the flow behaviour across the span. The range of flow free-stream speeds over the model for which each of the actuation modes, configurations and imaged planes were tested was from 5m/s to 20m/s. The flow over the model for each case was untripped and laminar till separation at the trailing edge, and the presence of vortex shedding and its various associated parameters for the baseline un-actuated flow was confirmed and calculated for the sake of flow characterisation.

The large amounts of time-resolved data obtained from 2C-PIV over all the modes, configurations, imaged planes and flow conditions presented a wealth of results in terms of instantaneous vortical structures, statistical flow fields, power spectra and flow modes obtained from Proper Orthogonal Decomposition of the velocity fields. The results for all the actuated modes indicate regions of

wide wakes with shear layers spread apart and narrow wakes with shear layers drawn inwards alternating along the span. This can be attributed to the generation of streamwise vorticity that was spatially steady and temporally stable for all the modes; the exact mechanism for this creation was however different for the different actuation modes. Additionally, correlation analyses of the velocities at different spanwise positions when considering the transverse planes at the shear layer for all the tested modes indicate a breakdown of the spanwise coherence of the shedding. Likewise, the actuation flow mechanism by which this breakdown is effected is different for the different actuation modes.

For the spanwise modulated transverse opposing mode, the actuation was responsible for the *indirect* creation of strong streamwise vorticity due to the presence of alternating regions along the span of forcing and no-forcing. The aligned transverse forcing from the upper and lower sides gave rise to spanwise flows that mutually reinforced each other, hence the generated streamwise vorticity was strong. This streamwise vorticity was generated at the expense of the baseline spanwise vorticity of the shear layers, thus weakening the latter to a large extent, as was achieved with the use of segmented trailing edges in [8]. The strong streamwise vorticity created gave rise to alternating regions of large and small wakes along the span that broke up the spanwise coherence of the shed Karman vortex rolls. For spanwise modulated staggered actuation, however it is expected that the induced spanwise flows due to the anti-aligned transverse forcing from the upper and lower sides would weaken each other and give rise to streamwise vorticity that would be significantly weaker than for transverse opposing actuation. The success of the transverse staggered actuation in vortex shedding suppression rested however on the asymmetry between the interacting shear layers on both sides due to the anti-aligned nature of the actuation over these surfaces. For the spanwise forcing actuation scheme, the *direct* creation of streamwise vorticity due to the forcing perpendicular to the inflow was expected, as seen in [20]. However, the modulation of the interacting shear layers across the span on both sides due to the alternating common-flow up and flow-down of the generated streamwise vorticity was responsible for the breakdown of the spanwise coherence of the shed vortex rollers across the span.

As with most three-dimensional flow control methods, whether passive [29] [8] or active [21] [22], it was not intended to suppress vortex shedding *all over the span*. Instead, the breakdown of the spanwise coherence meant that the shed vortices across the span were out of phase. When these out of phase vortices across the span are considered and their pressure fields summed up, it is expected that they would cancel each other out, leading to a suppression of the tonal acoustic noise as desired. Significant reduction in the energies of the first two POD modes are seen for the actuation modes at 11 m/s, which then rise to near baseline flow levels at 14 m/s. The cross-correlations of the velocity time signals across the span, when the transverse shear layer planes are imaged, also indicate a breakdown of spanwise coherence till a free stream of 11 m/s. The upper limit of actuation effectiveness in effecting significant vortex attenuation is hence between 11 and 14 m/s, an improvement compared to the limit seen in the case of spanwise uniform transverse actuation seen in Nati [27].

Contents

Preface	vii
Abstract	viii
List of Figures	xxi
List of Tables	xxii
Nomenclature	xxiii
1 Introduction	1
1.1 Background and Relevance	1
1.2 Scope of Current Work	3
1.3 Structure of this Report	4
2 Theory	5
2.1 Vortex Shedding	5
2.1.1 Mechanism of Vortex Shedding	5
2.1.2 Properties of the Von Karman Vortex Street	8
2.2 Vortex Shedding Control	15
2.2.1 Two-Dimensional Shedding Control	16
2.2.2 Three-Dimensional Shedding Control	18
2.3 Plasma Actuators	21
2.3.1 The Actuator Physics	22
2.3.2 Selected Applications of DBD Plasma Actuators in Fluid Flow	29
3 Experimental and Data Processing Techniques	35
3.1 Particle Image Velocimetry	35
3.1.1 Principle of 2C-PIV	35
3.1.2 Tracer Particles	37
3.1.3 Laser Sheet Illumination	40
3.1.4 Particle Imaging	41
3.1.5 Image Analysis	42
3.2 Proper Orthogonal Decomposition	45
3.2.1 Method of Snapshots	46
3.3 Power Spectral Density	47
3.4 Correlation Analysis	48

4	Experimental Setup	50
4.1	Dielectric Parametric Study	50
4.1.1	Background and Motivation	50
4.1.2	Experimental Setup	51
4.2	Wind Tunnel Experimental Model	54
4.2.1	Coordinate System	55
4.3	Plasma Actuator Configurations	56
4.4	Time Resolved PIV Campaign	58
4.4.1	Optical System Setup	60
4.4.2	Laser and Seeding System	61
4.4.3	Image Setup and Processing	62
4.4.4	Summary	63
5	Results	65
5.1	Dielectric Parametric Study	65
5.2	Baseline Flow Characterisation	68
5.2.1	Boundary Layer	68
5.2.2	Von Karman Vortex Street	70
5.2.3	Statistical flow fields	74
5.2.4	Transverse Planes	76
5.2.5	POD Analysis	77
5.3	Spanwise Uniform Transverse Actuation	79
5.3.1	Expected Mechanism of Actuation	79
5.3.2	Results and Conclusions	79
5.4	Spanwise Modulated Actuation Results	83
5.5	Transverse Opposing Actuation	84
5.5.1	Proposed Actuation Mechanism	99
5.6	Transverse Staggered Actuation	102
5.6.1	Proposed Actuation Mechanism	112
5.7	Spanwise Actuation	114
5.7.1	Proposed Actuation Mechanism	125
5.8	Statistical Flow Quantities for representative actuation configurations	128
6	Conclusions and Recommendations	132
6.1	Conclusions	132
6.2	Recommendations	134
	Bibliography	139
A	Flow of Experiments	140
B	Overview of Flow Facilities	143
C	Wind Tunnel Model Design Procedure	144
C.1	Laminar Boundary Layer	145
C.2	Physical and Similarity Considerations	147
C.3	Trailing Edge Flexibility	148
D	Design and Implementation of Plasma Actuator Configurations	150
D.1	A Background	150

D.2	Spanwise Uniform Transverse Actuation	153
D.3	Spanwise Modulated Transverse Opposing Actuation	155
D.4	Spanwise Modulated Transverse Staggered Actuation	157
D.5	Spanwise Actuation	158
E	Time Resolved PIV Experimental Matrix	161
F	Electric Field Analysis	166
F.1	Transverse Opposing Actuation	166
F.2	Transverse Staggered Actuation	168
F.3	Planar Actuator Configurations	171
G	POD Energies over all tested Free Stream Speeds	175
H	Spanwise Correlation for all Modes and Configurations over all tested $U'_\infty s$	181
H.1	Baseline flow cases	182
H.2	Spanwise Modulated Transverse Opposing Actuation	184
H.3	Spanwise Modulated Transverse Staggered Actuation	187
H.4	Spanwise Actuation	190

List of Figures

2.1	Von Karman Vortex Street behind a cylinder. Taken from [11]	5
2.2	Vortex Shedding behind a cylinder showing l_F , taken from [15]	6
2.3	Filament line sketch of the vortex formation region showing the various transverse fluid motions involved. Taken from Gerrard [14]	7
2.4	Infinite staggered double vortex array for calculating the induced velocity on a vortex	8
2.5	PSD's of the vertical velocity component at various positions downstream of an airfoil with a blunt trailing edge and at different inflow FST's. Image taken from [12]	11
2.6	Roadmap of shedding regimes showing variation in (a) St and (b) C_{pb} (solid line) and C_D (dashed line) with Re for flow behind a circular cylinder. The demarcation between the steady and unsteady and the two dimensional and three dimensional shedding regimes are shown. Taken from [40]	12
2.7	Flow visualisation of (a) Mode A instability at Re 200 and (b) Mode B instability at Re 270. Image taken from [39]	13
2.8	Time traces of the fluctuating base pressure over a D-shaped body. Taken from [28]	15
2.9	Classification of bluff body flow control methods, taken from [4]	15
2.10	St as a function of splitter plate length. Image from [14]	16
2.11	Sketch of experimental setup with D-shaped body in [28]	17
2.12	Normalised averaged C_{pb} and C_D with open loop harmonic actuation. Legend: Re 23000(\bullet), 35000(\circ), 46000(\times), 58000($+$), 70000($*$). Taken from [28]	18
2.13	The Segmented Trailing Edge studied in [29]	19
2.14	Forcing profiles along the upper and lower surfaces for in-phase (L) and out of phase distributed forcing (R), from [21]	20
2.15	Vortical structures at a Re of 4200 for (a) uncontrolled flow, (b) in-phase forcing and (c) out of phase forcing. Taken from [22]	21
2.16	Typical AC DBD Plasma Actuator electrode arrangement, sectional view. Taken from [26]	21
2.17	Schematic illustration of charge build-up on the surface during the input signal (a) negative; and (b) positive half cycle. Figure taken from [26]	22
2.18	Velocity profiles at several downstream positions from a plasma actuator. Taken from [13]	23
2.19	Variation of voltage, current and the induced horizontal and vertical velocities of the DBD Plasma Actuator versus time. Taken from [13]	24
2.20	(a) Relation between the induced thrust, voltage and frequency of the input signal; (b) Corresponding images of plasma for each frequency at point of maximum thrust (saturation). Image taken from [6], based on the work of [36]	25

2.21	Typical Velocity Profiles for different signal voltage amplitudes above an actuator; Taken from [26]	25
2.22	The various geometrical parameters in the plasma actuator layout. Taken from [27]	26
2.23	Variation of peak induced wind with grounded electrode width. Taken from [13]	27
2.24	Actuator saturation thrust versus dielectric constant of common dielectric materials. Taken from [36]	28
2.25	DBD Plasma Actuator Input signal for steady and unsteady actuation. Taken from [37]	29
2.26	(a) One downstream, one upstream and (b) Transverse plasma actuation configurations implemented by Nati [27]	30
2.27	Instantaneous images of the (a) velocity field and (b) vorticity field produced by the transverse actuation. Taken from Nati [27]	30
2.28	Smoke flow visualisation images for wake flow with and without plasma. Taken from [37]	31
2.29	Instantaneous flow field induced by a DBD actuator (shown in the left) forcing perpendicular to an incoming flow. This is a sectional view of the streamwise vortex induced, with a reference vector length of 1 m/s shown. Image taken from [20]	32
2.30	Vorticity magnitude and velocity vectors for (a) CoR DBD VGs and (b) CtR DBD VGs at a jet to free stream ratio of 0.63. The reference vector on the top left shows the U_∞ magnitude and the DBD actuator electrodes are shown on the horizontal axis. Taken from [20]	33
2.31	Schematic of the directional micro-jet device. Taken from [2]	34
3.1	Schematic overview of a 2C-PIV setup. Taken from Raffel et al [30]	36
3.2	Image windowing and discrete cross-correlation map. Taken from Scarano [32]	37
3.3	The motion of a tracer particle in flow. Taken from [25]	38
3.4	Distribution of the light intensity scattered by a 1 μm oil droplet particle in air. Source Raffel et al. [30].	40
3.5	Light sheet formation optics: a) side view, showing the expansion of the laser beam and b) top view, showing beam focus at measurement location. Figures taken from [32]	41
3.6	Particle sizes in image showing (a) Pixel peak locking and (b) too large particle diameter. Figure from Scarano (2007).	42
3.7	Camera and Laser Timing diagram for double frame image acquisition. Taken from Raffel et al [30]	43
3.8	Correlation map evaluation by Fourier Transform. Taken from [32]	44
4.1	Photograph of the experimental setup for the dielectric parametric study	52
4.2	Schematic of the setup used for the dielectric parametric tests, which were carried out in undisturbed flow conditions	53
4.3	Side view showing the flat plate model and the end fixture. All dimensions in mm	55
4.4	Experimental model three-dimensional view, showing coordinate axes adopted	55
4.5	Electrode layout for the various spanwise modulated actuation modes when viewed on the flat trailing edge of the experimental model: (a) Transverse opposing, (b) transverse staggered and (c) spanwise actuation. The various imaged $x-y$ planes of interest within a spatial actuation cycle are also shown	58
4.6	Schematic of the setup used for the time resolved PIV Campaign	59

4.7	Imaging FOV's: (a) $x - y$ plane; (b) $x - z$ plane with transverse actuation; (c) $x - y$ plane for baseline boundary layer measurement and (d) $x - z$ plane with spanwise actuation	61
5.1	Schematic of the setup used for the dielectric parametric tests, which were carried out in undisturbed flow conditions	66
5.2	Time-averaged variation of induced wind speed with voltage and frequency at various streamwise positions for a Cu tape actuator on a 3mm thick Makrolon dielectric sheet	67
5.3	Variation of cycle averaged power consumed per unit actuator length with voltage and frequency for a tested plasma actuator constructed on a 3mm thick Makrolon sheet as dielectric. The length of the plasma actuator tested was 100 mm	67
5.4	Boundary layer profiles over the experimental model at (a) $x = -15$ mm (b) $x = -7.5$ mm and (c) $x = 0$ mm at 5m/s free stream.	69
5.5	Boundary layer profile at the upstream extremity of the plate in the measurement FOV at $U_\infty = 5$ m/s.	70
5.6	Plot of normalised streamwise velocity PSD versus (a) frequency and (b) dimensionless St	71
5.7	Sequence of instantaneous vorticity fields in the Von Karman street for $U_\infty = 5$ m/s behind a bluff body, with non-dimensionalised time spacing $\Delta t^* = \Delta t \times U_\infty/h \simeq 0.32$. Images (a)-(e) represent one complete shedding period with (f) showing the start of the next period	73
5.8	Instantaneous vorticity map for calculating vortex street characteristic parameters, showing the coordinates of the vortices in the field of view	74
5.9	Statistical normalised baseline velocity fields: (a) u/U_∞ (b) v/U_∞ (c) u'/U_∞ and (d) v'/U_∞ for $U_\infty = 5$ m/s	75
5.10	Mean flow streamlines in the near wake for the $U_\infty = 5$ m/s baseline flow case .	75
5.11	Mean streamwise velocity (a) u/U_∞ and (b) mean flow streamlines for the baseline flow case in the wake centerline $x - z$ plane at $U_\infty = 5$ m/s	76
5.12	Wake shear layer $x - z$ plane (a) mean streamwise velocity map showing correlation points and (b) spanwise correlation coefficients for the baseline flow at $U_\infty = 5$ m/s	77
5.13	Velocity fields in m/s for the first two POD modes visualised the $U_\infty = 5$ m/s baseline flow case	78
5.14	Individual and cumulative shares of the Fluctuating KE of the wake captured by the first ten modes of the baseline flow at $U_\infty = 5$ m/s	78
5.15	Sequence of instantaneous vorticity fields in wake for spanwise uniform transverse actuation at $U_\infty = 5$ m/s with a non-dimensionalised time spacing $\Delta t^* = \Delta t \times U_\infty/h \simeq 0.32$	80
5.16	Sequence of instantaneous vorticity fields in near wake for spanwise uniform transverse actuation at $U_\infty = 5$ m/s with a non-dimensionalised time spacing $\Delta t^* = \Delta t \times U_\infty/h \simeq 0.06$	81
5.17	Streamwise velocity PSD for spanwise uniform transverse actuation at $U_\infty = 5$ m/s at ' $z1$ ' at three points in the wake, co-plotted along with the PSD of the baseline flow case	81
5.18	Individual shares of the Fluctuating KE of the wake captured by the first five POD modes with spanwise uniform actuated and un-actuated flow at $U_\infty = 5$ m/s	82
5.19	Zones of plasma due to the exposed-encapsulated electrode combinations on either side showing (a) Ideal non-overlapping and (b) overlapping zones	83

5.20	Schematic showing the electrodes, induced forcing and imaged $x - y$ planes in the spanwise modulated transverse opposing actuation mode	84
5.21	Sequence of instantaneous vorticity fields in wake for transverse opposing actuation with $\lambda^* = 5$, $U_\infty = 5$ m/s at ' $z1'$ ' with a non-dimensionalised time spacing $\Delta t^* = \Delta t \times U_\infty/h \simeq 0.32$	85
5.22	Sequence of instantaneous vorticity fields in wake for transverse opposing actuation with $\lambda^* = 5$, $U_\infty = 5$ m/s at ' $z2'$ ' with a non-dimensionalised time spacing $\Delta t^* = \Delta t \times U_\infty/h \simeq 0.32$	85
5.23	Sequence of instantaneous vorticity fields in wake for transverse opposing actuation with $\lambda^* = 5$, $U_\infty = 5$ m/s at ' $z3'$ ' with a non-dimensionalised time spacing $\Delta t^* = \Delta t \times U_\infty/h \simeq 0.32$	86
5.24	Statistical normalised velocity fields: (a) u/U_∞ (b) v/U_∞ (c) u'/U_∞ and (d) v'/U_∞ for transverse opposing actuation with $\lambda^* = 5$ and $U_\infty = 5$ m/s at ' $z1'$ '	87
5.25	Mean flow streamlines for spanwise location ' $z1'$ ' for transverse opposing actuation with $\lambda^* = 5$ and $U_\infty = 5$ m/s	87
5.26	Statistical normalised velocity fields: (a) u/U_∞ (b) v/U_∞ (c) u'/U_∞ and (d) v'/U_∞ for transverse opposing actuation with $\lambda^* = 5$ and $U_\infty = 5$ m/s at ' $z2'$ '	88
5.27	Mean flow streamlines for spanwise location ' $z2'$ ' for transverse opposing actuation with $\lambda^* = 5$ and $U_\infty = 5$ m/s	88
5.28	Statistical normalised velocity fields: (a) u/U_∞ (b) v/U_∞ (c) u'/U_∞ and (d) v'/U_∞ for transverse opposing actuation with $\lambda^* = 5$ and $U_\infty = 5$ m/s at ' $z3'$ '	89
5.29	Mean flow streamlines for spanwise location ' $z3'$ ' for transverse opposing actuation with $\lambda^* = 5$ and $U_\infty = 5$ m/s	90
5.30	Streamwise velocity PSD for transverse opposing actuation with $\lambda^* = 5$ and $U_\infty = 5$ m/s at ' $z1'$ ' at the three points of interest in the wake, co-plotted along with the PSD of the baseline flow case	91
5.31	Streamwise velocity PSD for transverse opposing actuation with $\lambda^* = 5$ and $U_\infty = 5$ m/s at ' $z2'$ ' at the three points of interest in the wake, co-plotted along with the PSD of the baseline flow case	91
5.32	Streamwise velocity PSD for transverse opposing actuation with $\lambda^* = 5$ and $U_\infty = 5$ m/s at ' $z3'$ ' at the three points of interest in the wake, co-plotted along with the PSD of the baseline flow case	92
5.33	Velocity fields in m/s for the first two POD modes visualised the $U_\infty = 5$ m/s baseline flow case	93
5.34	Velocity fields in m/s for the first two POD modes for transverse opposing actuation with $\lambda^* = 5$ and $U_\infty = 5$ m/s at ' $z1'$ '	93
5.35	Velocity fields in m/s for the first two POD modes for transverse opposing actuation with $\lambda^* = 5$ and $U_\infty = 5$ m/s at ' $z2'$ '	94
5.36	Velocity fields in m/s for the first two POD modes for transverse opposing actuation with $\lambda^* = 5$ and $U_\infty = 5$ m/s at ' $z3'$ '	95
5.37	Individual and cumulative shares of the Fluctuating KE of the wake captured by the first ten POD modes of flow with spanwise modulated transverse opposing actuated flow with $\lambda = 5h$ at $U_\infty = 5$ m/s	96
5.38	Time-averaged and normalised (a) u and (b) w velocity fields in the wake centerline plane for transverse opposing actuation with opposing actuation with $\lambda^* = 3$ and $U_\infty = 8$ m/s. The exposed electrode segments are also indicated in brown	97
5.39	Mean flow streamlines altered to indicate flow features, in the wake centerline plane for transverse opposing actuation with opposing actuation with $\lambda^* = 3$ and $U_\infty = 8$ m/s/ The exposed electrode segments are also indicated in brown	98

5.40	Time-averaged and normalised (a) streamwise and (b) spanwise velocity fields in the shear layer plane for transverse opposing actuation with $\lambda^* = 3$ and $U_\infty = 8$ m/s. The exposed electrode segments are also indicated in brown	98
5.41	Wake shear layer $x-z$ plane (a) mean streamwise velocity map showing correlation points and (b) spanwise correlation coefficients for spanwise modulated transverse opposing actuation with $\lambda^* = 3$ at $U_\infty = 5$ m/s. The exposed electrode segments are also indicated in brown	99
5.42	Schematic of proposed actuation mechanism for spanwise modulated transverse opposing actuation - (A) actuator forcing, (B) induced flows and (C) induced vorticity	101
5.43	Schematic showing the electrodes, induced forcing and imaged $x-y$ planes in the spanwise modulated transverse staggered actuation mode	102
5.44	Sequence of instantaneous vorticity fields in wake for transverse staggered actuation with $\lambda^* = 5$, $U_\infty = 5$ m/s at ' $z1'$ ' with a non-dimensionalised time spacing $\Delta t^* = \Delta t \times U_\infty/h \simeq 0.32$	103
5.45	Sequence of instantaneous vorticity fields in wake for transverse staggered actuation with $\lambda^* = 5$, $U_\infty = 5$ m/s at ' $z2'$ ' with a time-spacing of 0.75 ms	103
5.46	Statistical normalised velocity fields: (a) u/U_∞ (b) v/U_∞ (c) u'/U_∞ and (d) v'/U_∞ for transverse staggered actuation with $\lambda^* = 5$ and $U_\infty = 5$ m/s at ' $z1'$ '	104
5.47	Near wake mean flow streamlines at spanwise location ' $z1'$ ' for transverse staggered actuation with $\lambda^* = 5$ and $U_\infty = 5$	104
5.48	Statistical normalised velocity fields: (a) u/U_∞ (b) v/U_∞ (c) u'/U_∞ and (d) v'/U_∞ for transverse staggered actuation with $\lambda^* = 5$ and $U_\infty = 5$ m/s at ' $z2'$ '	105
5.49	Near wake mean flow streamlines at spanwise location ' $z2'$ ' for transverse staggered actuation with $\lambda^* = 5$ and $U_\infty = 5$	106
5.50	Streamwise velocity PSD for transverse staggered actuation with $\lambda^* = 5$ and $U_\infty = 5$ m/s at ' $z1'$ ' at the three points of interest in the wake, co-plotted along with the PSD of the baseline flow case	106
5.51	Streamwise velocity PSD for transverse staggered actuation with $\lambda^* = 5$ and $U_\infty = 5$ m/s at ' $z2'$ ' at the three points of interest in the wake, co-plotted along with the PSD of the baseline flow case	107
5.52	Velocity fields in m/s for baseline flow at $U_\infty = 5$ m/s	108
5.53	Velocity fields in m/s for the first two POD modes for transverse staggered actuation with $\lambda^* = 5$ and $U_\infty = 5$ m/s at ' $z1'$ '	108
5.54	Velocity fields in m/s for the first two POD modes for transverse staggered actuation with $\lambda^* = 5$ and $U_\infty = 5$ m/s at ' $z2'$ '	109
5.55	Individual and cumulative shares of the Fluctuating KE of the wake captured by the first ten POD modes of flow with spanwise modulated transverse staggered actuated flow with $\lambda = 5h$ at $U_\infty = 5$ m/s	110
5.56	Time-averaged and normalised (a) streamwise and (b) spanwise velocity fields in the shear layer plane for transverse staggered actuation with $\lambda^* = 3$ and $U_\infty = 8$ m/s. The exposed electrode segments are also indicated in brown	111
5.57	Wake shear layer $x-z$ plane (a) mean streamwise velocity map showing correlation points and (b) spanwise correlation coefficients for spanwise modulated transverse staggered actuation with $\lambda^* = 3$ at $U_\infty = 5$ m/s. The exposed electrode segments are also indicated in brown	112
5.58	Schematic of proposed actuation mechanism for spanwise modulated transverse staggered actuation - (A) actuator forcing, (B) induced flows and (C) induced vorticity	114

5.59	Schematic showing the electrodes, induced forcing and imaged $x-y$ planes for the spanwise actuation mode	115
5.60	Sequence of instantaneous vorticity fields in wake for spanwise actuation with $\lambda^* = 2$, $U_\infty = 5$ m/s at ' $z1$ ' with a non-dimensionalised time-spacing of $\Delta t^* = \Delta t \times U_\infty/h = 0.32$	116
5.61	Sequence of instantaneous vorticity fields in wake for spanwise actuation with $\lambda^* = 2$, $U_\infty = 5$ m/s at ' $z2$ ' with a non-dimensionalised time-spacing of $\Delta t^* = \Delta t \times U_\infty/h = 0.32$	116
5.62	Statistical normalised velocity fields: (a) u/U_∞ (b) v/U_∞ (c) u'/U_∞ and (d) v'/U_∞ for spanwise actuation with $\lambda^* = 2$ and $U_\infty = 5$ m/s at ' $z1$ '	117
5.63	Near wake mean flow streamlines at spanwise location ' $z1$ ' for spanwise actuation with $\lambda^* = 2$ and $U_\infty = 5$ m/s	118
5.64	Statistical normalised velocity fields: (a) u/U_∞ (b) v/U_∞ (c) u'/U_∞ and (d) v'/U_∞ for spanwise actuation with $\lambda^* = 2$ and $U_\infty = 5$ m/s at ' $z2$ '	118
5.65	Near wake mean flow streamlines at spanwise location ' $z2$ ' for spanwise actuation with $\lambda^* = 2$ and $U_\infty = 5$ m/s	119
5.66	Streamwise velocity PSD for spanwise actuation with $\lambda^* = 2$ and $U_\infty = 5$ m/s at ' $z1$ ' at the three points of interest in the wake, co-plotted along with the PSD of the baseline flow case	119
5.67	Streamwise velocity PSD for spanwise actuation with $\lambda^* = 2$ and $U_\infty = 5$ m/s at ' $z2$ ' at the three points of interest in the wake, co-plotted along with the PSD of the baseline flow case	120
5.68	Velocity fields in m/s for the first two POD modes visualised the $U_\infty = 5$ m/s baseline flow case	121
5.69	Velocity fields in m/s for the first two POD modes for spanwise actuation with $\lambda^* = 2$ and $U_\infty = 5$ m/s at ' $z1$ '	121
5.70	Velocity fields in m/s for the first two POD modes for spanwise actuation with $\lambda^* = 2$ and $U_\infty = 5$ m/s at ' $z2$ '	122
5.71	Individual shares of the Fluctuating KE of the wake $x-y$ plane captured by the first five POD modes for spanwise actuation configurations $\lambda^* = 2, 3$ and 4 over all imaged planes at $U_\infty = 5$ m/s. The reference baseline flow value is also shown	123
5.72	Time-averaged and normalised (a) streamwise and (b) spanwise velocity fields in the shear layer plane for spanwise actuation with $\lambda^* = 2$ and $U_\infty = 5$ m/s	124
5.73	Wake shear layer $x-z$ plane (a) mean streamwise velocity map showing correlation points and (b) spanwise correlation coefficients for spanwise actuation with $\lambda^* = 2$ at $U_\infty = 5$ m/s. The exposed electrode segments are also indicated	125
5.74	Schematic of proposed actuation mechanism for spanwise modulated transverse opposing actuation - (A) actuator forcing, (B) induced flows (C) induced streamwise vorticity and (D) shear layer modulation	127
5.75	TKE's over all λ^* 's and spanwise locations for spanwise modulated transverse (a) opposing and (b) staggered actuation at $U_\infty = 5$ m/s. The baseline flow TKE is also indicated as reference	129
5.76	TKE's over all λ^* 's and spanwise locations for spanwise actuation at $U_\infty = 5$ m/s. 'B' indicates baseline flow	129
5.77	Wake areas over all λ^* 's and spanwise locations for spanwise modulated transverse (a)opposing and (b) staggered actuation at $U_\infty = 5$ m/s	130
5.78	Wake sizes over all λ^* 's and spanwise locations for spanwise actuation at $U_\infty = 5$ m/s. 'B' indicates baseline flow	131

C.1	Diagram showing the (a) development of the boundary layer over a plate and the various terms associated with it and (b) the displacement thickness. Taken from [33]	146
C.2	Experimental model, side view, showing the tapered section near the trailing edge where the movable end fixture was fitted. All dimensions in mm	148
C.3	Side view, trailing edge fixture for the experimental model. All dimensions in mm	148
D.1	Schematic of a typical planar plasma actuator	153
D.2	Zones of plasma due to the exposed-encapsulated electrode combinations on either side showing (a) Ideal non-overlapping and (b) overlapping zones	154
D.3	Schematic showing the electrodes, induced forcing and imaged $x - y$ planes in the spanwise modulated transverse opposing actuation mode	156
D.4	Schematic showing the electrodes, induced forcing and imaged $x - y$ planes in the spanwise modulated transverse staggered actuation mode	158
D.5	Schematic showing the exposed and covered electrode placement on the upper and lower trailing edge end fixture surfaces and flat plate model surfaces, induced forcing and imaged $x - y$ planes in the spanwise actuation mode	160
F.1	Transverse Opposing electrode layout used for determining electric field and potential	167
F.2	Electric (a) potential and (b) field for transverse opposing actuation	167
F.3	(a) Electric field magnitude and (b) contours of electric field magnitude for 1×10^6 V/m and 2×10^6 V/m for transverse opposing actuation. The peak electric field is 1.866×10^7 V/m, occurring at the ends of the covered electrode	168
F.4	Transverse Staggered electrode layout used for determining electric field and potential	169
F.5	Electric (a) potential and (b) field for transverse opposing actuation	170
F.6	(a) Electric field magnitude and (b) contours of electric field magnitude for 1×10^6 V/m and 2×10^6 V/m for transverse staggered actuation. The peak electric field is 1.755×10^7 V/m, occurring at the end of the covered electrode closest to the exposed electrode	171
F.7	(a) Corner Actuator; (b) and (c) Planar Actuator configurations with and without overlap between the exposed and covered electrodes	172
F.8	Electric field contours of the corner actuator	173
F.9	Electric field contours of a planar actuator with electrode overlap. The peak electric field is 2.12×10^7 V/m at (0,0)	173
F.10	Electric field contours of a planar actuator without electrode overlap. The peak electric field is 2.02×10^7 V/m at (0,0)	174
G.1	Individual shares of the Fluctuating KE of the wake $x - y$ plane captured by the first five POD modes for $\lambda^* = 3$ and 5 configurations over all imaged spanwise locations for spanwise modulated transverse (a), (c) opposing and (b), (d) staggered actuation modes at $U_\infty = 5$ m/s. The Baseline flow values are also shown as reference in each	176
G.2	Individual shares of the Fluctuating KE of the wake $x - y$ plane captured by the first five POD modes for spanwise actuation configurations $\lambda^* = 2, 3$ and 4 over all imaged planes at $U_\infty = 5$ m/s. The reference baseline flow value is also shown	176

G.3	Individual shares of the Fluctuating KE of the wake $x - y$ plane captured by the first five POD modes for $\lambda^* = 3$ and 5 configurations over all imaged spanwise locations for spanwise modulated transverse (a), (c) opposing and (b), (d) staggered actuation modes at $U_\infty = 8$ m/s. The Baseline flow values are also shown as reference in each	177
G.4	Individual shares of the Fluctuating KE of the wake $x - y$ plane captured by the first five POD modes for spanwise actuation configurations $\lambda^* = 2, 3$ and 4 over all imaged planes at $U_\infty = 8$ m/s. The Baseline flow values are also shown as reference in each	177
G.5	Individual shares of the Fluctuating KE of the wake $x - y$ plane captured by the first five POD modes for $\lambda^* = 3$ and 5 configurations over all imaged spanwise locations for spanwise modulated transverse (a), (c) opposing and (b), (d) staggered actuation modes at $U_\infty = 11$ m/s. The Baseline flow values are also shown as reference in each	178
G.6	Individual shares of the Fluctuating KE of the wake $x - y$ plane captured by the first five POD modes for spanwise actuation configurations $\lambda^* = 2, 3$ and 4 over all imaged planes at $U_\infty = 11$ m/s. The Baseline flow values are also shown as reference in each	178
G.7	Individual shares of the Fluctuating KE of the wake $x - y$ plane captured by the first five POD modes for $\lambda^* = 3$ and 5 configurations over all imaged spanwise locations for spanwise modulated transverse (a), (c) opposing and (b), (d) staggered actuation modes at $U_\infty = 14$ m/s. The Baseline flow values are also shown as reference in each	179
G.8	Individual shares of the Fluctuating KE of the wake $x - y$ plane captured by the first five POD modes for spanwise actuation configurations $\lambda^* = 2, 3$ and 4 over all imaged planes at $U_\infty = 14$ m/s. The Baseline flow values are also shown as reference in each	179
G.9	Individual shares of the Fluctuating KE of the wake $x - y$ plane captured by the first five POD modes for $\lambda^* = 3$ and 5 configurations over all imaged spanwise locations for spanwise modulated transverse (a), (c) opposing and (b), (d) staggered actuation modes at $U_\infty = 17$ m/s. The Baseline flow values are also shown as reference in each	180
G.10	Individual shares of the Fluctuating KE of the wake $x - y$ plane captured by the first five POD modes for spanwise actuation configurations $\lambda^* = 2, 3$ and 4 over all imaged planes at $U_\infty = 17$ m/s. The Baseline flow values are also shown as reference in each	180
H.1	Spanwise velocity-correlations for baseline flow at $U_\infty = 5$ m/s	182
H.2	Spanwise velocity-correlations for baseline flow at $U_\infty = 8$ m/s	182
H.3	Spanwise velocity-correlations for baseline flow at $U_\infty = 11$ m/s	183
H.4	Spanwise velocity-correlations for baseline flow at $U_\infty = 14$ m/s	183
H.5	Spanwise velocity-correlations for baseline flow at $U_\infty = 17$ m/s	184
H.6	Spanwise velocity-correlations for transverse opposing actuated flow at $U_\infty = 5$ m/s	185
H.7	Spanwise velocity-correlations for transverse opposing actuated flow at $U_\infty = 8$ m/s	185
H.8	Spanwise velocity-correlations for transverse opposing actuated flow at $U_\infty = 11$ m/s	186
H.9	Spanwise velocity-correlations for transverse opposing actuated flow at $U_\infty = 14$ m/s	186

H.10	Spanwise velocity-correlations for transverse opposing actuated flow at $U_\infty = 17$ m/s	187
H.11	Spanwise velocity-correlations for transverse staggered actuated flow at $U_\infty = 5$ m/s	188
H.12	Spanwise velocity-correlations for transverse staggered actuated flow at $U_\infty = 8$ m/s	188
H.13	Spanwise velocity-correlations for transverse staggered actuated flow at $U_\infty = 11$ m/s	189
H.14	Spanwise velocity-correlations for transverse staggered actuated flow at $U_\infty = 14$ m/s	189
H.15	Spanwise velocity-correlations for transverse staggered actuated flow at $U_\infty = 17$ m/s	190
H.16	Spanwise velocity-correlations for spanwise actuated flow for $\lambda^* = 2$ at $U_\infty = 5$ m/s	191
H.17	Spanwise velocity-correlations for spanwise actuated flow for $\lambda^* = 2$ at $U_\infty = 8$ m/s	191
H.18	Spanwise velocity-correlations for spanwise actuated flow for $\lambda^* = 2$ at $U_\infty = 11$ m/s	192
H.19	Spanwise velocity-correlations for spanwise actuated flow for $\lambda^* = 2$ at $U_\infty = 14$ m/s	192
H.20	Spanwise velocity-correlations for spanwise actuated flow for $\lambda^* = 2$ at $U_\infty = 17$ m/s	193
H.21	Spanwise velocity-correlations for spanwise actuated flow for $\lambda^* = 4$ at $U_\infty = 5$ m/s	193
H.22	Spanwise velocity-correlations for spanwise actuated flow for $\lambda^* = 4$ at $U_\infty = 8$ m/s	194
H.23	Spanwise velocity-correlations for spanwise actuated flow for $\lambda^* = 4$ at $U_\infty = 11$ m/s	194
H.24	Spanwise velocity-correlations for spanwise actuated flow for $\lambda^* = 4$ at $U_\infty = 14$ m/s	195
H.25	Spanwise velocity-correlations for spanwise actuated flow for $\lambda^* = 4$ at $U_\infty = 17$ m/s	195

List of Tables

4.1	Experimental matrix for dielectric parametric test for each dielectric sheet of $t = 2$ and 3 mm	53
4.2	Spanwise modulated actuation modes and corresponding configurations tested during time resolved experimental PIV Campaign	56
4.3	Various actuation modes and corresponding no. of measured $x - y$ planes imaged	57
4.4	PIV Experimental Details Summarised for a representative measurement set	63
4.5	Various actuation modes and corresponding no. of measurement $x - y$ and $x - z$ planes imaged at each free stream velocity tested	64
5.1	Boundary layer parameters over the flat plate for various tested free stream speeds	69
5.2	St at the various tested free stream speeds for flow over the experimental model	71
5.3	Wake, Shear layer and Boundary layer states for flow over the experimental model at various tested free stream speeds, estimated using Fig 2.6(b)	72
C.1	Model characteristic values at the lower and upper tested $U'_\infty s$	147

Nomenclature

Abbreviations

2C-PIV	Two component particle image velocimetry
AC	Alternate current
A/D	Analog to digital converter
BL	Boundary Layer
CCD	Charge coupled device
CMOS	Complementary metal oxide semiconductor
DBD	Dielectric barrier discharge
FOV	Field of view
HVA	High Voltage Amplifier
Nd:YAG	Neodymium-doped yttrium aluminium garnet
PIV	Particle Image Velocimetry
POD	Proper orthogonal decomposition
PSD	Power Spectral Density
RMS	Root mean square
SVD	Singular value decomposition
TKE	Fluctuation kinetic energy

Greek Symbols

Δt	Laser pulse separation time, μs
δ^*	Boundary layer displacement thickness, mm
δ	Boundary Layer thickness, mm
δ_{99}	Boundary Layer thickness, mm
δ_z	Laser sheet depth of field, mm
ϵ_0	Faraday constant, C/mol
ϵ	Dielectric constant
Γ	Circulation, s^{-1}
λ	Wavelength of laser light, m
λ	Spanwise modulated spatial actuation wavelength, mm
λ^*	Nondimensionalised spanwise modulated spatial actuation wavelength
λ_{VK}	Vortex street spacing wavelength, mm
μ	Dynamic viscosity, kg/(m.s.)

ν	Kinematic viscosity, m^2/s
ω	Vorticity, s^{-1}
ϕ	POD spatial modes
ϕ	Electric potential, V
ψ	Orthogonal POD basis functions
ρ	Fluid density, kg/m^3
ρ_c	Net charge density, C/m^3
ρ_p	Tracer particle density, kg/m^3
τ_f	Characteristic flow time scale, s
τ_p	Tracer particle characteristic response time, s
θ	Boundary layer momentum thickness, mm

Latin Symbols

A	POD observation data matrix
B	Trailing edge bluntness parameter
C	Correlation matrix
D	Diameter, m
d_i	Image size, m
d_i	Object size, m
d_p	Particle diameter, μm
d_τ	Effective particle image size, μm
d_{diff}	Diffacted particle size, μm
d_{geom}	Geometric particle size, μm
E_0	Electric Field, V/m
E	Electric Field, V/m
E_b	Breakdown Electric Field, V/m
f	Focal length, m
f_{AC}	Plasma AC input signal frequency, Hz
f_{PIV}	PIV frequency of image-pair acquisition, Hz
f_s	Sampling frequency, Hz
f_{St_0}	Vortex shedding frequency, Hz
$f_\#$	Aperture number
f_{flow}	Characteristic flow frequency, Hz
F_v	Viscous force, N
F_{el}	Electrostatic force, N
g	Electrode gap, mm
H	Boundary layer shape factor
h	Trailing edge height, mm
I	Pixel intensity
L	Length, mm
M	Magnification factor
q_n	Net charge level, C
$R_{II'}$	Cross correlation matrix
R	Correlation coefficient
Re	Reynolds number

Re_{cr}	Critical Reynolds number
S	Symmetrical component of velocity gradient tensor
S	Diagonal matrix obtained from SVD of A
S_k	Stokes number
St	Strouhal number
St_0	Baseline shedding Strouhal number
t	Dielectric thickness, mm
t	Time coordinate, s
T_1	Pulse period, s
T_2	Pulse active actuation period, s
u	Mean streamwise velocity, m/s
u'	Streamwise velocity fluctuation, m/s
U_∞	Free stream velocity, m/s
\mathbf{U}_f	Fluid velocity, m/s
\mathbf{U}_p	Particle velocity, m/s
\mathbf{U}_s	Slipping velocity, m/s
v	Mean transverse velocity, m/s
v'	Transverse velocity fluctuation, m/s
U	Left singular vector
U_{conv}	Vortex street convection velocity, m/s
V_{pp}	Peak to peak voltage, V
V	Right singular vector
w	Mean spanwise velocity, m/s
w'	Spanwise velocity fluctuation, m/s
W	Anti-symmetric component of velocity gradient tensor
w	Electrode width, mm
w_c	Covered electrode width, mm
w_e	Exposed electrode width, mm
x	Streamwise coordinate, mm
Δx	Vector spatial resolution, streamwise direction, mm
y	Transverse coordinate, mm
Δy	Vector spatial resolution, transverse direction, mm
z	Spanwise coordinate, mm

Chapter 1

Introduction

1.1 Background and Relevance

Von Karman Vortex Streets are formed in the wakes of bluff bodies over a wide range of Reynolds numbers, from around 50 to more than a million. These Vortex streets are composed of vortices shed alternately and periodically from either side of a body in a fluid flow in the downstream direction when the flow is unable to follow the aft part of the body beyond the separation point. In the context of this Thesis, bluff bodies are non-streamlined bodies that give rise to vortex streets in their wake when in a fluid flow. They are broadly of two types:

1. Bluff bodies with non-fixed separation points for flow over them, depending on the flow regime. Examples include spheres and cylinders
2. Bluff bodies with fixed separation points for flow over them. Examples include objects with truncated or blunt trailing edges.

Vortex shedding occurs widely in engineering. For many applications like Wind Turbine blades, truncated or blunt and divergent Trailing Edges for airfoil sections have been explored. They are known to have several benefits like enhanced structural strength, for which they have been proposed for the inboard blade sections, where the airfoil sections are the thickest. Standish and van Dam [34] observed a significant enhancement of the aerodynamic performance after modifying their base line airfoil section for wind turbine blades to a blunt and divergent trailing edge one. They attributed these improvements to the downstream movement of the pressure recovery region to occur off the surface in the wake, and thus, reducing the adverse pressure gradients on both the pressure and suction sides. Such airfoils, however suffer from the adverse effects of large wakes and vortex shedding due to the flow separation at the sharp corners at the Trailing Edge. These effects include increased base drag, aeroelastic problems and unfavourable acoustic noise [12].

Noise control is a critical area of research in Aeroacoustics and Aerodynamics. The increase in civil aviation traffic coupled with larger populations around airports has resulted in continued efforts to reduce aircraft noise during takeoff and landing. The use of high-bypass jet engines has resulted in the reduction of the jet engine component in aircraft noise during take-off and landing, when the engines are throttled down. Now the airframe, specifically the landing gear and high lift system represents an important noise source due to the bluff body characteristics

of the landing gear. The large scale flow separation results in noise caused by the unsteady wake and large scale periodic vortex production [37].

Acoustic noise can also be caused by the vibration of the body itself due to the vortex shedding in its wake. A practical example is the "singing" of suspended telephone and power wires in high speed wind. This is because pressure fluctuations are induced by the shed vortices on the downstream base of the body, causing acoustic vibrations as well as fluctuating aerodynamic forces on the body. A particularly dangerous phenomenon is Vortex-Induced Vibration (VIV) which occurs when the frequency of vortex shedding matches the structural resonance frequency of the body. In this case, the structure begins to resonate and its motion becomes self-sustaining. This was the reason behind the violent oscillations and eventual destruction of several tall factory chimneys at many places around the world. VIV was responsible for the cracking suffered by one of the three steel support poles of a towering thrill ride at Cedar Point in Sandusky, Ohio in 2002, which led to its collapse [18].

To summarise, several undesirable effects are caused by vortex shedding from objects, particularly bluff bodies in flows. These include:

- Acoustic waves and noise
- Increased mean drag due to the low pressure region in the wake close to the body
- Fluctuating aerodynamic forces
- Vortex Induced Structural Vibrations

It is clear that real engineering benefits can be obtained from suppressing vortex shedding on a body in a flow, such as reduced structural fatigue and wear-and-tear, reduced noise, control over the wake flow, etc. Bluff body vortex shedding suppression and control is one of the most popular and widely researched and experimented areas in aerodynamics, due to the fact that such bodies are commonly encountered and are easy to experiment upon. Streamlined bodies are not so popular, however, due to the difficulties associated with the adverse pressure gradient to the flow.

Various methods of controlling and suppressing vortex shedding from bluff bodies have been devised, as classified by Choi et al [4]. Passive methods usually are static shape modifications to the trailing edge, in the form of splitter plates [14], [31], segmented [29] [8] and sinusoidal [38] trailing edges, etc. These methods are well investigated, but have drawbacks such as lack of controllability and adaptability. Active flow control techniques usually involve powered actuators with or without feedback from a sensor in the flow (termed open and closed loop methods, respectively). Currently many such techniques are being tested and researched upon due to the wider range of applications and flow conditions they can be applied to. Examples include distributed forcing [21] [22], harmonic closed loop forcing [28], body rotation [10], etc. Common drawbacks associated with such methods include cumbersome setup or excessive power requirements, etc.

A relatively novel and promising active flow control device that is not limited by the drawbacks of other such devices is the Dielectric Barrier Discharge (DBD) Plasma Actuator. These have been applied in various ways to aerodynamic flow control, such as separation delay over a circular cylinder [35], making a directional micro jet device [2], as vortex generators [20], etc. One of the popular and emerging areas of application of such devices is bluff body vortex shedding control, for e.g. from cylinders [19] [37] and D-shaped bluff bodies [27] etc.

1.2 Scope of Current Work

The broad objective of the research and experiments undertaken and described here was to overcome the problem of acoustic noise emission from airfoils with blunt trailing edges due to regular, periodic Karman vortex shedding. To reduce the complexity of the problem at hand, the experimental model that was tested upon was approximated as a D-shaped bluff body with the following features:

1. *Bluff body* from which vortex shedding takes place, so that vortex suppression techniques can be tested.
2. *Blunt trailing edge* so that the flow over it separates from it at fixed points.
3. *Flat plate* surfaces that offer no pressure gradient to the flow over the model.
4. *Rounded nose* to ensure attached flow and so that the model can approximate an airfoil.
5. *Laminar flow* everywhere over the model.

This Thesis aimed to extend the success of Nati's [27] use of spanwise uniform transverse mode plasma actuators on a D-shaped bluff body in suppressing vortex shedding by modulating the actuation in the spanwise direction. The mechanism of shedding, however, was expected to be strongly three dimensional and hence different from Nati's two dimensional mechanism. One of the goals of the thesis was to devise appropriate configurations that improve the effectiveness and desirability of plasma actuators in bluff body vortex shedding control, as well as to develop insights that add to the body of work concerning experimental three-dimensional bluff body vortex shedding control from a flow-physics perspective. To achieve this, the following were the main aspects of the study carried out:

- The phenomenon of vortex shedding was studied along with its characteristic features that can be utilised in suppressing it. Various vortex shedding control techniques were studied and reviewed for this purpose, along with their underlying mechanisms and limitations. Special attention was given to the differences between two-dimensional and three-dimensional control techniques, since the former is rather extensively studied, while the latter is what was attempted in this work.
- The principles of plasma actuation and the various geometrical and electrical parameters involved in designing and constructing them were studied. In order to build 'hands-on' familiarity with these actuators, an experimental parametric study was carried out where the various actuation parameters were varied to arrive at an optimum combination that brings about the maximum forcing.
- Various spanwise modulated configurations were tested on the experimental body using plasma actuators at various inflow speeds. A spanwise uniform configuration similar to the one that was found most effective by Nati [27], namely transverse actuation was implemented as a benchmark for the results obtained from spanwise modulated actuation, both in a quantitative and qualitative manner, in terms of the underlying effect of the actuation on the flow, etc.
- The primary flow measurement technique used in this work was time-resolved Particle Image Velocimetry. The mechanism of interaction between the induced wind generated by the various implemented configurations and the unsteady, dynamic vortex shedding in the near wake of the bluff body was established based on the planar, time-resolved velocity fields obtained from this measurement technique. Various analysis techniques were applied

on these velocity fields and the information obtained was used to construct a physical model that best describes the effect of the actuation on the flow. The upper limit of effectiveness of the various actuation modes in suppressing or strongly attenuating vortex shedding was also established.

- Suggestions for future work, based on reported successes in shedding control from literature as well as 'interesting' avenues of research that opened up based on the results obtained from this work but could not be tackled due to the time and material constraints present will be recommended.

1.3 Structure of this Report

This report is organised based on the sequence of steps that were followed during the course of the Thesis work. Chapter two is based on the Literature study that was undertaken at the beginning of the project. This was carried out in order to get an understanding of the problem at hand. It consists of sections reviewing the physics and properties of Von Karman Vortex Shedding, classification of popular vortex shedding methods along with examples, plasma actuators, and some common applications of plasma actuation in aerodynamic flow control. Chapter three describes the fundamentals of the flow measurement technique used - PIV and the techniques that will be used to process the PIV-obtained data in this study, such as Proper Orthogonal Decomposition (POD) and power spectral analysis. Chapter four describes the experimental aspects of this study - the setup and details of the dielectric parametric study and the PIV and descriptions of the plasma actuator configurations and their accompanying details that are essential to understand the various results that will be presented in Chapter five. Chapter five contains the obtained results of all the experiments carried out in this work - dielectric parametric study and time resolved PIV and also presents the proposed actuation mechanisms for the various modes and configurations. The conclusion of this research is presented in chapter six together with recommendations for future work.

Chapter 2

Theory

2.1 Vortex Shedding

2.1.1 Mechanism of Vortex Shedding

From the point of view of Vortex Theory, vortices are the sinews and muscles of separated flows. Separated flows from bluff bodies can be divided into steady (bubble flow) and unsteady separated flows. The Karman vortex street, which is our main concern in this study, is of the unsteady type [40].

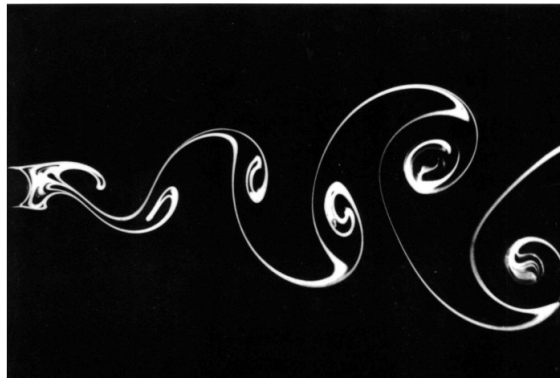


Figure 2.1: Von Karman Vortex Street behind a cylinder. Taken from [11]

Considering the flow behind a circular cylinder, at low Reynolds numbers ($4 < Re < 49$), a pair of standing vortices within separation bubbles is formed behind the cylinder due to a local topological bifurcation. A mathematical concept used in studying dynamical systems, bifurcation is said to occur when a smooth change to certain parameter values (in this case the flow Re) causes a sudden topological change in the system's behaviour.

At $Re \simeq 49$, the flow becomes linearly unstable with respect to two-dimensional disturbances and experiences a Hopf bifurcation, leading to laminar and parallel vortex shedding giving rise to

a vortex street that is linearly stable to three-dimensional disturbances. At this critical Reynolds number, disturbance waves travel downstream along the sides of the steady, closed separation bubbles. The velocity fluctuation causes a Reynolds stress which increases the base suction beyond what it would be in steady flow. A further increase in Re then causes a sudden inception of wake instability and growth of fluctuations, breaking the bubbles into the vortex shedding mode. This happens in the near-wake 'vortex formation region' which is crucial for the entire wake since it is the region where vortex shedding is initiated at all Re 's. The size of this region varies with the Re and the flow regime.

A mention of the vortex formation region is essential to the understanding of the physics of vortex shedding. In general, at all Reynolds numbers the end of the vortex formation region marks both the initial position of the fully shed vortex and the location at which its strength is a maximum, according to Griffin [15]. Several definitions of the vortex formation region length, or its extent in the streamwise direction, have been proposed over the years, and listed by Griffin:

1. The minimum of the mean pressure on the wake centreline;
2. The maximum of the wake velocity fluctuation off the wake centreline; this fluctuation is expected to occur at at the vortex shedding frequency;
3. The maximum of the wake velocity fluctuation on the wake centreline. Here, the fluctuation is expected to occur at twice the shedding frequency, due to the fact that at the wake centreline and close to it, the interaction between the shear layers on either side causes a movement of fluid from either side at twice the shedding frequency.
4. The minimum transverse spacing of the maxima of the velocity fluctuation field close to the body base region.

Fig 2.2 taken from [15] shows vortex shedding behind an oscillating cylinder visualised with smoke particles in the free stream. The vortex formation region is visible as the dark, low velocity region behind the cylinder. The vortex formation length is marked as l_F .



Figure 2.2: Vortex Shedding behind a cylinder showing l_F , taken from [15]

It is only in the *three-dimensional wake regime* at Re values of $O(10^2)$ and higher that the mechanism of vortex shedding changes to the one that we are interested in. At low Reynolds number,

as mentioned earlier, the wake vortices are formed due to a kinematic topological bifurcation. But it is only at these higher Re 's that a boundary layer and its separated shear layer can be sufficiently thin, and wake vortices be formed by shear layer rolling up. The change in the mechanism of Vortex Shedding as the Re changes is mentioned in some detail in Sec. 2.1.2.

At $Re \gg 1$ the interaction of the upper and lower separated shear layers plays an important role in the vortex formation region, as reported by Gerrard [14]. A transverse perturbation is also necessary to initiate instability and break the symmetry between the upper and lower shear layers separating from the bluff body. Due to the continuous feeding of vorticity from the upper separating shear layer, a vortex of increasing strength is formed with $\omega < 0$. Due to asymmetric transverse disturbance, suppose that this vortex is stronger than that formed with $\omega > 0$ from the lower side. It then entrains the lower side fluid across the wake to enter the upper side. This causes a vorticity cancellation at the upper side vortex, which weakens it and eventually cuts off the feeding shear layer, causing the vortex with $\omega < 0$ to be shed downstream. Due to this, the vorticity in the shed vortex is always much lesser than that in the separating shear layer from where it arose. The lower shear layer will then roll up into a stronger vortex, entraining fluid from the upper shear layer, and eventually causing a vortex to be shed with $\omega > 0$. This process is repeated to form a cycle giving rise to a Von Karman Vortex Street.

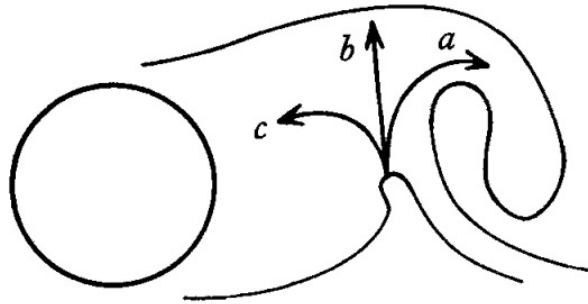


Figure 2.3: Filament line sketch of the vortex formation region showing the various transverse fluid motions involved. Taken from Gerrard [14]

Gerrard further proposed that the entrained fluid from one side enters different regions within the vortex growing on the other side. Looking at Fig 2.3, fluid from the lower side can be thought to split up into three streams - 'a' enters the growing vortex on the upper side and weakens it, fluid 'b' moves towards the feeding shear layer and eventually cuts it off, and fluid 'c' turns back around towards the lower shear layer and adds to the fluid in it that rolls up into the lower vortex. Hence, each shed vortex at one shear layer corresponds to a movement of fluid from the other side that goes towards it ('b') and one that turns back ('c'), thus two motions of fluid across the centreline. That is why the dominant frequency content along the centreline within the vortex formation region is at twice the shedding frequency.

2.1.2 Properties of the Von Karman Vortex Street

Physical Quantities and Parameters

It is instructive to start from the analysis of Von-Karman, who modelled the flow behind a bluff body by an infinite double array of point vortices. The characteristic feature of the street is that the pattern is stationary in the frame of reference of the bluff body. The convection velocity of the vortices can be calculated by calculating the velocity induced at one vortex by the others. The velocity generated by all the other vortices has to be such that the pattern remains undisturbed.

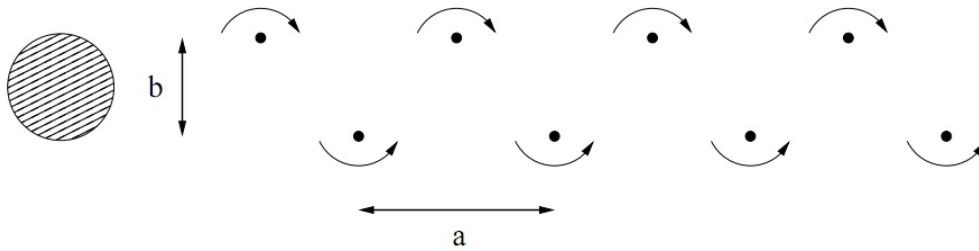


Figure 2.4: Infinite staggered double vortex array for calculating the induced velocity on a vortex

The street can be taken as infinitely extended in both directions. Sufficiently far from the bluff body, the effect of the body itself can be neglected. By making calculations based on the complex potentials of the vortices, it can be derived that the pattern convects at a constant speed $U_{vort} = (\Gamma/2a)\tanh(\pi b/a)$, upstream relative to the free stream, where Γ is the strength of each of the vortices in the co- and counter-clockwise rotating vortex rows, and a and b are the streamwise and transverse spacing respectively of successive vortices in the street as seen in Fig 2.4. Karman found in 1911 that the double row is only stable in the staggered configuration for b/a equal to 0.283.

There are various inherent characteristics of the vortex shedding process such as the strong symmetry that is required between the separating shear layers for interaction to take place between them. Asymmetry of flow around otherwise symmetric bluff bodies or asymmetries in the bluff bodies themselves are known to affect or even suppress periodic vortex shedding. This feature is exploited in various vortex shedding suppression mechanisms as will be shown in the sections that follow. An alternating and periodic Karman vortex street will not result if the two shear layers are too different to couple [10]. Bailey (2001) and Bailey et al. (2003) showed that for a coordinate system moving at the convective speed of two rows of vortices with unequal strengths Γ_1 and Γ_2 , a stable arrangement of vortices with spacing ratio 0.283 existed for only a range of circulation ratios shown in Eq. 2.1. For circulation ratios outside of this range, no stable configuration was found and the periodic vortex street was suppressed.

$$0.38 < \frac{\Gamma_1}{\Gamma_2} < 2.62 \quad (2.1)$$

Another requirement for a stable vortex street is the staggering between the vortices shed from the upper and lower surfaces. This is closely related to the fact that the wake is a region

of absolute instability. During the initial phases shedding, the interaction between the upper and lower vortex rows starts and any perturbation in the symmetry between them is amplified with the result that vortices in the far wake are aligned in an alternating order with a stretched spatial wavelength. The wake instability locks on to the large vortical structures. The alternating sequence of vortices in the far wake induces periodic perturbation in the near wake; hence the far wake vortices have an impact on the upstream processes. These vortices trigger an alternate shedding of larger vortices in the near wake. This requirement is exploited by some closed loop control methods in suppressing shedding, such as in [28], where the development of wake instabilities is prevented by enforcing in-phase shedding.

The main characteristic property of a vortex street is the frequency of shedding. Strouhal (1878) observed that the frequency f of vortex shedding behind a cylinder is proportional to U_∞/L , with the proportionality constant now being known as the Strouhal number:

$$St = \frac{fL}{U_\infty} \quad (2.2)$$

where U_∞ is the free stream speed, L is the bluffness geometric parameter, equal to the diameter D for a circular cylinder or the Trailing Edge height h for a object with fixed separation at the Trailing Edge. St is a constant that depends on the object geometry and to a smaller extent on the inflow condition. Assuming uniform inflow conditions and fixed object diameter, the frequency adjusts itself to U_∞ (and hence the Re) - an increase in free stream speed will cause an increase in shedding frequency, and so on. The St value is reported in many sources as 0.24 for a bluff body with a fixed separation location, for e.g. in [38]. For a circular cylinder, the value is around 0.2. For e.g. a value of 0.19 was observed in [10]. It is also important to note that vortex shedding is not a strictly periodic process, but is actually randomly modulated in frequency and phase, as established by Budny et al (1979).

Effect of Inflow Turbulence

The state of the incoming boundary layer has a significant effect on the wake and vortex shedding behind a bluff body. In the work of Zhang et al [41] the effect of Free Stream Turbulence (FST) and surface roughness on the shedding properties behind a symmetric airfoil was studied in detail. By comparing Power Spectral Density (PSD) profiles in the wake of the airfoil with different surface roughness acquired from hot-wire anemometry, it was concluded that increasing the roughness decreases the vortex shedding frequency. This is because (a) the boundary layer at the airfoil TE thickens, increasing the mixing and turbulent transport levels; and (b) surface roughness causes boundary layers to have higher rates of entrainment of freestream fluid, and thus, to grow faster. The increased turbulent boundary layer height increases the effective body thickness which for a given St and U_∞ causes a decrease in the shedding frequency. The resulting thicker turbulent boundary layers at the airfoil trailing edge change the vortex dynamics in the wake and giving rise to an increased separation region. This gives larger vortices and greater dissipation of momentum in the wake. This will cause vortex shedding frequency to shift to lower values, hence a decrease in the St .

The inflow FST also has an effect on the shedding frequency. This has been extensively studied and reported in many sources. According to Gerrard [14], higher FST results in lower wake shedding frequencies due to higher diffusion levels in the wake. This results in longer times for sufficient amounts of vorticity to be carried over in the crossflow from one side to another to initiate shedding. This was also confirmed by Zhang et al in [39] from PSD results at two FST values of 0.9% and 5.5%.

In the results from experiments on the effect of FST on the wake behind a blunt and divergent airfoil from El-Gammal et al [12], it is clear that increased FST (and the accompanying higher dissipation effects) leads to faster wake growth, broader wake mean velocity profiles, and a weaker vortex shedding that dies out quicker, due to the increased interaction between the streamwise and spanwise vortex systems in the near wake (which are also called the 'ribs' and 'rolls' respectively), which leads to roll dislocation. Fig. 2.5 shows the PSD of the vertical velocity component at $(1/12)$, 1.5 and 3.8 times chord streamwise downstream positions behind an airfoil with a blunt TE in the first, second and third image rows, with 0.3% FST (left column) and 5% FST (right column). It can be seen that close to the TE, the power spectra at both 0.3% and 5% FST show a strong shedding peak. However, further downstream at 1.5 times the chord, no shedding peak is seen for 5% FST whereas a weak peak is still seen at 0.3% FST.

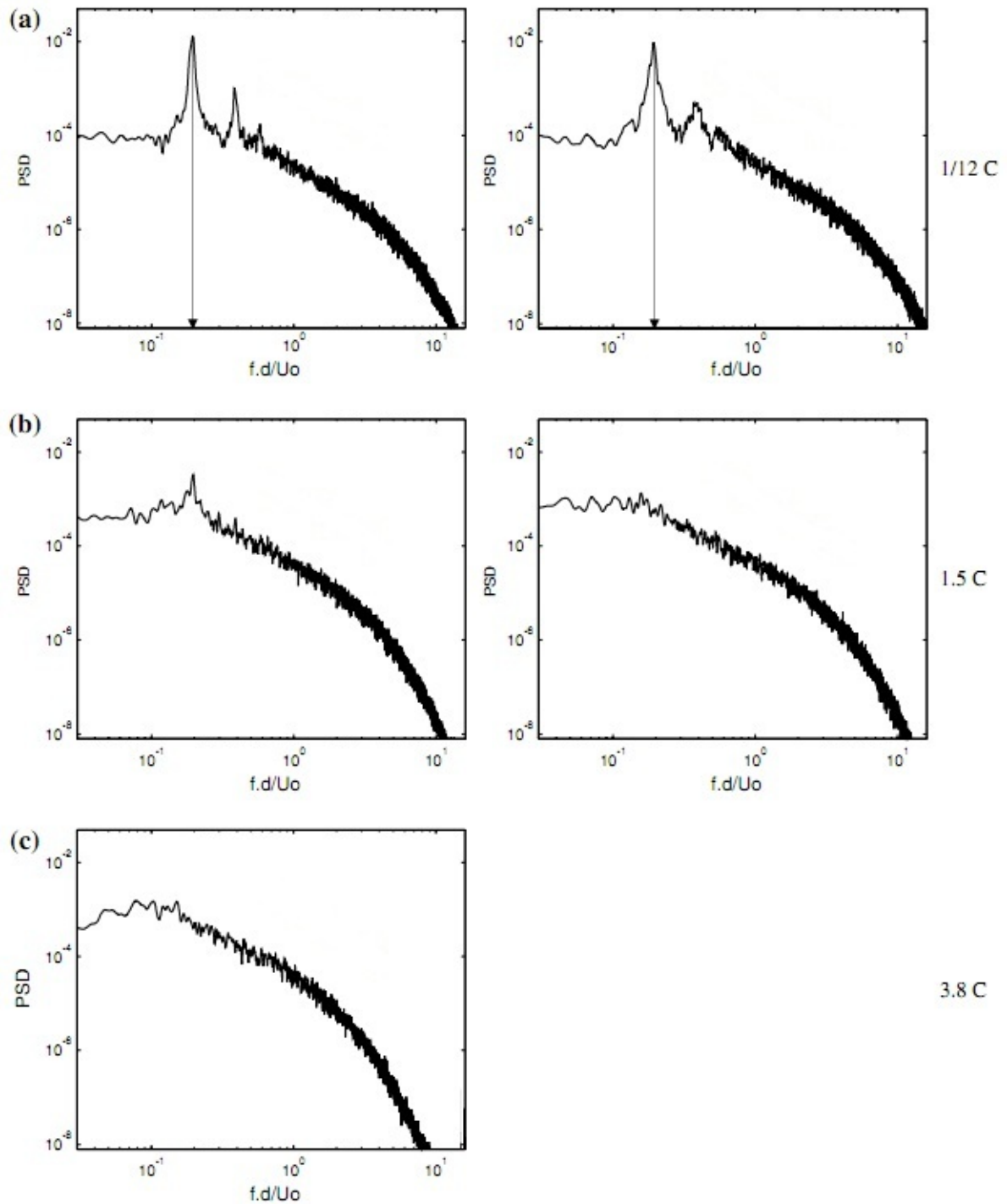


Figure 2.5: PSD's of the vertical velocity component at various positions downstream of an airfoil with a blunt trailing edge and at different inflow FST's. Image taken from [12]

Shedding regimes with Re

The behaviour and mechanism of the Von-Karman Vortex Street varies significantly over the range of inflow Re for flow over a bluff body. Considering a circular cylinder of diameter D , the curves showing the variations of the shedding St , base drag C_D and pressure coefficient $-C_{pb}$ with Re are shown in Fig 2.6 and divided into segments demarcated by points A to H, for ease of analysis. Each of these segments reflects the changing behaviour of the flow.

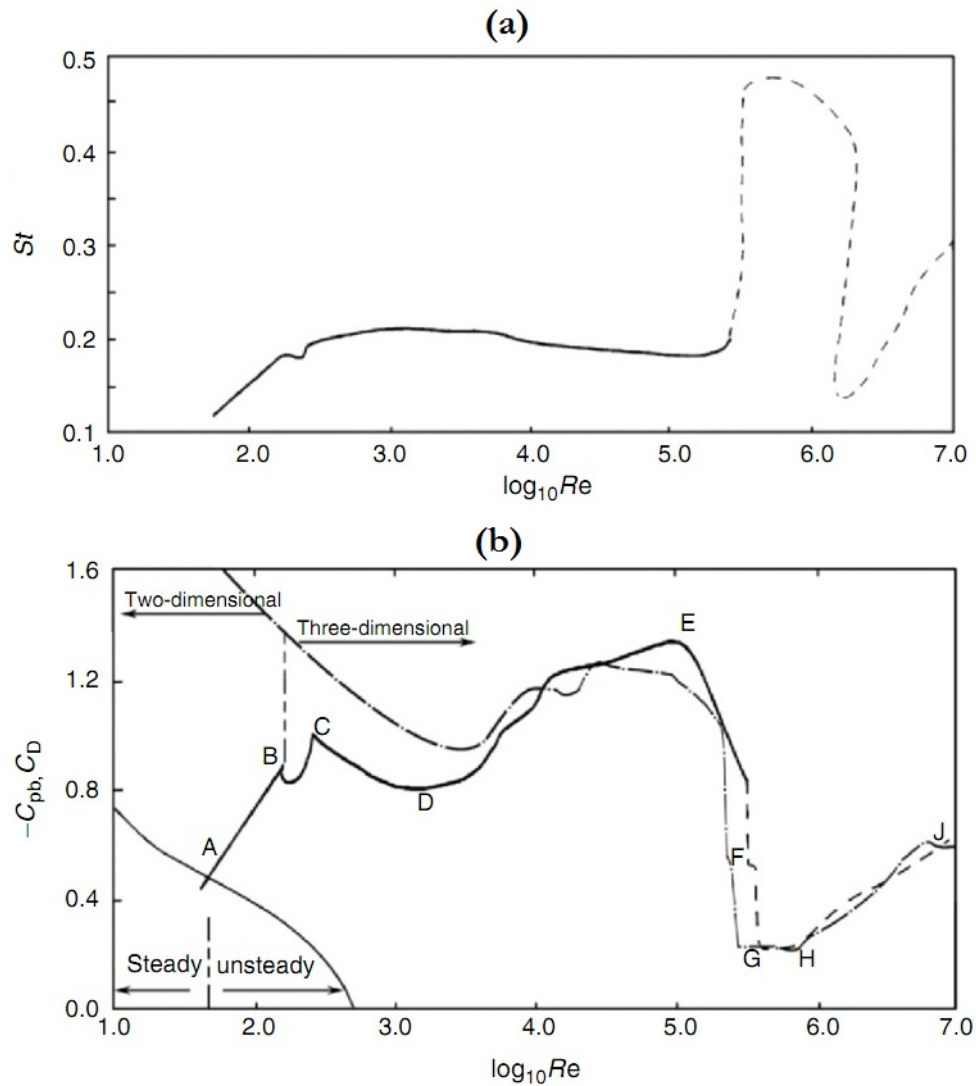


Figure 2.6: Roadmap of shedding regimes showing variation in (a) St and (b) C_{pb} (solid line) and C_D (dashed line) with Re for flow behind a circular cylinder. The demarcation between the steady and unsteady and the two dimensional and three dimensional shedding regimes are shown. Taken from [40]

The various shedding regimes are, from Williamson [39]:

1. $Re < 49$, before A:

As mentioned in Sec 2.1.1, a pair of standing vortices is formed behind the cylinder due to a local kinematic topological bifurcation. For $4 < Re < 49$, the flow is globally stable with respect to all three dimensional disturbances.

2. A to B, $49 < Re < 194$:

At $Re \simeq 49$, the flow becomes linearly unstable with respect to two dimensional disturbances and experiences a Hopf bifurcation, leading to laminar and parallel vortex shedding that is linearly stable to three dimensional disturbances.

For $Re > 64$ due to end conditions, unless carefully controlled the shedding becomes oblique with an angle θ so that the effective frequency decreases; $St_\theta = St_D \cos\theta$

3. B to C, $190 < Re < 260$

The formation of wake vortices changes in this regime. For small Re , vortices are formed due to a kinematic topological bifurcation; only for Re of $O(10^2)$ and above can a boundary layer and its separated shear layer be sufficiently thin and vortices formed by shear layer roll-up. The interaction between the shear layers on either side that give rise to vortices is mentioned in Sec 2.1.1.

The wake becomes intrinsically three dimensional due to bifurcations at $Re = 190$ and $Re = 260$. At $Re = 190$ the flow is linearly unstable with respect to spanwise wavelength $\lambda = 4D$ (called mode A). The formation of vortex loops and streamwise vortex pairs takes place due to the deformation of the primary vortices as they are shed. Then, for $Re = 230 - 260$, an energy transfer from mode A to mode B occurs, in which fine streamwise vortices with $\lambda \simeq 1D$ appear. In this regime, transition to a three dimensional wake occurs and local shedding phase differences along the span cause large scale dislocations of shed vortices.

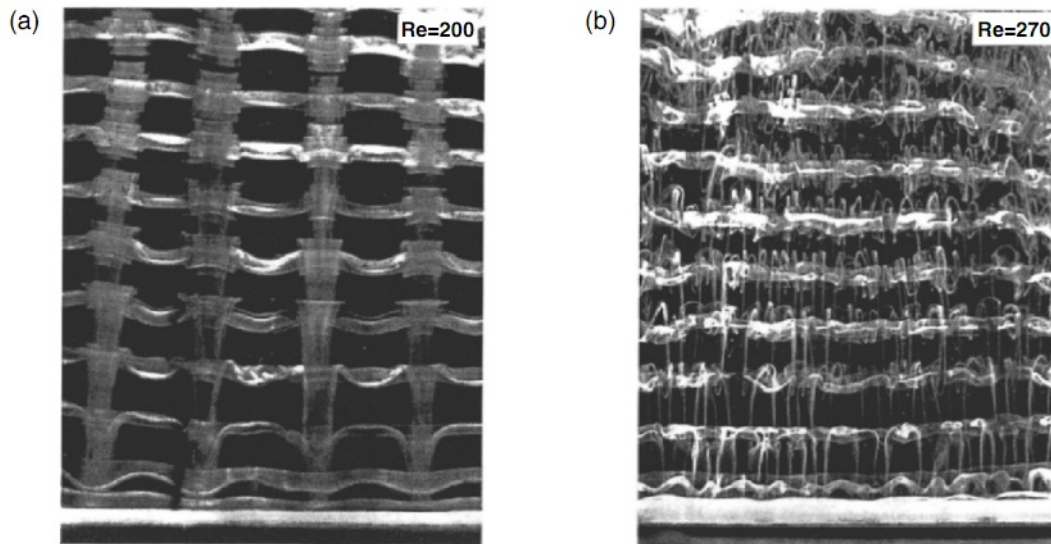


Figure 2.7: Flow visualisation of (a) Mode A instability at $Re = 200$ and (b) Mode B instability at $Re = 270$. Image taken from [39]

4. C to H, $Re > 260$

As Re increases beyond 260, the flow starts transition to turbulence. This first occurs in the wake, where fine scale three dimensional structures are increasingly disordered. This causes a decrease in base suction, increase in shedding frequency and length of vortex formation region in regime C to D.

The region from D to E is quite significant in terms of transition to turbulence of the various flow quantities. At D, corresponding to a Re of slightly more than 10^3 ($\log_{10} Re \simeq 3$), the wake transitions to turbulence. In between D and E, at a Re of around 10^4 ($\log_{10} Re \simeq 4$), free shear layer transition starts due to Kelvin-Helmholz (K-H) instabilities, leading to shear layer vortices called Bloor-Gerrard vortices that generate frequencies in the wake that vary roughly with $Re^{\frac{3}{2}}$ rather than with Re as seen for the Karman vortices. The significance of these vortices in the wake for Karman vortex control was shown by Chyu et al [5] when they found that the formation length of Karman vortices can be significantly reduced by forcing the cylinder in the cross-stream direction at the K-H frequency of the separating shear layer. As the shear layer becomes turbulent, $-C_{pb}$ and C_D increase while St and length of vortex formation region decrease.

The boundary layers on both sides are still laminar while the wake and shear layers are turbulent until $Re \simeq 3 \times 10^5$. At this point (E), the boundary layer on one side starts transition and can stay attached for longer downstream compared to the other side, causing an asymmetric state with non-zero mean lift. The St and $-C_{pb}$ reach a minimum and maximum respectively. On further increasing the Re , the C_D and $|-C_{pb}|$ start decreasing while the St starts increasing.

At higher Re 's the boundary layers on both sides are turbulent, causing a drastic drop in C_D and $|-C_{pb}|$ (the 'Drag Crisis') and a rise in St upto around 0.5, and a decrease in the vortex street formation region size as well as width of downstream wake.

5. H to J, $Re > 10^6$

Reappearance of periodic, turbulent vortex shedding, indicating that the alternate fully turbulent shear layer roll-up mechanism reappears at large Re . Boundary Layer separation occurs further upstream yielding higher drag and base suction and a wider downstream wake than the previous regime.

Pressure Field in the Near Wake

An important effect of the alternate vortex shedding on the bluff body is the fluctuating base pressure which is responsible for the emission of acoustic noise, among other undesired features. The pressure fluctuations occur at the same frequency as the vortex shedding. Given a snapshot of the wake velocity field, the corresponding pressure field can be calculated by solving the Poisson Equation [28]:

$$\Delta p = \nabla u \cdot \cdot \nabla u^T = W \cdot \cdot W - S \cdot \cdot S = Q \quad (2.3)$$

where ∇u is the Jacobian of the velocity, and $\cdot \cdot$ is the double contraction operator. The Jacobian can be decomposed into a symmetric tensor S and an antisymmetric tensor W , which represent the strain and rotation of a fluid element respectively. The local source Q is hence a difference of the double contraction of the rotation and strain tensors. Inside a vortex, rotation dominates ($Q > 0$), which indicates a lower pressure in the core. In a plain shear layer, rotation and

strain are balanced ($Q = 0$). On the convex side of a bent shear layer and between vortices are regions of significant entrainment of free stream flow, where strain dominates ($Q < 0$). These are regions with a higher pressure. The base pressure hence fluctuates as the shedding phase changes, causing vortices in the near wake to leave pressure reading 'footprints'. Since the shedding from the upper and lower trailing edges is out of phase, the corresponding pressure readings at these locations will be out of phase too, as shown in Fig. 2.8. In this figure, the time traces of the pressure on the upper and lower trailing edges of a D-shaped bluff body are shown by solid and dashed lines and the surface averaged base pressure by a gray line, as computed based on a reduced order vortex model.

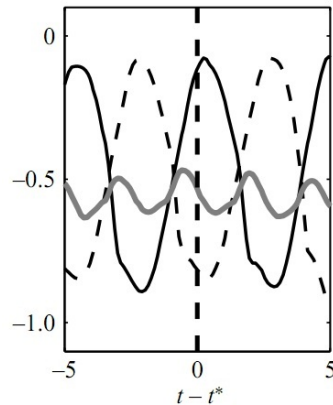


Figure 2.8: Time traces of the fluctuating base pressure over a D-shaped body. Taken from [28]

2.2 Vortex Shedding Control

There are a variety of means used for vortex shedding control of varying complexity that have been developed over the years. The various classifications and the evolution and implementation of such methods for bluff body flow control have been extensively reviewed in Choi et al [4].

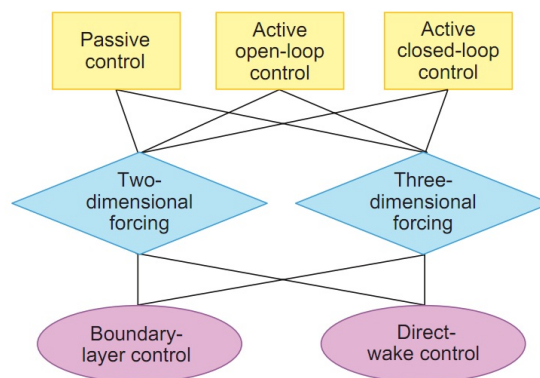


Figure 2.9: Classification of bluff body flow control methods, taken from [4]

Control mechanisms can be classified based on whether they act on the boundary layer of the body before or at separation or by acting in the wake itself. The former type, classified as Boundary Layer Control mechanisms, are popular on objects like cylinders and spheres with non-fixed flow separation points on their surfaces. Examples include dimples or roughness that delay separation and increase the base pressure in the wake, thereby reducing the drag. However, such methods do not directly act on the vortex shedding itself, hence are only tangentially concerned with our main aim in this study.

2.2.1 Two-Dimensional Shedding Control

Passive Methods

Passive methods are the oldest methods of vortex shedding control. The motivation behind their introduction was the reduction of drag on bluff bodies by modifying the wake by preventing the shear layers from interacting to create a vortex street, or raising the base pressure. They are implemented in a variety of ways, generally involving surface modifications - spanwise segmented [29] and sinusoidal [38] trailing edges, splitter plates, etc.

Splitter plates were one of the earliest passive shedding control methods. Fig 2.10, taken from the work of Gerrard [14] shows a splitter plate of length l on the downstream side of a circular cylinder of diameter d , along the wake centerline. As the length of the splitter plate is increased up to and beyond d (approximately the vortex formation length), the St is decreased. This is expected as the length of the formation region is increased by the insertion of the plate. We expect the cross-flow between the shear layers to be less easily set up in the presence of the splitter plate; some or most if it will be deflected away, and this results in an increased shedding period and decreased shedding frequency.

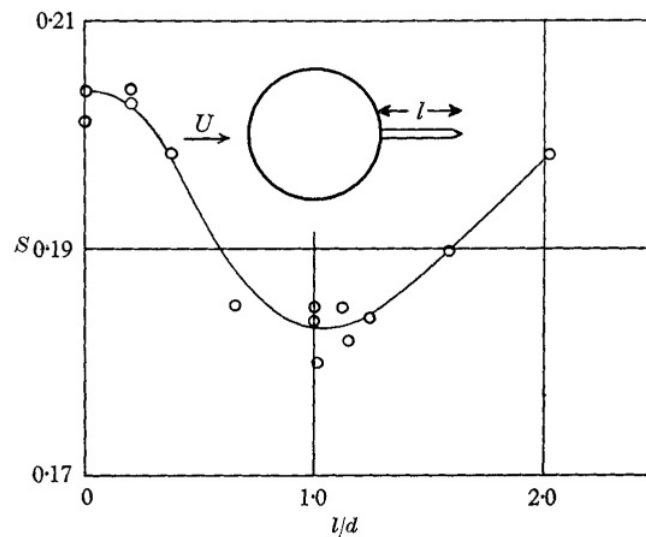


Figure 2.10: St as a function of splitter plate length. Image from [14]

Related experiments were also carried to see the effect of the splitter plate with a gap between

the upstream end and the cylinder by Roshko [31]. For small plate lengths, it was seen that when the gap was small the reduction in St was the same as found for a splitter plate no gap. For larger gaps, there is a large effect of the gap length (more specifically, the position of the leading edge of the plate). Beyond a certain gap length of around $0.7d$, the effect on the St is quite less. This can be explained as follows - with small gap lengths, the amount of vorticity crossing the wake from one side to another is insufficient to induce shedding. It will hence take longer for the weakened vortex to be shed downstream of the plate. However as soon as the gap is increased beyond the $0.7d$ threshold, the cross-flow upstream of the plate is strong enough to induce shedding and the frequency of shedding increases to the levels seen when no plate is present. This experiment demonstrates the importance of the interaction between the shear layers and the concomitant cross flow that is set up from either side in the vortex shedding process.

Active Open Loop Methods

Active means involve actuators with a power input, and can be further divided into two categories - open loop and closed loop. Open loop active control involves using one or more forcing devices to alter and modify the interacting shear layers, disrupting the vortex shedding process. Many such methods have been developed over the years - steady and time varying blowing and suction, electromagnetic forcing, body rotation [10], spatially distributed blowing and suction [21] [22], plasma actuation [35] [37], etc. Such methods generally aim to suppress vortex shedding in order to increase the base pressure and reduce the drag on the bluff body. To achieve this, the low velocity 'dead water' region in the near wake has to be elongated (as is done by splitter plates) and the alternating character of the wake has to be mitigated or delayed. There are at least four possible methods to achieve this:

1. direct opposition of vortices in the near wake;
2. mitigating the evolution of large-scale vortex formations by high-frequency forcing;
3. breaking large-scale vortex formations by forcing three-dimensional structures;
4. enhancing the initial symmetry by forcing synchronous vortex shedding.

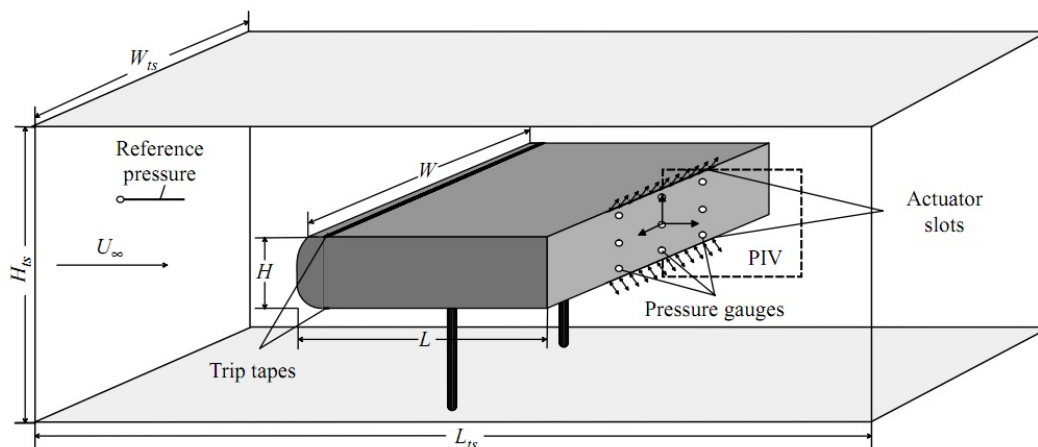


Figure 2.11: Sketch of experimental setup with D-shaped body in [28]

A good example of active open loop forcing implemented experimentally is in Pastoor et al [28]. Here sinusoidal time-varying actuators were placed on the upper and lower trailing edge surfaces of a D-shaped bluff body to give periodic blowing and suction, as shown in Fig. 2.11. The harmonic actuation was $g(t) = A\sin(2f_A t)$ with the actuation amplitude A and frequency f_A . It was seen that when the actuators operated with constant amplitude corresponding to a maximal induced velocity equal to the free stream velocity, a maximum base pressure at St_A of around 0.15 was found for all Re , yielding a drag reduction of almost 15%. Actuation at this frequency caused a synchronisation of the shedding from the upper and lower TE surfaces, hence a mitigation of the near wake instability and a cancelling of the alternate periodic shedding street in the near wake. The averaged base pressure and drag coefficient normalised with respect to their respective unactuated values for harmonic actuation over a range of actuation non-dimensionalised frequencies at constant amplitude are shown in Fig. 2.12.

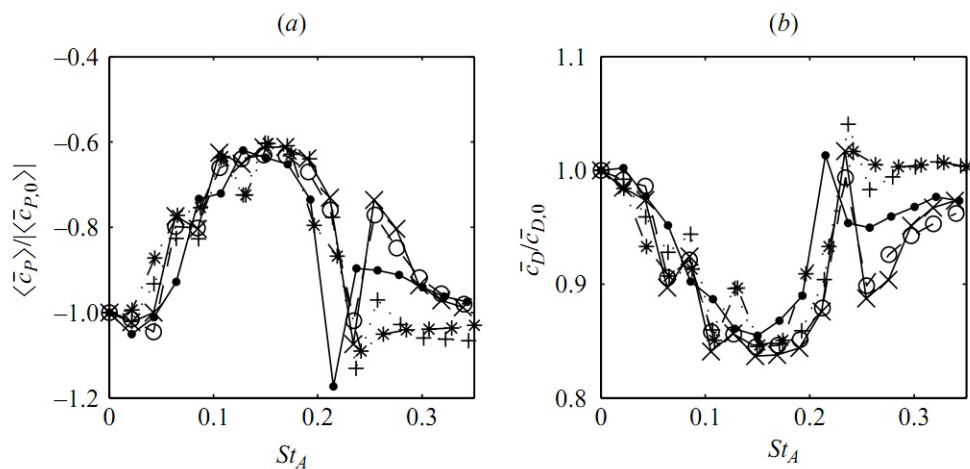


Figure 2.12: Normalised averaged C_{pb} and C_D with open loop harmonic actuation. Legend: Re 23000(\bullet), 35000(\circ), 46000(\times), 58000($+$), 70000($*$). Taken from [28]

2.2.2 Three-Dimensional Shedding Control

Three dimensional forcing methods work by breaking the strong two-dimensionality in the Von-Karman vortex rolls that are produced by the interaction between the shear layers on either side of the bluff body. This is done when a spanwise phase mismatch is introduced along the span of the rolls, so that the shedding phase is varying along the span. Some passive and active means to achieve this will be mentioned here.

Passive Methods

Passive means generally involve modifying the geometry of the body, especially close to the trailing edge. In Petrusma and Gai [29], pressure measurements from experiments on a segmented Trailing Edge airfoil were presented, and are very instructive on how spanwise variations in Trailing Edge geometry can have a significant effect on vortex formation in the near wake region.

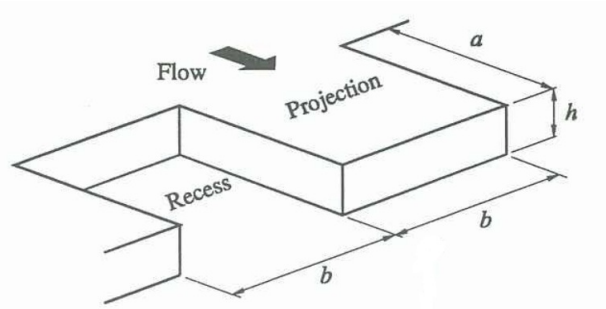


Figure 2.13: The Segmented Trailing Edge studied in [29]

It was seen that the vortex formation mechanism was significantly altered by the presence of the protrusions. The base pressure over the projections was greater than that in the recesses, due to the presence of a pair of stationary, counter-rotating streamwise vortices over each of the projections, which drew fluid from the recesses. There were hence two sources of replenishment of fluid in the wake from the shear layers – the first the separating shear layers drawn across the wake as for bodies with conventional unsegmented trailing edges, and the second the fluid drawn from the recesses to the projections, as mentioned above. This second replenishment process decreased the amount of fluid from the shear layer crossing the wake, hence increased the vortex formation length and the base pressure and reduced the drag of the body, which was the main motivation of the study. A similar but more extensive study was carried out by Deshpande and Sharma [8] on various geometries using symmetrical trapezoidal prismatic blocks attached to the base at regular intervals along the span. Strong three dimensionality in the vortex rolls was introduced which weakened them and inhibited their periodic shedding by segmenting the trailing edge. The segmented trailing edges were found to generate strong streamwise vortices that effectively transferred energy from the Karman vortices resulting in a suppression of the unsteadiness.

Another experimental study of interest dealing with vortex shedding behind a bluff body with a geometry varying in the spanwise direction was carried out by Tombazis and Bearman [38], who used a body with a sinusoidal span. The points where the span protruded outwards and inwards were denoted peaks and valleys respectively. Hot Wire Anemometry was carried out at a peak and valley to observe the shedding characteristics at these points. Due to the sinusoidal trailing edge geometry, distinct alternating shedding cells were created at the different regions along the span, each with its own shedding frequency. This caused vortex dislocation at the boundary between the cells due to the phase mismatch, thus breaking the two-dimensionality in the shedding process and greatly weakening or suppressing it altogether.

Active Methods

A powerful active three dimensional means of vortex control will be discussed - distributed forcing consisting of alternate blowing and suction along the spanwise direction on both the upper and lower surfaces of a bluff body. The actuation could be implemented in a spatially in-phase or out-of phase manner depending on whether the respective blowing and suction locations on both surfaces are lined up or not. As seen in Fig 2.14, the actuation can be thought of as sinusoidal in the spacewise direction along a surface and stationary in time. Distributed forcing was first

implemented numerically by Kim and Choi [21] for flow over a circular cylinder. The actuation was implemented along the 90° and -90° spanwise lines from the front stagnation point over a wide range of flow Re 's. It was found that in-phase forcing significantly reduced the mean lift and drag fluctuations by attenuating or suppressing Von Karman vortex shedding over all flow regimes. However no significant benefit was realised from out of phase forcing.

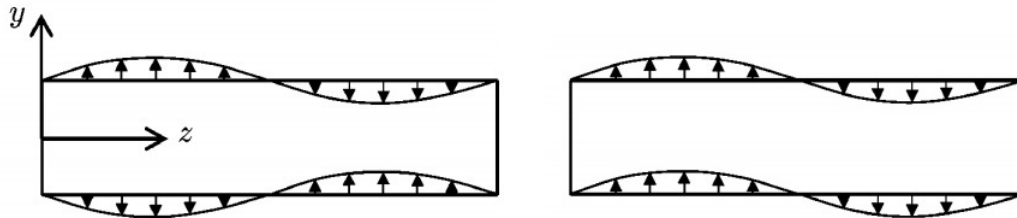


Figure 2.14: Forcing profiles along the upper and lower surfaces for in-phase (L) and out of phase distributed forcing (R), from [21]

In-phase forcing produced a spanwise phase mismatch in the vortex rolls, which broke up the two-dimensionality and reduced the strength of the vortical structures. Since suction accelerated the flow (by increasing the momentum of the boundary layer) and blowing decelerated the flow, the vortex formation position was shifted upstream at the blowing locations and downstream at the suction locations. Hence, the vortex rollers in the near wake were bent into a sinusoidal shape. This caused a phase difference between the flow at these locations, with the flow at the blowing locations leading the flow at the suction locations. When the alternating blowing and suction were arranged at the optimum spanwise wavelength, the phase difference between these locations was 180° and complete Von Karman vortex shedding suppression was achieved. The optimal in-phase spanwise wavelength for the cylinder of diameter d was found to be $3d$ to $4d$, which is very close to that of the mode-A instability of the Von Karman vortex shedding for a cylinder [39].

The numerical work done by Kim and Choi on distributed forcing on a circular cylinder was extended to D-shaped bluff bodies both numerically and experimentally by Kim et al [22]. For such a body, the separation locations for the flow were fixed at the sharp trailing edges. The forcing profiles that were implemented, however, were the same as in Fig 2.14, but with a forcing angle to the vertical. The chosen spanwise wavelength was set at $4h$ where h is the height of the flat trailing edge of the body. The alternate blowing and suction was experimentally implemented using a zero net mass flow rate fan arrangement. Both the numerical and experimental results showed that the in-phase forcing effectively changed the vortical structure in the wake from nominally two-dimensional to three-dimensional, and thus significantly attenuated the vortical strength. Since the model had fixed flow separation at the trailing edge, the mechanism involved a direct modification of the vortical structure in the wake rather than a separation delay. It was seen that the shedding frequency was different at the blowing and suction locations, with the dominant frequency higher at the suction location. Hence, the vortex shedding became essentially three dimensional. The success of in-phase forcing can be seen in Fig.2.15; out of phase forcing was ineffective in suppressing vortex formation.

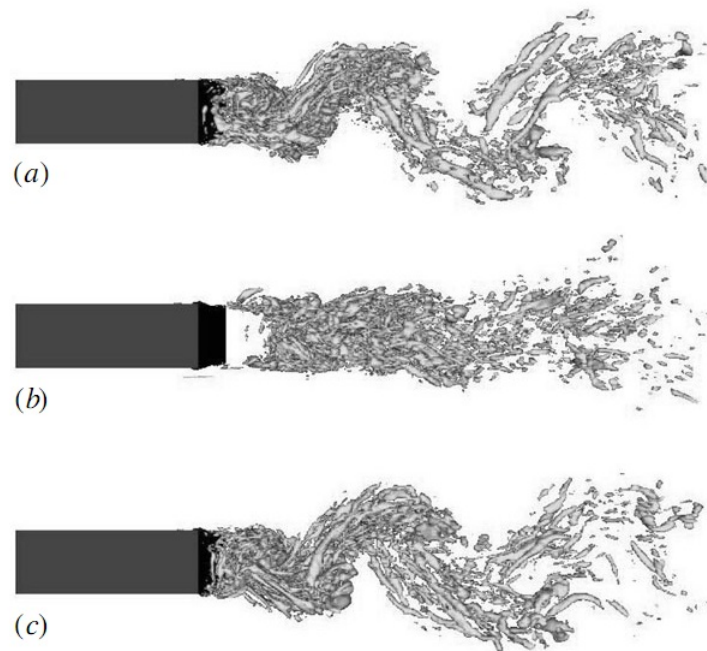


Figure 2.15: Vortical structures at a Re of 4200 for (a) uncontrolled flow, (b) in-phase forcing and (c) out of phase forcing. Taken from [22]

2.3 Plasma Actuators

AC Dielectric Barrier Discharge (DBD) actuators are Electrohydrodynamic active flow control devices consisting of two electrodes placed asymmetrically on each side of a dielectric. One electrode is placed on top of the dielectric, exposed to air, and energised with a High Voltage input, while the other is encapsulated under the dielectric layer and placed parallel to the exposed electrode with or without a gap between them. The action of the actuator is based on the creation of surface plasma above the covered electrode that gives rise to a body force on the air, which leads to an induced jet that can be used in airflow control.

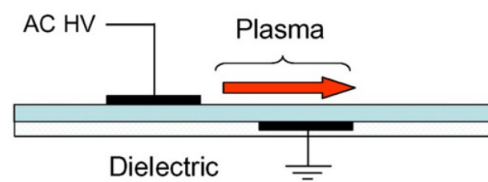


Figure 2.16: Typical AC DBD Plasma Actuator electrode arrangement, sectional view. Taken from [26]

The following sections will cover the physics behind the working of these actuators, the various

geometrical and electrical parameters that influence their performance, and some applications in aerodynamics so that their applicability and advantages as a flow control device become apparent.

2.3.1 The Actuator Physics

The generation of Plasma

In the context of physics, plasma is often considered a fourth state of matter. It is a state of matter similar to a gas in which a certain portion of the particles are ionised. The input signal that is given to the exposed electrode is harmonic, while the exposed electrode is electrically grounded. The signal switches polarity at the waveform frequency, which means that for half the signal period the exposed electrode is positive with respect to the covered electrode, and negative for the other half.

During the negative half cycle, as the magnitude of the applied electric field rises above the breakdown electric field E_b , which is minimum field needed to sustain electron-ion pairs in the gas, electrons are released from the exposed electrode towards the covered electrode, and these ionise the gas by collision, creating more electrons and resulting in an avalanche. The ionised air appears violet, which is due to the fact that as the ionised species recombine and de-excite, they release light primarily in the UV spectrum. These electrons build up on the dielectric surface above the covered electrode and oppose the further build-up of charges, which means that the applied voltage must continuously increase for the discharge to continue. During the positive half cycle, electrons travel from the dielectric surface to the exposed electrode. The flow of electrons is not continuous but occurs in the form of microdischarges, indicated by narrow spikes of light emission. However the microdischarges during both the half cycles are not the same. It is more homogeneous during the negative half cycle, when the electrons originate from the bare electrode, which is essentially an infinite source that readily gives them up. In the positive-going half-cycle, the electrons originate from the dielectric surface. These do not come off as readily, or when they do, they come in the form of fewer, larger microdischarges.

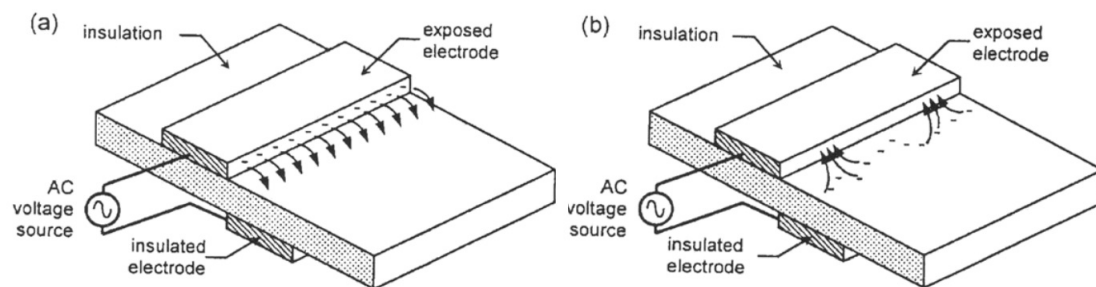


Figure 2.17: Schematic illustration of charge build-up on the surface during the input signal (a) negative; and (b) positive half cycle. Figure taken from [26]

The Plasma Induced Wind

The formation of the plasma gives rise to an effective body force on the ambient air through ionic repulsion and collisions of ions with the neutral particles. Using Coulomb's law, the aerodynamic

effect produced by plasma actuation can be represented by a body force vector $\mathbf{f} = \rho_c \mathbf{E}$ in the Navier-Stokes equation, where ρ_c is the net charge density and \mathbf{E} is the electric field. The body force can be tailored through the design of the electrode arrangement, which controls the spatial electric field. It is the resulting coupling of directed momentum to the surrounding air that forms the basis for flow control strategies. Although the direction of charge transfer varies during the two halves of the AC cycle that drives the actuator, the body force always has the same direction [36]. The overall induced flow by the DBD actuator consists of two components:

1. A downward induced flow (depression) towards the edge of the exposed electrode in the direction of the covered electrode, and
2. A jetting of the flow towards the far edge of the covered electrode

In the following figure, the velocity profiles of the jet at several downstream locations from a plasma actuator are shown [13]. The diffusion of the momentum transfer from the plasma to the air can clearly be seen the peak values diminish and the profiles get 'broader'. The maximum induced velocity is always reached at the end (limit) of the area of plasma (which is 10 mm in this case) and at a height of 0.5 mm above the surface.

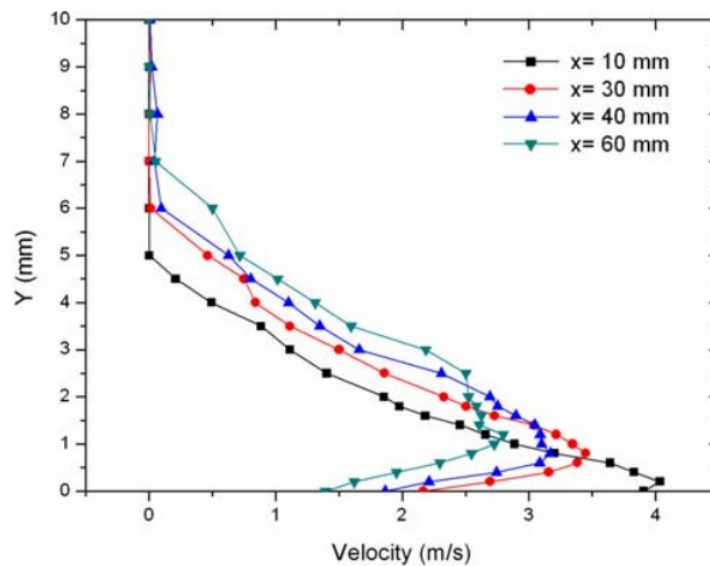


Figure 2.18: Velocity profiles at several downstream positions from a plasma actuator. Taken from [13]

Several differences can be identified between the positive and negative half cycles, based on the work by Forte et al [13], see Fig 2.19. One can see that the negative half cycle induces higher horizontal velocity than the positive one. Also the y -component shows negative values during the positive half cycle, indicating that the depression above the actuator is formed during the positive half cycle. It is clear that the mechanical effects in the negative half cycle are more favourable, due to the fact that it produces a more uniform discharge as mentioned earlier.

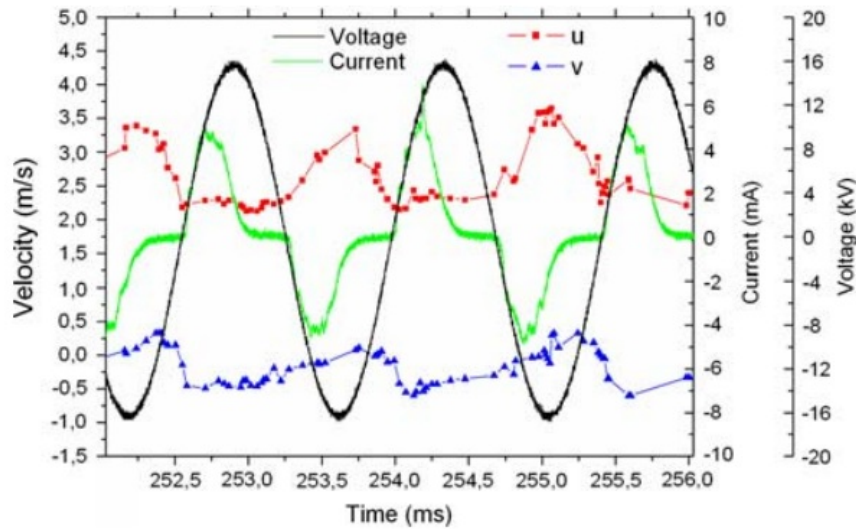


Figure 2.19: Variation of voltage, current and the induced horizontal and vertical velocities of the DBD Plasma Actuator versus time. Taken from [13]

Dependence on Electrical Parameters

The electrical parameters are typically as follows - the high voltage input from a few kV to 40 kV, and signal frequency between 100 Hz to many kHz. To maximise the portion of time where the electrons travel from the exposed to the covered electrode (the more uniform discharge), a positive sawtooth waveform is recommended, to produce the greatest net force for a given input power (based on the work of Van Dyken et al, reviewed in [26]). However it was shown by Kotsonis et al [23] that a square input waveform produces the absolute highest forcing, at the cost of a larger time averaged power consumption.

The relation between induced wind and the input voltage and frequency is well studied. In [26] it is mentioned that three studies demonstrate that the induced velocity increases with both voltage and frequency, but the curves themselves are quite different. The maximum induced velocity increases asymptotically with both the applied voltage and frequency with the other held fixed, but only till a certain optimum value of the input. Beyond this, the discharge loses a part of its mechanical effect when the transferred space charge is too high because the discharge becomes unstable and filamentary. This is because if the input is too high past the optimum, the power that would nominally go into producing body force will instead go into heating the air [7].

In Fig. 2.20(a), it can be seen that increasing the signal frequency increases the induced thrust produced at the same voltage; it also causes the actuator to saturate at lower voltage, which means further increasing the voltage does not increase the thrust produced. This ultimately limits the amount of thrust that can be produced by the actuator. Fig. 2.20(b) shows the increasing filamentary nature of the plasma discharge at higher frequencies.

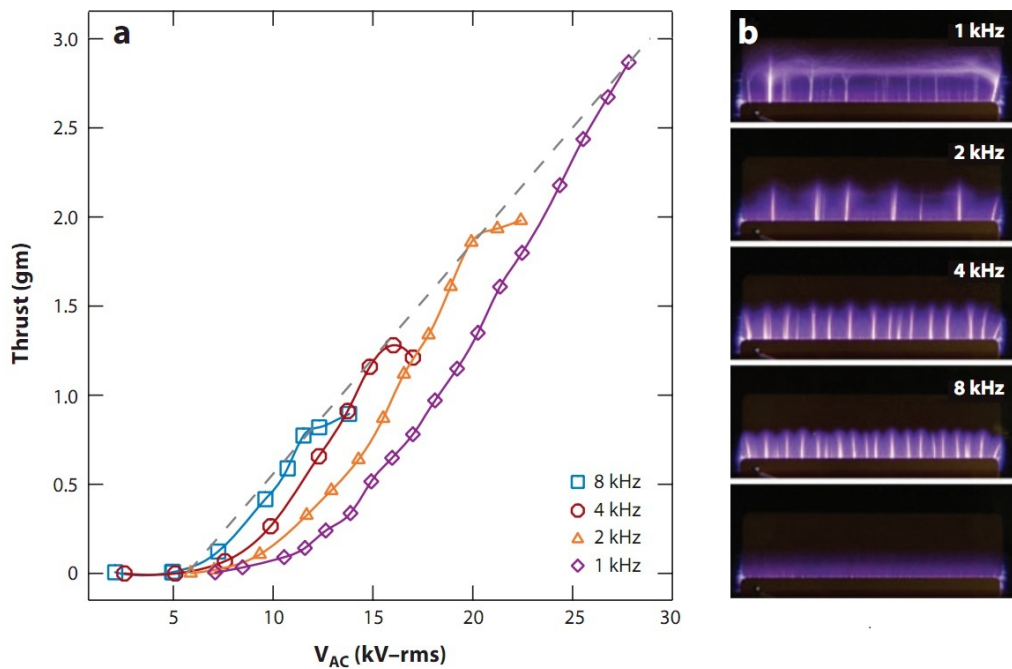


Figure 2.20: (a) Relation between the induced thrust, voltage and frequency of the input signal; (b) Corresponding images of plasma for each frequency at point of maximum thrust (saturation). Image taken from [6], based on the work of [36]

In Fig 2.21 shows the effect of voltage amplitude on the induced wind above an actuator consisting of a 4 mm thick glass plate, with electrode gap and electrode width of 5 mm at 300 Hz frequency. The peak jet velocity at all voltages occurs at a height around 0.5 mm above the surface. The almost linear increase in the maximum induced jet velocity with increase in voltage is apparent.

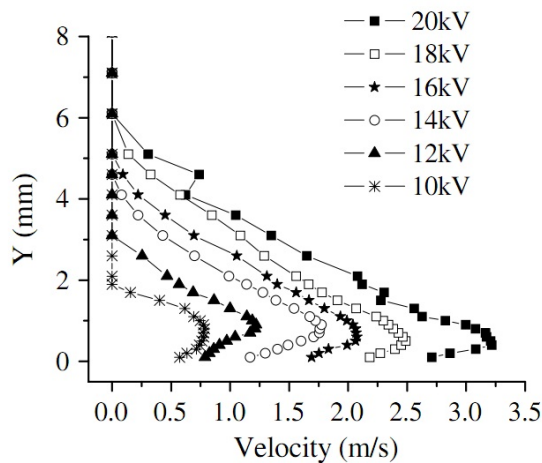


Figure 2.21: Typical Velocity Profiles for different signal voltage amplitudes above an actuator; Taken from [26]

Dependence on geometrical and physical parameters

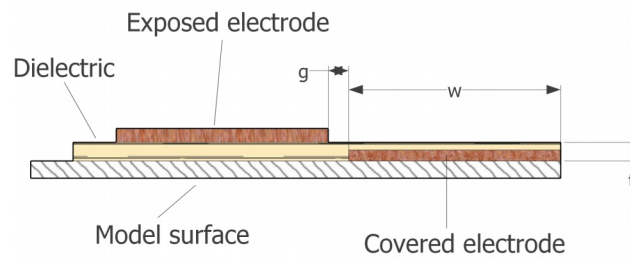


Figure 2.22: The various geometrical parameters in the plasma actuator layout. Taken from [27]

The typical values of the various geometrical parameters are as follows - width of the electrodes (w) a few mm to a few cm, gap between the electrodes (g) zero or a few mm, dielectric thickness (t) a few mm. Common dielectric materials include Kapton, Teflon, plexiglass, polycarbonate materials like Makrolon, etc.

A parametric study was performed on the effect of the various electrical and geometrical parameters on the induced wind by Forte et al [13]. A 2 mm thick PMMA flat plate with two 5 mm wide electrodes was used to study the effect of electrode gap g on the induced wind. It was seen that the induced velocity increased with the gap up to an optimum value, as the plasma ions were accelerated over a longer distance. However on increasing the gap beyond a certain value, the electric field strength reduced because the effective dielectric thickness between the electrodes increased. The optimum gap width g for induced wind was found to be between 0 and $2w$.

The effect of the grounded electrode width (w_G) was also studied for the same actuator as above with g set at 0 mm. An asymptotic relation between the maximum induced velocity and w_G was seen, see Fig 2.23. The increase of the induced wind speed with w_G is due to the fact that wider the electrode, the farther the plasma can expand and more the ions are accelerated. However, due to the dissipative nature of the plasma it cannot expand beyond a limit on the surface, which is why extending w_G beyond this limit is a waste of space and power [13]. The width of the exposed electrode, on the other hand, is not a significant factor, since the role of the exposed electrode is just to act as a source of electrons for the plasma.

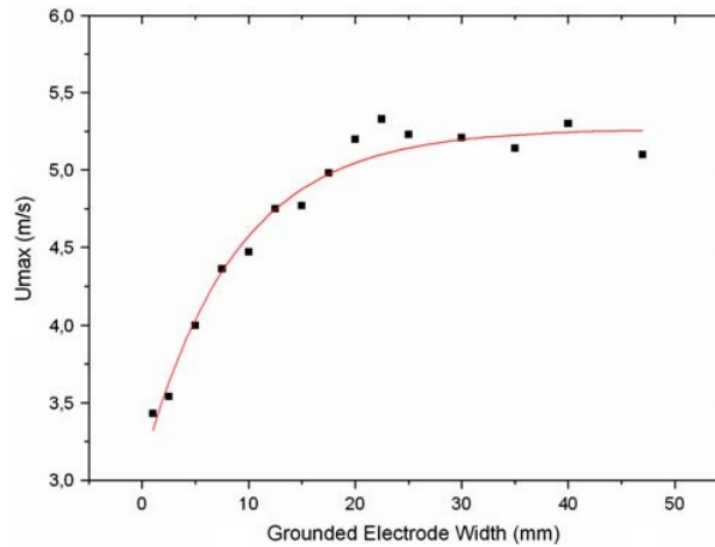


Figure 2.23: Variation of peak induced wind with grounded electrode width. Taken from [13]

As mentioned earlier, increasing the frequency beyond a point is counter-productive. However the voltage can be increased at will, as long as care is taken so that the dielectric does not undergo breakdown due to the large electric fields and charge transferred. At higher voltages, streamers and filaments of charge are formed which are dangerous to the dielectric material. Hence, it is also of interest to use the optimum dielectric that enables one to reach higher supply voltages to the actuators. In the work by Thomas, Corke, et al [36] a parametric experimental investigation was carried out aimed at optimising the body force and induced wind produced by an actuator, using various dielectric materials, thickness, electrode geometries, and electrical input parameters. It was demonstrated that actuators constructed with thick dielectric material of low dielectric constant produced a body force an order of magnitude larger than that obtained by the Kapton-based actuators used in many previous plasma flow control studies. These actuators allowed operation at much higher applied voltages without the formation of discrete streamers which led to body force saturation.

The general principle behind this is to lower the capacitance of the actuator. The capacitance is proportional to ϵ/h where ϵ is the dielectric coefficient and h is the material thickness. The power loss through the material is proportional to $f_{AC} \times \epsilon/h$. Hence, lowering the capacitance lowers the power loss through the dielectric, which allows higher voltages to be reached.

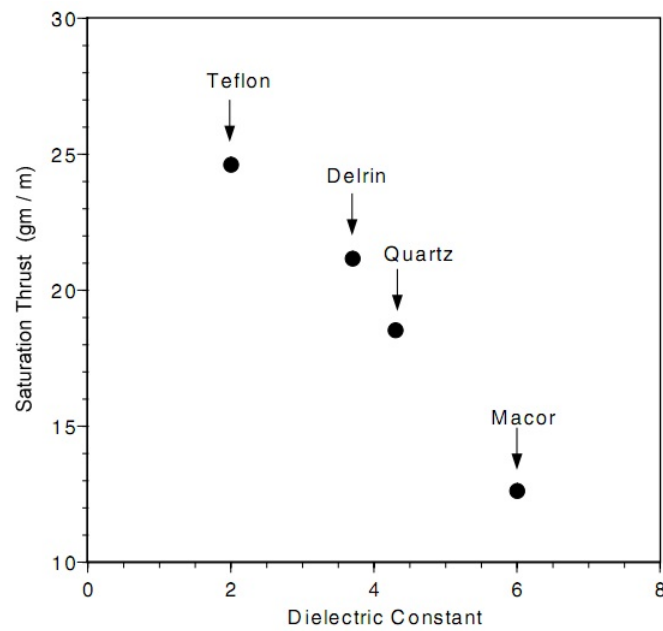


Figure 2.24: Actuator saturation thrust versus dielectric constant of common dielectric materials. Taken from [36]

Steady and Pulsed Actuation

As seen in Fig. 2.19, the induced velocity of the plasma actuator follows the high frequency AC input signal. These time scales are generally much smaller than those of the flow; hence the forcing and the body force of the actuator may be considered effectively steady for the flow. However unsteady actuation may also be applied using a signal generator, so that during a time interval T_1 the actuator could be 'on' only during subinterval T_2 . Hence, the actuation could take place with an effective frequency of $\frac{1}{T_1}$, which can be set to be much lower than that of the input signal. The time scale of the actuator induced quantities will now be correspondingly higher, so that they could interact with the fluctuating flow quantities. The duty cycle of actuation is now T_2/T_1 .

Unsteady actuation and the interaction between the actuated and natural flow unsteady flows is particularly relevant for applications involving control of vortex shedding. For example, control of vortex shedding using unsteady DBD plasma actuation was attempted by Thomas et al [37] and Jukes and Choi [19] over circular cylinders, and by Nati over a flat plate bluff body with a sharp trailing edge using a spanwise uniform transverse jet [27].

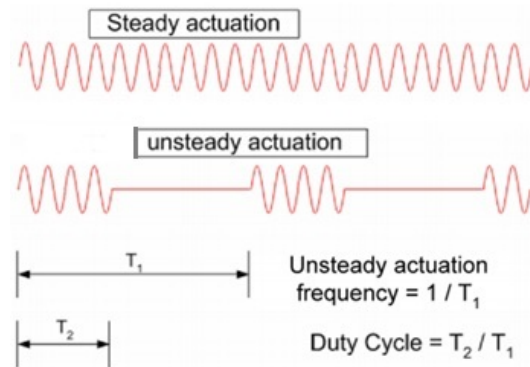


Figure 2.25: DBD Plasma Actuator Input signal for steady and unsteady actuation. Taken from [37]

2.3.2 Selected Applications of DBD Plasma Actuators in Fluid Flow

Both active and passive flow control methods have their respective advantages and disadvantages. Implementation of passive methods is generally infeasible for many engineering geometries. Such methods do not afford any sort of controllability, hence are generally unfavourable. Active methods on the other hand, can be more widely applied, but often require a considerable power input. Many of them also require moving parts, and/or complicated layouts and setting up. DBD Plasma Actuators do not have the disadvantages of most other control methods. These actuators are extremely easy to construct, occupy very less volume, are robust, consume very less power and have a very high frequency response.

AC Dielectric Barrier Discharge Plasma Actuators have been proven useful in many applications involving Aerodynamic flow control over the past few years. According to Moreau, airflow control by a plasma actuator was really born in 2000 [26]. These applications, along with the essential electrical and control characteristics of the actuators themselves, are extensively reviewed by Moreau [26] and Corke [7], [6]. These actuators have demonstrated their value in a multitude of Aerodynamic applications flat plate boundary layer control, separation delay over a circular cylinder [35], making a directional micro jet device [2], vortex generators [20], etc.

Vortex Shedding Control

In the work of Nati [27], various plasma actuator configurations were implemented to achieve Von Karman vortex suppression for Laminar flow over a flat plate bluff body. Based on POD analysis of the fluctuating energy share in the first two modes as well as the total fluctuating kinetic energy, it was seen that the one downstream, one upstream and the transverse configurations were the most effective in suppressing vortex shedding (see Fig 2.26). The actuation was uniform along the spanwise direction, which meant that the actuators were present all along the span of the body along the trailing edge. Both uniform and pulsed actuation was tested, with results indicating successful suppression upto U_{inf} of 7.5 m/s for the uniform transverse actuation configuration. It was seen that at pulse frequencies of 3 to 5 times the shedding frequency ($St \simeq 0.6 - 1$) the effectiveness of the actuator increases to that of steady actuation.

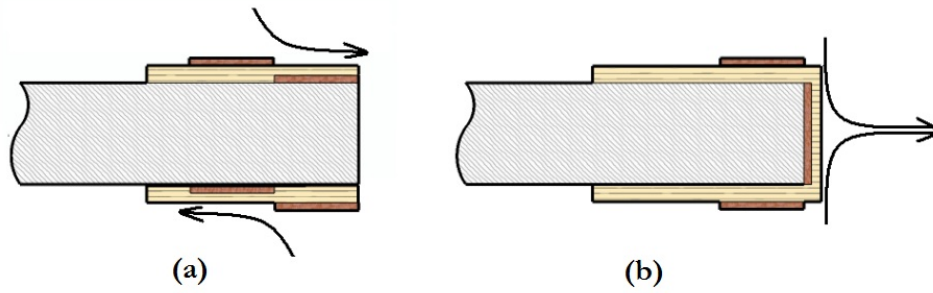


Figure 2.26: (a) One downstream, one upstream and (b) Transverse plasma actuation configurations implemented by Nati [27]

The success of the one downstream, one upstream configurations could be attributed to the asymmetric actuation with respect to the shear layers on either side - the circulation on one side (downstream actuation) was strengthened, while the circulation on the other side (upstream actuation) was lowered. The asymmetric actuation shifted the ratio of the circulation on either side outside the range mentioned in Eq 2.1, bringing about a suppression of vortex shedding.

The greatest benefit was realised with the transverse actuation. This configuration placed the plasma actuator electrodes on either side of the trailing edge in such a way that a streamwise jet was created by the merging of plasma induced transverse streams from the upper and lower surfaces (see Fig. 2.27(a)). This jet alters the near wake by reducing the velocity difference between the wake and the outer flow, thereby reducing the circulation in the shear layer below the circulation required for the generation of strong vortical structures. The jet in the near wake created vorticity on either of its sides, as in Fig 2.27(b), that were of opposite sign compared to the vortices present in the vortex shedding process. These interacted with the shear layers to reduce their circulation strength thereby delaying or preventing the growth of large and fully developed vortices required for stable vortex shedding.

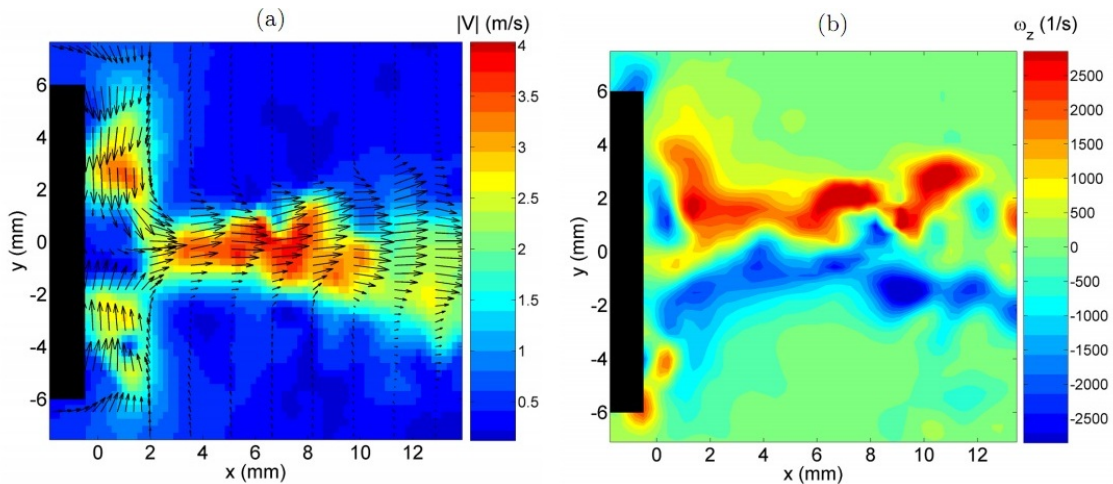


Figure 2.27: Instantaneous images of the (a) velocity field and (b) vorticity field produced by the transverse actuation. Taken from Nati [27]

Flow around circular cylinders is one of the oldest studied problems in fluid mechanics because of its wide engineering and practical significance and relative simplicity in experiment. Thomas et al [37] and Jukes and Choi [19] conducted experiments exploring the effect of steady and pulsed plasma actuation in vortex shedding suppression and on the wake properties and profiles behind a cylinder, among other quantities.

Thomas et al used four actuators mounted with their plasma generating edges at 90° and 135° with respect to the incoming flow, placed symmetrically with respect to the horizontal centreline. For pulsed actuation, both symmetric (all actuators firing on at the same times) and asymmetric (top and bottom actuator pairs firing out of phase with each other) configurations were implemented. It was found that both steady and pulsed actuation were successful in suppressing Karman vortex shedding and in greatly reducing both the wake turbulence and near field sound pressure levels. For pulsed actuation, for both symmetric and asymmetric modes the actuation frequency f corresponding to $St_D = fD/U_\infty = 1$ with a duty cycle of 25% was found the most effective. Hence, the frequency of actuation should match the intrinsic flow frequency of the separated wake region (U_∞/D) for optimum control. The value of the duty cycle was not found to be significant. The narrower wake and the reduced wake turbulence levels with plasma on can be seen in Fig 2.28. The velocity power spectra showed the removal of the Karman shedding peak and reduction of the broadband spectral levels.

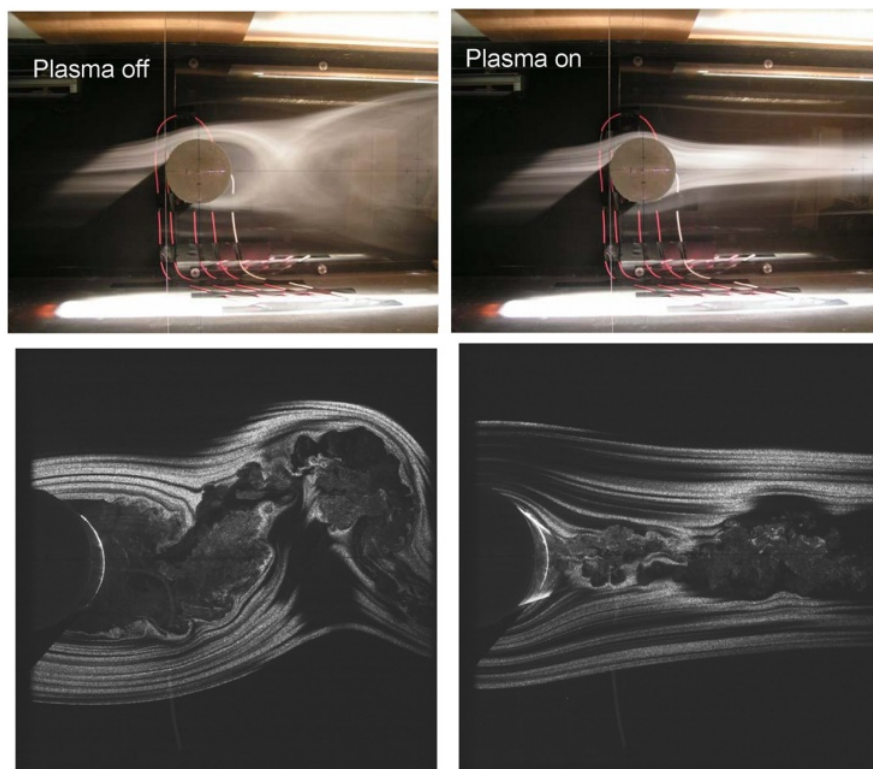


Figure 2.28: Smoke flow visualisation images for wake flow with and without plasma. Taken from [37]

With steady actuation the extent of the separated flow region was substantially reduced. The flow remained attached over a much larger extent of the surface than the canonical case, due to

the energising of the boundary layers; this Coanda-effect like behaviour served to channel high-momentum fluids into the near wake of the cylinder, hence, the circulation of the shear layers was reduced. Phase-locked flow field images of the symmetric, pulsed actuation wake field at $St_D = 1$ showed that small, compact and discrete vortices of opposite sign formed symmetrically on either side of the cylinder. These were formed close to the actuator and at the frequency of the actuation. These convected downstream along the shear layers that form the edge of the separated flow region and converged towards the centreline of the wake, where they underwent mutual annihilation. Asymmetric pulsed actuation also delivered the same results, with the difference that the vortices on the upper and lower row were staggered with respect to each other.

Vortex Generation

DBD Plasma Actuators can be used as Vortex Generators (VGs) to produce streamwise longitudinal vortices in a flow, similar to conventional VGs used in aviation and flow control, but with the added advantage of having no added profile drag since they do not protrude into the flow. The mechanism by which a streamwise vortex is produced by a single actuator arranged to produce forcing perpendicular to an incoming flow as given by Jukes and Choi in [20] is as follows - at the upstream tip of the actuator, the incoming boundary layer fluid is primarily sucked (due to mass continuity) towards the wall into the plasma and accelerated by the DBD body force to create a jet close to the wall perpendicular to the free stream. Hence fluid is drawn into the plasma from above it to take the place of that accelerated by the actuator, thereby setting up a circulation and hence a streamwise vortex above the wall jet. The formed vortex is a spatially and temporally steady structure. Due to the momentum of the incoming flow, the spanwise wall jet becomes twisted in the streamwise direction, with the result that the resultant jet becomes increasingly vectored in the streamwise direction with distance downstream from the upstream tip of the actuator. The resulting vortex hence twists away from the actuator and lifts up with distance downstream.

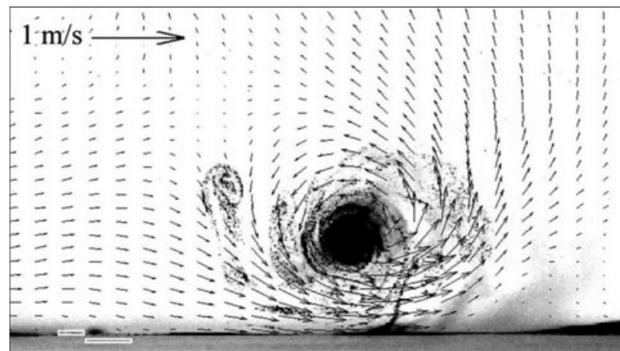


Figure 2.29: Instantaneous flow field induced by a DBD actuator (shown in the left) forcing perpendicular to an incoming flow. This is a sectional view of the streamwise vortex induced, with a reference vector length of 1 m/s shown. Image taken from [20]

As with conventional VGs, DBD VGs can be placed in arrays. Depending on the layout of the electrodes, arrays of co-rotating (CoR) or counter-rotating (CtR) streamwise vortices can be created. By placing the actuators in a row along their lengths, with a sufficient gap between

them so that plasma is formed only on one side of the successive exposed electrodes, an array of co-rotating vortices can be created as shown in Fig 2.30(a). If covered electrodes are placed on either side of an exposed electrode, the plasma is formed on either side of the exposed electrode giving rise to jets on both these sides pointing away from each other, which interact with the incoming flow to give rise to two vortices spinning in opposite directions through the above described mechanism. If two such double-sided jet actuators are placed next to each other with the appropriate spacing based on the amount the vortices move away from the actuators of origin, the vortices from the adjacent ends of both these actuators can come together to form a counter-rotating vortex pair with a common flow-up configuration. A counter-rotating vortex array can be created in this manner as shown in Fig 2.30(b).

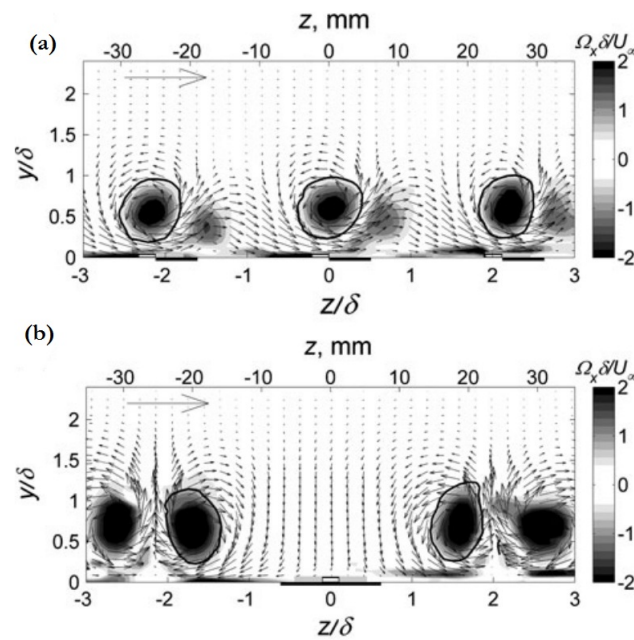


Figure 2.30: Vorticity magnitude and velocity vectors for (a) CoR DBD VGs and (b) CtR DBD VGs at a jet to free stream ratio of 0.63. The reference vector on the top left shows the U_∞ magnitude and the DBD actuator electrodes are shown on the horizontal axis. Taken from [20]

When comparing the performance of co- and counter-rotating DBD vortex arrays, it is shown that for the jet to free stream velocity ratio of 0.63 the circulation of each vortex in the co-rotating array was significantly weaker than that of the counter-rotating array, which in turn, was weaker than that of a single DBD actuator vortex. The reason for this was the adverse interaction between adjacent vortices where the upwash of one vortex interacted with the downwash of the adjacent vortex due to insufficient spacing between them, which led to a loss of useful circulation. Hence, the spacing between the vortices (and hence the actuators) is critical in ensuring that the circulation generated is optimally utilised for flow control purposes. The jet to free stream velocity ratio determines the distance a vortex moves in the transverse direction. An optimal spacing wavelength based on empirical data is given in [20]. In the same published work CoR and CtR vortex arrays then were applied to flow separation control over a trailing edge ramp to simulate the trailing edge of airfoils at high angles of attack, and the results were encouraging.

Directional Micro Jet Device

A micro-jet with adjustable direction based on the differential actuation of two DBD plasma actuators placed next to each other was created by Benard et al [2]. The two actuators were placed so that the induced jet created by them blew into each other and lifted up to form a vertical jet.

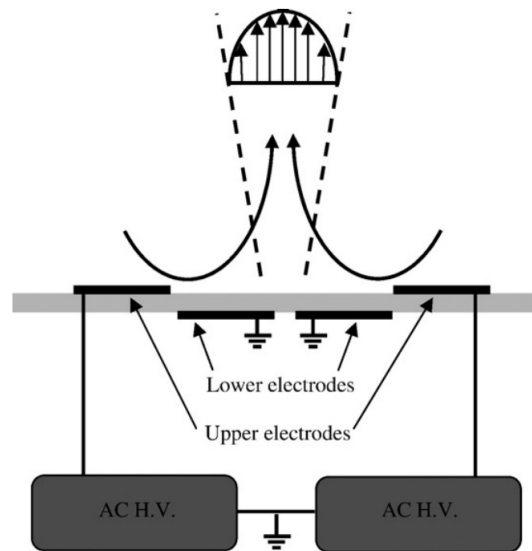


Figure 2.31: Schematic of the directional micro-jet device. Taken from [2]

With the same input signal to both actuators, the jet produced by them was the same as well, thus creating a perfectly vertical wall normal jet. With unequal inputs, the jets were of unequal strength; the lift up of the interfering streams was not perfectly vertical and instead tilted away from the actuator with the stronger jet. Further, it was found that when the input to one of the actuators was held fixed at 20kV, the strength of the created jet (its peak velocity magnitude) and the total power consumed by both the actuators did not change for the input to the other actuator between 17 and 20 kV; the orientation of the jet however did change by more than 20° . Hence by varying the amplitude of the high voltage applied to each DBD actuator the jet could be inclined to around 20° without any loss in power.

Chapter 3

Experimental and Data Processing Techniques

This chapter presents the theory behind the flow measurement technique of choice for this study—Two component particle image velocimetry, and the various data reduction techniques that were used to analyse the obtained velocity fields like Proper Orthogonal Decomposition (POD), Power Spectral and Correlation Analysis.

3.1 Particle Image Velocimetry

Particle Image Velocimetry (PIV) is a relatively new and successful measurement technique developed and employed for instantaneous velocity field determination in the past decades. Over the past decades, due to advances in cameras, lasers and computer processing power, it has developed from a qualitative to quantitative flow measurement technique. It is employed to acquire instantaneous measurements of the velocity field of fluid flow in a two-dimensional plane with two-component PIV (2C-PIV (Willert et al. 1991)) or in three-dimensional space with tomographic PIV (Elsinga et al. 2006). The basics of PIV relevant to the experimental campaigns carried out in the current work will be mentioned in this section. A more advanced and comprehensive detailed picture is given in the book by Raffel et al, [30].

3.1.1 Principle of 2C-PIV

PIV measurement technique is based on the tracking of tracer particles within a fluid flow. A schematic overview of a 2C-PIV setup is depicted in Fig 3.1. A typical 2C-PIV system consists of a seeding system (not displayed) that introduces small tracer particles into the flow, a laser system with laser optics to produce a laser-light sheet, and a digital imaging and recording system consisting of at least one camera with imaging optics.

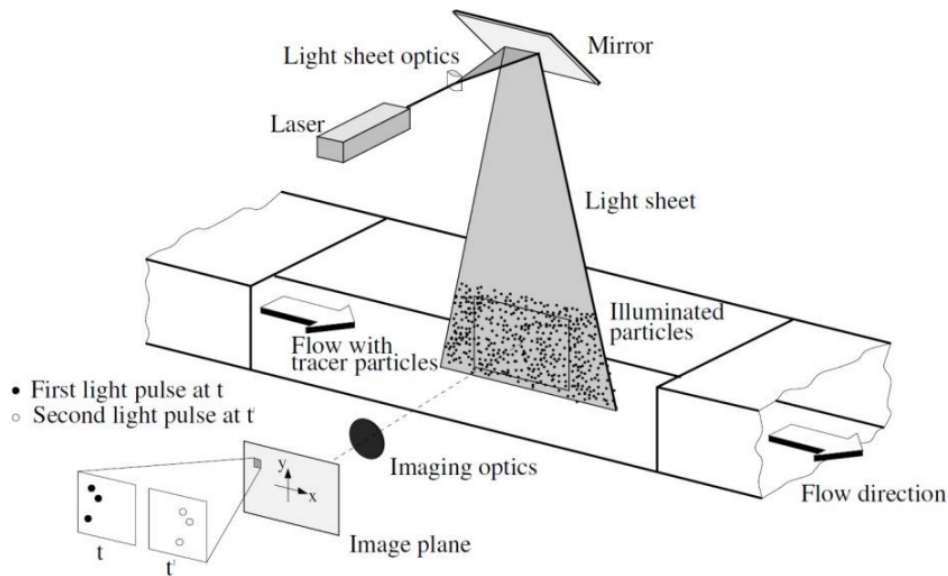


Figure 3.1: Schematic overview of a 2C-PIV setup. Taken from Raffel et al [30]

Tracer or 'seed' particles are introduced by the seeding system into the flow at a suitable location so that the particles are uniformly dispersed into the flow at a desired volume concentration. In the case of wind tunnel tests, the plenum is a suitable location for the introduction of the particles. These particles have to be sufficiently small so that they follow the flow accurately and do not change the properties of the fluid or flow to be measured. A pulsed light source such as a laser generates a light sheet in the region of interest at discrete instants Δt apart so that tracer particles in the flow are illuminated at these instants. For example, in the current work, the wake downstream of the experimental model was the region of interest (see Fig. 4.6). Simultaneously with the laser pulses, a CCD camera, placed perpendicular to the measurement plane, will record the light scattered by the particles in two subsequent image frames. The two image frames, $I(x, y, t)$ and $I(x, y, t + \Delta t)$, will contain the specific particle positions.

To obtain the average displacement of the particles the images are divided into a number of segments, the so-called interrogation windows. A cross-correlation between the interrogation windows of the two images allows for detection of the average particle displacement in pixels inside such a window over the time-step Δt separating the images. This principle is shown in Fig. 3.2. Evaluating the particle displacement with cross-correlation has the advantage that no explicit particle detection is required. By taking into account the magnification factor the displacement vector can be expressed in physical units. Furthermore, by considering the time separation between the subsequent images, Δt , the velocity vector can be determined, and hence the velocity field can be reconstructed. The density of vectors in the space can be adjusted based on the size of the interrogation window used. However care must be taken to ensure that the size of window exceeds the average particle displacement in the period Δt .

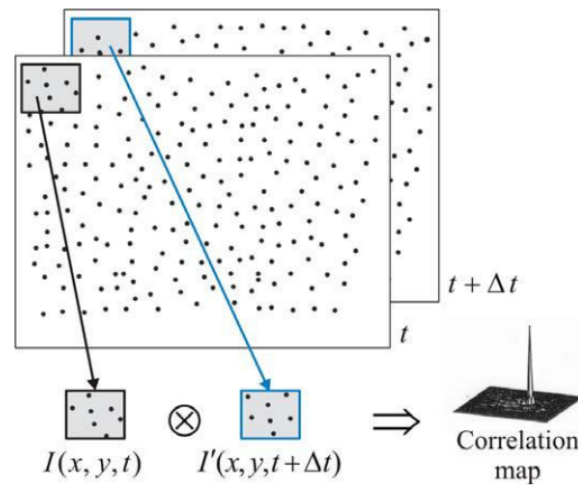


Figure 3.2: Image windowing and discrete cross-correlation map. Taken from Scarano [32]

With the cameras and laser placed outside the flow only the particles are present in the flow. Once the tracer particles are chosen so they do not alter the flow or its properties, this measurement technique is considered to be non-intrusive. Furthermore PIV permits to the measurement of instantaneous velocity fields of both small and large areas of interest with high spatial resolution, while most other velocity measurement methods allow only instantaneous single point measurements. The temporal resolution (image-pair acquisition frequency) of PIV is increasing with advances in technology, though it is still limited by camera storage and laser repetition rate.

3.1.2 Tracer Particles

The tracer particles inserted into a fluid flow act as a tracking device and are typically employed with Particle Image Velocimetry or Laser Doppler Velocimetry. As described above, they are required to follow the flow accurately without altering the fluid flow characteristics. Consequently, the tracer particles' characteristic response time has to be smaller than the smallest characteristic time scale of the fluid flow. Moreover, for the illuminated particles to be detectable by cameras, they should scatter enough light towards the camera.

Mechanical Properties

For accurate PIV measurements, the tracer particles need to faithfully follow the motions of the flow. This can be achieved, by ensuring the velocity difference between the particles and the fluid is very small. The velocity difference or slipping velocity, illustrated in Fig. 3.3, is $\mathbf{U}_s = \mathbf{U}_p - \mathbf{U}_f$, where \mathbf{U}_p is the particle velocity vector and \mathbf{U}_f is the fluid velocity vector.

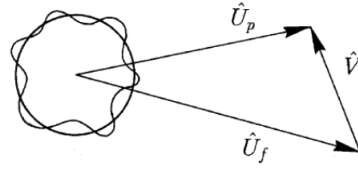


Figure 3.3: The motion of a tracer particle in flow. Taken from [25]

The exact particle motion in a moving fluid is rather complicated, but an accepted model to (qualitatively) describe the motion of seeding particles is Hinze's model [17]. For very small tracer particles, as applied in PIV, the approximation of the equation of motion can be reduced to:

$$\frac{\pi}{6}d_p^3\rho_p\frac{d\mathbf{U}_p}{dt} = -3\pi\mu d_p\mathbf{U}_s \quad (3.1)$$

where d_p and ρ_p represent the particle diameter and density respectively, and μ the fluid dynamic viscosity. The terms on the left and right hand side of the equation represent, respectively, the force required to accelerate a particular particle in the flow field and the quasi steady viscous force in the form of Stokes' drag.

Electrostatic effects

In Eq. 3.1 it is assumed that the tracer particles are spherical, which is a valid assumption for small droplets and disperse solid particles of uniform size. It is also assumed that the external body forces on a particular particle are negligible. However, the ionization of fluid particles during the plasma actuation results in tracer particles getting charged by ion impact, at which point the electrostatic forces can affect the trajectory of the tracer particles. Hence, an electrostatic force needs to be added to the right hand side of Eq. 3.1. This force is determined by the maximum net charge level q_n that is obtained after a certain exposure time to the electric field and the electric field strength E_0 .

$$F_{elec} = q_n E_0 \quad (3.2)$$

Artana et al [1] found the maximum attainable net charge level q_n for droplets of hydrocarbon to be

$$q_n \simeq 1.5\pi d_p^2 \epsilon_0 E_0 \quad (3.3)$$

with ϵ_0 the Faraday constant. This equation shows the influence of electric forces becomes less when the seeding particle diameter is very small. Considering a typical tracer particle of diameter $1\mu m$ and a maximum electric field E of 10^6 V/m the ratio between the viscous and electrostatic forces can be expressed as [1]

$$\frac{F_v}{F_{el}} = \frac{-3\mu d_p \mathbf{U}_s}{1.5\pi d_p^2 \epsilon_0 E^2} \simeq 4\mathbf{U}_s \quad (3.4)$$

where \mathbf{U}_s is the slipping velocity seen earlier. The relation is directly dependent on the slipping velocity and is inversely proportional to the squared of the electric field strength. Hence, lower the slipping velocity (as desired, for tracers to follow the flow closely), lower the influence of the electrostatic forces.

One can conclude that the electrostatic forces can be neglected for electric fields below 10^6 V/m for particle diameters of $1\mu m$. A maximum electric field of 2×10^6 V/m results in a ratio equal to the slipping velocity between the viscous and electrostatic forces, according to Eq. 3.4. For typical plasma actuator induced velocities of several m/s, the viscous forces are still several times ($O(1)$) larger than the electrostatic forces. In general, electrostatic effects on tracer particles are a concern in cases with plasma actuation, due the high electric fields that are generated by the electrodes in the surrounding region. App. F contains the analysis of the electric fields generated by the various electrode layouts of the actuation modes tested, where the electrostatic effects on tracer particles in the flow are taken into account.

Characteristic Parameters

The fidelity of the tracer particles to track the fluid flow the particle response time can be determined by the dimensionless particles Stokes number, S_k , which defines the ratio between the particle characteristic response time τ_p and the characteristic flow time scale τ_f .

$$S_k = \frac{\tau_p}{\tau_f} \quad (3.5)$$

where the flow characteristic time τ_f may be estimated by a dimensional analysis:

$$\tau_f = \frac{1}{f_{flow}} \quad (3.6)$$

where f_{flow} is a characteristic flow time scale, for example the shedding frequency when flow with Karman vortex shedding is considered. The particle characteristic time τ_p is given by

$$\tau_p = d_p^2 \frac{\rho_p}{18\mu} \quad (3.7)$$

From a practical point of view it can be stated that for $S_k < 0.1$ an acceptable flow tracing accuracy with errors below 1% is achieved. The use of these parameters in characterising the tracers used in the current PIV experimental setup in the presence of baseline un-actuated flow is given in Sec. 4.4.2.

Light Scattering Properties

In order to track particles in a fluid use is made of the particle's reflective behaviour when illuminated. Illumination of the particles is performed with a laser sheet, which is required to be thin in order to ensure focus only on particles in a specific plane. In three-dimensional PIV a thicker laser sheet is required to capture out of plane motion. The light scattered by small particles is a function of the ratio of the refractive index of the particles to that of the surrounding medium, their size, shape and orientation. Furthermore, the light scattering also depends on polarisation and observation angle. For spherical particles with diameters d_p larger

than the wavelength of the incident light λ , Mies scattering theory can be applied. Fig. 3.4 shows the scattered light intensity as a function of the scattering angle for a particle of $1\mu\text{m}$ diameter.

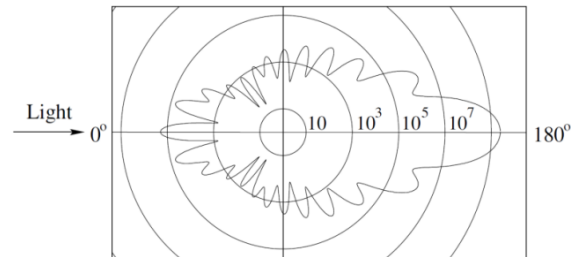


Figure 3.4: Distribution of the light intensity scattered by a $1\mu\text{m}$ oil droplet particle in air. Source Raffel et al. [30].

The scattered light has a maximum at 180° and another at 0° . At 90° , which is the typical orientation of a camera with respect to the illuminated particles, a minimum is found. Due to this minimum it is important to maximise the scattered light by selecting particles with a high refractive index and the largest size possible limited by the particles flow tracing fidelity. Other improvements can directly involve the emitted light wavelength and power. These variables are seldom free, however, due to expensive lasers and CCD sensors and optics normally employed.

3.1.3 Laser Sheet Illumination

For illumination of the tracer particles lasers are commonly used in PIV. This is because they emit monochromatic light with a high energy density, which can be easily bundled into thin light sheets. During the measurement the tracer particles are illuminated twice by a laser sheet produced by two laser pulses. These pulses need to have a very short duration to avoid the appearance of particle streaks on the camera image. As a laser pulse leaves the laser head, it passes through a set of lenses and is deflected by mirrors before a thin light sheet is eventually obtained at the measurement location. The light intensity of this sheet needs to be sufficient for the tracer particles to be detected by the camera. The laser sheet has also to be thin enough such that only the particles in a plane are illuminated.

The typical arrangement of the lenses is a cylindrical lens, which linearly expands the laser beam as shown in Fig. 3.5(a), followed by one or more spherical lenses that converge the laser beam as shown in Fig. 3.5(b), such that a thin laser sheet results. Sec. 4.4.2 describes the laser sheet setup that was used in the PIV Setup used in the tests carried out.

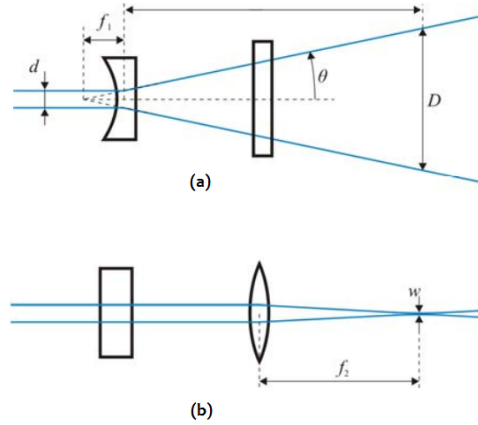


Figure 3.5: Light sheet formation optics: a) side view, showing the expansion of the laser beam and b) top view, showing beam focus at measurement location. Figures taken from [32]

3.1.4 Particle Imaging

The image of the tracer particles in the light sheet is focused on the camera sensor using a photographic lens. The imaging system is characterized by its focal length f , aperture number $f_{\#}$ and the image magnification M . The aperture number $f_{\#}$ is defined as f/D , where D is the aperture diameter of the camera. The image magnification is defined as

$$M = \frac{d_i}{d_o} = \frac{\text{Image size (pixels)}}{\text{FOV (m}^2\text{)}} \quad (3.8)$$

where d_i is the image distance and d_o is the object distance. The focal length, image and object distance are related through the lens equation. The lenses are finite and therefore diffraction limited, which means that point sources will appear as Airy disks and rings on the image sensor. The size of such a disk d_{diff} can be approximated by

$$d_{diff} = 2.44 f_{\#} \lambda (M + 1) \quad (3.9)$$

Then the minimal image particle diameter, as observed on the image sensor, is determined by

$$d_{\tau} = \sqrt{(M d_p)^2 + (d_{diff})^2} \quad (3.10)$$

For small particles of $d_p \leq 1 \mu\text{m}$ this minimal image particle diameter is typically dominated by the diffraction limit d_{diff} , although d_{diff} can be controlled to some extent with the aperture number $f_{\#}$. Finally, the depth of the field δ_z can be approximated by

$$\delta_z = 2 f_{\#} d_{diff} (M + 1) / M^2 \quad (3.11)$$

A significantly large aperture diameter is required to gather sufficient light from all of the particles, and also to decrease the size of the diffraction pattern. However, a big aperture diameter decreases the depth of field, which is needed to have all the illuminated particles within the laser sheet in focus. An optimal particle image size is around 2 - 2.5 pixels [32]. A lower value can indicate only the presence of a particle and will not result in an accurate particle position due

to the absence of intensity distribution in neighbouring pixels (i.e. under sampling). This is called 'peak locking'. This is shown in Fig 3.6(a). A slight spread of the particle intensity over a few pixels is desirable as then sub-pixel interpolation techniques can be applied to increase the particle image pixel resolution to sub-integer values. A too large value for $f_{\#}$ will however lead to overlap of the individual particle images, due to increased diffraction and depth of focus, decreasing the image contrast and thereby the spatial resolution of the measurement. This is shown in Fig 3.6(b)

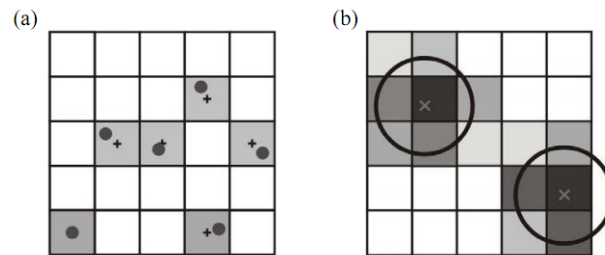


Figure 3.6: Particle sizes in image showing (a) Pixel peak locking and (b) too large particle diameter. Figure from Scarano (2007).

To accurately determine the velocity vectors from PIV measurements a proper choice of the seeding density and pulse separation is required. In order to achieve an error in the particle displacement of 1-2%, the pulse separation time has to be chosen, such that the particle displacement is approximately 10 pixels. Obtaining this pixel shift will result in a high number of particle pairs, meaning the majority of the imaged particles are located in the same window during both exposures. Thereby the particle displacement can be determined accurately from the correlation peak. The displacement must be large enough to correctly establish the velocity vectors and yet small enough to ensure that the majority of the particles do not move out of the window between the images in the image pair. This is closely related to the one-quarter rule for in-plane particle image displacements: the maximum in-plane displacement should be smaller than $1/4$ of the window size [32].

As far as the seeding is concerned, the distribution should be uniform. The seeding density should have an equal distribution of the particles and provide a sufficient number of particles in an interrogation window (at least 10 [32]). A density that is too low will induce individual particle tracking, which is not necessarily representative for the flow locally, while too high a particle density can reduce particle recognition during data processing and prevent a realistic reconstruction of the velocity field.

3.1.5 Image Analysis

Image Recording

The particle images are recorded on a Charge Coupled Device (CCD) or Complementary Metal Oxide Semiconductor (CMOS) sensor. The CCD is an electronic sensor that converts light (photons) into free electrons. When discharged, current and voltage proportional to the charge accumulated are produced. Two-dimensional array sensors for imaging are obtained by placing the individual sensitive elements (pixels) on a Cartesian grid. Modern CCDs have a typical

size of several Megapixels. During exposure the pixels are exposed to a light intensity which is converted into electrons. The accumulated charge is read out sequentially on a row-by-row basis by a charge to voltage converter and digitised by an A/D converter. The readout process is limited to 10 - 20 MHz allowing only for frames in the order of 10 - 30 Hz.

For fast, time-resolved recordings of several kHz such as was carried out during the current experimental work, CMOS sensors are used. The CMOS sensors are based on the active pixel sensor (APS) technology in which, in addition to the photodiode, a readout amplifier is incorporated into each pixel. This converts the charge accumulated by the photodiode into a voltage which is amplified inside the pixel and then transferred in sequential rows and columns to further signal processing circuits [30]. Together with highly parallel readout electronics storage devices this allows for the recording and handling of several thousand frames per second (3000 on full sensor size, up to 10,000 on smaller sensor size) at acceptable noise levels. Cameras can have memories up to 16GB on board to store the large amount of data, recorded within seconds [30]. The 'double-frame' recording mode was used for the image acquisition due to which the raw images are obtained as image-pairs. The camera aperture opening instants are synchronised with the laser pulsing instants. The laser repetition rate and the camera recording rate are set to the desired Δt separating the pulses.

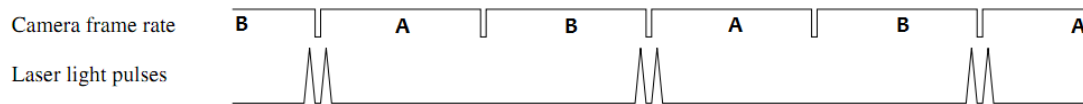


Figure 3.7: Camera and Laser Timing diagram for double frame image acquisition. Taken from Raffel et al [30]

Image Processing

The processing of the acquired images is based on a cross-correlation between interrogation windows resulting from the image pair, as briefly introduced in Sec. 3.1.1 (Fig. 3.1). During evaluation the two images, containing the specific particle positioning at time t and $t + \Delta t$, are subdivided into smaller windows, the interrogation windows. The interrogation window size is chosen such to contain at least ten particle images [32]. An interrogation window consists of $N \times N$ pixels. The intensity of the scattered light by the particles contained in the interrogation window of the first image, I , is determined. Subsequently a window of the same size and at the same location is shifted over the second image and I' of the image is determined and the cross-correlation between the particles in the images is performed. The cross-correlation is determined by:

$$R_{II'} = \sum_{i=-K}^K \sum_{j=-L}^L I(i, j) I'(i + x, j + y) \quad (3.12)$$

The implementation of the two-dimensional correlation according to its definition is a computationally intensive operation. An efficient implementation of the cross-correlation operator makes use of the Fourier Transform (FT) based on the Wiener-Khintchine theorem, which says that for two functions $f(x, y)$ and $g(x, y)$

The inverse Fourier transform of the product of two Fourier transformed functions $G(p, q)$ and $F(p, q)$ yields the correlation of $g(x, y)$ and $f(x, y)$

The FFT requires that the number of rows and columns of the interrogation window have an exponent of 2, reducing the possible interrogation window sizes to 64×64 , 32×32 , 16×16 , etc. The steps of the above procedure is shown in Fig. 3.8.

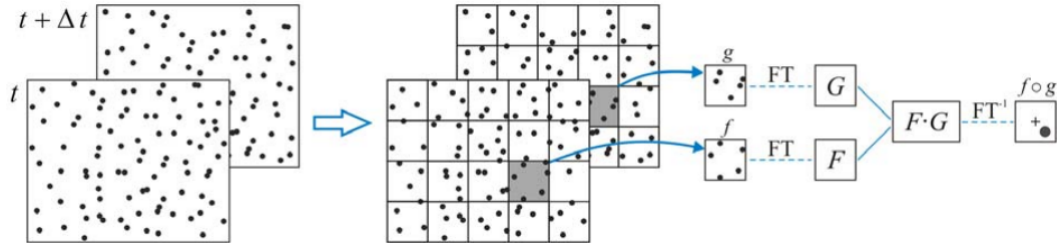


Figure 3.8: Correlation map evaluation by Fourier Transform. Taken from [32]

A high value for $R_{II'}$ corresponds to a close resemblance between the particles inside the two interrogation windows and the cross-correlation peak location indicates the shift for which particles in the first image match with particles in the second image. The position of the cross-correlation peak determines the average displacement of the particles over the time-step Δt separating the image pair. To obtain a high number of imaged particles in the same interrogation window the window size should be as large as possible, resulting in a high number of imaged pair. However a large window size results in a poor spatial resolution. To increase the spatial resolution and maintain the high-signal-to noise ratio from large window size, a multi-pass interrogation with offset can be applied. With large window size the local averaged displacement is determined. After the first interrogation the obtained result will be used as a predictor. In the second step a finer windowing is obtained by reducing the first window in all directions. Based on the predictor the interrogation area of the second image can be given an offset to maximise the number of particle matches. This allows to obtain a high number of particle images and a high spatial resolution. Applying an overlap between adjacent interrogation windows can further increase the spatial resolution.

Data Processing

The velocity fields obtained through the image processing can be used for data processing. Matlab was the software application of choice used for this. The velocity fields are represented by a large matrix containing the velocities in the FOV. The matrix is two-dimensional for planar PIV and three-dimensional for tomographic PIV. The velocity fields are processed to obtain flow field properties such as vorticity, streamlines, field statistics (average and RMS velocity components), time and frequency domain calculations such as power spectral or correlation analyses, or to extract information on dominating flow phenomena (POD), etc. All of the flow-field related results shown in Chapter 5 for the baseline flow case and various actuation modes are obtained by processing the correlation obtained PIV velocity fields using Matlab. Some of these data processing techniques are described in the following sections.

The calculation procedure for the vorticity field from the processed velocity field will be described here. First the velocity field (whether average or instantaneous) needs to be decomposed into its mutually orthogonal components. Based on the coordinate system adopted here (App. 4.2.1), considering for eg. the $x - y$ plane, the velocity field can be decomposed into its u and v

components. The corresponding vorticity field is calculated at each velocity vector location based on the circulation estimate. This was calculated using a standard integration scheme such as the trapezoidal rule over a small rectangular contour around each point, bounded by the surrounding points. This way, the circulation at each point (i, j) in the velocity field is estimated from the neighbouring 8 points, which makes it more accurate than other differencing schemes:

$$(\omega_z)_{i,j} \simeq \frac{\Gamma_{i,j}}{4\Delta x\Delta y} \quad (3.13)$$

where

$$\begin{aligned} \Gamma_{i,j} = & \frac{1}{2}\Delta x(u_{i-1,j-1} + 2u_{i,j-1} + u_{i+1,j-1}) + \frac{1}{2}\Delta y(u_{i+1,j-1} + 2u_{i+1,j} + u_{i+1,j+1}) \\ & - \frac{1}{2}\Delta x(u_{i+1,j+1} + 2u_{i,j+1} + u_{i-1,j+1}) - \frac{1}{2}\Delta y(u_{i-1,j+1} + 2u_{i-1,j} + u_{i-1,j-1}) \end{aligned} \quad (3.14)$$

and Δx and Δy are the physical dimensions of the area around each velocity vector (the spatial resolution of the velocity field).

3.2 Proper Orthogonal Decomposition

Proper Orthogonal Decomposition (POD) is used in computationally processing large amounts of high-dimensional data with the aim of obtaining low-dimensional descriptions that capture much of the phenomena of interest. It has been applied to obtain approximate, low-dimensional descriptions of turbulent fluid flows, structural vibrations, dynamic systems, etc. In the context of the present Thesis work, its application to a sample of velocity fields is in evaluating the degree of presence of regular, periodic and coherent structures, such as a Karman vortex street, for example. The first two POD modes (explained in the subsequent paragraphs) can spatially represent the vortex shedding process. This is explained in Sec. 5.2.5 where POD is carried out on the baseline (un-actuated) flow vortex street from the trailing edge of the experimental model tested upon.

The mathematical basics of POD as was used in this work will be briefly be built up here. Consider a general function $z(x, t)$; we can approximate it as a finite sum over a domain of interest in a variable separated form:

$$z(x, t) = \sum_{k=1}^M a_{k(t)} \phi_k(x) \quad (3.15)$$

The above representation is not unique; the set of basis functions $\phi_k(x)$ can be chosen to be Fourier polynomials, Legendre polynomials, etc. For each of these set of functions, the sequence of time-functions $a_{k(t)}$ will be different. The functions can also be chosen to be orthogonal to each other. The POD is concerned with finding one possible choice of orthogonal basis functions $\phi(x)$ so that the first say k of these functions gives the best possible k -term approximation of the system. These special, ordered orthonormal functions are called the proper orthogonal modes for the function $z(x, t)$. With these functions, the RHS of Eq 3.15 is called the POD of $z(x, t)$ [3].

The discrete version of the POD is the Singular Value Decomposition (SVD) of matrices. The mathematical properties of the SVD, as well as the geometrical interpretations are given in detail in the review by Chatterjee [3]. In practical applications such as the cases of interest here, where

measured data is stored in discrete vectors and not continuous functions, the formulation of the POD is as follows - consider a system where different scalar state variables, or different scalar components of a vector quantity, for example x and y velocity components from a PIV velocity field, are measured at m different physical locations and N different time instants. The data is then arranged out into an $N \times m$ matrix A , so that element A_{ij} is the j^{th} measured quantity or component at the i^{th} time instant. It is common to subtract from each column of A the mean value of that column. Now, the SVD of A is computed, which is as follows:

$$A = USV^T \quad (3.16)$$

where U is an $N \times N$ orthogonal matrix, V is an $m \times m$ orthogonal matrix and S is an $N \times m$ matrix with all elements zero except along the diagonal. U and V are also unitary matrices, and their columns are called respectively the left and right singular vectors. The diagonal elements S_{ii} consist of $r = \min(N, m)$ non-negative numbers σ_i which are arranged in decreasing order. These are called the singular values of A and are unique. Since they are arranged in a specific order, the index k of the k^{th} singular value will be called the singular value number. Now if we assign $US = Q$, then the matrix Q is $N \times m$, and $A = QV^T$. Letting q_k be the k^{th} column of Q and v_k be the k^{th} column of V , we can write the matrix product in Eq 3.16 as:

$$A = QV^T = \sum_{k=1}^m q_k v_k^T \quad (3.17)$$

Eq. 3.17 is the discrete version of Eq. 3.15. The functions $z(x, t)$, $a_{k(t)}$ and $\phi_k(x)$ are represented here by the matrix A , column matrix q_k and row matrix v_k^T respectively. The columns of V , which are orthogonal, represent the proper orthogonal modes of the system. While significant differences exist between them, SVD is closely related to Eigenvalue decomposition. On premultiplying Eq. 3.16 with its transpose and noting that $V^{-1} = V^T$, we see that V is the matrix of eigenvectors of the symmetric $m \times m$ $A^T A$ matrix, while the squares of the singular values are the $r = \min(m, N)$ largest eigenvalues of $A^T A$. Similarly, on premultiplying the transposed Eq. 3.16 with itself and noting that $U^{-1} = U^T$, we see that U is the matrix of eigenvectors of the symmetric $N \times N$ matrix AA^T and the squares of the singular values are the $r = \min(m, N)$ largest eigenvalues of AA^T .

3.2.1 Method of Snapshots

Since high spatial resolution velocity fields were obtained from PIV over a small time period ($m \gg N$), the *method of snapshots* was used. Instead of directly finding the POD modes in V by the SVD of A , it was more efficient to first compute the matrix U as the matrix of eigenvectors of AA^T and premultiplying Eq. 3.16 by U^T to obtain

$$U^T A = SV^T \quad (3.18)$$

The quantities of interest were contained in the right-hand side of the above equation. The norms of the rows of SV^T were the singular values, and normalising them to unit magnitude gave the corresponding proper orthogonal modes. Certain points were kept in mind while carrying out the POD - The velocity fields must be uncorrelated and collected with a time spacing much larger than the inherent dynamics of the system. The velocity fields were hence down-sampled before being selected for POD computation. 500 images were considered for the POD

analysis from each tested case, roughly 1 for every 6 measured velocity fields, considering that the rate at which raw image-pairs were recorded by the PIV system was 3000 Hz. The POD is also sensitive to coordinate changes; it processes numbers, whose physical meaning it does not know [3]. Inappropriate scaling of the variables being measured can lead to misleading if not meaningless results.

The eigenvalues of AA^T (or the squares of the singular values of A) are sometimes referred to as the energies corresponding to the proper orthogonal modes. They represent the fluctuating Kinetic Energy of the fluid. However these are not true physical energies. They can be used in finding the relative amount of energy contained in each mode as a fraction of the total, rather than the true physical energy of each mode itself. The actual total fluctuating Kinetic energy of the flow is calculated as

$$TKE = \sum_{i=1}^{N_{vectors}} \frac{1}{2} \left((u'_i)^2 + (v'_i)^2 \right) \Delta x \Delta y \quad (3.19)$$

where u'_i and v'_i are the individual vectors in the fluctuating (RMS) velocity field, and Δx and Δy are the dimensions of the interrogation window around each velocity vector in the imaged plane. The use of POD here is in quantifying the degree of success of the suppression of the vortex shedding in the flow field. In cases where the shedding is strong, as mentioned earlier, the first two modes will account for the majority (around 80%) of the fluctuating kinetic energy in the flow, and the TKE calculated from Eq 3.19 will be high. This will not be so in cases where the actuation is successful in suppressing the vortex shedding or attenuating it to a large extent.

3.3 Power Spectral Density

Power spectral analysis follows closely from Fourier analysis of time varying signals. Fourier analysis is a widely used tool in engineering to detect an underlying harmonic component in a time signal. In the current work, Fourier analysis is used in processing the time-resolved velocity field data from high speed time-resolved PIV. The Fourier transform acts on a continuous time series $f(t)$ in the following manner, giving a series of its various frequency components $F(\omega)$, or its frequency domain signal:

$$F(\omega) = \int_{-\infty}^{\infty} f(t) e^{-i\omega t} dt \quad (3.20)$$

For discrete signals, such as time-resolved velocity signals from flow measurement techniques, the form of the fourier transform is slightly different:

$$F(m\omega_s) = \sum_{k=0}^{N-1} f_k e^{-im\omega_s k} \quad (3.21)$$

where $\omega_s = \frac{2\pi}{N}$. The above is called the Discrete Fourier Transform (DFT) of the signal $f(t)$. Hence, a time signal, for example a vector f of N time domain samples of duration t (hence, taken at a sampling frequency $f = t/N$) returns a vector F of samples $F(m\omega_s)$, $m = 0, 1 \dots (N-1)$ after the DFT computation. In general, F is complex; the magnitude of F at each frequency ω_s gives the harmonic amplitude at that frequency. Hence, the peaks seen on plotting the magnitude of vector F against the frequencies gives the dominant harmonic frequencies and the corresponding amplitudes.

In this work, MATLAB was used to run DFT routines (called Fast Fourier Transforms, or FFTs) on the various time signals of interest, which were the velocity signals at various points of interest in the velocity fields considered sampled at the frequency of PIV image-pair acquisition, 3000 Hz. The general method is as follows:

1. The mean of the signal was subtracted from the signal and the *fft* routine run on it.
2. Only the real (amplitude) components of the frequency domain signal are of interest, hence the magnitude is taken of the obtained signal, after which it is normalised by $(N/2)$, where N is the length of the signal.
3. The output of the FFT from Matlab corresponded to a frequency range of 0 to $2f_s$, where f_s was the sampling frequency of the time signal. However, the part of F from f_s to $2f_s$ was nothing more than the negative frequency part of F . Hence, the output needed to be shifted to obtain the zero frequency components at the center. Since the negative frequency part of F contained the same data as the positive frequency part, it was discarded.

The absolute value of the FFT of a signal is an indication of the total amount of information contained at a given frequency, while the square of the absolute value is considered the power of the signal. The Power Spectral Density (PSD) was calculated by the squaring of the absolute value of the signal obtained from the FFT after the steps mentioned above. The PSD is measured in W/Hz, and is a better means of ascertaining the power of the harmonic fluctuations contained in the signal at the various frequencies than the FFT-obtained Fourier series, especially when comparing two signals in the frequency domain.

3.4 Correlation Analysis

In this work, correlation analysis is used in quantifying the degree of spanwise coherence in the shed Karman vortex rolls from the trailing edge in the streamwise-spanwise ($x - z$) planes at a transverse position y of the upper shear layer. For any two time varying signals $f(t)$ and $g(t)$, the *covariance* between them is a measure of how the two signals change with respect to each other. If the greater values of one variable mainly correspond with the greater values of the other variable, and the same holds for the smaller values, i.e., the variables tend to show similar behaviour, the covariance is a positive number. In the opposite case, when the greater values of one variable mainly correspond to the smaller values of the other, i.e., the variables tend to show opposite behaviour, the covariance is negative. The sign of the covariance therefore shows the tendency in the linear relationship between the variables. For the two signals considered, the covariance $\sigma(f, g)$ is calculated as

$$\sigma(f, g) = E[(f - E[f])(g - E[g])] \quad (3.22)$$

where $E[x]$ is the expected value of x , also known as the mean of x . The magnitude of the covariance is not that easy to interpret. Hence, in this present work, the normalized version of the covariance, the correlation coefficient $R(f, g)$ is used, which shows by its magnitude the strength of the linear relation. The correlation coefficient has values in the interval between and including 1 and -1.

$$R(f, g) = \frac{\sigma(f, g)}{\sqrt{\sigma(f, f)\sigma(g, g)}} \quad (3.23)$$

In the shear layer $x - z$ planes of the representative cases considered for the various actuation modes, twenty spanwise points along six fixed streamwise positions at $x/h = 0.5, 1, 1.5, 2, 2.5$

and 3 were considered where the streamwise velocity time signals were gathered from the time resolved PIV velocity fields. With a reference point close to the mid-span as the reference point, the correlation coefficients of the velocity signal at this point with the other points for each of the streamwise positions were calculated and plotted against the spanwise location of these points. High values of correlation coefficients that do not fall off rapidly on moving away from the reference point indicate a high degree of spanwise coherence, as was seen for the baseline flow case 5.12(b). However, the correlation coefficients are seen to fall off rapidly with distance away from the reference point for the actuated flow fields of the various modes, as seen in Figures 5.41(b), 5.57(b) and 5.73(b).

Chapter 4

Experimental Setup

This chapter deals with the practical aspects of the various experiments carried out. For the chronological sequence of tasks and experiments carried out over the course of this Thesis work, the reader is advised to refer to App. A. The first section within this chapter will describe the setup of the dielectric parametric study that was carried out as a prelude to the flow measurement tests. The coordinate system adopted for describing the results and the various spanwise modulated plasma actuator configurations along with the imaged $x - y$ planes for flow measurement will then be discussed, followed by a section dedicated to the experimental aspects and details of the time resolved PIV campaign, which was the source of the bulk of the results that will be presented in Chap. 5.

4.1 Dielectric Parametric Study

4.1.1 Background and Motivation

When selecting the dielectric material between the exposed and covered electrodes for a plasma actuator, two main factors have to be taken into consideration:

- *Minimum thickness:* Its minimum thickness should be sufficient for the material to not break down under the applied voltage. However this required thickness is very small and easily achieved. For example, for the most commonly used material Kapton polyamide a few layers of dielectric film tape is enough to ensure this. The standard thickness of such tapes is 2 mils or $50.8 \mu\text{m}$.
- *Dielectric coefficient:* Recently, in Corke et al [6] it was suggested that it is beneficial to use thicker dielectrics that have low dielectric coefficients (ϵ), so that the power loss which is proportional to $f_{AC} \times \epsilon/t$ can be minimised, where f_{AC} is the frequency of the AC input signal to the plasma actuator and t is the thickness of the dielectric. Additionally, in Thomas et al [36] it was reported that a thick Teflon dielectric ($\simeq 6\text{mm}$ thick) has the highest actuator saturation thrust, due to the lower dielectric constant which allowed it to achieve higher voltages before the onset of streamer formation. Hence, it is clear that thicker materials with lower dielectric constants are preferred due to the higher electric fields they can withstand before saturation or breakdown.

Based on these considerations, it was decided that Makrolon would be used as the dielectric material instead of Kapton Polyamide. Makrolon is a polycarbonate material that is used in glazing and industrial applications. It has high impact strength and other favourable physical properties. Among its electrical properties, it has a dielectric constant of around 2.96 - 3.1 (Source: General Purpose Product Data Sheet for Makrolon[®] GP, Bayer). This is lower than Kapton, which has a dielectric constant of 3.4 - 3.5 (Source: Product Data Sheet, Kapton[®] polyimide film, DuPont). Hence, a thick layer of Makrolon as a dielectric can be expected to withstand higher voltages before saturation, thereby giving rise to higher body forces and induced wind. With the dielectric material defined and fixed, it was desired to 'get to know' the plasma actuator in greater detail. The two main factors motivating the dielectric parametric study are as follows:

1. *Characterising the actuator properties:* It is of interest to characterise the properties of a planar plasma actuator constructed on Makrolon dielectric from the point of view of the two main parameters that determine the performance of an active flow control actuator:
 - (a) Induced Wind Speed: This is a direct measure of the body force exerted by the plasma on the surrounding air in channelling it into a jet. The magnitude of the induced jet speed as it evolves in the downstream direction can be measured in the absence of external flow (i.e. quiescent condition) using a pitot tube or PIV at the appropriate locations.
 - (b) Consumed electric power: An important parameter when choosing an actuator for an application. Since the input signal is cyclic, it is more useful to know the amount of power consumed averaged per cycle, and normalised by the actuator length (more specifically, the length of the interface between the exposed and covered electrodes).
2. *Parameter Optimisation:* It is of interest to find the right combination of the governing parameters of the plasma actuator to obtain the optimum amount of forcing by it. These parameters are of two types:
 - (a) Geometrical and physical parameters: These include the geometrical parameters such as widths of the covered and exposed electrodes, the gap between them, the thickness of the dielectric sheet, as well as the dielectric constant, electrode material, etc.
 - (b) Electrical parameters: For the plasma actuator, the governing electrical parameters are the frequency (f_{AC} Hz) and the peak-to-peak amplitude (V_{pp} kV) of the input AC signal, which was continuous (non-pulsed) and sinusoidal.

4.1.2 Experimental Setup

Since the actuators needed to be tested for the induced wind that they can generate, it was necessary to enclose them and the measuring instruments to prevent the influence of external airflows. A suitable box with transparent faces made of plexiglass was used for this purpose. Long, thin pitot tubes made of glass were used so that the airflow they measured could settle fast and the small pressure differences caused by the actuator's induced wind could easily be measured; the longer the tube, the farther the holding apparatus at its end could be from the actuator itself, giving more accurate results. To measure the streamwise evolution of the induced wind speed, a suitable traverse mechanism was used that allowed the pitot tube to be moved in the streamwise direction with sufficient accuracy and convenience. The experimental setup is shown in Fig. 4.1. A long pipe connected the end of the pitot tube away from the actuator

to one of the pressure ports of a pressure transducer. The other pressure port of the pressure transducer was open to the atmosphere, so that it measured the pressure difference between the ports, which was the dynamic pressure of the induced wind from the actuator. From this, the wind speed itself can be easily found and read in real time and stored during the experiments through a National Instruments (NI) DAQ board. A Virtual Instrument (VI) program panel on NI's Labview program was used to supply the electrical input parameters and control the HVA, which was a TREK 20/20C high voltage amplifier (± 20 kV, ± 20 mA, 1000W, gain 2kV/V). The current output from the HVA was not directly connected to the DAQ board due to the fact that the filamentary nature of the microdischarges between the electrodes occur at frequencies that are too high for the HVA to resolve. Instead, the current output cable was connected to a resistor connected across the ground terminal the voltage output across this resistor was divided by its resistance to obtain the discharge current, and this gave a much more accurate, time resolved picture of the current. The power was calculated as the product of the instantaneous voltage and current, averaged over the number of cycles and divided by the length of the overlap between the exposed and covered electrodes. The averaging was significant as the instantaneous current was highly unsteady in nature, consisting of microdischarges.

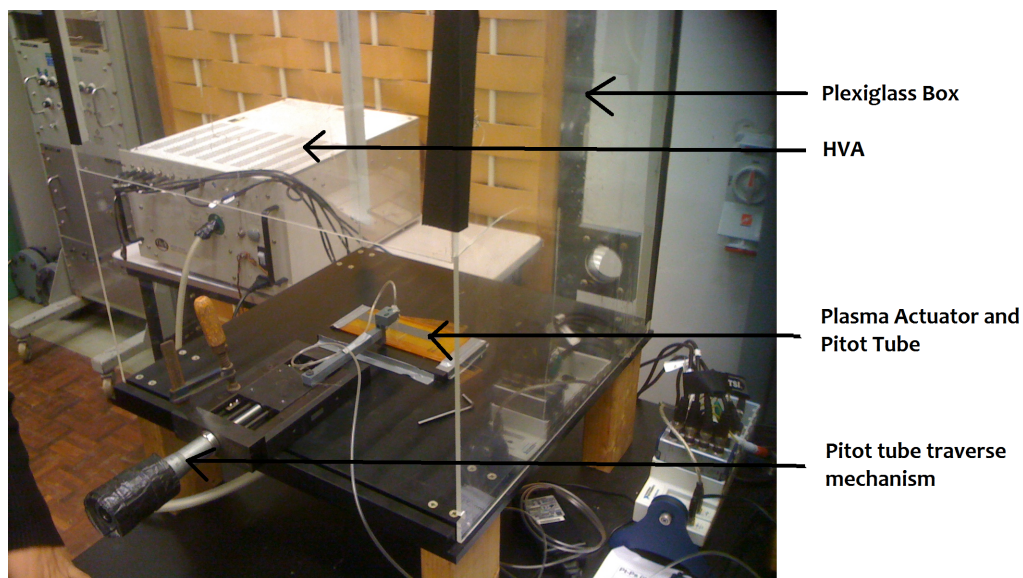


Figure 4.1: Photograph of the experimental setup for the dielectric parametric study

A schematic of the experimental setup within the enclosing box is shown in Fig. 4.2. The exposed and covered electrodes are denoted by E and C, and their widths w_e and w_c were 25 mm and 10 mm respectively. The Makrolon dielectric sheet is denoted by M, and its thickness t . Actuators constructed on different samples of $t = 2$ and 3 mm were tested. The length of the overlap between them (in the z direction) was 100 mm. The flow measurement instrument of choice, a capillary pitot tube was used to measure the speed of the wind induced by the actuator at various positions downstream of the interface between the exposed and covered electrodes. The tube was kept as close to the dielectric surface as possible, in fact touching it. This was done so that the induced wind speed close to the surface could be measured, since the peak wind velocity was expected to occur at around 0.5mm above the surface [13], [26]. Since it was made of a non-conducting material, there were no risks of plasma effects on it. The small angle between the

tube and the horizontal was measured, and the velocities measured were corrected for this angle. Considering the downstream direction of plasma forcing as the $+x$ axis and the interface as $x = 0$, the positions at which the velocity of the induced jet was measured were $x = 0, 5, 10$ and 15 mm. As mentioned earlier, the electrical parameters that were varied were the input signal V_{pp} in kV and frequency f_{AC} in Hz. Their testing ranges were from 0 to 40 kV in steps of 5 kV and 0 to 1250 Hz in steps of 250 Hz respectively. The 40 kV value is the upper limit as it is the maximum that can be delivered by the High Voltage Amplifier (HVA) in the Aerodynamics Laboratory. The experimental matrix that lists the flow, electrical and measurement conditions for each dielectric sheet of $t = 2$ and 3 mm during this experimental campaign is given in Table 4.1. The results of the dielectric parametric will be discussed in Sec. 5.1.

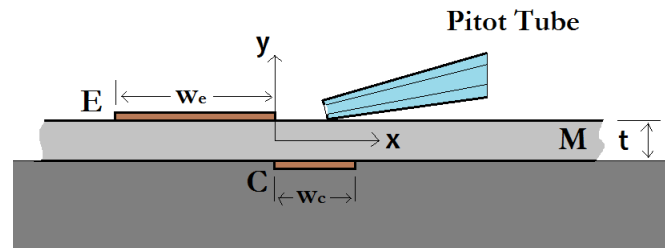


Figure 4.2: Schematic of the setup used for the dielectric parametric tests, which were carried out in undisturbed flow conditions

Pitot tube position	V_{pp} kV	f_{AC} Hz
$x = 0, 5, 10, 15$ mm	20	500
		750
		1000
		1250
	25	500
		750
		1000
		1250
	30	500
		750
		1000
		1250
	35	500
		750
		1000
		1250
40	500	
	750	
	1000	
	1250	

Table 4.1: Experimental matrix for dielectric parametric test for each dielectric sheet of $t = 2$ and 3 mm

4.2 Wind Tunnel Experimental Model

In order to test the effectiveness of the various Plasma Actuator configurations on Vortex Shedding in the Wind Tunnel a suitable experimental model was designed based on a variety of considerations. This was done keeping the larger goal of the current experimental campaign in mind - the control of vortex shedding from practical non-streamlined (bluff) objects and/or streamlined objects with truncated trailing edges. The problem of tonal acoustic noise caused by the periodic shedding induced pressure fluctuations on the base of such objects was discussed earlier in Sec. 1.1. Airfoils with truncated trailing edges, encountered commonly in Wind Turbines for example, are among bodies in flow that suffer from the adverse of vortex shedding. In order to represent such objects a flat plate bluff body was chosen. This is undoubtedly a simplification of the problem complexity at hand. The advantages of this simplification include:

- Fixed flow separation locations at the upper and lower trailing edges
- No external tripping, hence laminar flow everywhere over the model
- Zero pressure gradient applied to the flow across its length.

After the geometry of the model was decided, the following considerations were kept in mind while designing and manufacturing it. These aspects will be discussed in detail in App. C.

- Polycarbonate Makrolon was the material of choice for the model, which was light in weight and easy to manufacture.
- The desired boundary layer characteristics for flow over the model, and the occurrence of vortex shedding;
- To obtain results that could be compared with earlier experimental studies using Plasma Actuators in Vortex Shedding Control carried out in similar experimental facilities by Nati [27];
- To enable arranging and easily varying the plasma actuator electrode spanwise configurations and the PIV imaging planes during the experiments, etc.

Keeping in mind the above considerations, the wind tunnel experimental model was designed so that it consisted of two parts - a flat plate bluff body model and a flexible trailing edge fixture. The fixture smoothly fitted on to the aft part of the flat plate model and will hence also be called the end fixture. The fixture had 'arms' that were 3mm thick. The upper and lower arms acted as the dielectric layer between the exposed and covered electrodes. The fixture also served to encapsulate the grounded electrode when the latter was appropriately laid out. Finally, the flexibility of the fixture facilitated easy relative motion with respect to the flat plate model which was held fixed at the wind tunnel test section. This enabled the imaging of different spanwise planes at the model trailing edge by the PIV laser without disturbing the other instruments and components involved in the setup. These aspects will be made clear in App. C and Sec. 4.4. The flat plate model and end fixture are shown in Fig 4.3:

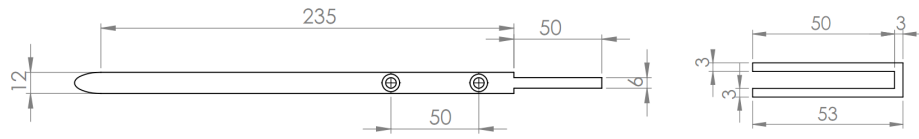


Figure 4.3: Side view showing the flat plate model and the end fixture. All dimensions in mm

4.2.1 Coordinate System

The coordinate system adopted in this work for the experiments was left-handed cartesian, and shown in Fig. 4.4. The origin of the coordinate system was set at the middle of the flat trailing base of the experimental body. When viewed in an $x - y$ plane at any spanwise location, and with h as the trailing edge height, the upper and lower model surfaces were hence be located at $y = 0.5h$ and $-0.5h$ respectively.

- Streamwise downstream direction was set as the $+x$ axis;
- Transverse direction pointing upwards (with respect to the ground) was set as the $+y$ axis;
- Spanwise direction was set as the z axis, with the positive direction determined by the left hand thumb rule.

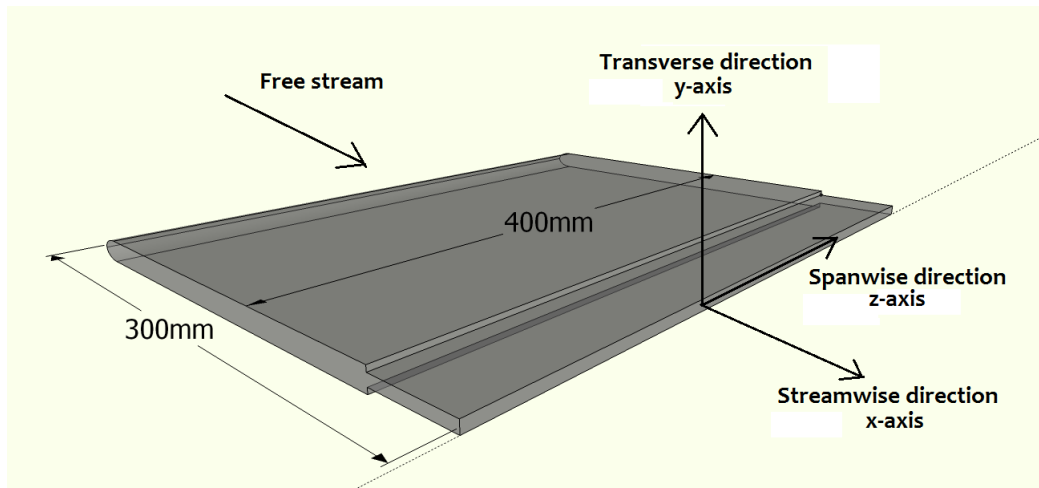


Figure 4.4: Experimental model three-dimensional view, showing coordinate axes adopted

When analysing the statistical flow fields, it was useful to decompose the flow velocities in the respective directions into the mean and fluctuating components as follows:

$$U_x = u + u' \quad (4.1a)$$

$$U_y = v + v' \quad (4.1b)$$

$$U_z = w + w' \quad (4.1c)$$

4.3 Plasma Actuator Configurations

The terms 'mode' and 'configuration' will now be strictly defined in the context of plasma actuation in the present work to avoid ambiguity: A mode will refer to a specific layout scheme of the electrodes with respect to each other. The actuation induced by each of these modes was spatially cyclic along the span. For each mode, the spatial cycle of actuation was varied by varying the spatial interval over which the arrangement of electrodes repeats itself. These arrangements, obtained by varying the spacing between the electrodes in one spatial actuation cycle for a mode, will be called 'configurations'. Modes were characterised by the direction of forcing (and additionally by the arrangement scheme of electrodes, if required) while the configurations by the spatial interval (or 'wavelength' λ) over which the electrode arrangement (and hence the induced actuation) repeated itself along the span. The various modes and configurations tested are listed in Table 4.2. App. D will describe the various plasma actuation arrangements that were tested over the course of the various experimental campaigns, along with the rationale that went into their design.

Spanwise Modulated Actuation Mode	Configuration λ
Transverse Opposing	$3h$
	$5h$
Transverse Staggered	$3h$
	$5h$
Spanwise	$2h$
	$3h$
	$4h$

Table 4.2: Spanwise modulated actuation modes and corresponding configurations tested during time resolved experimental PIV Campaign

Due to the spatially varying actuation within one spatial actuation cycle for the various spanwise modulated actuation modes, different flow behaviour was expected in the wake, especially the near wake. Based on the electrode configuration, it was decided to laser-illuminate $x - y$ planes at different spanwise positions within one actuation spatial cycle for the various actuation modes during the PIV time-resolved measurements. The $x - y$ planes were imaged for all tested configurations and were chosen in order to have as good a picture of the flow field of the near wake as could be obtained through as few imaging planes as possible, and close to the middle of the span of the model to avoid end-effects associated with the wind tunnel walls. The various actuation modes and configurations, along with the corresponding spanwise $x - y$ planes imaged are shown in Table 4.3.

The electrode layout and the expected plasma-induced forcing for the various actuation modes implemented, for a configuration of spatial wavelength of actuation λ are shown in Fig. 4.5. The various spanwise $x - y$ planes imaged are also shown. Within the spatial actuation cycle for the transverse opposing actuation mode (Fig. 4.5(a)) centered at $z1$, five salient spanwise locations could be identified - $p1, p2, p3, p4$ and $p5$ as shown. $x - y$ planes at $p1$ and $p5$ both lay at the middle of a spanwise section with covered electrodes on both sides, hence were expected to have similar actuator induced flow physics. The same is true of the $x - y$ planes at $p2$ and $p4$ which both lay at the spanwise interface of regions with and without exposed electrode segments. Hence, three salient locations were chosen for $x - y$ plane laser-illumination where unique actuator induced flows were measured, corresponding to the $p1, p2$ and $p3$ locations. In a similar manner salient

Actuation Mode	Configuration λ	No. of $x - y$ planes imaged
Baseline	n.a.	1
Baseline, Boundary Layer	n.a.	1
Spanwise Uniform	n.a.	1
Transverse Opposing	$3h$	3
	$5h$	3
Transverse Staggered	$3h$	2
	$5h$	2
Spanwise	$2h$	2
	$3h$	2
	$4h$	2

Table 4.3: Various actuation modes and corresponding no. of measured $x - y$ planes imaged

locations within the spatial actuation cycle were defined for the transverse staggered actuation mode in Fig. 4.5(b). The actuator induced flow was expected to behave similarly in the $x - y$ planes at $p1$, $p3$ and $p5$ due to the transverse antisymmetry in the electrode placement at these locations. Hence only one of these needed to be imaged for measurement. The same holds true for $x - y$ planes at $p2$ and $p4$, both of which lay at spanwise interface regions between exposed electrode and no-electrode regions. Hence, two salient locations are chosen for $x - y$ plane laser-illumination where unique actuator induced flows were measured, corresponding to $p2$ and $p3$. Considering the spanwise actuation mode in Fig. 4.5(c), three salient spanwise locations can be identified - $p1$, $p2$ and $p3$ as shown. Using arguments similar to those put forward for the spanwise modulated transverse actuation modes, two salient spanwise locations were chosen for $x - y$ plane laser-illumination where unique actuator induced flows can be measured, corresponding to $p1$ and $p2$. The detailed description of these locations, and other electrode placement related details can be found in App. D.

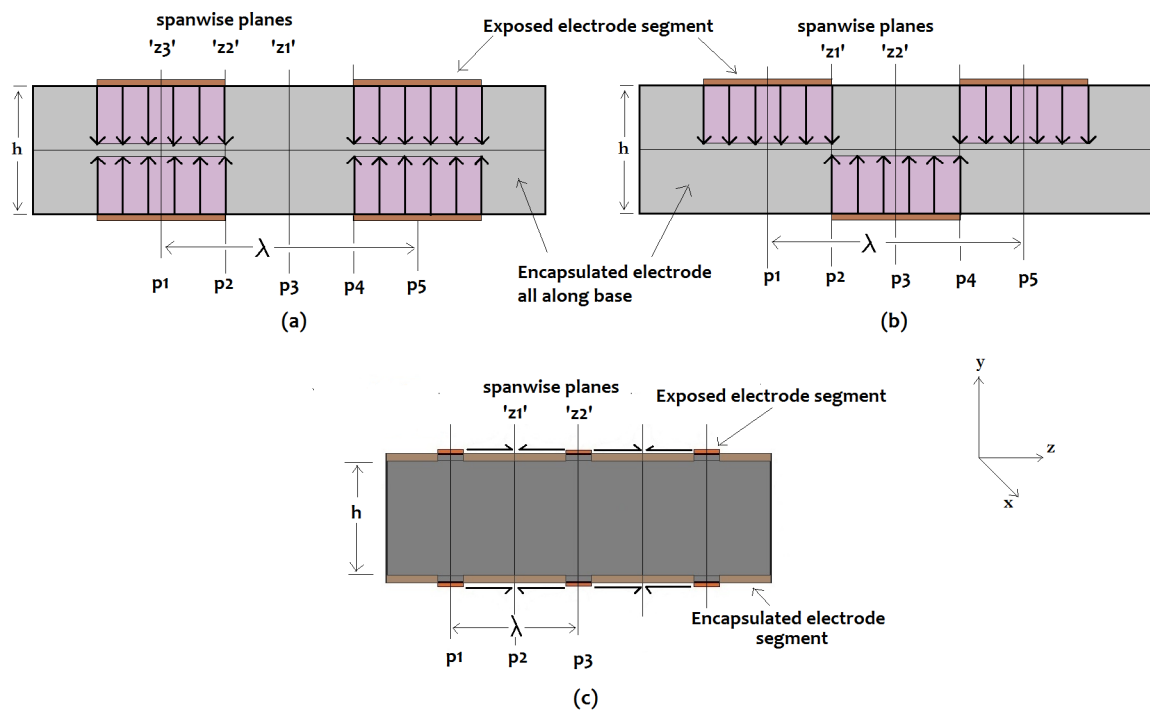


Figure 4.5: Electrode layout for the various spanwise modulated actuation modes when viewed on the flat trailing edge of the experimental model: (a) Transverse opposing, (b) transverse staggered and (c) spanwise actuation. The various imaged $x - y$ planes of interest within a spatial actuation cycle are also shown

4.4 Time Resolved PIV Campaign

High speed time resolved Particle Image Velocimetry (PIV) was the flow measurement technique of choice used in this Thesis. Its advantages are many, and those relevant to this experimental campaign and the results that were obtained from it are as follows:

1. Non-invasive imaging of large spatial fields of view with high spatial resolution.
2. A high frequency of velocity field acquisition and reconstruction enabling time and frequency domain analysis techniques like correlation and spectral analysis.

Chapter 5, with the exception of Sec. 5.1 contains the results obtained from this particular experimental campaign. The principle of PIV is discussed in Sec. 3.1, and this section will be dedicated to describing the setup details of this experimental campaign. The experimental setup for imaging an $x - y$ plane in the wake (according to the coordinate system described in App. 4.2.1) is shown in Fig. 4.6. The various experimental steps and details are as follows:

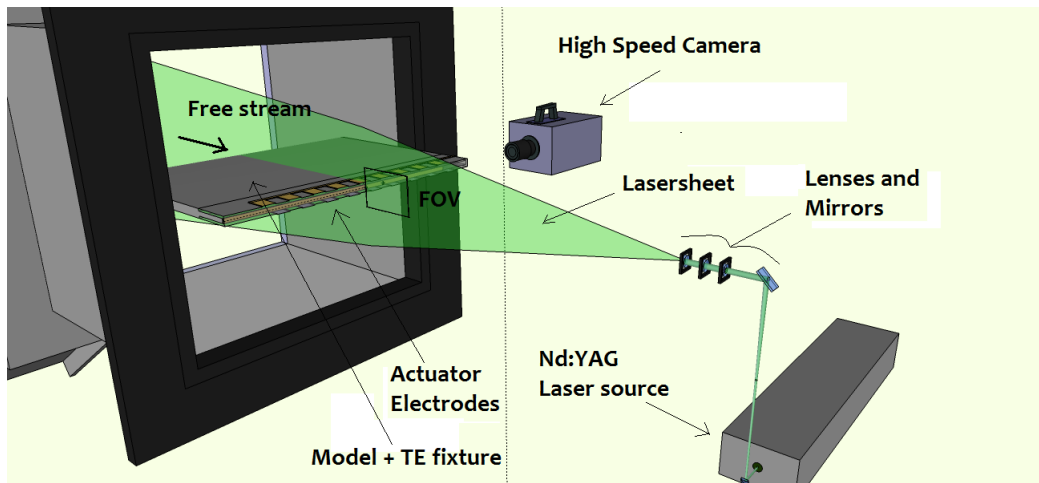


Figure 4.6: Schematic of the setup used for the time resolved PIV Campaign

The wind tunnel facility used was the M-Tunnel described in App. B. Time resolved PIV flow field measurement was carried out for each of the actuation modes, configurations and imaged planes at free stream speeds U_∞ from 5 to 17 m/s in steps of 3 m/s. The respective electrodes were then laid out on the flat plate model and the Makrolon end fixture, the parts mated and the model tightly bolted to the tunnel front face. It was positioned such that the rounded leading edge faced the oncoming flow with no angle of attack, and a length of approximately 120 mm protruded outside the tunnel exit. As in the dielectric parametric study, the HVA used for plasma actuation was the TREK 20/20C high voltage amplifier (± 20 kV, ± 20 mA, 1000W, gain 2kV/V). The laser beam generated by the laser source was diverted, focused and spread into the desired direction by a system of mirrors and lenses. The position of the laser sheet is now fixed and undisturbed throughout the campaign. If $x - y$ planes are to be imaged, then the model is clamped/bolted as shown in Fig. 4.6 so that the laser sheet falls on a section located approximately at the spanwise mid-section of the trailing edge. For imaging different $x - y$ planes at different spanwise positions, only the trailing edge end fixture needed to be moved by the appropriate spanwise distance. If transverse $x - z$ planes were to be imaged, then the experimental model was flipped perpendicular to the position shown in Fig. 4.6, so that the laser sheet illuminated the required plane. The number of $x - y$ and $x - z$ planes imaged for the various actuation modes and configurations is shown in Table. 4.5, and the locations of these planes is described in App. D for each of the actuation modes. The placement of the high speed CMOS camera was done keeping its line of sight parallel to the spanwise axis with the intention of focusing on a square patch of the near and intermediate wake. This field of view (FOV) was located just behind the trailing edge as shown in Fig. 4.6. A seeding machine was appropriately positioned at the plenum of the Wind Tunnel so that a uniform concentration of seed particles was found in the airstream around the experimental model. The desired time-resolution of the velocity fields to be obtained, f_{PIV} (frequency of the raw image-pair acquisition by the camera, in Hz) was set through the controlling software to 3000 Hz, along with additional parameters pertaining to the laser and camera system (see below). The time duration of measurement for each observation set was $\simeq 1$ second, so that the number of time resolved velocity fields that were obtained for each observation set was $\simeq 3000$. The raw image pairs were processed and using the controlling software in the manner described in Sec. 4.4.3, and the obtained time resolved velocity fields were post-processed using Matlab to generate the qualitative and quantitative

results shown in Chap. 5.

4.4.1 Optical System Setup

Camera

A Photron Fast CAM SA1 with a 12-bit complementary metal-oxide-semiconductor (CMOS) sensor of 992×1024 pixels (pixel pitch $20 \mu\text{m}$) was used to image the FOV. The applicability of CMOS cameras is described briefly in Sec. 3.1.5. The lens used was a Nikon objective with a focal length of 105 mm. A green filter was fitted to the lens to allow only light that fell within a narrow band around that of the laser wavelength to pass through to the camera. The camera was operated in the double frame mode, with image-pairs captured at a frequency of 3000 Hz that was set through the controlling software. A synchroniser was used for high frequency PIV tests such as these, that synchronised the laser pulses (see below) with the camera capture instants and allowed these instruments to be controlled by the user using the controlling software, which was LaVision DaVis 8.0.

The f-stop ($f_{\#}$ or aperture number), which is the ratio of focal length to camera aperture diameter, could be set between 2.8 and 32 for the selected lens. As a thumb rule, increasing the $f_{\#}$ increases the depth of field and reduces the aperture size (since the focal length is fixed). While focusing and calibration, it is desired to have a small depth of field, hence a small $f_{\#}$, as long as care is taken to ensure that the camera pixels do not saturate due to the larger amount of light allowed in by the larger aperture. The $f_{\#}$ was set at 2.8 for both calibration and while the experiments were run, which corresponded to a relatively large aperture size and narrow depth of field.

A seed particle displacement in the flow corresponding to a pixel displacement of 15 pixels in the camera (after correlation analysis and processing of the raw image pair) was desired based on which the time-spacing between the images in the pair (dt) was set in the controlling software. This is higher than the standard desired value of 10 pixels (Sec. 3.1.4) due to the presence of relatively high speed shear layers in the flow field along with the low velocity near wake ('dead-water') region. To obtain this pixel displacement, the dt values for the tested wind speeds of $U_{\infty} = 5, 8, 11, 14$ and 17 m/s were set at respectively 150, 95, 68, 53 and $44 \mu\text{s}$. However, to ensure that both the camera aperture opening instants and the corresponding laser pulses were correctly aligned in time, it was necessary to vary and find the right value of the laser pulse offset for both pulses. This was done through trial and error for each free stream velocity (i.e. for each dt value).

Field of View

For the spanwise $x - y$ plane imaging tests, the field of view of the camera was chosen just downstream of the trailing edge, symmetric with respect to the wake axis, with an area of approximately $50 \text{ mm} \times 50 \text{ mm}$ in the $x - y$ plane. This same FOV size was used when the baseline (un-actuated) flow boundary layers were imaged, with the difference that the position of the FOV was shifted slightly so that the last $\simeq 18$ mm of the aft part of the model and the trailing edge (model base) were included. The same FOV size was also used for the transverse $x - z$ plane imaging tests for the transverse actuation cases, with the FOV now including the last few mm of the trailing edge of the model for reference and for identifying the position of the

exposed electrodes. For the transverse $x-z$ plane imaging tests for the spanwise actuation cases however, the camera FOV was enlarged so that a much larger part of the trailing edge of the trailing edge of the model was included. This was done to measure the effect of the actuation on the boundary layers over the model before they separated. A larger section of the span and the wake could also be imaged. The FOV size was then set to around $100\text{ mm} \times 100\text{ mm}$ by zooming-out the camera appropriately. Of course, the larger FOV came at the cost of reduced spatial resolution of the imaged velocity field. The FOVs for the above mentioned cases are schematically shown in Fig. 4.7.

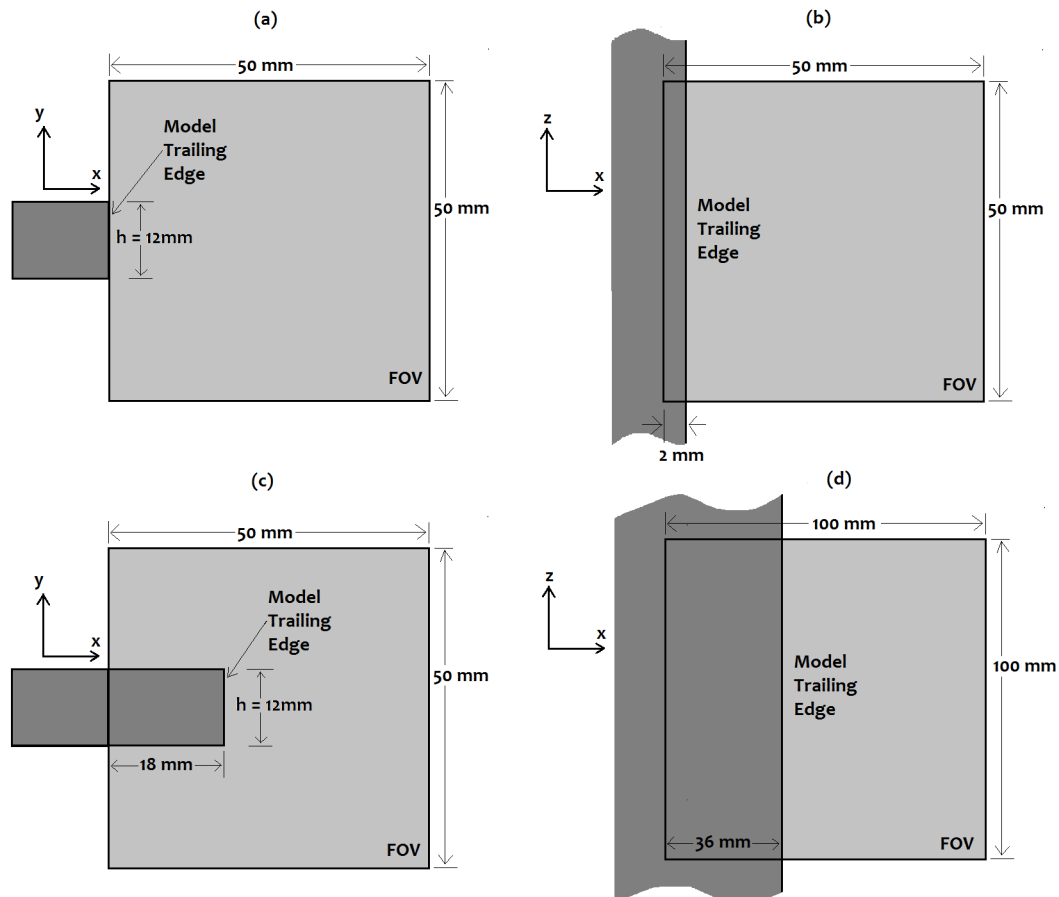


Figure 4.7: Imaging FOV's: (a) $x-y$ plane; (b) $x-z$ plane with transverse actuation; (c) $x-y$ plane for baseline boundary layer measurement and (d) $x-z$ plane with spanwise actuation

4.4.2 Laser and Seeding System

The Laser source that was used was a Quantronix DarwinDuo Laser System. It generated a double pulsed Nd:YAG laser consisting of two cavities producing infrared light at a wavelength of 1054 nm. A second harmonic generator halved the wavelength to 527 nm (so that it fell in the visible range corresponding to visible green, for safety reasons). Its average output is 80 W with

energy 2×13 mJ per pulse. The laser beam diameter was 3 mm at the output with a pulse width of approximately 150 ns. The beam was initially emitted in the direction perpendicular to the direction of interest. Using a system of mirrors, it was directed in the desired direction, and then a concave-convex lens system focused the beam into one of the required diameter. Finally, this beam was spread out into a thin vertical sheet of thickness $\simeq 2$ mm by a cylindrical lens towards the location of interest at the model trailing edge. The laser intensity, which was controlled by its allowed current consumption, was set at 18 A during the experiments. The pulses generated by the laser were controlled through the Davis LaVison software mentioned earlier, where the repetition rate (frequency at which image pairs are captured, 3000 Hz) and other parameters were set.

A Safex Fog Generator was placed in the plenum of the wind tunnel to give uniform seeding in the airstream at the test section. It generated a non-toxic water-glycol based fog with a particle diameter of $1 \mu\text{m}$ and density (in liquid form) of 103 kg/m^3 . The characteristic response time (τ_p) of these particles from Eq. 3.7 is $3 \mu\text{s}$, which corresponded to a frequency of 360 kHz. It is advised that the particle response frequency should be smaller than the smallest time scale of the flow. Since this frequency is much higher than any expected frequency in the flow of interest (corresponding to bluff body vortex shedding), the particle response time criterion was satisfied. The fidelity of the flow tracers in flows is quantified by the particles Stokes number S_k , defined as the ratio between τ_p and the characteristic flow time scale τ_f . At the maximum tested free stream of 20 m/s, the shedding frequency was around 420 Hz, corresponding to a characteristic time scale of 0.0024 s. Hence, the S_k was nearly $(\frac{3 \times 10^{-6}}{2 \times 10^{-3}}) = 0.0015$, which satisfied the criterion of S_k required less than 0.1.

4.4.3 Image Setup and Processing

Calibration and Focusing

PIV calibration consisted mainly of two steps - focusing on the required plane as illuminated by the lasersheet and determining the image dimensions. To perform these steps a plate covered with graph paper, allowing a fast and accurate calibration, was aligned with the lasersheet. Images were taken to both focus the camera and to ensure that the plate was perpendicular to the camera allowing the entire plate to be in focus. The last step was to convert a pixel displacement between two points as sensed by the camera to the real distance expressed in millimetres. Additionally a point of reference (0,0) could be set.

Once the experimental model was fixed and positioned, wind tunnel was turned on, laser system activated, camera calibrated and the flow 'seeded' to a low density, the area of the FOV was observed through the camera image for the particles in the flow. If the individual particles were seen to sharply occupy one pixel, 'peak locking' could occur and the reconstructed location of the particles after cross-correlation analysis of the raw images could be expected to have a spatial resolution limited to integer pixel locations (as sub-pixel interpolation techniques cannot be applied). This is explained in Sec. 3.1.4. To avoid this, the lens was unfocused slightly so that the size of a particle in the camera image was 2×2 pixels.

Image Processing

With the flow and seeding activated, the camera system was operated at a frequency of 3000 Hz for a time duration of $\simeq 1$ second, to give a set of $\simeq 3000$ raw image-pairs. Data processing of these was required to reconstruct the flow field. Noise present on every image in the set of raw images was obtained by taking the minimum intensity present on every image and averaging them. This minimum was subtracted from every image to give a noise-subtracted raw image-pair set. Each of the noise-subtracted raw image-pairs in this set was processed with a multi-pass cross-correlation using the controlling software mentioned earlier. A first correlation with 64×64 pixel interrogation window with 75% overlap and single pass was followed by a 32×32 pixel interrogation window with 75% overlap and two passes. The result of this was the instantaneous velocity field corresponding to a raw image-pair.

Based on all the image-pairs present in the measurement set, time-resolved velocity fields were obtained that contained a wealth of information. These time-resolved velocity fields were post-processed using Matlab using a variety of statistical and time-domain analysis techniques such as wake power spectra analysis, statistical flow field analysis, spanwise correlation analysis, Proper Orthogonal Decomposition of the instantaneous velocity fields, etc. These techniques, along with their results will be described in detail in Chap. 5.

4.4.4 Summary

Table 4.4 summarises the salient experimental details pertaining to the time-resolved PIV measurement for a set with the basic FOV as shown in Fig. 4.7(a) at U_∞ 5 m/s. Table 4.5 summarises the various actuation modes and corresponding no. of measurement $x-y$ and $x-z$ planes imaged at each free stream velocity tested. It is clear that for each velocity, a total of 27 planes were imaged and measured. Hence, a total of $27 \times 5 = 135$ velocity fields were imaged and measured over all free stream in the time resolved PIV Experimental Campaign. The experimental details of all the tested modes and configurations will be given in the Experimental Matrices in App. E.

Plane imaged	$x - y$
Free stream U_∞	5 m/s
Seed particle diameter	1 μm
Camera lens focal length f	105 mm
Camera aperture no. $f_\#$	2.8
Velocity field temporal resolution	3000 Hz
Measurement period	0.9386 s
No. of velocity fields	2816
Laser pulse separation time	150 μs
FOV mm	50 mm \times 50 mm
FOV pixels	1024 \times 992 pixels
Pixel size	20 μm
Final Interrogation Window	32 \times 32 pixels
Final Interrogation Window Overlap	75 %
Velocity Vectors per FOV	128 \times 124
Spatial resolution	6250 vectors/m

Table 4.4: PIV Experimental Details Summarised for a representative measurement set

Actuation Mode	Configuration λ	No. of $x - y$ planes imaged	No. of $x - z$ planes imaged
Baseline	n.a.	1	2
Baseline, Boundary Layer	n.a.	1	0
Spanwise Uniform	n.a.	1	1
Transverse Opposing	$3h$	3	2
	$5h$	3	0
Transverse Staggered	$3h$	2	1
	$5h$	2	0
Spanwise	$2h$	2	1
	$3h$	2	0
	$4h$	2	1
-	-	Total: 19	Total: 8

Table 4.5: Various actuation modes and corresponding no. of measurement $x - y$ and $x - z$ planes imaged at each free stream velocity tested

Chapter 5

Results

The results obtained from the various tests and experiments carried out over the course of the Thesis are presented and described in this chapter. The first section will contain the results from the dielectric parametric study. The second section will discuss the baseline flow through the characterisation of the boundary layer over the D-shaped bluff body model, and the measured and calculated properties associated with the Von Karman shedding. This will be followed by three sections describing in detail the results gathered and calculated for the tests of the various spanwise modulated actuation modes - transverse opposing, transverse staggered and spanwise actuation. For each of these modes, the results will be described for a representative configuration over all the PIV imaged planes. The proposed mechanism of actuation will also be explained as well as the actuator performance in terms of the various parameters like POD modal energies, wake velocity deficit area and fluctuating kinetic energy.

While analysing the results of the time-resolved PIV velocity fields, an important aspect that must be remembered is that the flow system being considered is *unsteady and dynamic*. A purely statistical analysis of the wake flow fields through the mean velocity fields and topology alone will not be enough to understand the instantaneous, time varying nature of the flow, whether baseline (un-actuated) or in the presence of actuation. This is because the interaction between the actuators and the unsteady Karman Wake comes into play. This is why equal importance must be given to the analysis of the fluctuating and instantaneous dynamics of the flow system. The individual sub-sections in this chapter will clearly attempt to demarcate these aspects of the flow system while analysing each actuation mode, so that when considered together a complete understanding of the underlying flow physics can be reached.

5.1 Dielectric Parametric Study

The results of the dielectric parametric study described in Sec. 4.1 are discussed in this section. To recapitulate, the salient aims of this experimental campaign were as follows:

1. Optimisation of electrical parameters: to arrive at the optimum combination of input signal voltage and frequency to achieve maximum forcing.
2. To measure the speed of the induced wind from a simple planar plasma actuator at various streamwise positions of the induced jet. Despite the electrode layout in the spanwise

modulated transverse actuation modes being different from that of a conventional planar plasma actuator, it can be expected that the induced wind will be similar in magnitude for these cases despite being different in direction.

The details of the experimental setup and of the dielectric parametric study can be found in Sec 4.1. The schematic of this experiment is given in Fig 5.1.

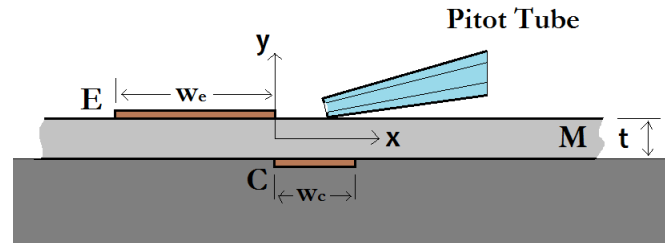


Figure 5.1: Schematic of the setup used for the dielectric parametric tests, which were carried out in undisturbed flow conditions

It was found that the induced wind velocity was approximately equal at $x = 5, 10$ and 15 mm. This can be seen in Fig. 5.2, which shows the speed of the induced wind measured at various downstream positions from the electrode interface for a tested plasma actuator constructed using Cu tapes on a 3 mm thick Makrolon sheet as dielectric. The error bars indicate variation of the quantity over the 10 second measurement period at the appropriate voltage and frequency of measurement. It can be expected that beyond $x = 15$ mm dissipative effects start taking effect resulting in diminished jet strength. The peak induced wind was around 4.5 m/s at the optimum voltage-frequency combination. This is less than the peak time averaged single actuator plasma-induced wind velocity reported in some works, for eg. Forte et al [13] where a wind of $\simeq 6$ m/s was measured for PMMA dielectric sheets of $t = 2$ and 3mm. It is consistent, however with typical values measured and used in other reported works, for Eg. [26]. An input frequency of 1250 Hz was seen to be the optimum in terms of induced wind. Higher frequencies did not cause an increase in the wind due to saturation, but an increase in power consumed. The wind speed was also seen to increase with peak to peak voltage amplitude all the way till the upper limit that could be supplied by the high voltage amplifier, which was 40 kV peak to peak; hence a 40 kV and 1250 Hz combination for the input signal was found ideal and used as actuator input in all the subsequent experiments.

It was found that samples constructed on 3mm thick Makrolon dielectric sheets induced nearly the same amount of wind and consumed nearly the same amount of power as those on 2mm thick samples. However the latter showed a more filamentary, unstable discharge. These discharges were also responsible for some 2mm thick samples undergoing dielectric breakdown at high voltage - frequency (at $\geq 30kV - 1000Hz$) combinations. It was reasoned that the high electric field in these cases led to degradation of the dielectric material for the 2mm thick samples. The 3mm thick samples, however, could easily withstand the higher voltage amplitudes and showed a uniform discharge. These observations that the thicker dielectric sheets enabled the use of higher electric field strengths agree with what was observed by Thomas et al [36] and Forte et al [13]. As can be seen in Fig. 5.3, the variation of the cycle-averaged power consumed per unit actuator length as a function of voltage at different frequencies was cubic in nature, similar to what was reported in literature, for eg. in [13]. Again, the error bars represent the variations in the power

measured over the 10 second measurement period at the appropriate voltage and frequency of measurement.

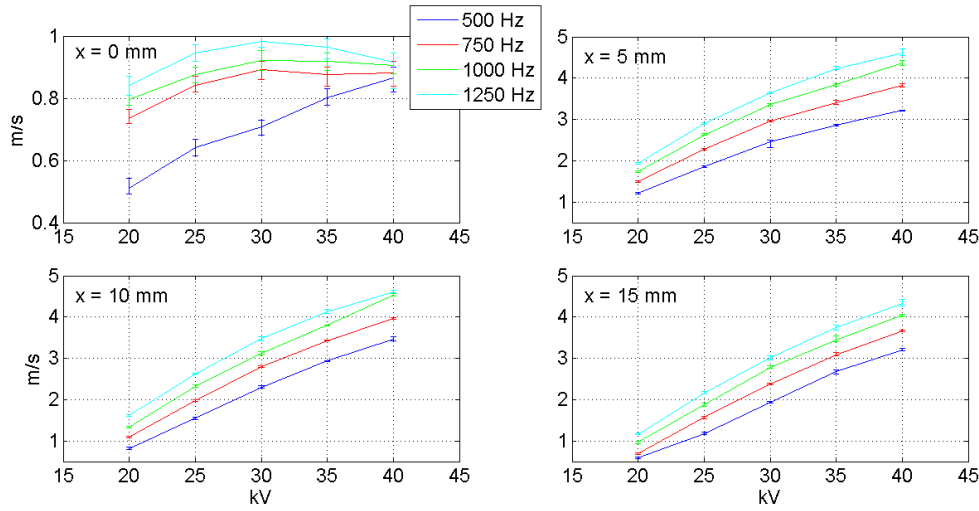


Figure 5.2: Time-averaged variation of induced wind speed with voltage and frequency at various streamwise positions for a Cu tape actuator on a 3mm thick Makrolon dielectric sheet

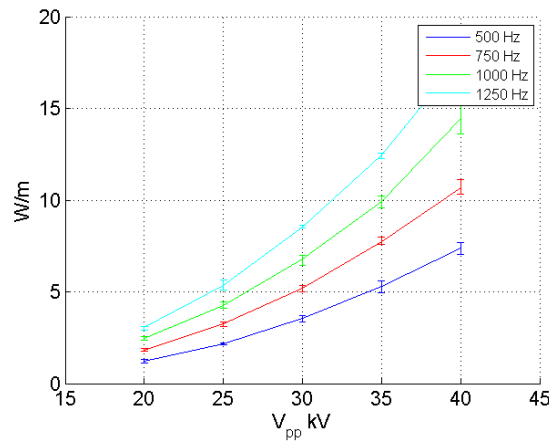


Figure 5.3: Variation of cycle averaged power consumed per unit actuator length with voltage and frequency for a tested plasma actuator constructed on a 3mm thick Makrolon sheet as dielectric. The length of the plasma actuator tested was 100 mm

Regarding the electrode material, Copper tapes were easier and more convenient to use than conductive spray. The performance of actuators with sprayed electrodes was heavily dependent on the uniformity of the sprayed layer; a thick coating that was not uniform everywhere gave rise to fluctuating, non-uniform wind. Also, the sharper-defined the edge of the electrodes sprayed, the better the discharge. However, these were very difficult to ensure, leaving the conductive spray an undesirable choice. The effect of adding Kapton tape on either side between the

Makrolon dielectric and the electrodes seemed almost negligible on the strength of the induced wind, apart from enabling more uniform (less streamer-like) discharges due to its homogenising effect on the discharge. This effect was responsible for a slight reduction in the amount of power consumed by the actuator.

5.2 Baseline Flow Characterisation

5.2.1 Boundary Layer

In all the experimental campaigns carried out, the flow over the experimental model was untripped at all wind speeds, hence expected to be laminar. The boundary layer is the low velocity layer of fluid close to the model that develops into a shear layer on either side after separation at the trailing edge. Due to the importance of the shear layers in the vortex shedding process, it is important to study and characterise the boundary layer before it separates from the model. For this purpose, several PIV images were taken over a modified field of view that included the last 15 mm of the plate and the trailing edge face at all the tested free stream speeds so that boundary layer profile could be captured over the upper and lower surfaces and parameters such as the displacement and momentum thickness and shape factor calculated. Because the experimental model was not held at an angle of attack in the wind tunnel, it was expected that the boundary layer profiles on both the upper and lower sides would be identical. It must be mentioned that due to the reflective nature of the plexiglass material of the model the region close to the model surface was often 'contaminated' by excess illumination, which after processing gave rise to spurious velocity vectors.

It was observed that due to the curvature of the streamlines caused by the separation of the flow into strong shear layers at the trailing edge, the boundary layer profiles on either side became increasingly jet-like as one moved from the upstream extremity of the field of view towards the trailing edge. This is clear from Fig. 5.4 which shows the flow accelerating at around $y = 4$ mm above the surface.

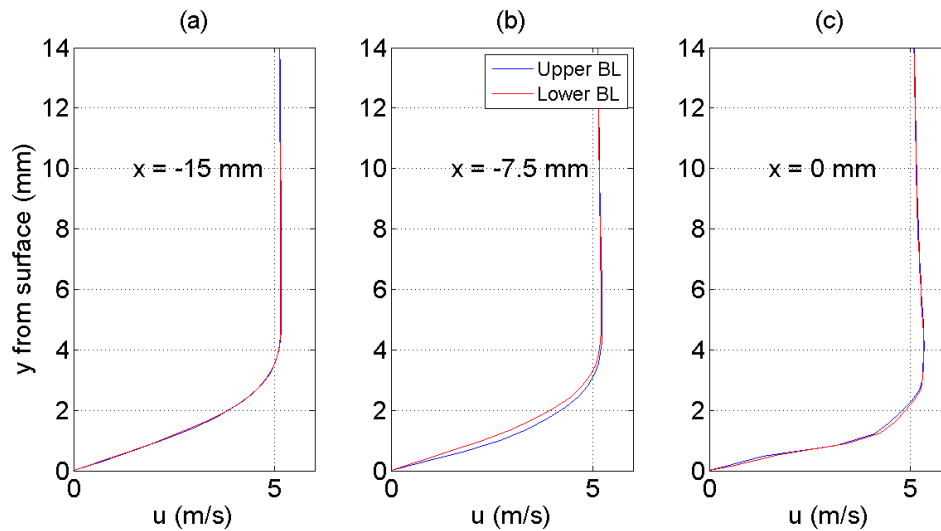


Figure 5.4: Boundary layer profiles over the experimental model at (a) $x = -15$ mm (b) $x = -7.5$ mm and (c) $x = 0$ mm at 5m/s free stream.

To represent the boundary layer over the plate, the profiles at the left-extremity of the plate in the FOV ($x = -15$ mm), where the effect of the low pressure in the wake are felt the least, were used to calculate the various integral parameters in Eq. C.3. These were used to calculate the boundary layer parameters at the various tested wind speeds, shown in Table 5.1. Conventionally, $H = 2.59$ is typical of flat plate (Blasius) laminar boundary layers, while $H = 1.3-1.4$ is typical of turbulent boundary layers. The range of values of the shape factor indicates a Laminar boundary layer over the plate at all tested speeds. The differences in the top and bottom boundary layer parameters can probably be attributed to the influence of spurious velocity vectors close to the plate surface and/or an unintended slight angle of attack of the plate with respect to the free stream.

U_∞ m/s	BL top				BL bottom			
	δ_{99} mm	δ^* mm	θ mm	H	δ_{99} mm	δ^* mm	θ mm	H
5	4.30	1.30	0.48	2.73	4.15	1.28	0.44	2.90
8	3.80	0.90	0.32	2.83	3.82	1.11	0.45	3.16
11	3.70	1.20	0.61	1.95	3.65	1.01	0.51	2.00
14	3.70	1.11	0.55	2.0	3.80	1.22	0.60	2.00
17	3.50	1.14	0.60	1.911	3.60	1.40	0.75	1.90

Table 5.1: Boundary layer parameters over the flat plate for various tested free stream speeds

The boundary layer at $U_\infty = 5$ m/s is as shown in Fig. 5.5 along with the analytical Blasius boundary layer as reference. The differences between the measured and ideal (Blasius) profiles could be attributed to the flow acceleration due to the streamline curvature around the trailing edge.

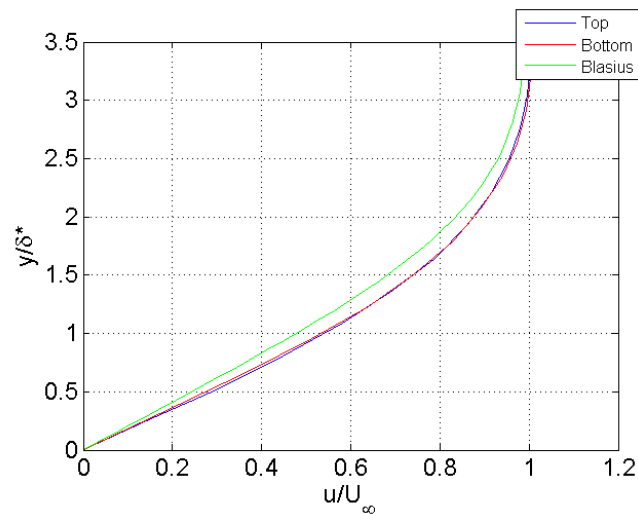


Figure 5.5: Boundary layer profile at the upstream extremity of the plate in the measurement FOV at $U_\infty = 5$ m/s.

5.2.2 Von Karman Vortex Street

This section describes the measured parameters pertaining to the baseline flow in the wake of the bluff body, containing the Von Karman Vortex street.

Strouhal Number

The Strouhal number (St) is a dimensionless number describing the shedding frequency, see Eq. 2.2. The St presented here is calculated from the time-resolved velocity fields obtained using PIV. A point in the wake at $(x, y) = (1.2h, 0.5h)$, which lay in the upper shear layer close to and downstream of the point where Karman vortices were shed, was chosen for calculating the undisturbed shedding properties for the baseline flow cases at the various tested wind speeds. The result is shown in Fig. 5.6(a) which shows the normalised Power Spectral Density (PSD) of the streamwise velocity time signal at the selected point in the wake for the various cases. A linear increase in the frequency corresponding to the (shedding) peak can be seen with the free stream speed. The peaks themselves show decreasing amplitudes and broader base-widths, which can be attributed to the increasing levels of dissipation in the wake flow with increasing Re .

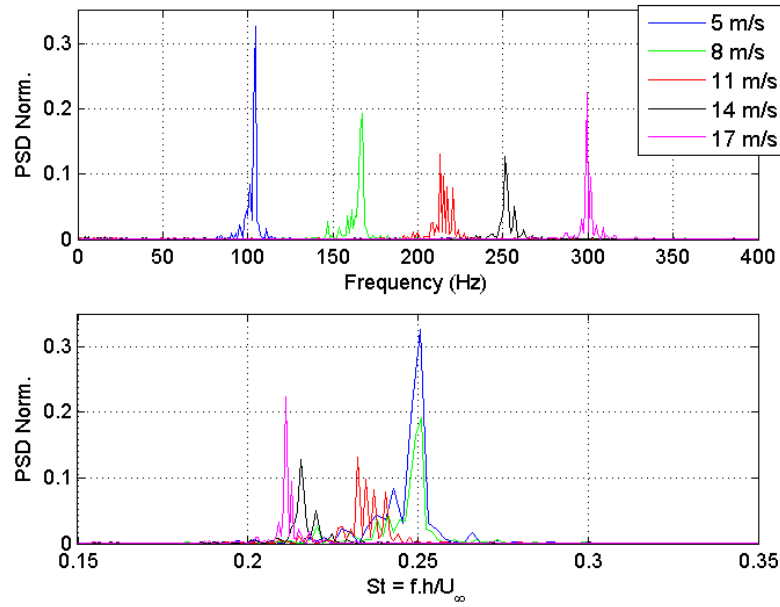


Figure 5.6: Plot of normalised streamwise velocity PSD versus (a) frequency and (b) dimensionless St

Fig. 5.6(b) shows the streamwise velocity PSD versus the St . It can be seen that at the lower free stream speeds, the shedding peak is found at $St \simeq 0.25$. This value agrees with what is reported in literature, for eg. [38]. At the higher speeds of 11, 14 and 17 m/s however, the St falls. This is consistent with the fall in St with increasing inflow Re that is reported in literature, for eg. Zhang [41]. Table 5.2 shows the shedding frequency f_{St_0} at the various tested free stream speeds.

U_∞ m/s	f_{St_0} Hz	St_0
5	104.4	0.25
8	169.4	0.25
11	225.9	0.23
14	251.4	0.21
17	299.4	0.21

Table 5.2: St at the various tested free stream speeds for flow over the experimental model

The fall in shedding St with increasing Re_D (calculated with respect to diameter for a circular cylinder) was mentioned in Sec. 2.1.2. For the purpose of characterising the baseline flow, Table 5.3 is constructed. To maintain consistency with the curve shown in Fig 2.6(b) the Re for the flow here is calculated with respect to the trailing edge height h . Using Fig 2.6(b) and visualisations of the fluctuating velocity fields at the various free streams (not shown here) as reference, the state of the wake, shear layers and boundary layers is estimated. The transition of the shear layers to turbulence (occurring as $\log_{10}(Re_h)$ reaches and exceeds a value around 4) is responsible for the diminished St values at 11, 14 and 17 m/s free stream.

U_∞ m/s	$Re_h = \frac{U_\infty h}{\nu}$	$\log_{10}(Re_h)$	Wake State	Shear Layer State	Boundary Layer State
5	4×10^3	3.6	Turbulent	Laminar	Laminar
8	6.4×10^3	3.8	Turbulent	Laminar	Laminar
11	8.8×10^3	3.95	Turbulent	Turbulent	Laminar
14	1.12×10^4	4.05	Turbulent	Turbulent	Laminar
17	1.36×10^4	4.13	Turbulent	Turbulent	Laminar

Table 5.3: Wake, Shear layer and Boundary layer states for flow over the experimental model at various tested free stream speeds, estimated using Fig 2.6(b)

Shedding properties

The shedding cycle is studied through the time-resolved velocity fields acquired from PIV. A visual description of one cycle at a free stream of 5 m/s is shown in Fig. 5.7. The instantaneous vorticity fields are calculated using the corresponding velocity field components in Eq. 3.13. To acquire this sequence of $n = 6$ images, the image-increment between the successive sub-images in the sequence should be:

$$\text{Image increment} = \frac{f_{PIV}}{f_{St_0} \times n} = \frac{3000}{104.4 \times 6} \simeq 5 \quad (5.1)$$

where f_{St_0} is the vortex shedding frequency 104.4 Hz for $U_\infty = 5\text{m/s}$ as mentioned in table 5.2 and f_{PIV} is the rate of image-pair acquisition by the time-resolved PIV system, which was 3000 Hz. The corresponding time increment between images is $\Delta t \times (\text{image increment}) = 150 \times 10^{-6} \times 5 = 0.75 \times 10^{-4}$ seconds. Δt is the time interval between the snapshots of an image-pair acquired by the time resolved system, which was $150\mu\text{s}$ for $U_\infty = 5\text{m/s}$. It is preferable, however to non-dimensionalise the time with respect to extrinsic (non-shedding related) parameters such as the trailing edge and free stream speed. The non-dimensionalised time $t^* = t \times U_\infty/h$ will be used in the plots showing instantaneous vortical structures from this point onwards.

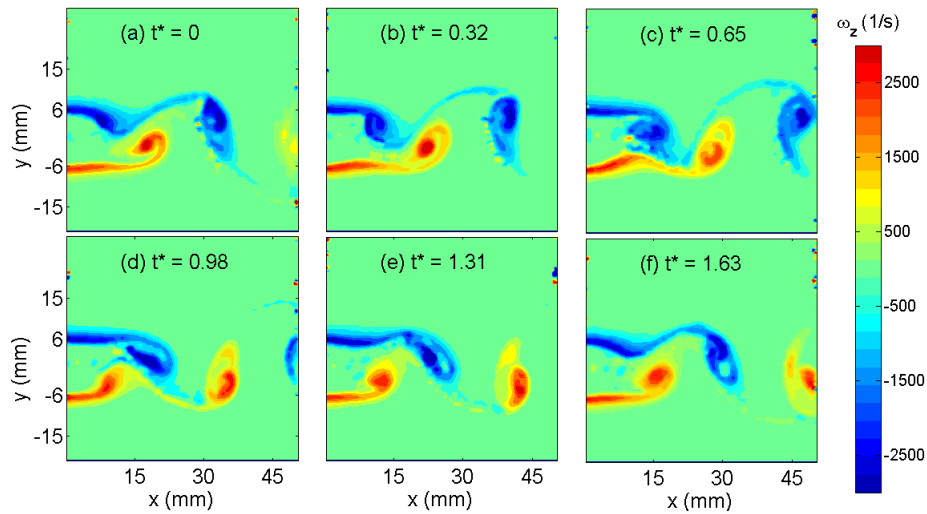


Figure 5.7: Sequence of instantaneous vorticity fields in the Von Karman street for $U_\infty = 5$ m/s behind a bluff body, with non-dimensionalised time spacing $\Delta t^* = \Delta t \times U_\infty/h \simeq 0.32$. Images (a)-(e) represent one complete shedding period with (f) showing the start of the next period

The vortex street convection velocity U_{conv} , characteristic wavelength λ_{VK} , and the transverse and streamwise vortex spacing are calculated from an instantaneous vorticity image at $U_\infty = 5$ m/s as in Fig 5.8. The upper left vortex in the image is just about to be shed from the upper shear layer. U_{conv} is the distance travelled by the vortex street over a full cycle divided by the cycle time. Due to the wave-like periodic nature of the shedding, it can be found as the product of the shedding frequency in Hz and the wavelength of the street λ_{VK} . λ_{VK} is the distance between two successive vortices of the same sign in the street. The coordinate of the vortices (the points with local vorticity maxima or minima) are: $(x_1, y_1) = (15.48 \text{ mm}, 2.00 \text{ mm})$, $(x_2, y_2) = (27.78 \text{ mm}, -4.74 \text{ mm})$ and $(x_3, y_3) = (46.46 \text{ mm}, 4.38 \text{ mm})$.

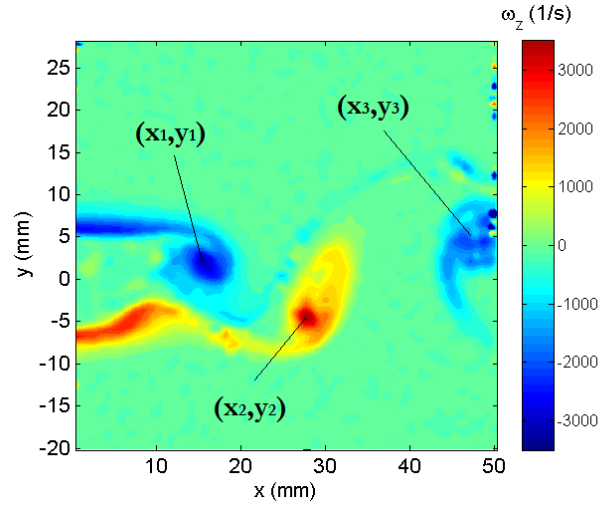


Figure 5.8: Instantaneous vorticity map for calculating vortex street characteristic parameters, showing the coordinates of the vortices in the field of view

$$\frac{\text{Transverse spacing}}{\text{Streamwise spacing}} = \frac{y_3 - y_2}{x_3 - x_1} = 0.2740 \quad (5.2)$$

$$\lambda_{VK} = x_3 - x_1 = 30.97 \text{ mm} \quad (5.3)$$

$$U_{conv} = f_{St0} \lambda_{VK} = 3.233 \text{ m/s} = 0.64 U_{\infty} \quad (5.4)$$

The transverse to streamwise spacing ratio of the vortex street agrees with the value of 0.2811 calculated by von Karman. The ratio of vortex convection speed to free stream speed of 0.64 matches the value of 0.6 for laminar vortices in a bluff body wake by Lin and Hsieh [24].

5.2.3 Statistical flow fields

The harmonic, unsteady and time varying aspects of the vortex street have been dealt with in the previous section. Now, the wake flow itself will be looked at using the statistical mean and RMS velocity fields of the wake. These are obtained by analysing over all the velocity fields recorded during the measurement interval of the PIV experimental run. The normalized averaged and RMS velocity fields for the baseline flow at $U_{\infty} = 5 \text{ m/s}$ are shown in Fig 5.9:

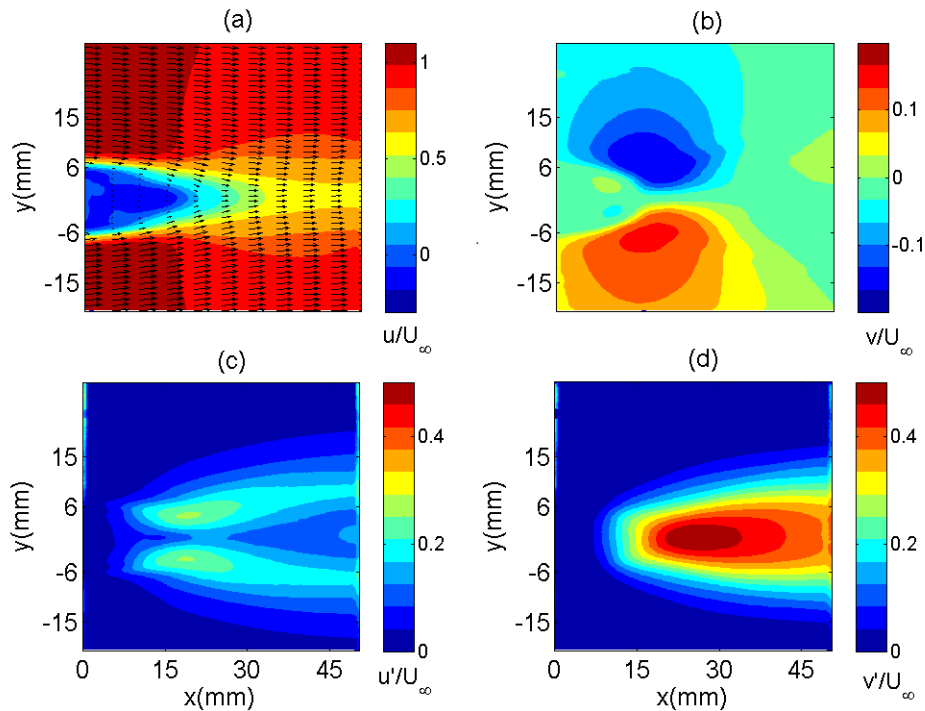


Figure 5.9: Statistical normalised baseline velocity fields: (a) u/U_∞ (b) v/U_∞ (c) u'/U_∞ and (d) v'/U_∞ for $U_\infty = 5$ m/s

To get a good picture of the *topology* of the wake, however, it is instructive to also view the streamlines of the average flow in the near wake of the model:

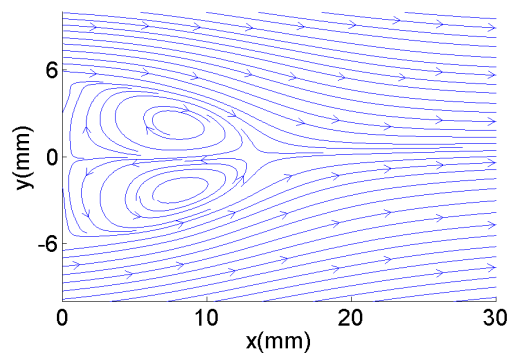


Figure 5.10: Mean flow streamlines in the near wake for the $U_\infty = 5$ m/s baseline flow case

Looking at Fig 5.10 one can conclude that a separated region with back flow is found near the base of the plate, and that the streamwise extent of this region is around 15 mm ($1.25h$). Beyond this, as seen in Fig. 5.9 regions of large transverse velocity (both v/U_∞ and v'/U_∞) towards the

wake centerline from either side are present. The large v'/U_∞ region centered on the wake centerline and beyond the $x = 20\text{mm}$ point indicates strong fluid flow across this region from either side of the wake - the cross-wake transverse motion associated with vortex shedding.

5.2.4 Transverse Planes

The flow field analysis so far has concerned the $x - y$ plane. In addition to this, the wake centerline $x - z$ plane was imaged to get a qualitative idea of the flow topology. The mean streamwise velocity map of the flow in this plane as well as the streamlines of the average flow are shown in Fig. 5.11. In the streamline plot the envelope that marks the streamwise end of the recirculation region is parallel to the span of the model and located at roughly $x = 15\text{ mm}$ as seen in Fig. 5.10. This envelope also roughly corresponds to the location where the Karman vortices are shed from the shear layers. Hence the presence of two dimensional flow and Karman shedding is confirmed for the baseline flow case. The downward ($-z$) flow tendency in the recirculation region seen in the streamlines is not expected, however, and can be attributed to slight errors in the experimental set-up and/or external influences in the laboratory.

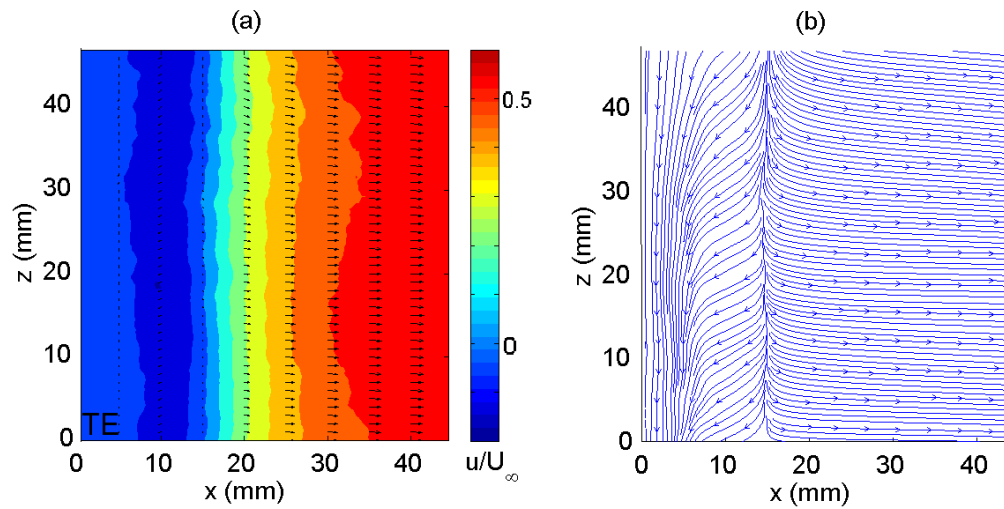


Figure 5.11: Mean streamwise velocity (a) u/U_∞ and (b) mean flow streamlines for the baseline flow case in the wake centerline $x - z$ plane at $U_\infty = 5\text{ m/s}$

Spanwise coherence is one of the properties of the shed von Karman vortex rolls. This property can be verified by analysing the shear layer transverse plane of the baseline flow. This $x - z$ plane is located at a transverse height of $y = 0.5h + 2\text{ mm}$. Since the vortices are shed from the shear layers, the streamwise velocity in their vicinity will fluctuate at the vortex shedding frequency. For the shed vortex rolls to be coherent along the span, the streamwise velocities along the span streamwise location must fluctuate at the same frequency and phase. This can be verified by collecting the time-resolved streamwise velocity signal at points located along the span at fixed streamwise positions and finding their mutual correlation coefficients. Twenty spanwise points along six fixed streamwise positions at $x/h = 0.5, 1, 1.5, 2, 2.5$ and 3 were selected, their

streamwise velocity time signals gathered from the time resolved PIV velocity fields and cross-correlation carried out. These points are shown in Fig. 5.12(a). Taking a point at the middle of the span in the field of view as the reference point, the correlation coefficients of the velocity signal at this point with the other points are plotted against the spanwise location of these points. This is shown in Fig. 5.12(b). The high correlation coefficient values at $x/h = 0.5$ and 1, which are located within the separation bubble in the near wake indicate a high degree of spanwise coherence. Further downstream, the correlation coefficient values are seen to dip slightly but indicate spanwise coherence nevertheless. The spanwise correlations of the baseline flow cases over all the tested U_∞ cases are shown in App. H.

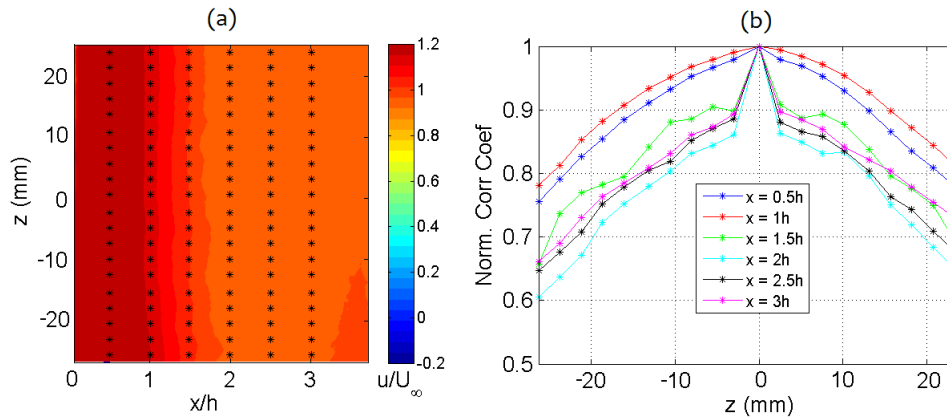


Figure 5.12: Wake shear layer $x - z$ plane (a) mean streamwise velocity map showing correlation points and (b) spanwise correlation coefficients for the baseline flow at $U_\infty = 5$ m/s

5.2.5 POD Analysis

The concept of Proper Orthogonal Analysis (POD) was described in Sec. 3.2 along with its applicability to the study of Von Karman vortex shedding. The POD modes of the baseline flow case are visualised in Fig 5.13. The visualisation of the modes show distinct regions with positive and negative velocities. Combining the results from the u and v components, the rotation centers of vortical structures can be recognised in between the regions with opposing velocity directions. Considering any one of the visualisations, the distance between the centers of two successive regions with the same velocity direction gives the wavelength of the velocity field induced by the periodic vortex shedding. This length is found to be around 28 mm, which closely agrees with what was found from the time resolved velocity field calculation in Sec. 5.2.2. The first two modes also appear as phase-shifted versions of each other with similar magnitudes, indicating that the combination of these two modes produce a representation of the Von karman vortices at any shedding phase.

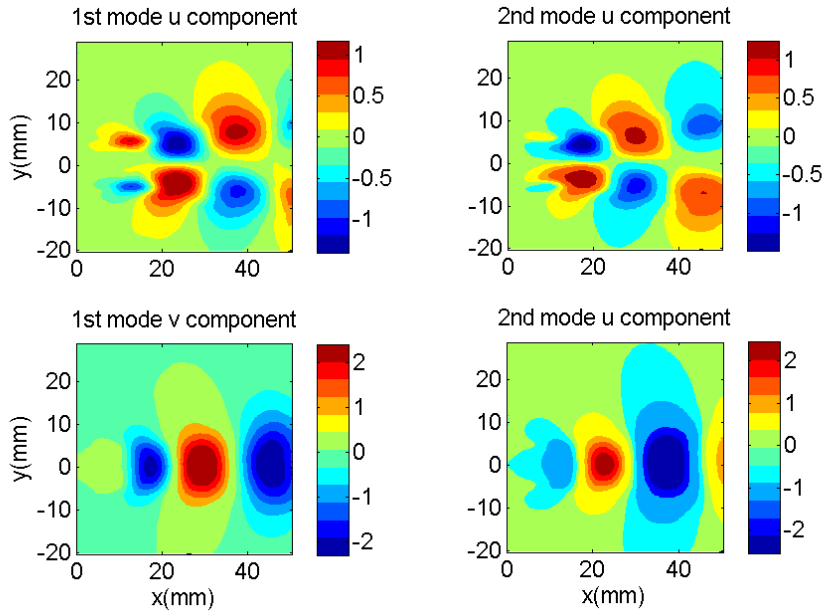


Figure 5.13: Velocity fields in m/s for the first two POD modes visualised the $U_\infty = 5$ m/s baseline flow case

The fact that the first two modes can spatially represent the vortex shedding process can be confirmed by the fact that the around 80% of the fluctuating energy contained in the wake, when resolved into modes, is contained in the first two modes. The plot of the energy content of the first ten modes shown in Fig. 5.14.

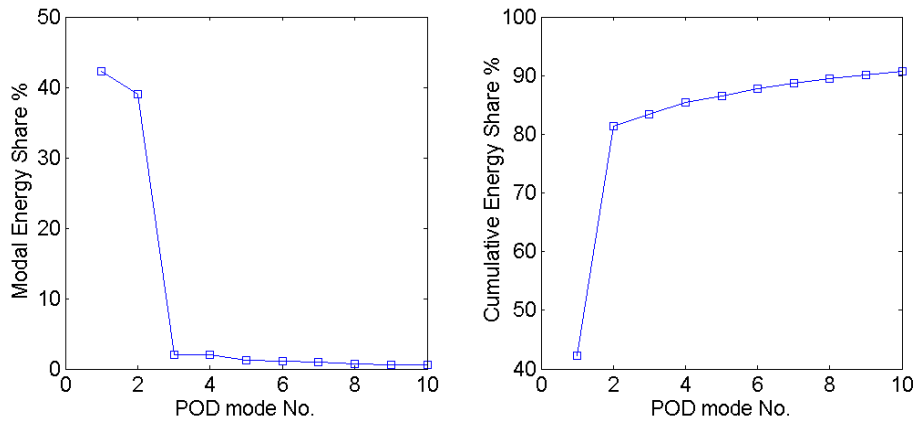


Figure 5.14: Individual and cumulative shares of the Fluctuating KE of the wake captured by the first ten modes of the baseline flow at $U_\infty = 5$ m/s

5.3 Spanwise Uniform Transverse Actuation

5.3.1 Expected Mechanism of Actuation

Spanwise uniform transverse actuation for Karman vortex shedding suppression was successfully implemented by Nati [27], reviewed here in Sec. 2.3.2. The important aspects and results from [27] relevant to the results and discussion of the present work will be summarised here:

- The electrodes were placed uniformly along the span of the model. When viewed in any spanwise $x - y$ plane transverse jets from both the upper and lower sides are formed that were directed parallel to and close to the flat base of the model. These jets converge around the mid-point of the base and close to it. This gives rise to a local stagnation point, from which a jet emerges in the streamwise direction perpendicular to the base. The streamwise jet strength (in m/s) was however not simply a sum of the induced transverse jet strengths, and depended on the plasma actuation input voltage and frequency. It was found that the streamwise jet was the driving parameter responsible for the vortex shedding suppression, rather than the transverse jets.
- The actuation had the following effects on flow in the wake:
 - The induced transverse flow near the trailing edge corners served to channel momentum out of the shear layers and redirect it along the base. This caused the shear layers to deflect slightly towards the wake centerline, thus narrowing the wake velocity defect region.
 - Due to velocity differences between the jet and the rest of the flow in the near wake, vortices grew at the edges of the jet on either side in the region from the base centerline to the shear layers. The axes of these vortices was also oriented along the spanwise (z) direction, but opposite with respect to the shear layers on the corresponding sides. These vortices actively interacted with the shear layers to diminish their vortical strength and gave rise to a turbulent wake.
 - The jet energised the normally 'dead-water' recirculation region in the near wake. This region got filled with small, turbulent vortices due to the interaction between the jet-induced and shear layer vorticity. This reduced the velocity difference between the outer flow and the inner wake.

Due to spanwise uniform nature of the actuation, the above mechanism occurred at every spanwise location along the actuator. The success of this kind of actuation hence depended on cancelling or reducing the shear layer vorticity by creating opposite vorticity through a streamwise jet. This is fundamentally different from the mechanism of three-dimensional actuation implemented in this work. A selected review of popular three dimensional vortex control methods is carried out in Sec. 2.2.2.

5.3.2 Results and Conclusions

The purpose of this actuation mode was to have a benchmark for comparing the results obtained from spanwise modulated actuation, both quantitatively and qualitatively. App. D.2 contains the practical details related to the implementation of this actuation mode. This section describes the instantaneous, spectral and statistical results obtained from processing the time-resolved, PIV imaged flow fields at $U_\infty = 5$ m/s. The instantaneous vortical structures in the $x - y$

plane at the imaged spanwise location are shown in Fig. 5.15. The images indicate the presence of organised, regular periodic shedding of vortices formed through the interaction between the shear layers. This is unlike what was seen by Nati [27] who used a similar experimental model in similar inflow conditions but with a different plasma actuator. And as shall be explained later, the plasma actuation is where the most significant difference lies. The main difference when compared with the un-actuated baseline flow case seen in Fig 5.7 is that the shear layers are turbulent, and that they interact and shed vortices closer to the base of the model.

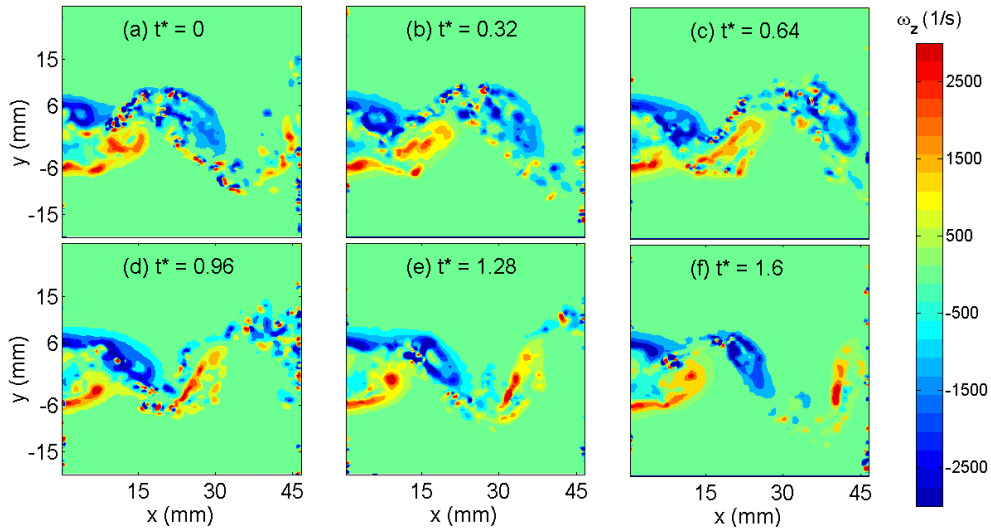


Figure 5.15: Sequence of instantaneous vorticity fields in wake for spanwise uniform transverse actuation at $U_\infty = 5$ m/s with a non-dimensionalised time spacing $\Delta t^* = \Delta t \times U_\infty/h \simeq 0.32$

To look at the near wake in greater detail, a sequence of vorticity field images with a zoomed-in field of view of the near wake taken with a smaller time spacing are presented in Fig. 5.16. Weak ω_z structures can be seen on either side of and between the wake centerline and the shear layers, of opposite sign to the corresponding shear layers. This is indicative of a weak streamwise jet in this region. However, the jet (and the vorticity it gives rise to) is too weak to have a significant effect on the shear layers. The interaction does induce turbulence in the shear layers and makes them interact further upstream than they would without actuation, but this effect is far weaker than one would expect, and vortex shedding continues unabated.

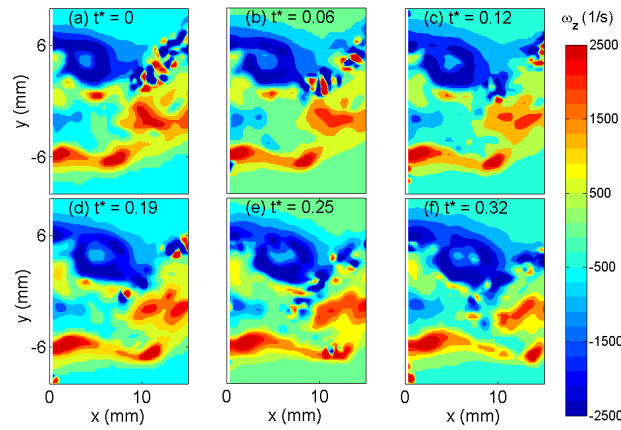


Figure 5.16: Sequence of instantaneous vorticity fields in near wake for spanwise uniform transverse actuation at $U_\infty = 5$ m/s with a non-dimensionalised time spacing $\Delta t^* = \Delta t \times U_\infty/h \simeq 0.06$

The presence of vortex shedding is confirmed by the well defined shedding peaks in Fig 5.17 at the shear layer positions ($y = 0.5h$ and $-0.5h$ at $x = 1.2h$) in the power spectra at three selected wake points shown. At the wake centerline point, the presence of a peak at the shedding frequency that is not seen in the baseline flow case indicates the presence of shed vortices at the streamwise position of the point considered ($x = 1.2h$). This point is hence beyond the point at which vortices are shed for the present flow configuration, unlike what is seen in baseline flow where the vortices are shed a little further downstream. The existence of Karman vortex shedding is also clear through the high energy content of the first two POD modes, almost as much as that of the baseline flow case, shown in Fig 5.18.

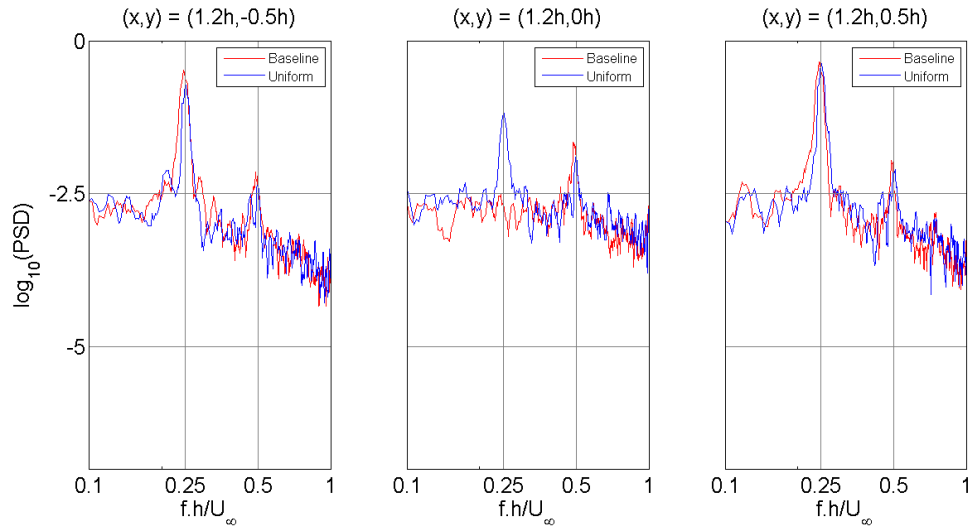


Figure 5.17: Streamwise velocity PSD for spanwise uniform transverse actuation at $U_\infty = 5$ m/s at $'z1'$ at three points in the wake, co-plotted along with the PSD of the baseline flow case

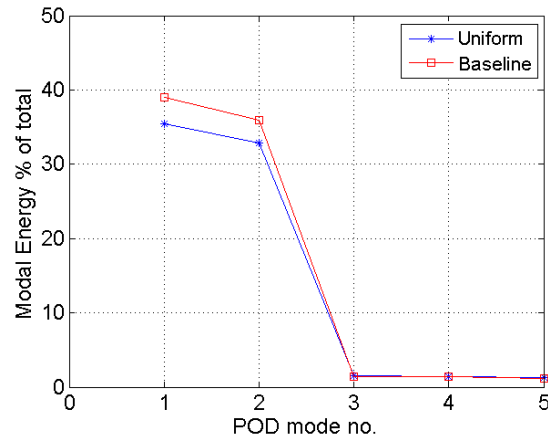


Figure 5.18: Individual shares of the Fluctuating KE of the wake captured by the first five POD modes with spanwise uniform actuated and un-actuated flow at $U_\infty = 5$ m/s

The ineffectiveness of spanwise uniform actuation in suppressing vortex shedding this case should be attributed to the geometric and/or electric parameters of the plasma actuator implementation, rather than a shortcoming of the induced flow mechanism, which has been proven successful by Nati [27]. As mentioned in Sec. 5.1, the dielectric material used (3 mm thick Makrolon) enabled the use of actuation input signals with large amplitudes. The signal used was $40 kV_{pp}$ and 1250 Hz sinusoidal. The high amplitude means that a strong electric field is created, much stronger than that in Nati [27], who used a $200 \mu m$ thick Kapton dielectric with $18 kV_{pp}$ actuation signal. For a typical actuator, plasma is formed over the covered electrode, and its extent is governed by the strength of the electric field. The electric fields generated in this case by the exposed-encapsulated electrode combination on either side were similar in magnitude and sign due to the identical actuation input and geometry of the combination. Hence, in the region of overlap, the electric fields cancelled out and the ions ceased to be accelerated. This greatly reduces the effective forcing from either side, and hence only a weak streamwise jet was formed. A greater trailing edge thickness (h) would ensure that the encapsulated electrode would be wide enough to prevent an overlap of the plasma regions. Alternatively, lower peak to peak input signal amplitudes would give rise to smaller regions of plasma, which would not overlap over the base of the model. Fig. Fig. 5.19 shows the plasma zones formed on either side of the trailing edge. An analysis of the electric field for the present electrode layout and actuation conditions is given in App. F.1. It is clear that the present experimental model was not optimum for spanwise uniform actuation with the current geometric and electric actuation parameters.

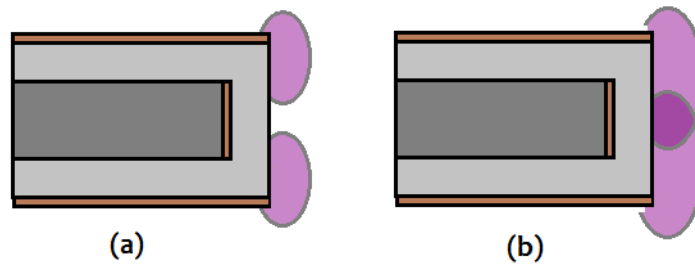


Figure 5.19: Zones of plasma due to the exposed-encapsulated electrode combinations on either side showing (a) Ideal non-overlapping and (b) overlapping zones

5.4 Spanwise Modulated Actuation Results

The motivation behind the implementation of spanwise modulated transverse actuation was to extend the effectiveness of the spanwise uniform configuration that was found most effective by Nati [27] in suppressing vortex shedding, namely the transverse actuation mode. Inspired by the 'in-phase' and 'out-of-phase' actuation schemes implemented in distributed forcing [21], [22], two different spanwise modulated transverse actuation modes were implemented in this work which were the 'opposing' and the 'staggered' modes, described in Apps. D.3 and D.4. Spanwise actuation was also implemented, in order to test the effect of placing streamwise-oriented actuators forcing along the span of the model perpendicular to the inflow, modelled on the works of Jukes and Choi [20] and Hennevelt [16]. These results from time-resolved PIV tests of these actuation modes will be explained in the sections that follow.

The transverse 'opposing' and 'staggered' and spanwise actuation modes had $x-y$ planes imaged at three, two and two different salient spanwise locations respectively within one spatial cycle of actuation using time-resolved PIV, in order to measure and study the different flow behaviours at these locations. In addition, $x-z$ planes were also imaged for each at appropriate transverse (y) heights in order to get a qualitative understanding of the induced flow physics across the span. These imaged planes are reiterated along with the results of each of these modes for ease of reference.

Considering the large number of configurations that were tested for each of the modes (Table 4.5), it is necessary to illustrate the results using representative configurations. Unless otherwise specified, all the results for the spanwise modulated transverse actuation modes that will be presented in this Chapter are of the configuration with spanwise spatial 'wavelength' of actuation $\lambda^* = \lambda/h = 5$. For the spanwise actuation mode, the configuration with $\lambda^* = 2$ will be used for illustration. Also, for each of these, the results for the lowest tested free stream of $U_\infty = 5$ m/s will be shown for phenomenological reasons, since the effect of the actuation on the flow is most apparent when the inflow momentum is low. The results that will be shown for the various actuation modes will be broadly organised into the following categories:

1. Instantaneous vortical structures
2. Statistical flow fields and topology of the actuation-induced flow
3. Power spectra at selected points in the wake

4. POD analysis
5. Analysis of transverse ($x - z$) planes imaged
6. Proposed mechanism of actuation

5.5 Transverse Opposing Actuation

The placement of electrodes and expected forcing scheme with this actuation mode, along with the imaged planes are shown in Fig 5.20.

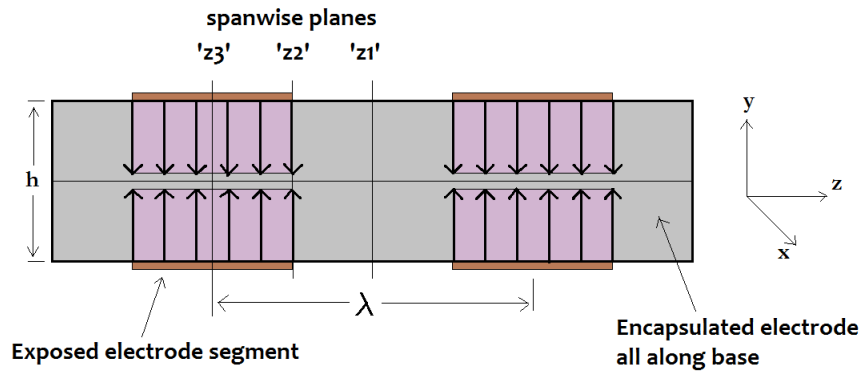


Figure 5.20: Schematic showing the electrodes, induced forcing and imaged $x - y$ planes in the spanwise modulated transverse opposing actuation mode

The imaged spanwise $x - y$ planes in one actuation cycle are:

1. The middle of a spanwise location without any exposed electrode on either side; $z = z1$
2. The spanwise location at the interface between the regions having exposed electrode and no-electrode on the upper and lower sides, displaced by $\lambda/2$ along the span from $z1$; $z = z2$
3. The middle of a spanwise location with exposed electrodes on either sides, and displaced by $\lambda/2$ along the span from $z2$; $z = z3$

Instantaneous Vortical Structures

Visualising the instantaneous vortical structures in each of the flow fields $x - y$ planes is essential to observe the effect of the actuation on the Karman vortex shedding. The instantaneous vorticity fields were calculated using the corresponding velocity field components using Eq. 3.13. The instantaneous vortical structures at the ' $z1$ ' spanwise location are shown in Fig. 5.21. The absence of large, coherent vortical structures as seen for the baseline case in Fig. 5.7 indicates that the interaction between the shear layers leading to the formation of Karman vortices has been suppressed, as if a splitter plate was present, at least over a streamwise extent corresponding to the x -length of the imaged field of view. The shear layers can be seen to break up into small, incoherent vortices.

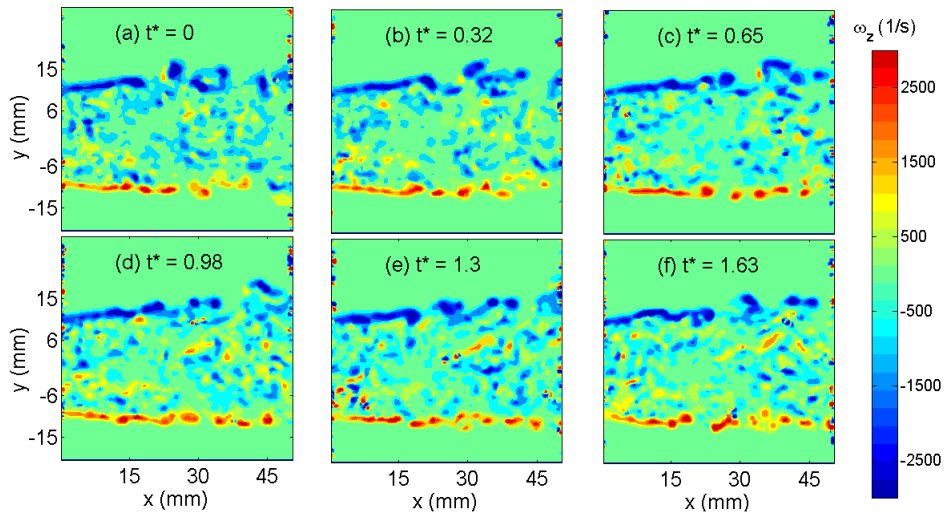


Figure 5.21: Sequence of instantaneous vorticity fields in wake for transverse opposing actuation with $\lambda^* = 5$, $U_\infty = 5$ m/s at z_1' with a non-dimensionalised time spacing $\Delta t^* = \Delta t \times U_\infty / h \simeq 0.32$

The instantaneous vortical structures at the z_2' spanwise location are shown in Fig. 5.22. The shear layers from either side were pushed inwards towards each other, towards the wake centerline, and much closer to the base of the model than for the baseline flow case. However their interaction did not seem to give rise to large, coherent vortical structures, and instead small, incoherent structures of concentrated vorticity were formed that only seemed to have a weak tendency towards periodic transverse motion across the wake.

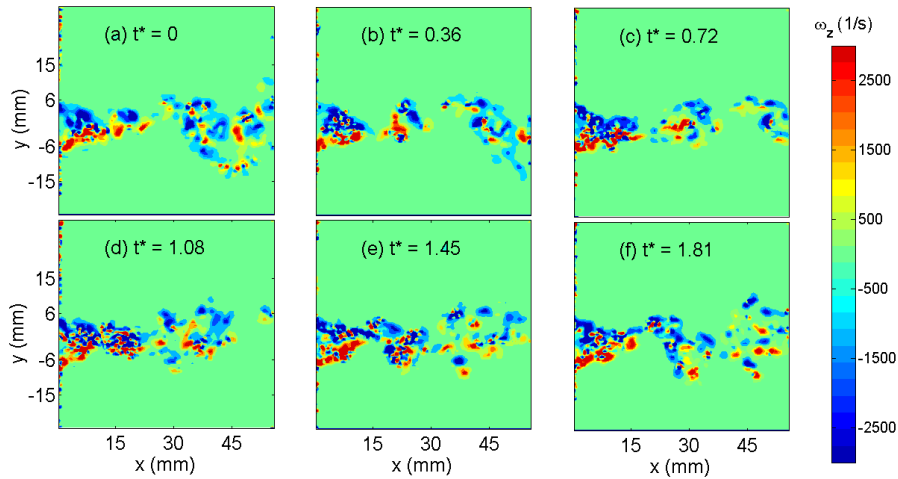


Figure 5.22: Sequence of instantaneous vorticity fields in wake for transverse opposing actuation with $\lambda^* = 5$, $U_\infty = 5$ m/s at z_2' with a non-dimensionalised time spacing $\Delta t^* = \Delta t \times U_\infty / h \simeq 0.32$

The instantaneous vortical structures at the z_3' spanwise location are shown in Fig. 5.23. It can be seen that the shear layers from either side interacted with each other closer to the model base than

in the baseline un-actuated flow case. Out of this interaction, large, turbulent vortical structures were formed; regular, periodic transverse motion could be identified based on the movement of the vortical structures in the image sequence.

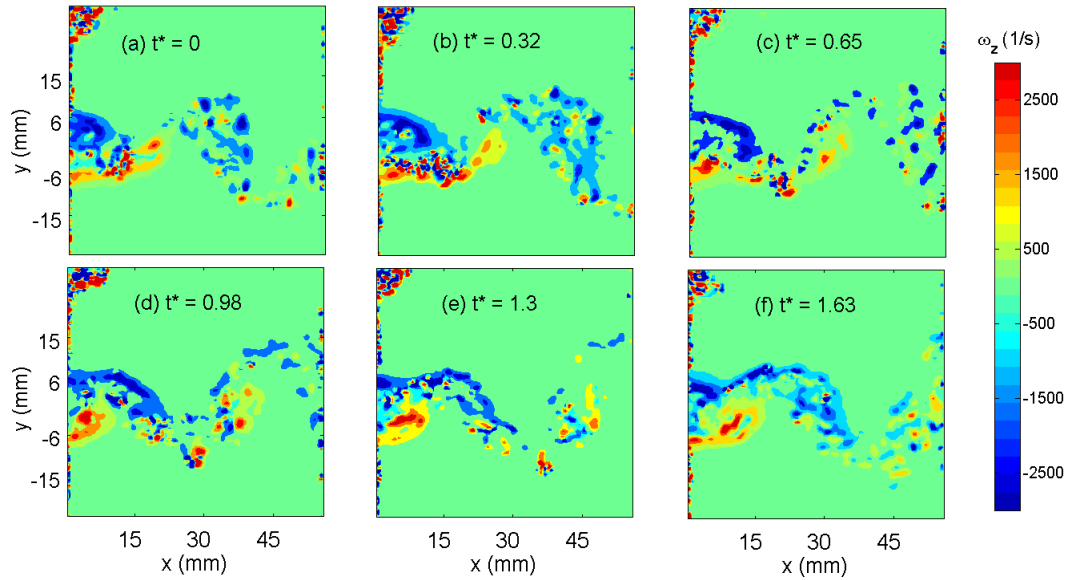


Figure 5.23: Sequence of instantaneous vorticity fields in wake for transverse opposing actuation with $\lambda^* = 5$, $U_\infty = 5$ m/s at $'z3'$ with a non-dimensionalised time spacing $\Delta t^* = \Delta t \times U_\infty / h \simeq 0.32$

Statistical Characterisation of the Flow Field

To indicate the mean and fluctuating wake flow quantities in the $x - y$ plane at the $'z1'$ location, the normalised averaged and RMS velocity fields of the flow in the wake are shown in Fig 5.24. It can be seen that the wake region of streamwise velocity deficit with respect to the free stream was much larger than the baseline un-actuated case seen in Fig 5.9(a). The transverse velocity fluctuations v'/U_∞ were also much reduced compared to what is seen in Fig 5.9(d), indicating that the cross-wake fluid motions associated with vortex shedding was suppressed. To get an idea of the wake topology at this location, the mean flow streamlines are in Fig 5.25. From the streamline plot it can be seen that a large fraction of the shear layers on either side was lifted up away from the wake centerline, while the smaller remaining portions moved towards the wake centerline to converge at a reattachment point located at around $x = 6\text{mm} = h/2$. It is clear that the fluid motion in the wake beyond this point was oriented away from the wake centerline on either side. These motions are corroborated by the averaged transverse velocity map, Fig 5.24(b). Alternate regions of positive and negative velocity were seen in the transverse velocity field in the wake in a symmetric manner on either side of the centreline. This indicates that at a height of a few mm above the upper and lower surfaces, large parts of the incoming shear layers got spread out in the transverse direction, overpowering their tendency to move into the wake towards the centreline. Further downstream, the mean transverse velocity map indicates the tendency of the fluid in the wake on either side to move away from the wake centerline.

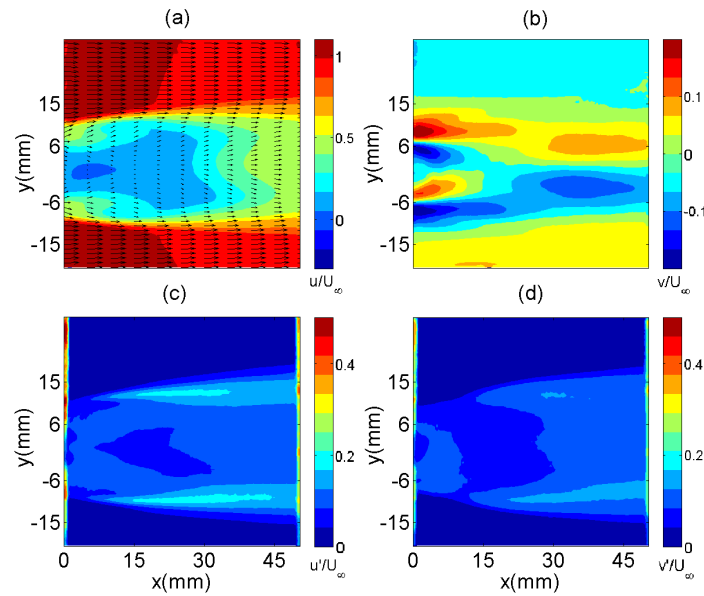


Figure 5.24: Statistical normalised velocity fields: (a) u/U_∞ (b) v/U_∞ (c) u'/U_∞ and (d) v'/U_∞ for transverse opposing actuation with $\lambda^* = 5$ and $U_\infty = 5$ m/s at ' $z1$ '

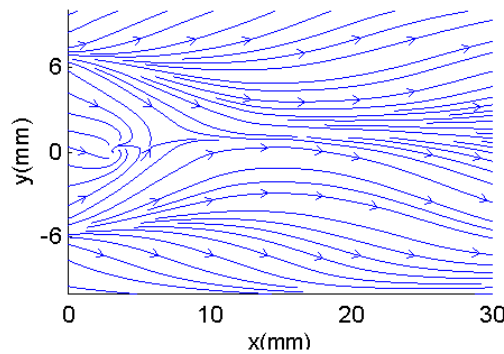


Figure 5.25: Mean flow streamlines for spanwise location ' $z1$ ' for transverse opposing actuation with $\lambda^* = 5$ and $U_\infty = 5$ m/s

The normalised averaged and RMS velocity fields of the flow in the wake in the $x-y$ plane at the ' $z2$ ' location are shown in Fig 5.26. At this spanwise location a smaller and narrower velocity defect region in the wake was seen compared to the baseline flow case, Fig 5.9. Also can be seen are enlarged regions of high transverse flow on both sides of the model, Fig. 5.26(b). These observations, along with the strong tendency of the shear layers to move inwards seen in Fig 5.22, indicate that the shear layers were deflected towards the wake centerline. The v'/U_∞ flow field in Fig. 5.26(d) shows a smaller and weaker region of transverse velocity fluctuations compared to the baseline flow case Fig 5.9(d). This indicates that the regular transverse cross-wake motion of fluid associated with Karman vortex shedding was significantly weakened. As before, a look at the streamlines at this location is necessary to get an idea of the topology of the mean flow. The

tendency of the shear layers to get deflected inwards, giving a narrow wake is also reflected in the mean flow streamlines in the near wake at this location, which show a 'reattachment point' much closer to the base of the model than in the un-actuated baseline case in Fig 5.27.

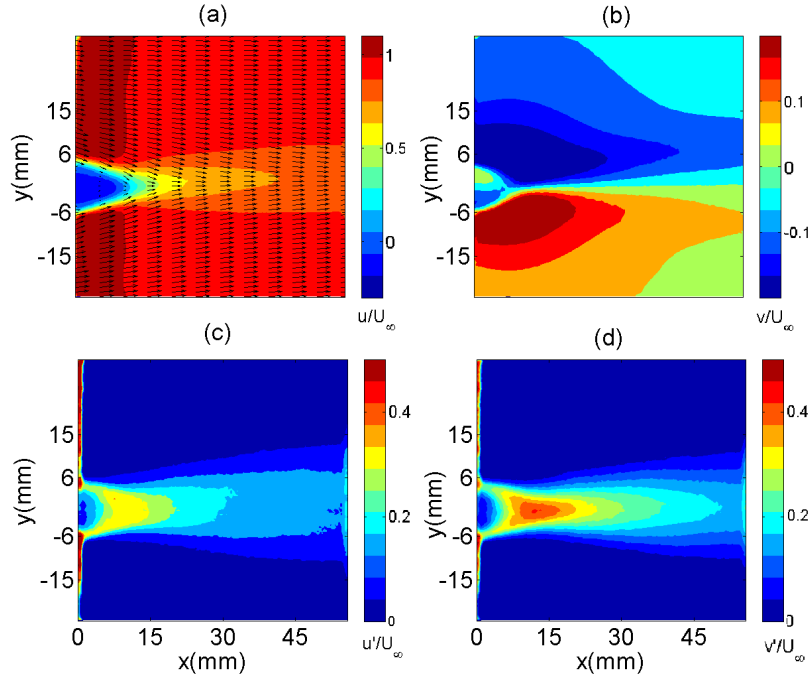


Figure 5.26: Statistical normalised velocity fields: (a) u/U_∞ (b) v/U_∞ (c) u'/U_∞ and (d) v'/U_∞ for transverse opposing actuation with $\lambda^* = 5$ and $U_\infty = 5$ m/s at 'z2'

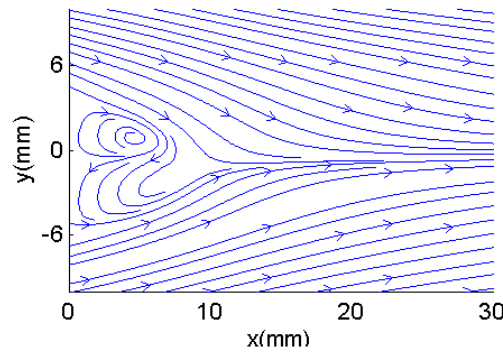


Figure 5.27: Mean flow streamlines for spanwise location 'z2' for transverse opposing actuation with $\lambda^* = 5$ and $U_\infty = 5$ m/s

To indicate the mean and fluctuating wake flow quantities in the $x - y$ plane at the 'z3' location, the normalised averaged and RMS velocity fields of the flow in the wake are shown in Fig 5.28.

The overall topology of the various flow contours in the statistical flow fields at this ' $z3'$ ' location do not differ much from that for the un-actuated baseline flow case in Fig 5.9; however they are slightly closer to the base of the model with respect to those in the baseline case. The defect region has a size and shape similar to that of the baseline flow case. The u'/U_∞ and v'/U_∞ fields indicate the presence of fluctuations very close to the model base itself; the v'/U_∞ field is slightly weaker than for the baseline case, but of similar shape and extent. This, along with the sequence of instantaneous vorticity images in Fig 5.23 indicates the presence of regular periodic transverse fluid motion. The mean flow topology seen in the streamlines in Fig 5.29 is very similar to that of the baseline flow case, Fig 5.10, with a slightly smaller recirculation region.

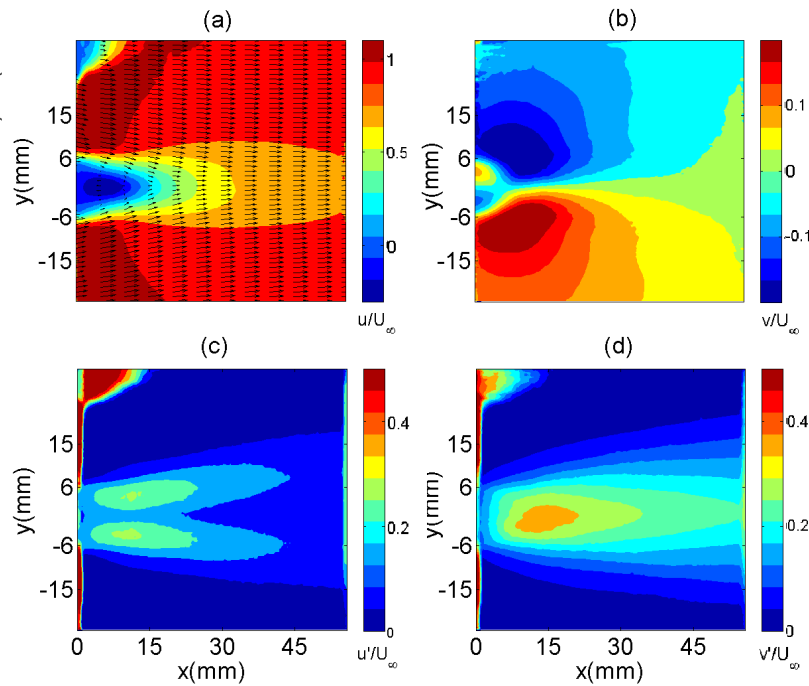


Figure 5.28: Statistical normalised velocity fields: (a) u/U_∞ (b) v/U_∞ (c) u'/U_∞ and (d) v'/U_∞ for transverse opposing actuation with $\lambda^* = 5$ and $U_\infty = 5$ m/s at ' $z3'$ '

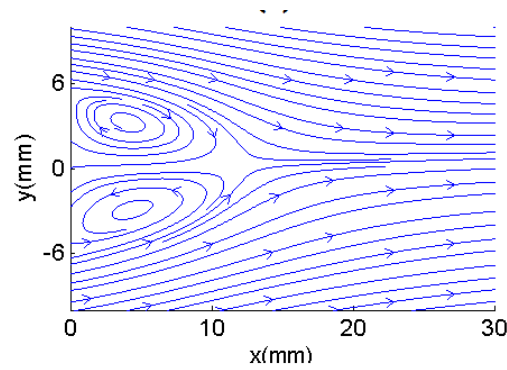


Figure 5.29: Mean flow streamlines for spanwise location ' $z3$ ' for transverse opposing actuation with $\lambda^* = 5$ and $U_\infty = 5$ m/s

Wake Spectra

The streamwise velocity at a point in the wake beyond the vortex formation length and close to shear layers on either side is expected to fluctuate at the frequency of vortex shedding. Hence, the frequency spectrum of such a time signal will show a peak at the frequency of shedding. Close to the wake centerline and within the vortex formation region, the dominant frequency content is expected at twice the shedding frequency, due to the two motions of fluid across the wake for every shedding cycle. In this work, the streamwise velocity time signals are collected at points in the wake at a streamwise distance $x = 1.2h$ and located respectively in the upper shear layer ($y = 0.5h$), centerline ($y = 0$) and lower shear layer ($y = -0.5h$). The signal spans over the interval of measurement, at a sampling frequency of the PIV frequency of acquisition, 3000 Hz.

Considering the ' $z1$ ' spanwise location for transverse opposing actuation, the streamwise velocity at the points mentioned above are collected and the Power Spectral Density (PSD) is found for these time signals and plotted against the non-dimensionalised frequency, the St in Fig 5.30. As a reference for comparison, the PSD of the baseline un-actuated case is also co-plotted at each of the points. The baseline PSD shows strong shedding peaks at $St = 0.25$ and 0.5 at the shear layers and centerline respectively as expected. It can be seen that the energy level of the fluctuations at ' $z1$ ' with actuation is much reduced compared to the baseline case. The presence of only extremely weak peaks indicates that the periodicity in the wake corresponding to vortex shedding has almost completely been mitigated. At the centerline location, a weak peak at the shedding frequency can be seen, unlike that in the baseline case where a peak at the first harmonic of the shedding frequency is seen due to the point being located before the end of vortex formation region. This indicates that the regular motion of fluid across the wake, associated with this harmonic peak have been suppressed.

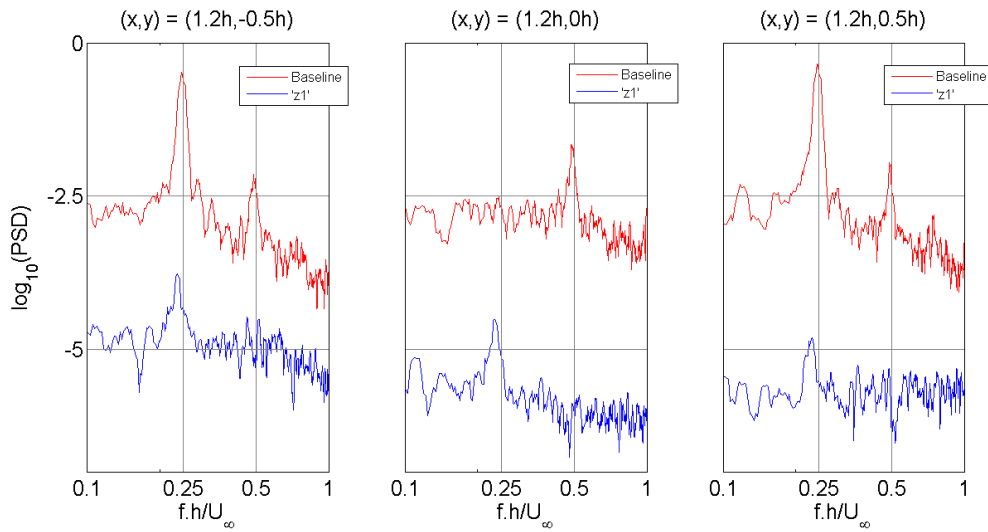


Figure 5.30: Streamwise velocity PSD for transverse opposing actuation with $\lambda^* = 5$ and $U_\infty = 5$ m/s at 'z1' at the three points of interest in the wake, co-plotted along with the PSD of the baseline flow case

At spanwise location 'z2', frequency peaks in the shear layers close to but lower than the shedding frequency are seen but of a lower energy when compared to the baseline un-actuated flow case. No peaks are seen at the point in the centerline, indicating that no periodic flow activity occurs at this point.

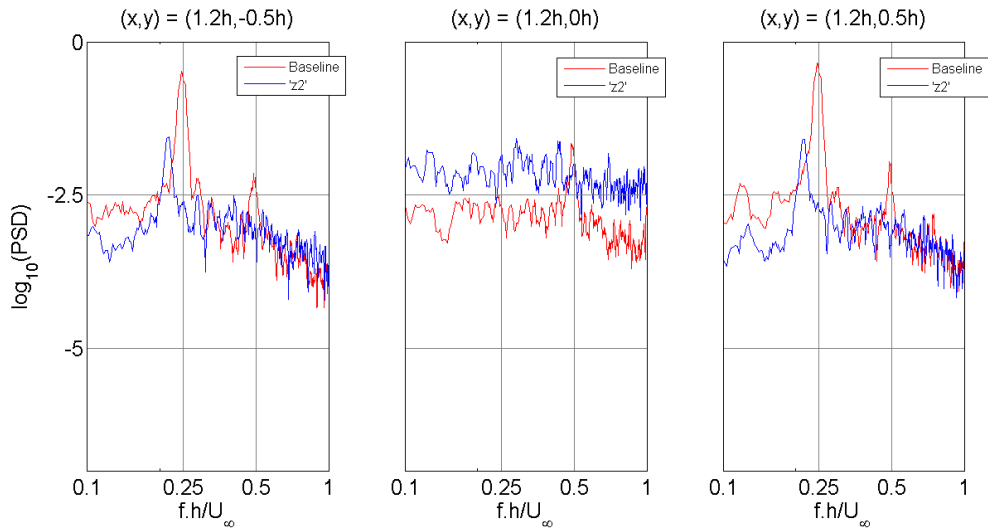


Figure 5.31: Streamwise velocity PSD for transverse opposing actuation with $\lambda^* = 5$ and $U_\infty = 5$ m/s at 'z2' at the three points of interest in the wake, co-plotted along with the PSD of the baseline flow case

At spanwise location ' $z3'$ ', shedding peaks of slightly lower frequency compared to the baseline case can be seen at the shear layer locations. These peaks are as strong as those in the baseline flow PSD, indicating the presence of periodic vortex shedding at this location.

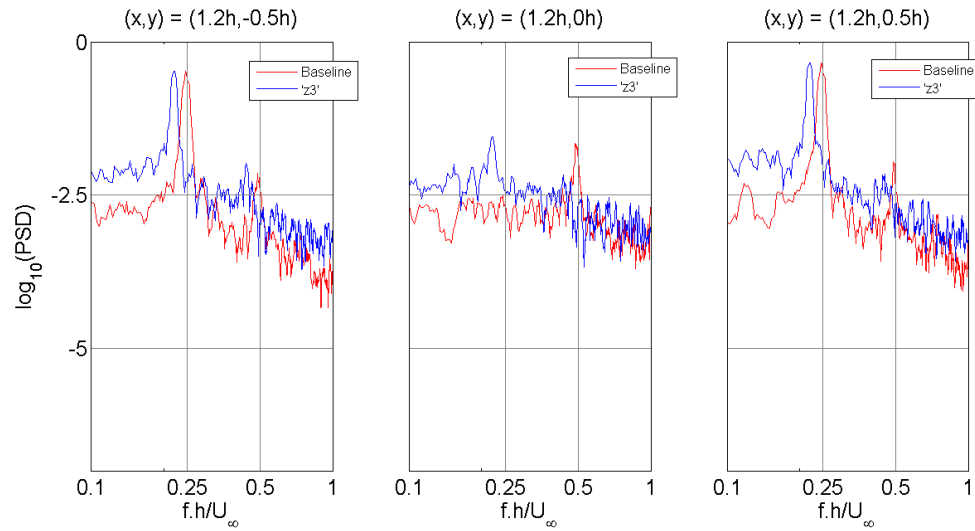


Figure 5.32: Streamwise velocity PSD for transverse opposing actuation with $\lambda^* = 5$ and $U_\infty = 5$ m/s at ' $z3'$ ' at the three points of interest in the wake, co-plotted along with the PSD of the baseline flow case

POD Analysis

The POD modes of the flow for transverse opposing actuation with $\lambda^* = 5$ and $U_\infty = 5$ m/s at ' $z1'$ ' are visualised in Fig. 5.34. To make comparison easier, the baseline POD structures visualised are also shown in Fig 5.33. It is clear that the strongest structures are pushed downstream and are much weakened compared to the baseline flow case. The disarray in the structures indicates a suppression of the coherent structures associated with Karman vortex shedding in the wake.

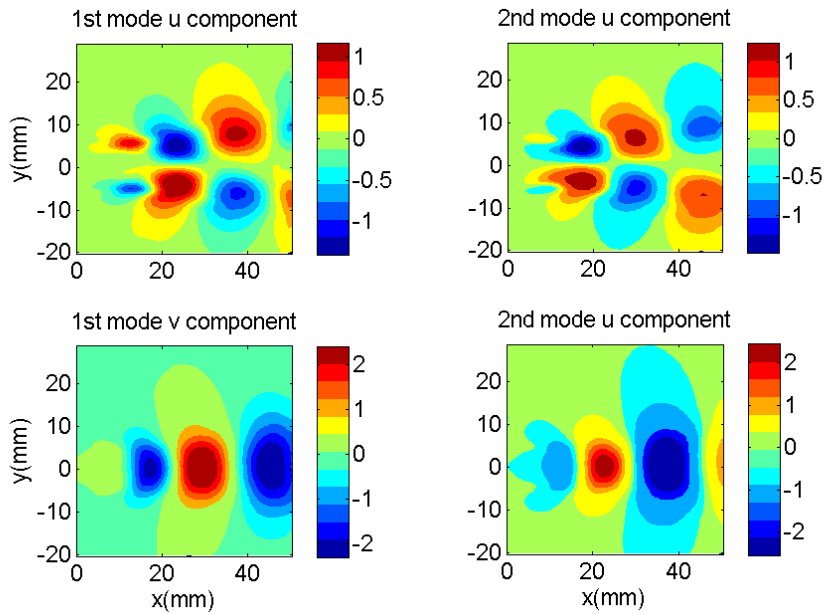


Figure 5.33: Velocity fields in m/s for the first two POD modes visualised the $U_\infty = 5$ m/s baseline flow case

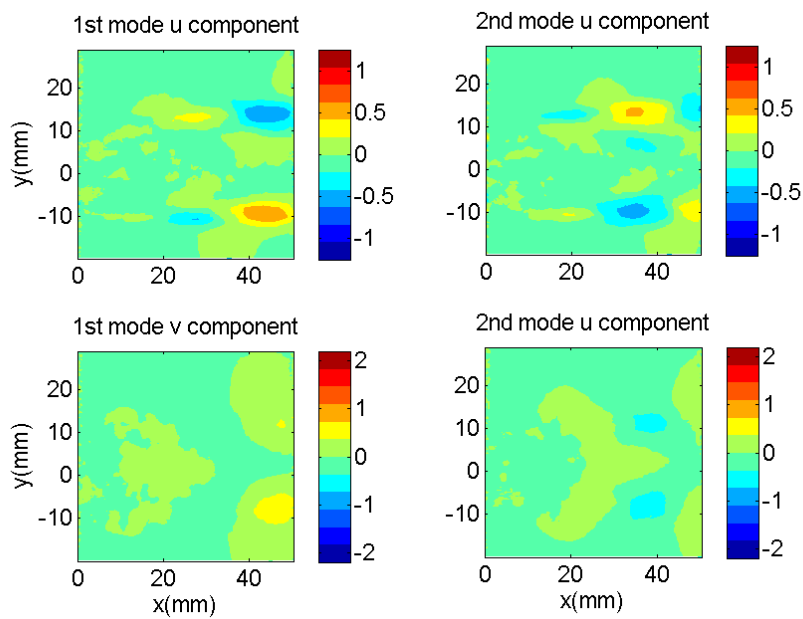


Figure 5.34: Velocity fields in m/s for the first two POD modes for transverse opposing actuation with $\lambda^* = 5$ and $U_\infty = 5$ m/s at 'z1'

At spanwise location ' z_2 ' the structures in the modes can be identified but they are distorted and of a much lower energy than the baseline un-actuated flow case.

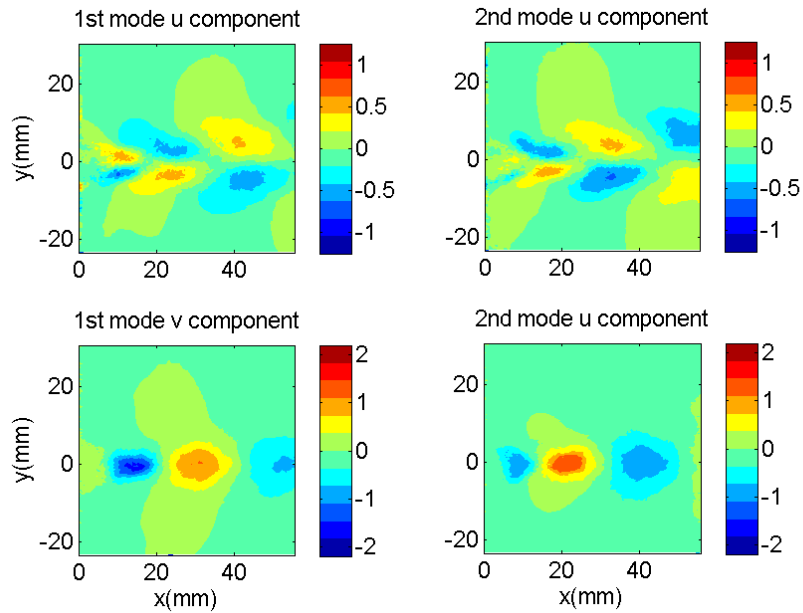


Figure 5.35: Velocity fields in m/s for the first two POD modes for transverse opposing actuation with $\lambda^* = 5$ and $U_\infty = 5$ m/s at ' z_2 '

At spanwise location ' z_3 ' the structures in the modes are easily defined and of almost the same strength as for the baseline un-actuated flow case. This indicates the presence of regular periodic vortex shedding that can be represented through the first two POD modes.

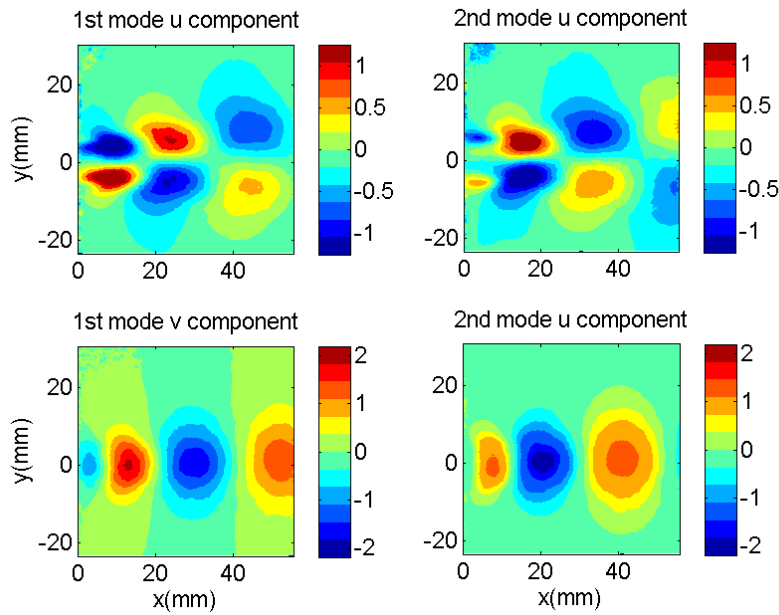


Figure 5.36: Velocity fields in m/s for the first two POD modes for transverse opposing actuation with $\lambda^* = 5$ and $U_\infty = 5$ m/s at ' $z3'$

The plot showing the energy content of the first ten modes for the present considered mode at $\lambda = 5h$ at $U_\infty = 5$ m/s is shown in Fig. 5.37. The lower the energy in the first two POD modes, the more successful the suppression of Karman vortex shedding. The baseline un-actuated flow modal energies are also shown, so that a comparison can easily be made to determine the degree of success of the actuation in each case and for each spanwise location based on the level to which the energy share of the first two POD modes is reduced to. It is seen that the suppression is strongest at ' $z1'$ ' and weakest at ' $z3'$ '. This could be expected since the instantaneous vortical structures at these locations (Figs. 5.21 and 5.23) show no organisation and relatively large periodic organisation respectively. This was also reflected in the wake power spectra at these locations (Figs. 5.30 and 5.32).

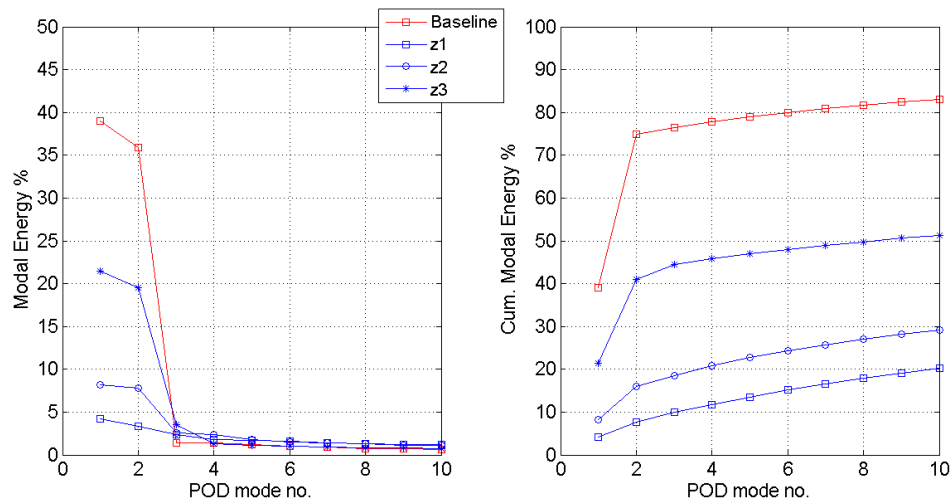


Figure 5.37: Individual and cumulative shares of the Fluctuating KE of the wake captured by the first ten POD modes of flow with spanwise modulated transverse opposing actuated flow with $\lambda = 5h$ at $U_\infty = 5$ m/s

Transverse Planes

Two $x - z$ planes in the wake of the bluff body were imaged at the salient transverse locations of $y = 0$ and $y = (0.5h + 2 \text{ mm})$, representing respectively the wake mid-plane and shear layer planes. The purpose of this was to study the spanwise flows in the wake that would normally be out-of-plane in the $x - y$ planes imaged. This was essential since the flow field was expected to be strongly-three dimensional due to the influence of the actuation. The effect of spanwise modulated actuation on the two-dimensionality of the shed Karman rollers was also studied.

The $y = 0$ and $y = (0.5h + 2 \text{ mm})$ wake mid-plane and shear layer planes are shown in Figs. 5.38 and 5.40 respectively, and the mean flow streamlines in Fig 5.39. In each of these figures, the spanwise positions where the $x - y$ planes were imaged are shown along with the last few mm of the experimental model with the locations of exposed electrode segments indicated in brown. The following induced flow effects could be identified:

- Spanwise flows close to the model base that originated from ' $z3$ ' in both directions. These flows were undoubtedly created when the plasma-induced spanwise jets from the upper and lower trailing edges converged to a stagnation point at the base-midplane and turned away to the sides. This is explained in Sec. 5.5.1. Due to the shear caused by these spanwise jets in the 'dead water' near wake, circulation was created along the y axis. This is clearly seen and indicated in the streamline plots. In Fig. 5.39, the spanwise flows and the approximate centers of the vorticity created by them are indicated in orange and blue respectively. A pair of counter-rotating vortices are formed at every exposed electrode segment by the spanwise jets.
- Further downstream at $x = 30\text{mm}$ and beyond and on either side of the ' $z1$ ' spanwise line, areas of oppositely directed spanwise flows were seen. These spanwise flows converged along the stagnation line and lifted-up on either side in the transverse (y) direction. This

lift-up transported low velocity fluid from the wake centerline area towards the outer flow. This is seen in Fig. 5.40, where low velocity fluid is seen in the shear layer transverse plane at $'z1'$. This was the reason the shear layers at this spanwise location were deflected away from the wake centerline and the wake broadened, and the zone of low-velocity fluid elongated in the streamwise direction. The spanwise flows referred to here are indicated in orange and blue around the $z1$ line close to $x = 30$ mm. At these streamwise locations, the spanwise flows when taken in conjunction with the transverse flows directed away from the wake centerline seen in Fig 5.24(b) are definite indicators of the presence of spatially fixed streamwise vorticity.

- From the various $x - y$ planes analysed so far, it is clear that the wake was narrowest at $'z3'$ and broadest at $'z1'$, meaning that the saddle points (that mark the streamwise end of the recirculating flow regions in the near wake) at these spanwise locations were respectively closest and farthest from the model base. The locus of these saddle points, which was straight and parallel to the base in the baseline flow case (Fig 5.11), is now bent in a smooth manner along the span, shown in red in Fig 5.39(b). In one actuation cycle, two maxima in streamwise extent can be seen, at $'z1'$ and $'z3'$ with minima at the electrode-no electrode interface positions ($'z2'$'s). Hence, the actuation has regulated and twisted the locations along the span where the shear layers interact. The two-dimensionality in the formation of Karman rollers shed has hence been broken.

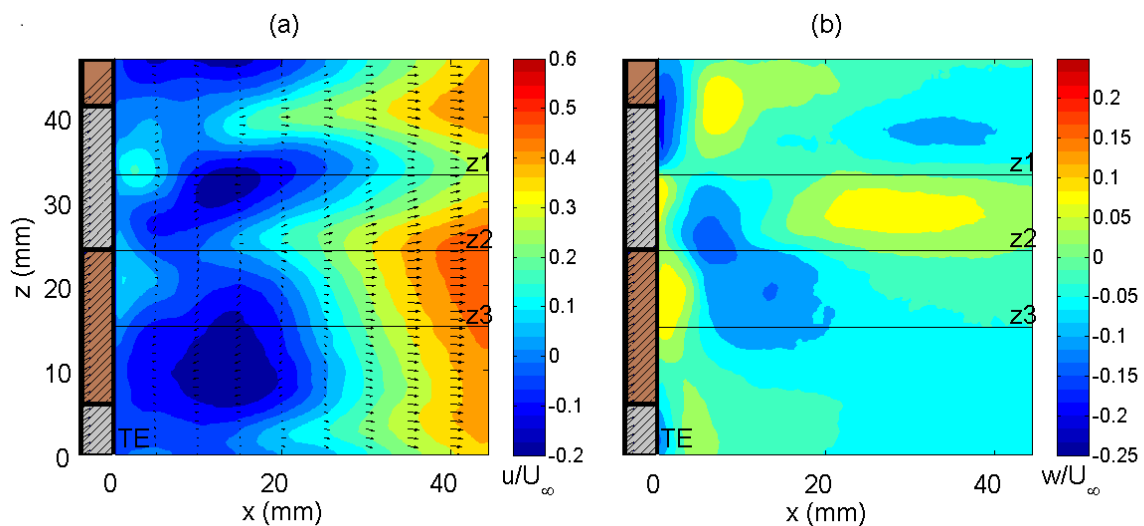


Figure 5.38: Time-averaged and normalised (a) u and (b) w velocity fields in the wake centerline plane for transverse opposing actuation with opposing actuation with $\lambda^* = 3$ and $U_\infty = 8$ m/s. The exposed electrode segments are also indicated in brown

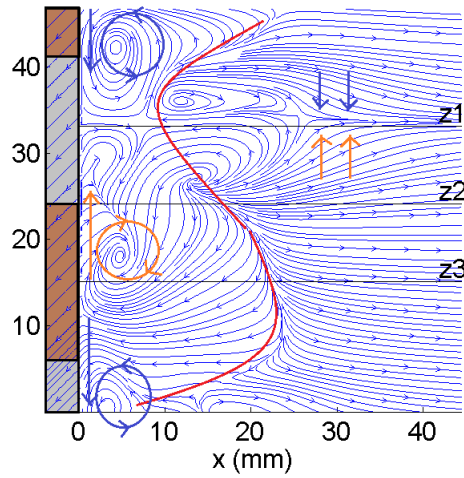


Figure 5.39: Mean flow streamlines altered to indicate flow features, in the wake centerline plane for transverse opposing actuation with opposing actuation with $\lambda^* = 3$ and $U_\infty = 8$ m/s/ The exposed electrode segments are also indicated in brown

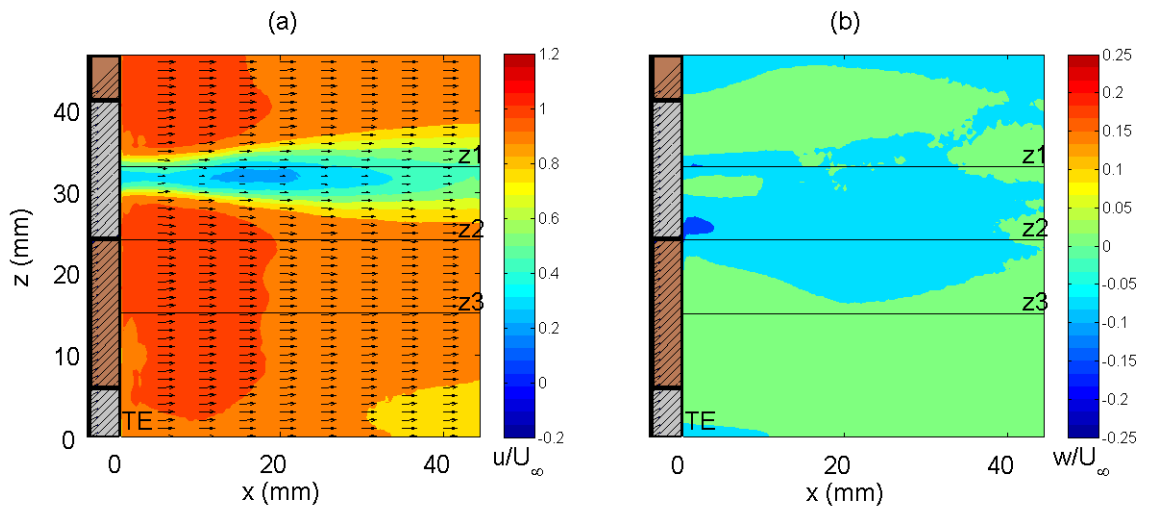


Figure 5.40: Time-averaged and normalised (a) streamwise and (b) spanwise velocity fields in the shear layer plane for transverse opposing actuation with $\lambda^* = 3$ and $U_\infty = 8$ m/s. The exposed electrode segments are also indicated in brown

The mean flow wake topology as seen in the preceding sections suggests that the shedding of Karman rollers from the trailing edge is modulated in the spanwise direction. To confirm that the rollers have indeed lost their spanwise coherence, however, one must get back into the time domain for cross-correlation analysis of the velocity time signals themselves, as was done for the

shear layer transverse plane for the baseline flow case, shown in Fig 5.12. Fig 5.41(a) shows the twenty spanwise points along the six fixed streamwise positions at $x/h = 0.5, 1, 1.5, 2, 2.5$ and 3 where the streamwise velocity time signals were gathered from the time resolved PIV velocity fields. With a point at the ' $z2$ ' spanwise as the reference point, the correlation coefficients of the velocity signal at this point with the other points are plotted against the spanwise location of these points in Fig. 5.41(b). The coefficients are seen to fall quite rapidly along the span away from the reference point (with the fall being sharper at the low velocity region at ' $z1$ '). The generally low correlation coefficient values compared to the baseline flow case in Fig. 5.12 indicates that the spanwise coherence of the shed rollers along the span has indeed been broken. The spanwise correlations of the various spanwise modulated transverse opposing actuation flow cases over all the tested U_∞ cases are shown in App. H.

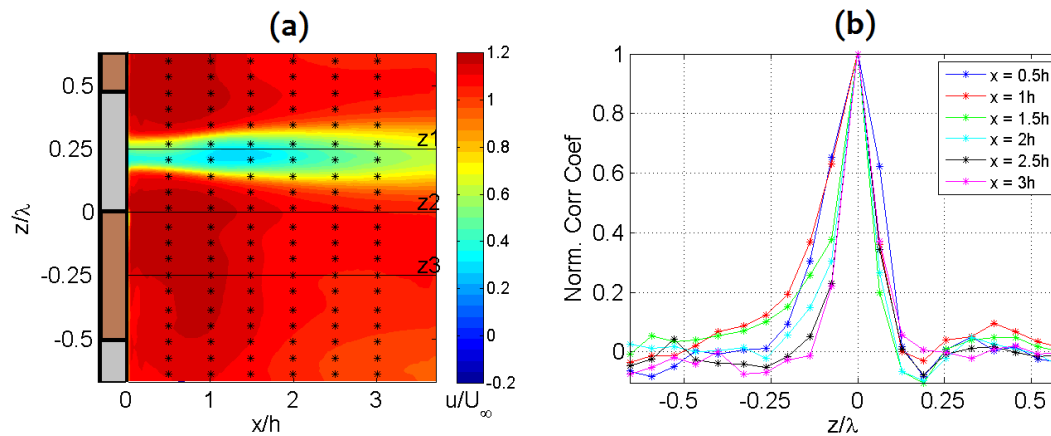


Figure 5.41: Wake shear layer $x - z$ plane (a) mean streamwise velocity map showing correlation points and (b) spanwise correlation coefficients for spanwise modulated transverse opposing actuation with $\lambda^* = 3$ at $U_\infty = 5$ m/s. The exposed electrode segments are also indicated in brown

5.5.1 Proposed Actuation Mechanism

The proposed mechanism of actuation here is constructed using the flow features and results shown in the sections above as 'clues'. It must be able to explain these features as well as be physically plausible from the point of view of flow and actuator physics. The following are the 'clues' that will be used to construct the model for the spanwise modulated opposing actuation mode:

1. A 'lift-up' of the shear layers at spanwise location ' $z1$ ' to give a broad wake.
2. A 'pushing-in' of the shear layers at spanwise location ' $z2$ ' to give a narrow wake.
3. In the wake centerline plane:
 - spanwise flows close to the model base directed away from ' $z3$ ' towards the sides;
 - further downstream, formation of streamwise 'tubes' of spanwise flows that converge into each other along the ' $z1$ ' line.

4. In the shear layer plane, region of low streamwise velocity along the $'z1'$ line.

The proposed model that explains the above features is shown in Fig. 5.42. At $t = 0$, the start time instant of actuation, the expected forcing will be as shown in Fig. 5.42(A), i.e. only along the transverse (y) direction. However the presence of alternate regions of presence and absence of actuation along the span will soon induce three-dimensional flows along the span. The spanwise flows that were seen in the base centerline $x - z$ plane in Fig 5.38(a) are shown in red and blue in Fig. 5.42(B). These flows are created at the middle of the spanwise locations with exposed electrodes on both sides when the transverse jets from either side converge and flow apart. These transverse jets tend to flow apart in the spanwise direction instead of the streamwise direction, as was seen by Nati [27] with spanwise uniform transverse actuation. This is due to the presence of regions with no forcing along the span. The spanwise flow-apart creates a local stagnation point at the $'z3'$ location. Such points are shown in Fig. 5.42(B) and denoted by (a) and (c). When the spanwise flows from two such adjacent regions (a) and (c) come together at the $'z1'$ location, they create another local stagnation point (b) and flow apart along the transverse direction on either side. This transverse flow at $'z1'$ lifts the stagnant, low velocity fluid behind the model base towards the outer flow, and causes the separating shear layers to move apart away from the wake centerline.

As was seen in the centerline plane velocity fields and streamlines, the plasma induced spanwise flows are responsible for the creation of transverse vorticity, ω_y . Once created, these vortices themselves induce significant spanwise flows in the near wake region at and close to the spanwise positions of the exposed electrode-no electrode interfaces. At $'z2'$ which is located at an interface, a combination of flow effects is seen - the interaction between ω_y and the shear layers, the significant ω_y induced spanwise flows and the forcing shear caused by the sharp discontinuity between the transverse actuated and non-actuated regions (which tends to effectively strengthen the transverse forcing). These are responsible for the shear layers quickly turning turbulent and getting pushed inwards, seen in Fig. 5.22. The narrowing of the wake and reduced streamwise extent of the recirculation region are caused by this. At $'z3'$, due to the channelling of much of the transverse forcing stream to the sides, the effective transverse forcing is quite weak, hence the shear layers and wake sizes are not largely affected as was also seen earlier. The vortex shedding is hence largely undisturbed at this location.

It is quite clear that the flow behaviour is significantly altered along the span. The motion of fluid induced from the exposed electrodes initially flowing towards the centerline along y , that is redirected along $\pm z$ and then upwards away from centerline again gives rise a streamwise circulation ω_x that is spatially fixed and temporally steady. The network of counter-rotating streamwise vorticity created is shown in Fig. 5.42(C). The common flow up of these counter-rotating vortices is responsible for the lift-up of the shear layers on either side. At the same time, the transverse vorticity induced by the spanwise flows is responsible for inducing the shear layers at the $'z2'$ interface locations to turbulence. The near wake region is hence a region of significant interplay between the baseline spanwise vorticity ω_z , and the induced streamwise and transverse vorticity (ω_x and ω_y). The success of the spanwise modulated transverse opposing actuation mode rests on the energy transfer from ω_z in the shear layers to ω_x and to a lesser extent ω_y . This weakens/suppresses the Von Karman vortex shedding and increases the base pressure [29]. It is conjectured in Deshpande et al [8] that strong streamwise vortices with spatially fixed positions are instrumental in creating dislocation of the Karman vortex along the span. In that work, the trailing edge of the experimental model was modified in multiple configurations to induce strong three dimensionality, and generate strong streamwise vortices that effectively transfer energy from the Karman vortices resulting in suppression of the unsteadiness.

Instead of achieving vortex suppression all over the span as is done with two-dimensional control methods, it is enough to introduce spanwise dislocations and irregularities that instead aim to break up the two-dimensionality of the Karman vortex shedding process, as is attempted here. That is why even though an unsteady fluctuating wake was seen at the $'z3'$ $x - y$ plane, the shed vortices are going to be out of phase across the span with those at other locations. Hence, the fluctuations, when averaged across the span are not going to be regular and period, but instead random and uncorrelated, and incapable of generating tonal acoustic noise, which was the overarching objective of this work. However as the free stream U_∞ increases, the momentum of the incoming shear layers increases and it becomes harder for the fixed energy-input actuation to deflect momentum from the inflow and create streamwise vorticity. This explains why the performance of the actuation in suppressing/weakening vortex shedding deteriorates as U_∞ increases.

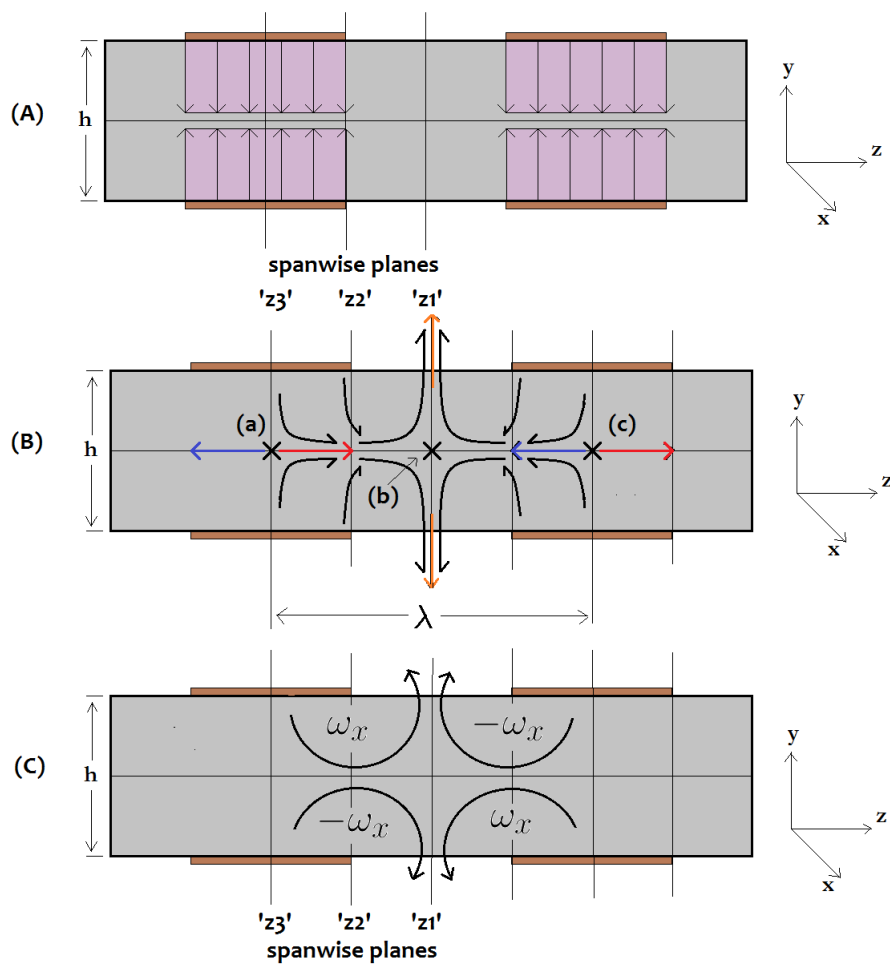


Figure 5.42: Schematic of proposed actuation mechanism for spanwise modulated transverse opposing actuation - (A) actuator forcing, (B) induced flows and (C) induced vorticity

5.6 Transverse Staggered Actuation

For spanwise modulated transverse staggered actuation, the expected forcing scheme is as shown in Fig 5.43. The spanwise $x - y$ planes images are as follows:

1. The spanwise location at the interface between the regions having exposed electrode and no-electrode on the upper and lower sides; $z = z_1$.
2. The middle of a spanwise location without exposed electrode on one side and an exposed electrode on the other, displaced by $\lambda/2$ along the span from z_1 .

Instantaneous Vortical Structures

The instantaneous vorticity fields at the different imaged $x - y$ planes can give a visual picture of the effect of the actuation on the shear layers on either side and the interaction between them. The instantaneous vortical structures at the spanwise ' z_1 ' location are shown in Fig. 5.44. It can be seen that the shear layers were bent towards each other, facilitating early interaction between them and giving rise to small, turbulent vortical structures that formed a narrower wake than the canonical case. The flow behaviour seems to resemble that at spanwise location ' z_2 ' of the spanwise modulated opposing actuation mode.

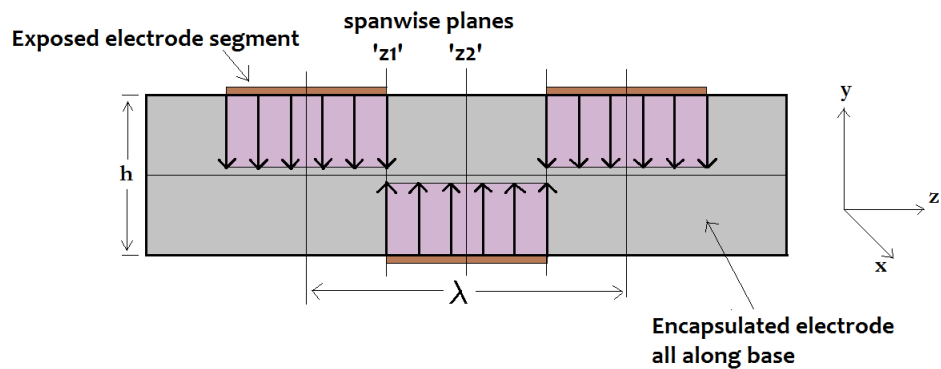


Figure 5.43: Schematic showing the electrodes, induced forcing and imaged $x - y$ planes in the spanwise modulated transverse staggered actuation mode

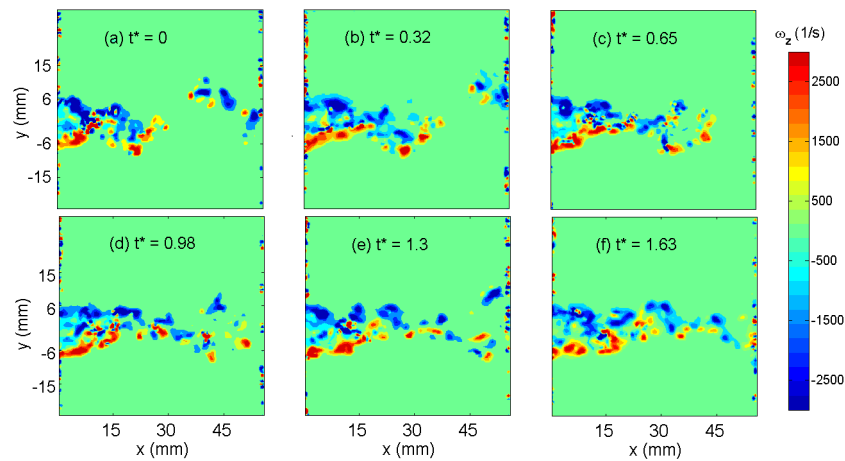


Figure 5.44: Sequence of instantaneous vorticity fields in wake for transverse staggered actuation with $\lambda_* = 5$, $U_\infty = 5$ m/s at $'z1'$ with a non-dimensionalised time spacing $\Delta t^* = \Delta t \times U_\infty / h \simeq 0.32$

The instantaneous vortical structures at the spanwise $'z2'$ location, when actuation is turned on, is shown in Fig 5.45. It was seen that the shear layers persisted longer downstream and are spread far apart, indicating that they are prevented from interacting close to the base of the model. A large, turbulent wake was created. The flow field was asymmetric with respect to the wake centerline as can be seen, deflected away from the side of forcing (lower side in this case). The forcing caused the shear layer on that side to break up earlier than that on the other side.

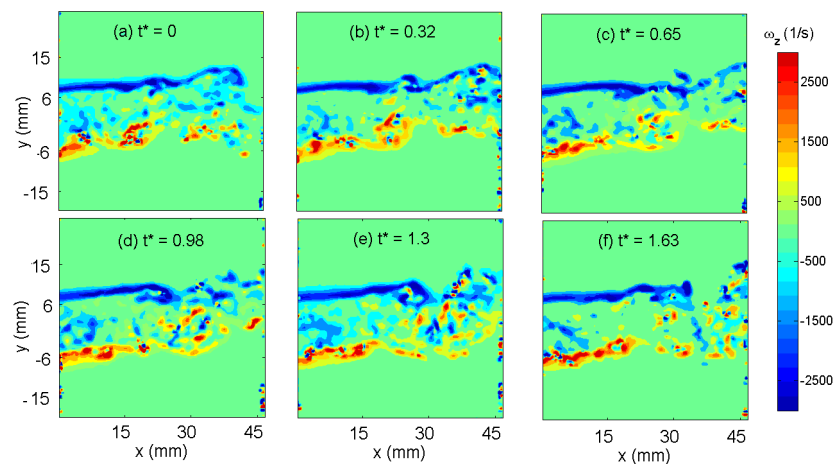


Figure 5.45: Sequence of instantaneous vorticity fields in wake for transverse staggered actuation with $\lambda_* = 5$, $U_\infty = 5$ m/s at $'z2'$ with a time-spacing of 0.75 ms

Statistical Characterisation of the Flow Field

To indicate the mean and fluctuating wake flow quantities in the $x - y$ plane at the $'z1'$ location, the normalised averaged and RMS velocity fields of the flow in the wake are shown in Fig 5.46.

When compared to the baseline flow maps shown in Fig 5.9, the following were seen - a smaller, narrower wake (velocity defect region in u/U_∞), larger regions of enhanced cross-wake transverse fluid motion (in v/U_∞) but at the same time reduced transverse velocity fluctuations (in v'/U_∞). The last of these observations indicates a suppression of the regular, periodic cross-wake transverse motion associated with vortex shedding. The reduced size of the recirculation region behind the base of the model is also seen in the streamline plot in Fig. 5.50(a), which shows a reattachment point at approximately $x = 12$ mm.

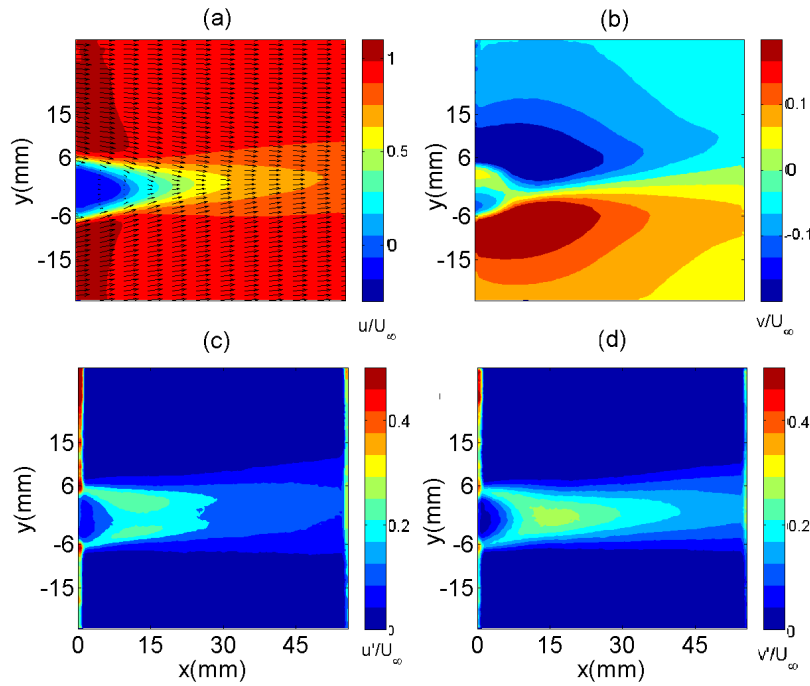


Figure 5.46: Statistical normalised velocity fields: (a) u/U_∞ (b) v/U_∞ (c) u'/U_∞ and (d) v'/U_∞ for transverse staggered actuation with $\lambda^* = 5$ and $U_\infty = 5$ m/s at 'z1'

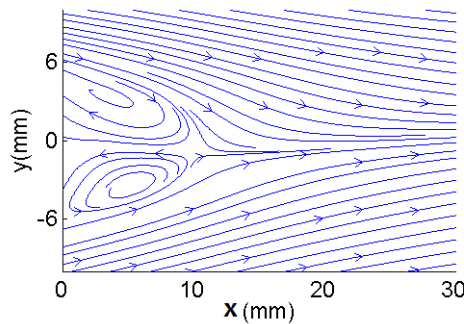


Figure 5.47: Near wake mean flow streamlines at spanwise location 'z1' for transverse staggered actuation with $\lambda^* = 5$ and $U_\infty = 5$

The statistical flow fields at spanwise location ' z_2' ' are shown in Fig 5.48. The asymmetry in the induced flow is clearly seen in the streamwise velocity mean map u/U_∞ , where the wake was noticeably lifted up on the upper side away from the side where the exposed electrode segment is located. This is also reflected in the mean transverse flow field v/U_∞ , where the transverse forcing from the lower side was predominant. Also, at the location of the upper shear layer, a region of positive transverse velocity is seen, indicating that the shear layer on this side was lifted-up. Due to the forcing asymmetry, only a single recirculation 'bubble' is seen behind the model base, as seen in Fig. 5.49. The transverse velocity RMS map v'/U_∞ indicates much reduced fluctuations compared to the baseline flow case, indicating that regular, periodic organised transverse cross-wake fluid flow associated with Karman vortex shedding had been curbed.

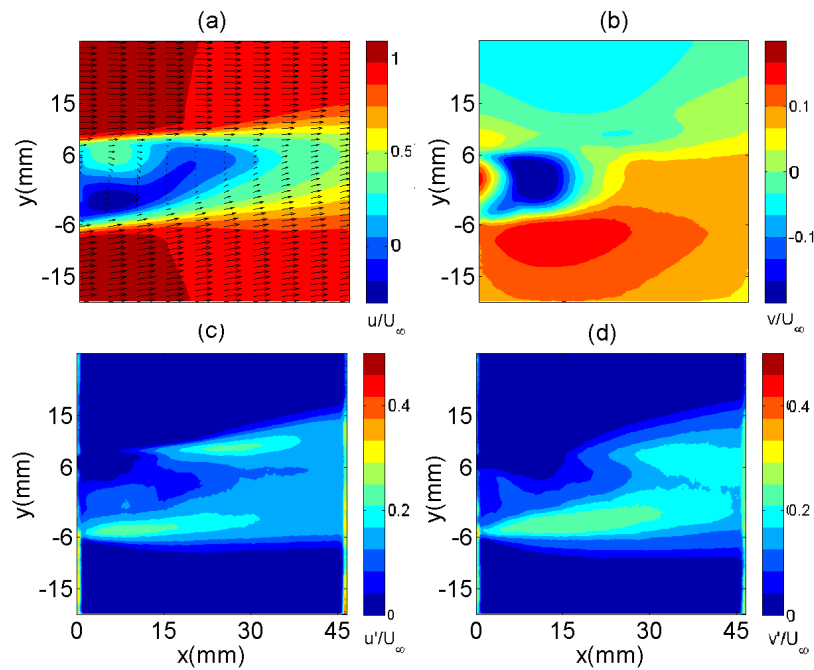


Figure 5.48: Statistical normalised velocity fields: (a) u/U_∞ (b) v/U_∞ (c) u'/U_∞ and (d) v'/U_∞ for transverse staggered actuation with $\lambda^* = 5$ and $U_\infty = 5$ m/s at ' z_2' '

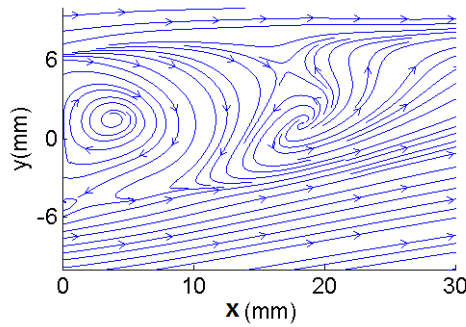


Figure 5.49: Near wake mean flow streamlines at spanwise location ' z_2 ' for transverse staggered actuation with $\lambda^* = 5$ and $U_\infty = 5$

Wake Spectra

At the ' z_1 ' and ' z_2 ' spanwise locations for transverse staggered actuation, the streamwise velocity at the three points of interest located along the shear layers and wake centerline are collected and the Power Spectral Densities (PSD's) are found for these time signals and plotted against the non-dimensionalised frequency, the St in Figures 5.50 and 5.51. As before, the baseline flow PSD is co-plotted as a reference for comparison. It is clear that no frequency peaks indicative of regular flow activity in the wake are present in either spectra, pointing to the suppression of regular periodic Karman shedding in the wake at these locations.

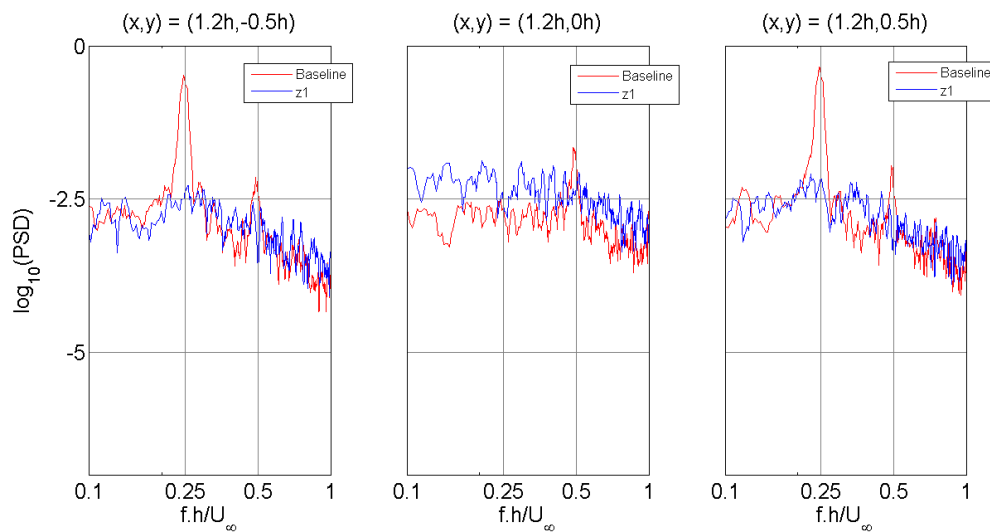


Figure 5.50: Streamwise velocity PSD for transverse staggered actuation with $\lambda^* = 5$ and $U_\infty = 5$ m/s at ' z_1 ' at the three points of interest in the wake, co-plotted along with the PSD of the baseline flow case

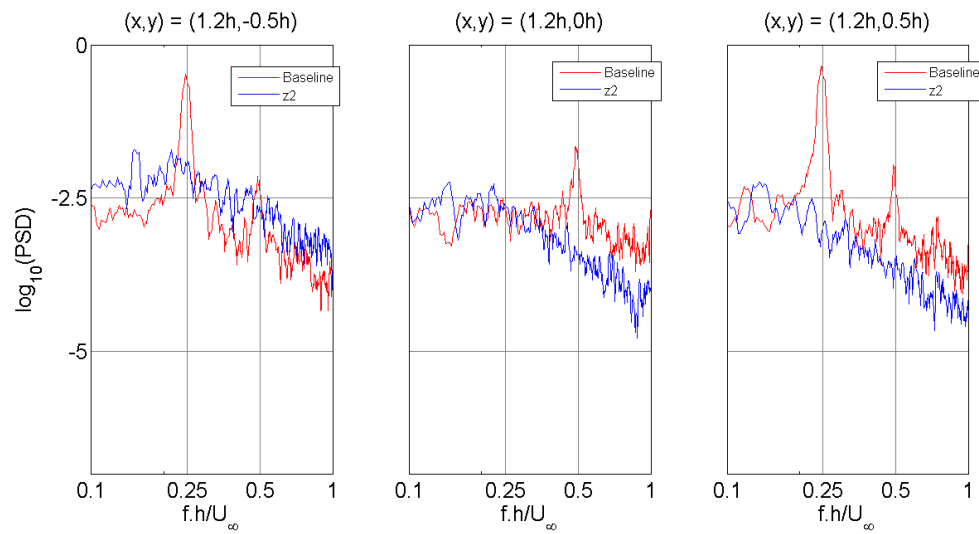


Figure 5.51: Streamwise velocity PSD for transverse staggered actuation with $\lambda^* = 5$ and $U_\infty = 5$ m/s at $'z2'$ at the three points of interest in the wake, co-plotted along with the PSD of the baseline flow case

POD Analysis

The first two POD modes of the flow for transverse staggered actuation with $\lambda^* = 5$ and $U_\infty = 5$ m/s at $'z1'$ are visualised in Fig. 5.53. To make comparison easier, the baseline flow POD mode visualisations are shown in Fig 5.52. Organised structures can be identified in the visualisations, albeit much weakened compared to the baseline case. The modes at $'z2'$, shown in Fig. 5.54 show significant weakening and disarray in the coherent structures, which indicates low energy content and consequently successful suppression. Also, they are thrown further downstream away from the base of the model.

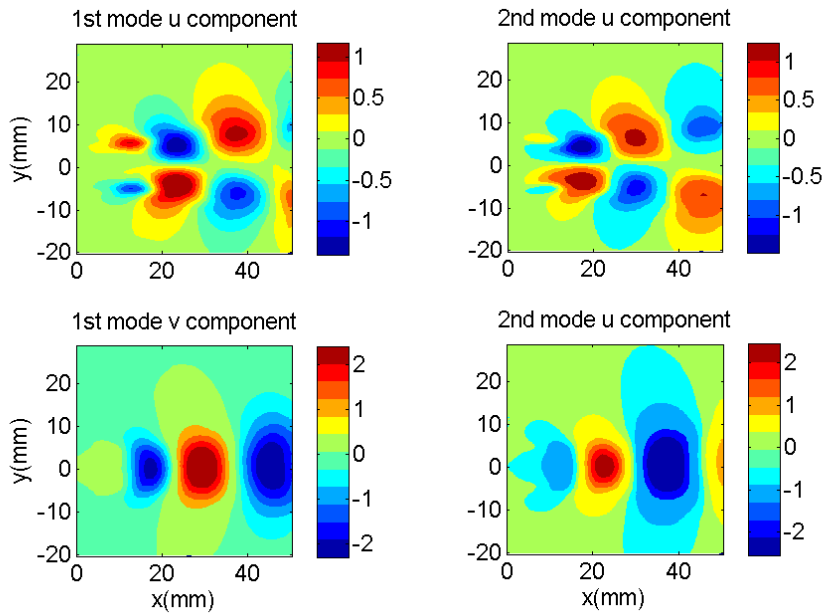


Figure 5.52: Velocity fields in m/s for baseline flow at $U_\infty = 5$ m/s

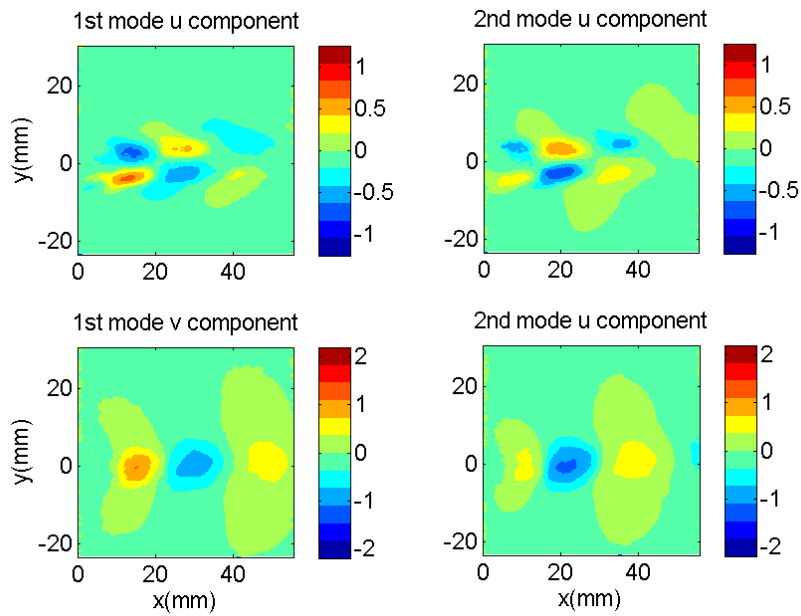


Figure 5.53: Velocity fields in m/s for the first two POD modes for transverse staggered actuation with $\lambda^* = 5$ and $U_\infty = 5$ m/s at 'z1'

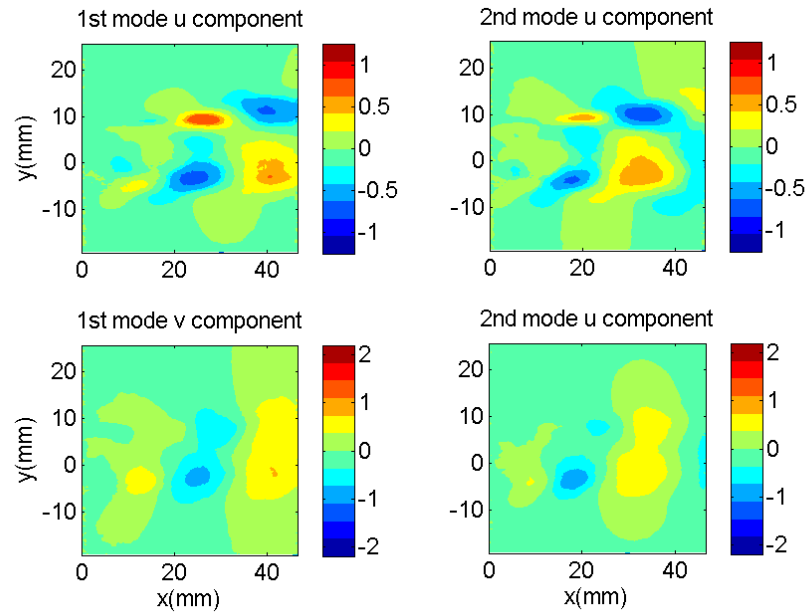


Figure 5.54: Velocity fields in m/s for the first two POD modes for transverse staggered actuation with $\lambda_* = 5$ and $U_\infty = 5$ m/s at ' z_2 '

The plot showing the energy content of the first ten modes for the present considered mode at $\lambda = 5h$ at $U_\infty = 5$ m/s is shown in Fig. 5.55. As mentioned earlier, the lower the energy in the first two POD modes, the more successful the suppression of Karman vortex shedding. The baseline un-actuated flow modal energies are also shown, so that a comparison can easily be made to determine the degree of success of the actuation in each case and for each spanwise location based on the level to which the energy share of the first two POD modes is reduced to. It can be seen that the suppression is stronger at ' z_2 ' than at ' z_1 '. This could be attributed to the higher degree of transverse asymmetry between the interacting shear layers at ' z_2 ' than at ' z_1 ', preventing the shedding of coherent Karman-like vortical structures.

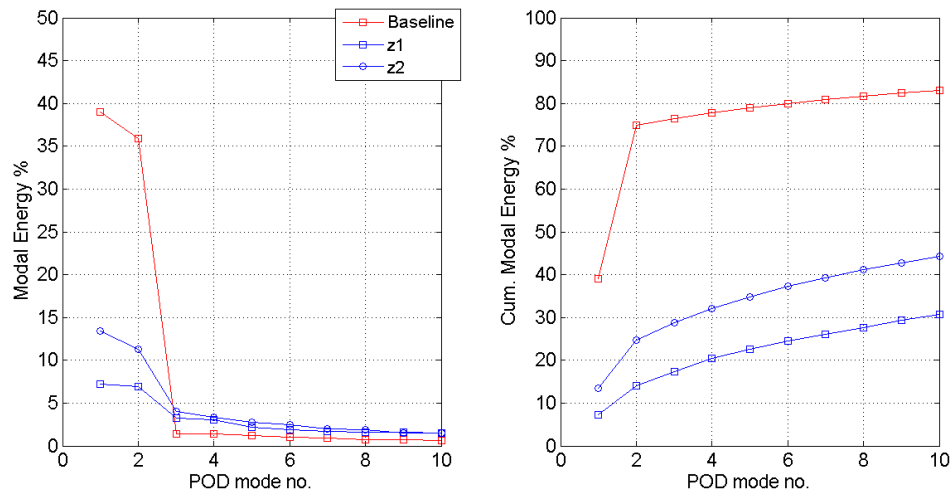


Figure 5.55: Individual and cumulative shares of the Fluctuating KE of the wake captured by the first ten POD modes of flow with spanwise modulated transverse staggered actuated flow with $\lambda = 5h$ at $U_\infty = 5$ m/s

Transverse Planes

The wake flow in the transverse $x - z$ plane located at $y = 0.5h + 2$ mm was imaged and measured by time-resolved PIV for spanwise modulated staggered actuation. The wake centerline transverse $x - z$ plane located at $y = 0$ could unfortunately not be measured. Based on the results and mechanism of spanwise modulated transverse opposing actuation, however, it can be guessed that streamwise and perhaps spanwise vorticity will be generated by the actuation-induced flows for this mode as well. An expected actuation mechanism is proposed in Sec. 5.6.1. From the $x - y$ planes imaged at the two spanwise locations for this mode ' $z1$ ' and ' $z2$ ', it was seen that the wake topology at these locations is significantly different. Hence, one can expect that the wake topology will also be significantly altered and modulated along the span compared. The exact shape of the envelope of the shedding locations, however, is not known due to the non-availability of imaged data in the wake centerline transverse plane. Looking at the mean flow velocity maps in the shear layer plane in Fig 5.56, no significant flow features can be seen. Considering the streamwise velocity map, one can conclude that the shear layer lift-up on the side without an exposed electrode segment on the surface, which was seen in Figs 5.45 and 5.48 is not strong enough to transport the low velocity fluid in the inner wake to the outer flow as far as the transverse location of the $x - z$ plane which was imaged by the PIV (2 mm above upper trailing edge surface). Hence, the lift-up in this actuation mode is weaker than for the opposing actuation mode. This will be analysed in Sec. 5.6.1 where the differences in the induced flow effects between these two modes will be discussed.

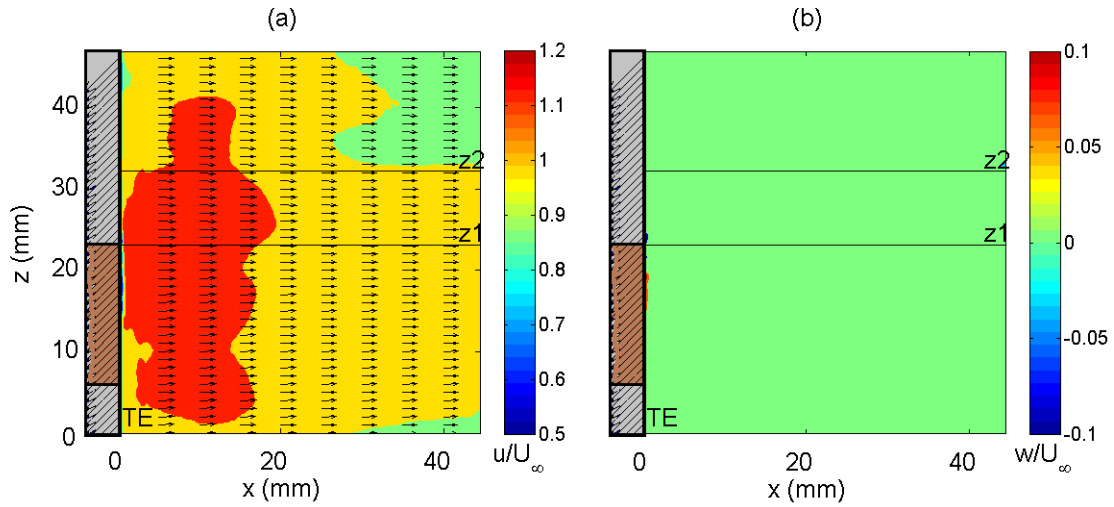


Figure 5.56: Time-averaged and normalised (a) streamwise and (b) spanwise velocity fields in the shear layer plane for transverse staggered actuation with $\lambda^* = 3$ and $U_\infty = 8$ m/s. The exposed electrode segments are also indicated in brown

As before, the confirmation that the Karman shedding has been suppressed along the span due to the modulated spanwise actuation can only be obtained through an analysis of the spanwise coherence in the streamwise velocities. The result is shown in Fig 5.57. Fig 5.57(a) shows the twenty spanwise points along the six fixed streamwise positions at $x/h = 0.5, 1, 1.5, 2, 2.5$ and 3 where the streamwise velocity time signals were gathered from the time resolved PIV velocity fields. With a point at 'z1' as the reference point, the correlation coefficients of the velocity signal at this point with the other points are plotted against the spanwise location of these points in Fig. 5.57(b). As for the transverse opposing mode, it is seen that the correlation coefficients fall off quite rapidly to low values away from the reference point along the span, when compared to the baseline flow case in Fig 5.12. This indicates that the actuation is responsible for the breakage of the spanwise coherence of the shed Karman rolls, and hence vortex shedding suppression. The spanwise correlations of the various spanwise modulated staggered opposing actuation flow cases over all the tested U_∞ cases are shown in App. H.

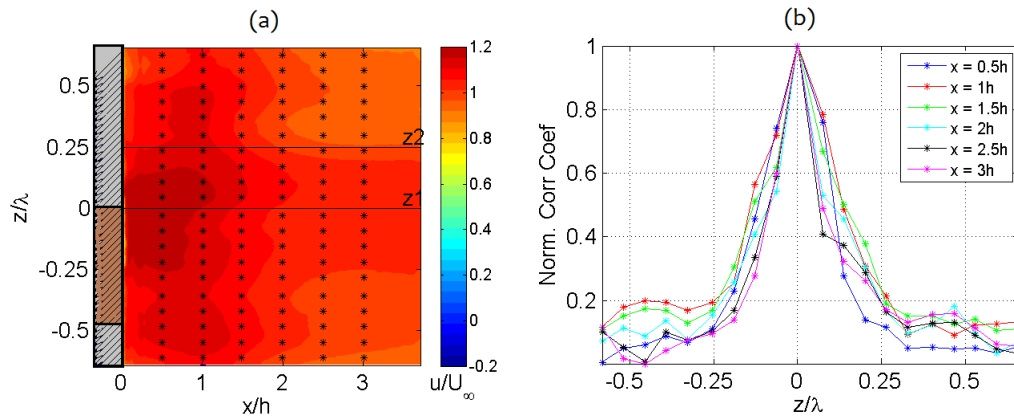


Figure 5.57: Wake shear layer $x - z$ plane (a) mean streamwise velocity map showing correlation points and (b) spanwise correlation coefficients for spanwise modulated transverse staggered actuation with $\lambda^* = 3$ at $U_\infty = 5$ m/s. The exposed electrode segments are also indicated in brown

5.6.1 Proposed Actuation Mechanism

As was done in Sec. 5.5.1, the mechanism of actuation must be constructed using the flow features and results shown in the sections above as 'clues'. It must be able to explain these features as well as be physically plausible from the point of view of flow and actuator physics. The following are the 'clues' that will be used to construct the model for the spanwise modulated staggered actuation mode:

1. A 'pushing-in' of the shear layers at spanwise location ' $z1'$ ' to give a narrow wake.
2. A lift-up of the shear layer on the side with no plasma actuator at that spanwise location at ' $z2'$ '.

The model that explains the above features is shown in Fig. 5.58. Due to the lack of velocity field data from the wake centerline plane, the amount of available information to construct the model is unfortunately reduced. However, using the mechanism for transverse opposing actuation in Sec. 5.5.1 and Fig. 5.42 and some educated extrapolation, it is still possible to construct a plausible model for this actuation mode. At $t = 0$, the start time instant of actuation, the forcing will be as shown in Fig. 5.42(A), only along the y direction. As for transverse opposing actuation, the presence of alternating regions of transverse forcing and no-forcing along the span on one side of the trailing edge will induce spanwise flows as shown in Fig. 5.42(B). Streamwise circulation will be set up as shown in Fig. 5.42(C) with counter rotating vortices having a common flow at the ' $z2'$ ' location giving rise to a shear-layer lift up one side (shown in orange) as seen earlier. These spanwise flows will give rise to transverse vorticity ω_y at and around the exposed electrode-no electrode interface regions. As seen in the case of the transverse opposing actuation mode at the ' $z2'$ ' location, the near wake region especially close to the interfaces is a region where the various flow effects combine and interact - the spanwise flows, transverse vorticity interacting with the shear layer and significant transverse forcing shear. These factors induce the transition to turbulence in the shear layers, channel momentum from them inwards into the dead-water region and bend them inwards, giving a narrow wake. As seen in Fig. 5.42(B), the induced spanwise flows at the interfaces on either side of the wake centerline are symmetric but

in opposite directions. When imaged along the $x - y$ plane at these spanwise locations, however the flow appears symmetric with respect to the wake centerline, unlike at the ' z_2 ' locations.

The flows induced by the spanwise circulation on the upper and lower sides will be in opposite directions in the centerline plane and close to it, due to the staggering of the exposed electrode segments on these two sides. These oppositely-directed spanwise flows in the centerline plane will tend to weaken/cancel each other, hence the induced streamwise circulation will also be lower. This conclusion is supported by the fact that the shear layer lift-up for this actuation mode is not as strong as that seen for the transverse opposing actuation mode.

The success of spanwise modulated transverse opposing actuation rested on the conversion of the baseline spanwise vorticity to streamwise vorticity - the stronger the streamwise vorticity set up, the weaker the shear layers get and correspondingly the more the Karman shedding is suppressed. Since the streamwise vorticity set up by spanwise modulated staggered actuation is not as strong, one would imagine that this actuation mode is less successful in suppressing Karman vortex shedding. However, the POD and wake power spectrum results say otherwise. The success of this actuation mode hence depends more on the disruption of the transverse symmetry between the interacting shear layers than the setting up of streamwise vorticity. The streamwise vorticity that is set-up, weak though it is, is still strong enough to introduce significant dis-similarity between the shear layers at any spanwise location. Due to the strong transverse symmetry between the shear layers that is required for vortex shedding (Sec. 2.1.2, [10], etc.), the shear layers are too dis-similar along the span to give rise to Karman vortex shedding. As mentioned in the case of opposing actuation earlier in Sec. 5.5.1, the ability of the fixed-energy input actuation here in diverting momentum from the shear layers into streamwise vorticity and manipulating them reduces as U_∞ (and inflow momentum) increases. The vortex shedding performance of the actuation hence decreases as U_∞ increases.

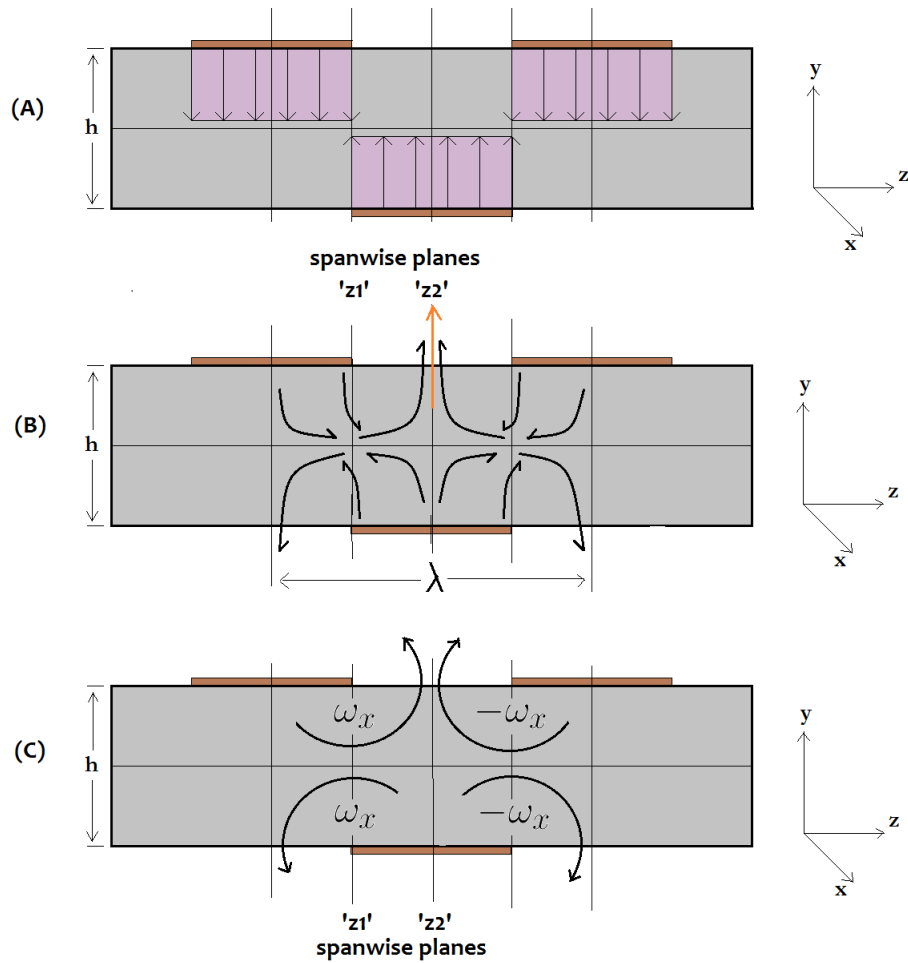


Figure 5.58: Schematic of proposed actuation mechanism for spanwise modulated transverse staggered actuation - (A) actuator forcing, (B) induced flows and (C) induced vorticity

5.7 Spanwise Actuation

For spanwise actuation, the expected forcing scheme is as shown in Fig 5.59. The spanwise $x - y$ planes images are as follows:

1. The middle of the region between two exposed electrode segments; $z = z_1$.
2. Over an exposed electrode segment and displaced by $\lambda/2$ along the span from z_1 ; $z = z_2$.

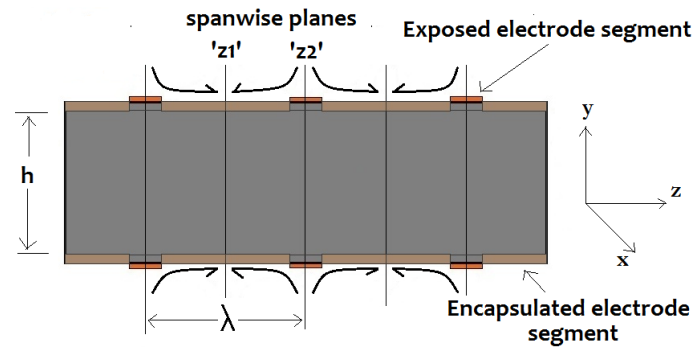


Figure 5.59: Schematic showing the electrodes, induced forcing and imaged $x - y$ planes for the spanwise actuation mode

The actuation principle of spanwise actuation is in using plasma actuators placed along the span in the streamwise direction to create spanwise jets that 'lift-up' when they converge. The use of opposing plasma induced flows to create a jet here is similar to that in Benard [2], Henneval [16], etc. These jets are formed within the incoming boundary layer, hence the flow is manipulated before separation itself over a length equal to the length of the streamwise length of the actuators. The alternate regions of lift-up and downward flow along the span, located at the appropriate spatial wavelength, are expected to introduce significant spanwise discontinuities in the shear layers as they separate and get shed into von Karman vortex rolls. The flow in the wake was imaged and measured using time-resolved PIV at two spanwise $x - y$ planes in a spatial cycle of actuation, located at the middle of the covered electrode (denoted ' $z1'$ ') and exposed electrode (denoted ' $z2'$ ') respectively. The results shown in this section will concern the configuration with actuation spatial wavelength $\lambda/h = \lambda^* = 2$. As for the spanwise modulated transverse actuation case, the results will be organised into the following categories for each of the imaged spanwise $x - y$ planes:

1. instantaneous vortical structures
2. statistical flow fields of the actuation-induced flow
3. power spectra at selected points in the wake
4. POD analysis
5. Analysis of transverse ($x - z$) planes imaged

Instantaneous Vortical Structures

A sequence of instantaneous vortical structures at a time-spacing of $\Delta t = 0.75$ ms and $\Delta t^* = \Delta t \times U_\infty/h = 0.32$ is shown in Fig. 5.60. It can be seen that the shear layers were thrown far apart. However, weak secondary channels of vorticity from either side of the model were bent inwards towards each other close to the base and interact in a highly turbulent manner. The interaction between these 'secondary vorticity channels' gave rise to small, incoherent turbulent vortical structures that convected randomly downstream.

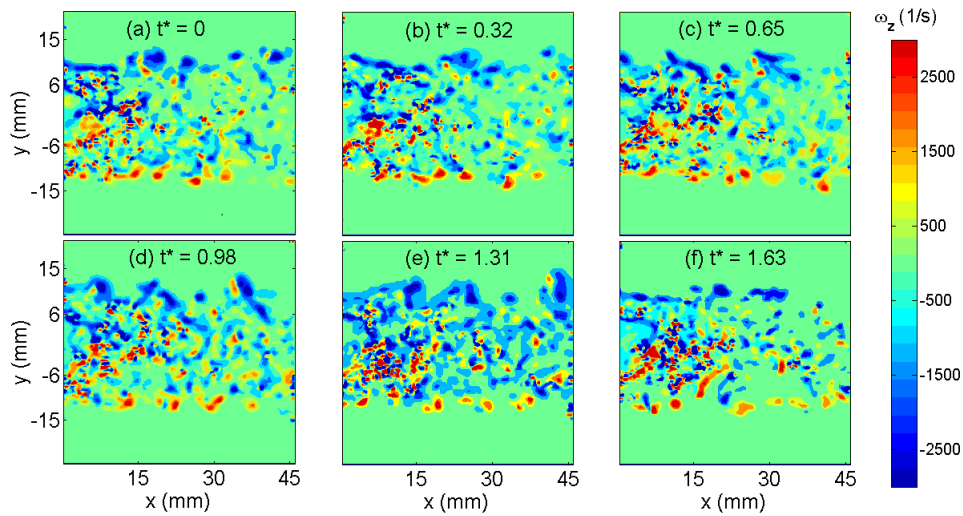


Figure 5.60: Sequence of instantaneous vorticity fields in wake for spanwise actuation with $\lambda^* = 2$, $U_\infty = 5$ m/s at ' $z1$ ' with a non-dimensionalised time-spacing of $\Delta t^* = \Delta t \times U_\infty / h = 0.32$

At location ' $z2$ ' the shear layers were bent inwards towards each other under the influence of the induced flow which is oriented towards the wake centreline from either side at that spanwise location. The interaction between them gave rise to small, concentrated vortical structures compared to the baseline flow case. A weak periodicity in the vortical structures formed as they convect downstream can be identified, nevertheless.

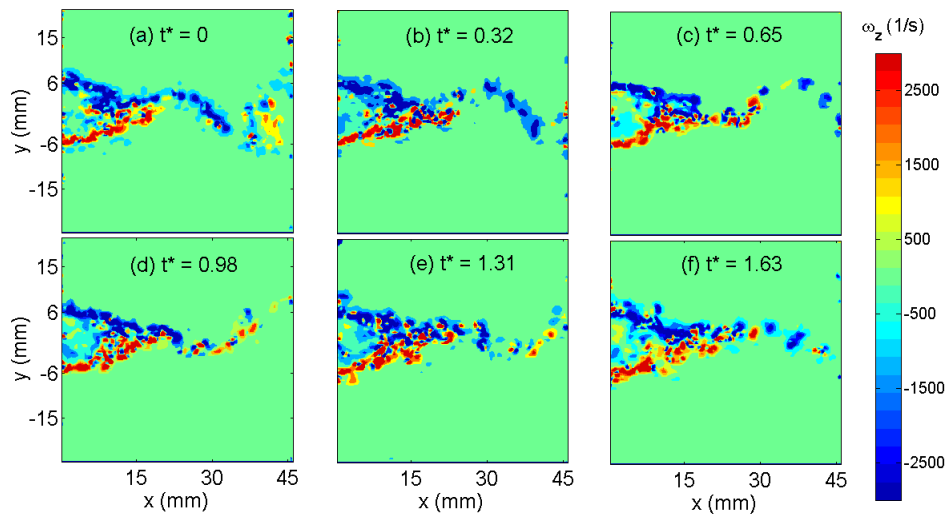


Figure 5.61: Sequence of instantaneous vorticity fields in wake for spanwise actuation with $\lambda^* = 2$, $U_\infty = 5$ m/s at ' $z2$ ' with a non-dimensionalised time-spacing of $\Delta t^* = \Delta t \times U_\infty / h = 0.32$

Statistical Characterisation of the Flow Field

In the statistical velocity fields at ' $z1$ ' seen in Fig. 5.62, the streamwise velocity defect region is large, caused undoubtedly by a 'lift-up' of the shear layers. As was seen for the case of streamwise forcing with $\lambda = 5h$ at $z1$, alternate regions of positive and negative velocity are seen in the transverse velocity field v/U_∞ in a symmetric manner on either side of the centreline. The reason is again quite similar – at the height of a few mm above the upper and lower surfaces, the tendency of the shear layers to spread outwards due to the lift up caused by the actuation at this location counteracted and overpowered their tendency to move inwards towards the wake centreline. However, the normative tendency of the shear layers to move inwards was regained closer to the surfaces and in the near wake. The transverse velocity fluctuation map v'/U_∞ indicates much reduced fluctuations compared to the baseline flow case in Fig. 5.9, indicating a suppression of the regular transverse periodic velocity fluctuations associated with Karman shedding. The streamlines of the average flow in Fig 5.63 shows a reattachment point at $x = 12$ mm for the shear layers with counter-rotating recirculation bubbles smaller than that at ' $z2$ ' (Fig 5.65) and the baseline case. This indicates that the portion of the shear layers flowing inwards and recirculating was small, and that the larger portion was lifted up and moved away from the wake centerline.

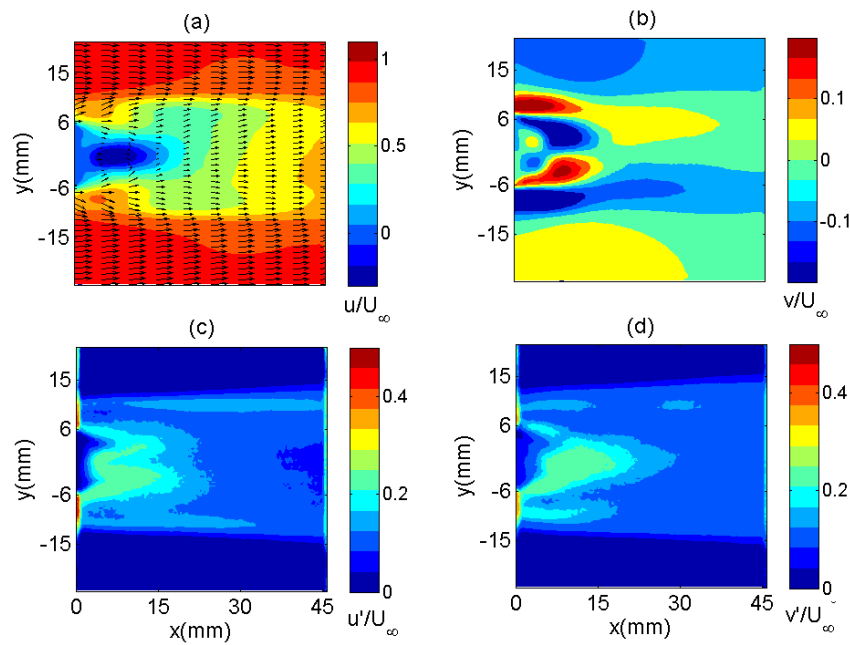


Figure 5.62: Statistical normalised velocity fields: (a) u/U_∞ (b) v/U_∞ (c) u'/U_∞ and (d) v'/U_∞ for spanwise actuation with $\lambda^* = 2$ and $U_\infty = 5$ m/s at ' $z1$ '

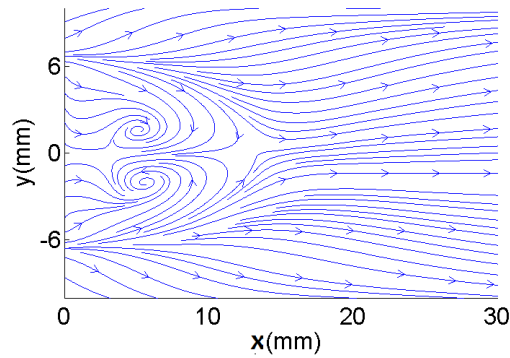


Figure 5.63: Near wake mean flow streamlines at spanwise location ' z_1 ' for spanwise actuation with $\lambda^* = 2$ and $U_\infty = 5$ m/s

At location ' z_2 ', Fig. 5.64, the plasma induced downward flow caused the shear layers to bend inwards, thinning the wake. The effect of the induced downward flow is reflected in the stronger transverse flows taking place in the regions on either side of the centreline, compared to the canonical case. The transverse velocity fluctuation map v'/U_∞ shows a region of relatively intense fluctuations (albeit weaker than that of the baseline flow). The streamlines at this location in Fig. 5.65 show large, prominent recirculating bubbles indicating a strong tendency of the shear layers to move inwards towards the wake centerline, under the influence of the downward flow.

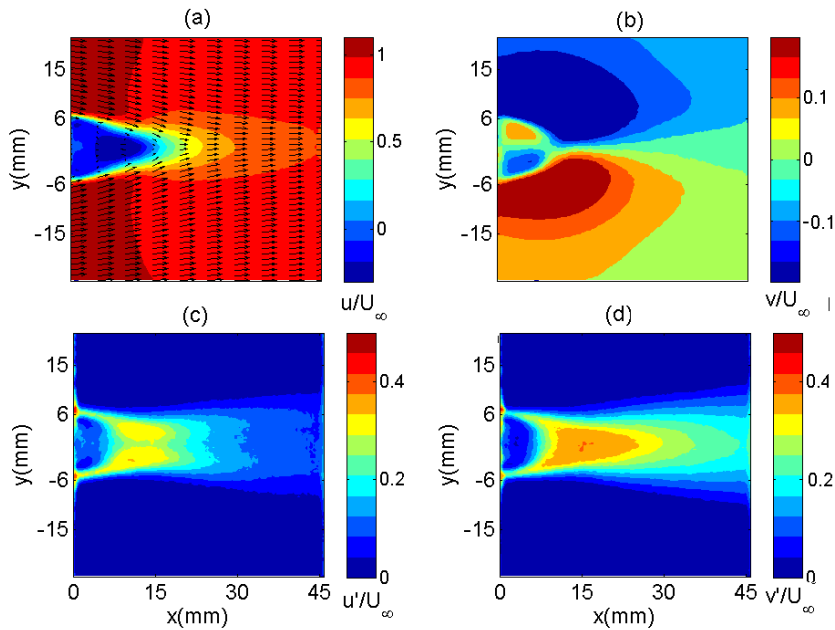


Figure 5.64: Statistical normalised velocity fields: (a) u/U_∞ (b) v/U_∞ (c) u'/U_∞ and (d) v'/U_∞ for spanwise actuation with $\lambda^* = 2$ and $U_\infty = 5$ m/s at ' z_2 '

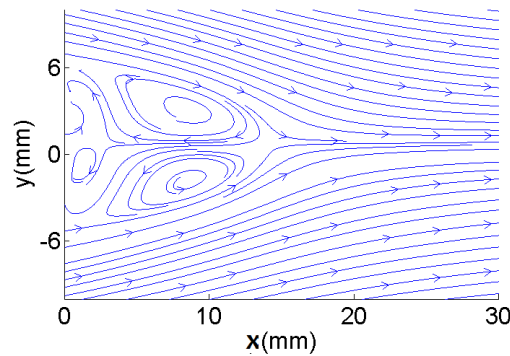


Figure 5.65: Near wake mean flow streamlines at spanwise location ' $z2$ ' for spanwise actuation with $\lambda^* = 2$ and $U_\infty = 5$ m/s

Wake Spectra

At the ' $z1$ ' and ' $z2$ ' spanwise locations for spanwise actuation, the streamwise velocity at the three points of interest located along the shear layers and wake centerline are collected and the Power Spectral Densities (PSD's) are found for these time signals and plotted against the non-dimensionalised frequency, the St in Figures 5.66 and 5.67. As before, the baseline flow PSD is co-plotted as a reference for comparison. At $z1$, no peaks are seen over the power spectra, hence one can say that the periodicity in the wake has been suppressed. At $z2$, weak peaks do exist in the power spectra at the points, but at a frequency higher than the shedding frequency in the baseline case.

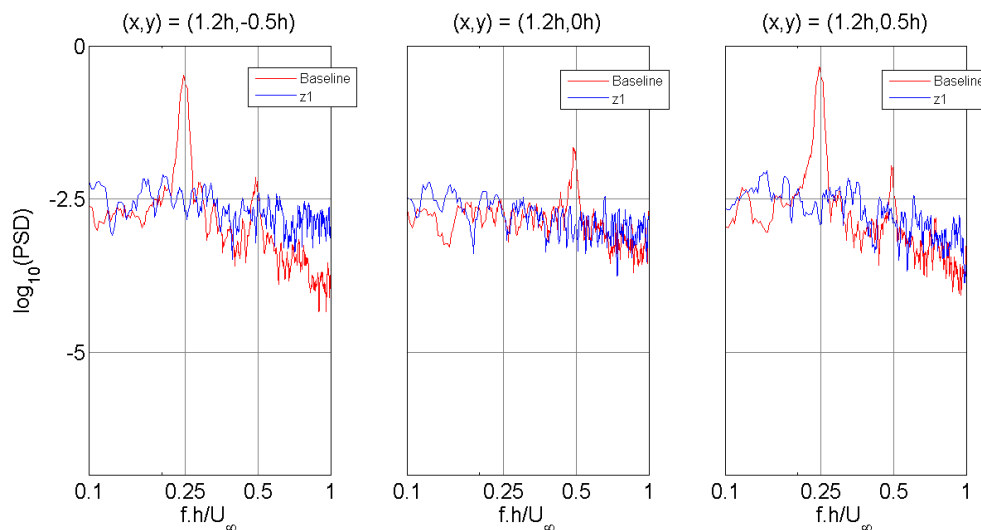


Figure 5.66: Streamwise velocity PSD for spanwise actuation with $\lambda^* = 2$ and $U_\infty = 5$ m/s at ' $z1$ ' at the three points of interest in the wake, co-plotted along with the PSD of the baseline flow case

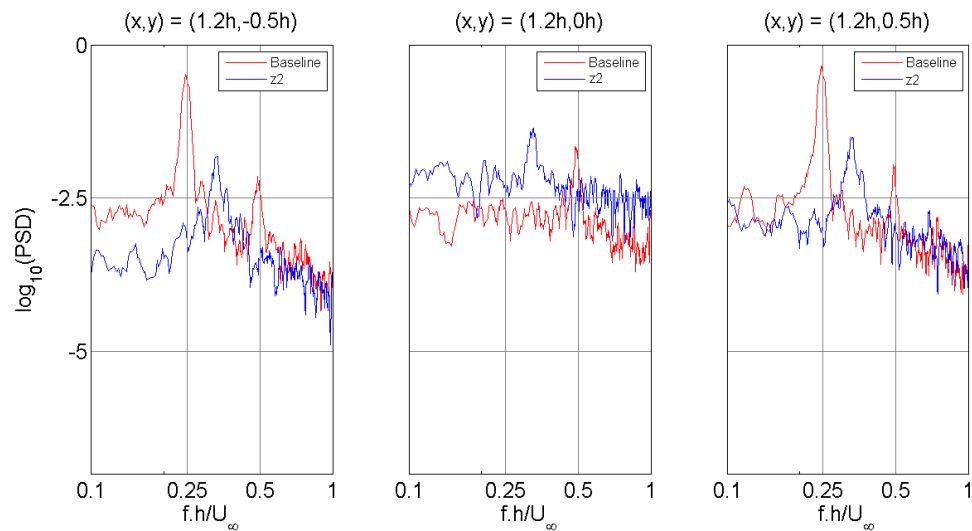


Figure 5.67: Streamwise velocity PSD for spanwise actuation with $\lambda^* = 2$ and $U_\infty = 5$ m/s at ' $z2$ ' at the three points of interest in the wake, co-plotted along with the PSD of the baseline flow case

POD Analysis

The velocity fields for the first two POD modes are visualised in Figs. 5.69 and 5.70 for spanwise locations ' $z1$ ' and ' $z2$ ' respectively. To make comparison easier, the baseline POD structures visualised are also shown in Fig 5.68. It is clear that the modes are much weaker at ' $z1$ ' compared to the baseline flow case. This lack of visible coherent structures in the velocity field indicates a suppression in the modes corresponding to Karman vortex shedding. At ' $z2$ ' the alternating regular coherent structures can be identified, but they are still weaker compared to those in the the baseline case. Their presence however indicates a presence of periodicity in the wake flow, as was seen in the instantaneous vortical structures in Fig 5.61 earlier.

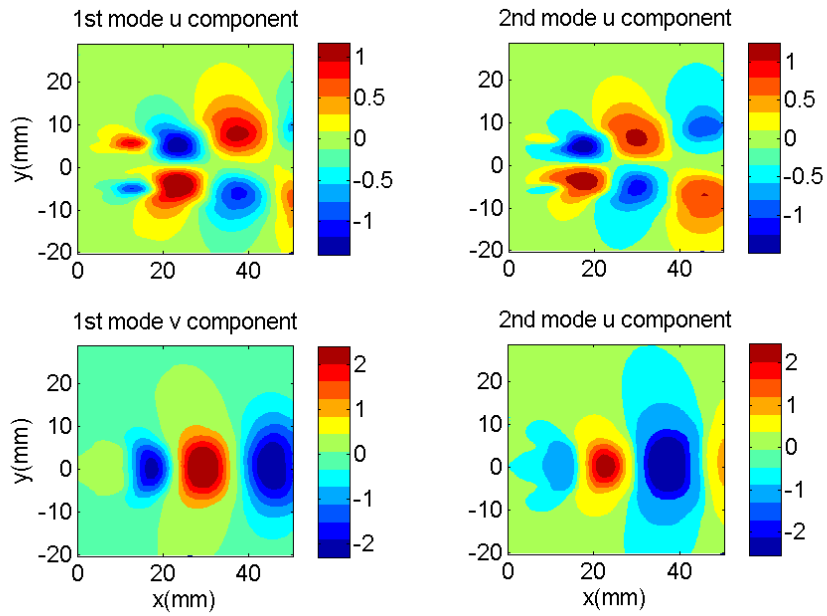


Figure 5.68: Velocity fields in m/s for the first two POD modes visualised the $U_\infty = 5$ m/s baseline flow case

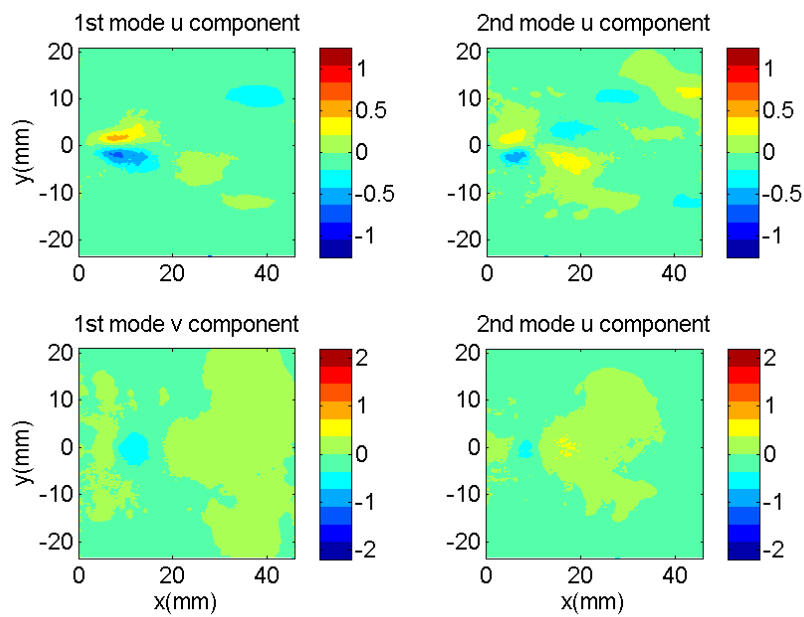


Figure 5.69: Velocity fields in m/s for the first two POD modes for spanwise actuation with $\lambda^* = 2$ and $U_\infty = 5$ m/s at 'z1'

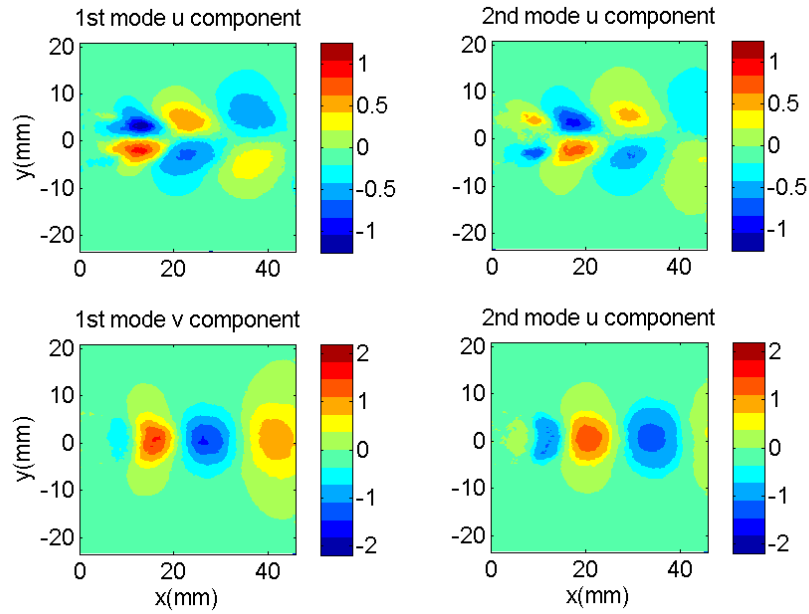


Figure 5.70: Velocity fields in m/s for the first two POD modes for spanwise actuation with $\lambda^* = 2$ and $U_\infty = 5$ m/s at ' z_2 '

The modal energy shares for the first five POD modes for the present actuation mode over all the tested configurations $\lambda^* = 2, 3$ and 4 are shown in Fig 5.71. The corresponding baseline flow energies are also shown. It can be seen that the energy share of the first two modes at the ' z_2 ' spanwise location in an actuation spatial cycle is relatively independent of the spanwise λ^* of actuation. This is to be expected as the wake at ' z_2 ' is dominated by the effect of the plasma-induced downward flow, the strength of which is independent of the λ^* for the experiments conducted in this work. The energy share of the modes at ' z_1 ' however, are dependant on the λ^* of actuation. At ' z_1 ' the wake is dominated by the lift-up of the shear layers caused by the flow-up of the converging plasma-induced spanwise jets, see Fig. 5.74. The stronger the lift-up, the more the shear layers are thrown apart, the weaker their mutual interaction and stronger the vortex shedding suppression. Naturally, the stronger the jets are at the point when they converse, the stronger the lift-up. From the dielectric parametric study in Sec 5.1 it was seen that the plasma induced jet is strong upto 15 mm downstream of the electrode interface, and it can be expected that they get weaker further away. For $\lambda = 2, 3$ and 4, the distances the induced jets have to cover before they cover are respectively $1h, 1.5h$ and $2h$, i.e. 12 mm, 18 mm and 24 mm. It is hence natural that the lift-up and consequently the shedding suppression deteriorates as this distance is increased. This is reflected in the higher energy share of the first two POD modes for $\lambda^* = 4$.

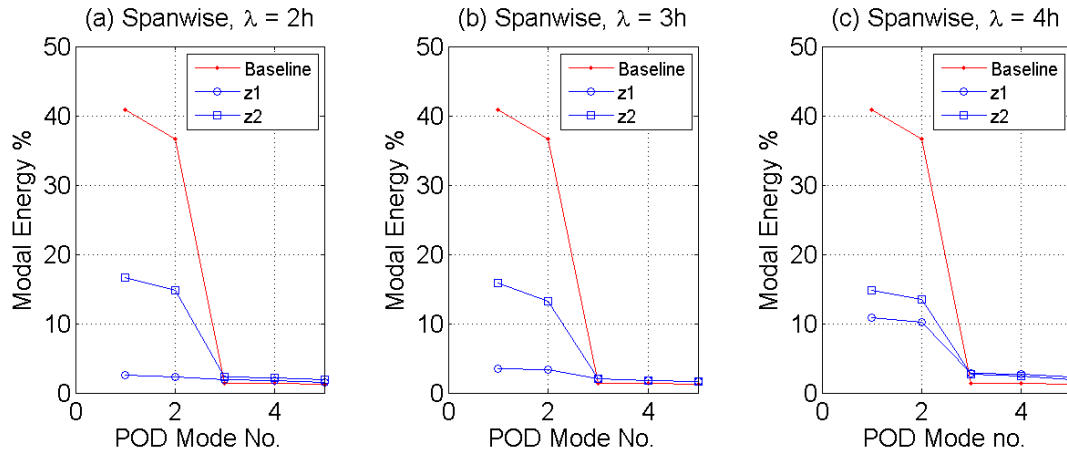


Figure 5.71: Individual shares of the Fluctuating KE of the wake $x - y$ plane captured by the first five POD modes for spanwise actuation configurations $\lambda^* = 2, 3$ and 4 over all imaged planes at $U_\infty = 5$ m/s. The reference baseline flow value is also shown

Transverse Planes

The wake flow in the transverse $x - z$ plane located at $y = 0.5h + 2$ mm was imaged and measured by time-resolved PIV for spanwise actuation. The wake centerline transverse $x - z$ plane located at $y = 0$ could unfortunately not be measured. The mean flow results are shown in Fig. 5.72(a). The streamwise velocity map shows clear, narrow regions of low velocity in the shear layer plane at the ' $z2$ ' spanwise locations. The low velocity fluid at these locations indicates that the imaged plane cuts through the wide wake formed by the shear layers being 'lifted-up' away from the wake centerline. The effect of the actuation can even be seen before the trailing edge, indicating that the spanwise forcing acts on the boundary layers before they separate. The merging of the opposing spanwise jets from either side at the ' $z2$ ' locations created a lift up within the boundary layer. This lift-up continues beyond the separation itself, where the lifted-up boundary layers continue to convect downstream as widely separated shear layers on either side. This is to be expected, based on the results and mechanism of the streamwise oriented spanwise forcing actuators perpendicular to the inflow laid out as a CtR VG array in [20]. Correspondingly, at the ' $z1$ ' locations, the shear layers after separation are seen to be accelerated in the streamwise direction, due to the influence of the flow depression above the exposed electrode segments that 'charges' the spanwise jets. This flow depression is channeled by the inflow in the streamwise direction, increasing the momentum of the shear layers at this location. As seen earlier, this flow depression is responsible for pushing the shear layers inwards and creating a narrow, reduced wake velocity deficit region. The alternate lift-up and flow down will give rise to streamwise vorticity, as shown in Fig. 5.74(C). The spanwise flow map Fig. 5.72(b) does not indicate clear, flow patterns. This too can be expected, as the shear layer plane imaged here is 2mm above the surface of the model, at which height the plasma induced flows can be expected to be negligible. The spanwise forcing from the streamwise oriented actuators will have their maximum effect closer to the surface, since the peak plasma-jet occurs at $\simeq 0.5$ above the surface [26].

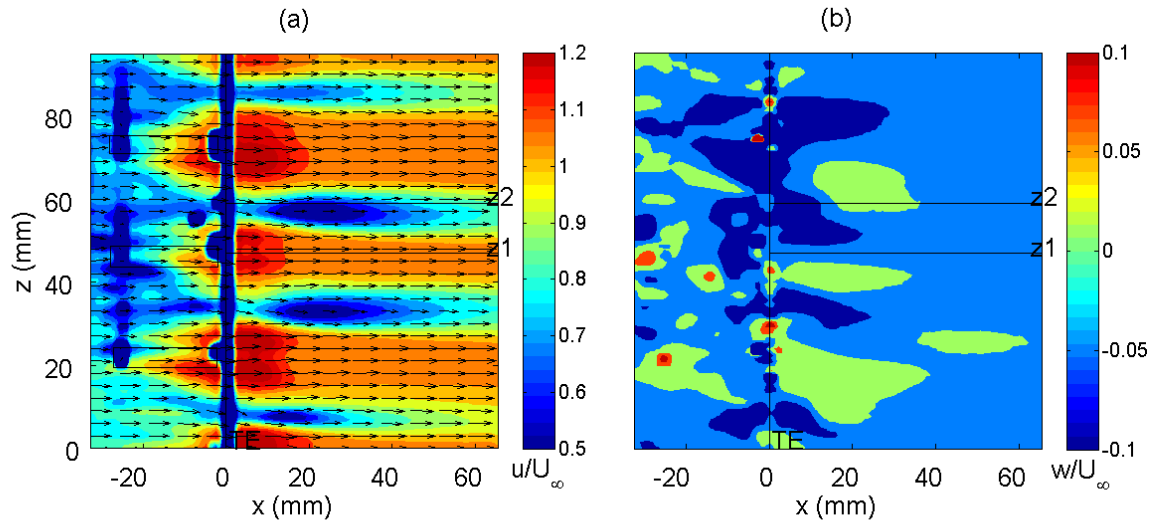


Figure 5.72: Time-averaged and normalised (a) streamwise and (b) spanwise velocity fields in the shear layer plane for spanwise actuation with $\lambda^* = 2$ and $U_\infty = 5$ m/s

As before, the confirmation that the Karman shedding has been suppressed along the span due to the modulated spanwise actuation can only be obtained through an analysis of the spanwise coherence in the shed vortices across the span. This can be done by analysing the correlation between the streamwise velocities along the span. The result is shown in Fig 5.73. Fig 5.73(a) shows the twenty spanwise points along the six fixed streamwise positions at $x/h = 0.5, 1, 1.5, 2, 2.5$ and 3 where the streamwise velocity time signals were gathered from the time resolved PIV velocity fields. With a point at the ' $z1$ ' spanwise as the reference point, the correlation coefficients of the velocity signal at this point with the other points are plotted against the spanwise location of these points in Fig. 5.73(b). As for the other actuated modes seen so far, it is seen that the correlation coefficients fall off quite rapidly to low values away from the reference point along the span, when compared to the baseline flow case in Fig 5.12. Multiple actuation spatial wavelengths λ are imaged in the FOV in Fig. 5.73(a), but it is clear that the correlation coefficients do not show local maxima at intervals of λ . This indicates that the actuation is responsible for the breakage of the spanwise coherence of the shed Karman rolls, and hence vortex shedding suppression. The mechanism by which this occurs is explained in Sec. 5.7.1. The spanwise correlations of the various spanwise actuated flow cases over all the tested U_∞ cases are shown in App. H.

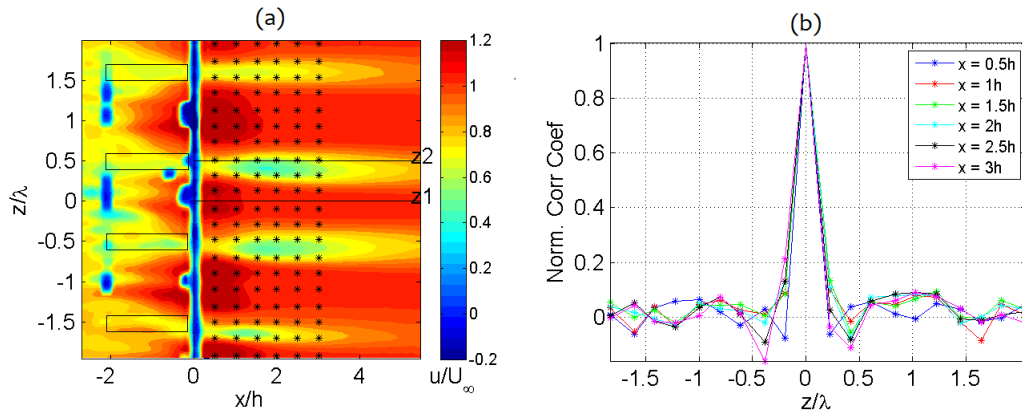


Figure 5.73: Wake shear layer $x - z$ plane (a) mean streamwise velocity map showing correlation points and (b) spanwise correlation coefficients for spanwise actuation with $\lambda^* = 2$ at $U_\infty = 5$ m/s. The exposed electrode segments are also indicated

5.7.1 Proposed Actuation Mechanism

As was done earlier, the mechanism of actuation must be constructed using the flow features and results shown in the sections above as 'clues'. It must be able to explain these features as well as be physically plausible from the point of view of flow and actuator physics. The following are the 'clues' that will be used to construct the model for the spanwise actuation mode:

1. A lift-up of the shear layers at spanwise location at ' $z1$ ' to give a broad wake.
2. A 'pushing-in' of the shear layers at spanwise location ' $z2$ ' to give a narrow wake.

A proposed physical model that accounts for the above features is shown in Fig 5.74. The mechanism by which the lift-up and down-flow (shown in red and blue respectively in Fig 5.74(B)) are generated, as explained in [16] where a similar actuator layout is used is as follows - plasma is created above the covered electrode (in the region between exposed electrode segments) and exerts a body force on the air, accelerating it along the surface away from the exposed electrode. When jets directed away from two adjacent exposed electrodes converge above the middle of the covered electrode at ' $z1$ ' a stagnation point is created. Since the jets can only move in the upward direction, a lift-up is created at this location. This pushes the separating shear layers away from the wake centerline at the trailing edge. To ensure actuation mass balance, the air that is channeled by the actuation in the spanwise direction is taken from above the exposed electrodes, at ' $z2$ '. Hence a depression will be created in this region. The air that flows downwards here is responsible for pushing the shear layers inwards and narrowing the wake. Unlike in the case of transverse actuation where the actuation takes its effect on the shear layers only at and beyond the model base, the actuation in this case takes place all over the streamwise length of the electrodes. Hence in this case the actuators act on the boundary layers before they separate, as was seen in Fig. 5.72(a).

An array of counter-rotating spatially fixed streamwise vortices were created as shown in Fig. 5.74(C). The spatial pitch of one such vortex-pair was equal to the spatial actuation wavelength λ . The actuator layout and mechanism by which the vortex array was created was very similar to that in Jukes and Choi [20], where plasma actuators were used as VG's in flow separation control.

As explained in that work, the creation of streamwise circulation commences at the upstream end of the actuator. The oncoming boundary layer fluid was primarily sucked towards the wall into the plasma, then accelerated in the spanwise direction and lifted up. With increasing free stream U_∞ and inflow momentum, it became more difficult for the actuation to deflect the inflow perpendicular to itself, hence the circulation created was also expected to fall.

The streamwise vorticity that was generated here was directly due to the plasma induced jets, unlike in the case of spanwise modulated transverse opposing actuation where the forcing gave rise to the streamwise vorticity in a more indirect manner. In the case of spanwise actuation, the spanwise vorticity of the shear layers did not transfer its energy or get converted into streamwise vorticity. Instead, it was the modulation of the interacting shear layers along the span that was responsible for breaking up the two-dimensionality in the vortex shedding. The alternate lift-up and depression along the span gave rise to a significant variation in the interacting shear layers along the span as shown in Fig 5.74(D). This meant that their interaction at different spanwise positions was uncorrelated.

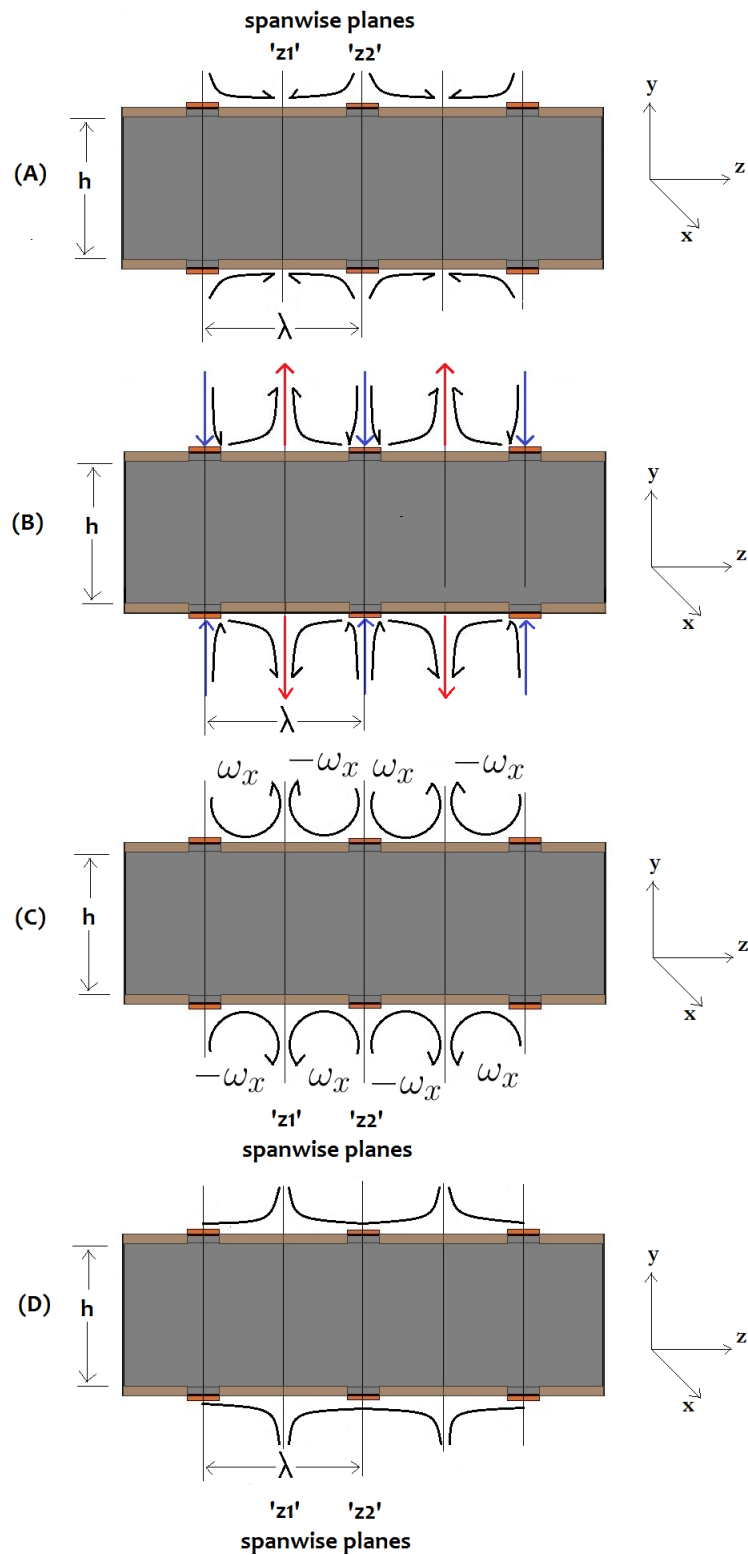


Figure 5.74: Schematic of proposed actuation mechanism for spanwise modulated transverse opposing actuation - (A) actuator forcing, (B) induced flows (C) induced streamwise vorticity and (D) shear layer modulation

5.8 Statistical Flow Quantities for representative actuation configurations

This section contains quantitative, statistical information regarding the effect of the three spanwise modulated actuation modes tested on the flow in the wake obtained from the statistical flow fields. Table 4.5 lists the tested actuation modes and configurations at the free stream of $U_\infty = 5$ m/s, the results of which were described in the previous sections for representative cases. The following quantities calculated from the statistical flow fields were used to obtain deeper insights into the effect of the spanwise modulated actuation modes on the wake flow:

1. Wake Fluctuating turbulent kinetic energy (TKE), calculated from the RMS fluctuating flow fields at the various imaged $x - y$ planes;
2. Wake velocity deficit area, calculated from the mean flow fields at the various imaged $x - y$ planes.

The calculated information contained here will be displayed graphically for the various actuation. It must be kept in mind that *due to the significantly different actuation induced flow mechanisms of these modes, they must not be compared directly solely on the basis of these quantities*. Instead, the objective behind showing the various plots together is to present this information in one place.

Wake Fluctuating TKE

The kinetic energy of the velocity fluctuations per unit mass is determined by the summation of the individual contribution of each velocity vector in the PIV field of view, multiplied by an area with sides equal to the spatial resolution:

$$TKE = \sum_{i=1}^{N_{vectors}} \frac{1}{2} \left((u'_i)^2 + (v'_i)^2 \right) \Delta x \Delta y \quad (5.5)$$

where u'_i and v'_i are the individual vectors in the fluctuating (RMS) velocity field. The TKE's of the opposing and staggered transverse actuation modes at the various spanwise imaged location in a spatial actuation cycle at $U_\infty = 5$ m/s are shown in Fig 5.75. The general trends in TKE for the transverse actuation modes at $U_\infty = 5$ m/s are:

- For the opposing mode, the TKE at the ' $z1'$ ' spanwise location was the least, indicating the least amount of organised fluctuating motion in the wake. At ' $z2'$ ', the TKE was lower than that of the baseline wake but higher than that at ' $z1'$ ', indicating that a small degree of organised fluctuations exist. At ' $z3'$ ' the TKE was around the same value as that of the baseline wake, indicating similar flow behaviour.
- For the staggered mode, the TKE at ' $z2'$ ' was the least, while that at ' $z1'$ ' was slightly higher but still lower than the baseline flow case. A possible inference from this is that organised fluctuating fluid flow like that which occurs with Karman vortex shedding was curbed over the entire span.

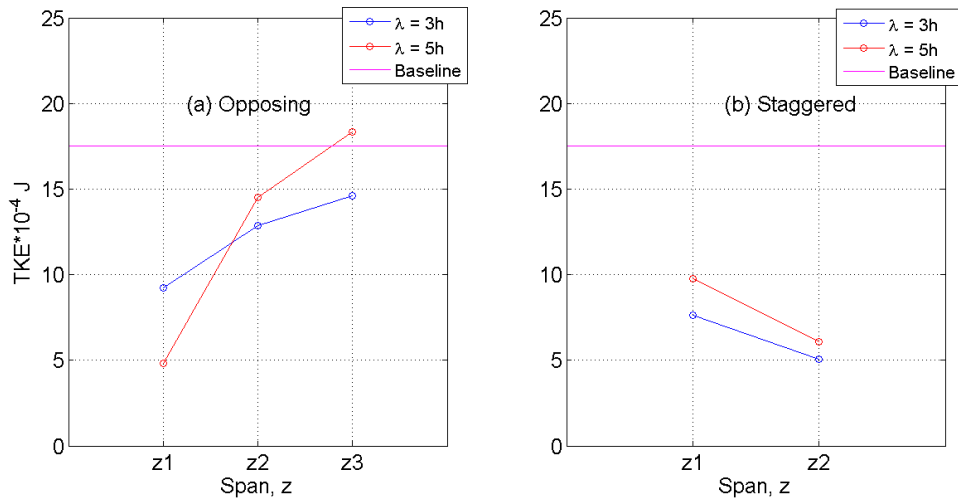


Figure 5.75: TKE's over all λ 's and spanwise locations for spanwise modulated transverse (a) opposing and (b) staggered actuation at $U_\infty = 5$ m/s. The baseline flow TKE is also indicated as reference

The TKE's of the tested spanwise actuation configurations at the various spanwise imaged location in a spatial actuation cycle at $U_\infty = 5$ m/s are shown in Fig 5.76. The general trends in TKE over the imaged spanwise locations are:

- Compared to the baseline un-actuated flow, the TKE at ' z_1 ' is much reduced indicating a suppression of the regular flow fluctuations in the wake.
- The TKE at ' z_2 ' is reduced compared to the baseline, but higher than at ' z_1 '.

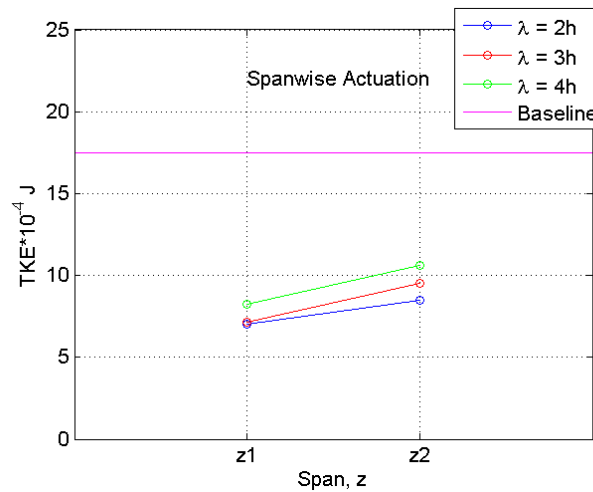


Figure 5.76: TKE's over all λ 's and spanwise locations for spanwise actuation at $U_\infty = 5$ m/s. 'B' indicates baseline flow

Wake Size

The wake size (analogous to wake area) used here is calculated as that area in the wake of the model where the average streamwise velocity is less than 80% of the free stream U_∞ . It is a good parameter to quantify the effect of the actuator on the wake, when used in conjunction with the baseline wake deficit area. The deficit areas of the opposing and staggered transverse actuation modes at the various spanwise imaged location in a spatial actuation cycle at $U_\infty = 5$ m/s are shown in Fig 5.77. The general trends in deficit areas, explained using the actuation mechanisms described in Sections 5.5.1 and 5.6.1 for the transverse actuation modes at $U_\infty = 5$ m/s are:

- For the opposing mode, among all the spanwise locations the wake size at ' $z1$ ' was the highest due to the lift-up that the shear layers underwent. At ' $z2$ ', the opposite was true - the wake at this location was the narrowest due to the push-down that shear layers experience. At ' $z3$ ', due to the fact that the majority of the induced forcing from the corresponding exposed electrode segment was channelled away into streamwise vorticity, the actuation had the least effect on the wake topology and hence the wake size was around that of the baseline flow case.
- For the staggered mode, the wake area at ' $z2$ ' was the highest along the span in one spatial actuation cycle, due to the lift-up that the shear layer on the non-forcing side underwent. Because the lift-up took place on only one side, the wake area was smaller than that at ' $z1$ ' for transverse opposing actuation. At ' $z1$ ' in staggered mode, the shear layers were pushed inwards, hence the wake was narrower than the corresponding baseline flow case, much like what occurred at the ' $z2$ ' location for transverse opposing actuation.

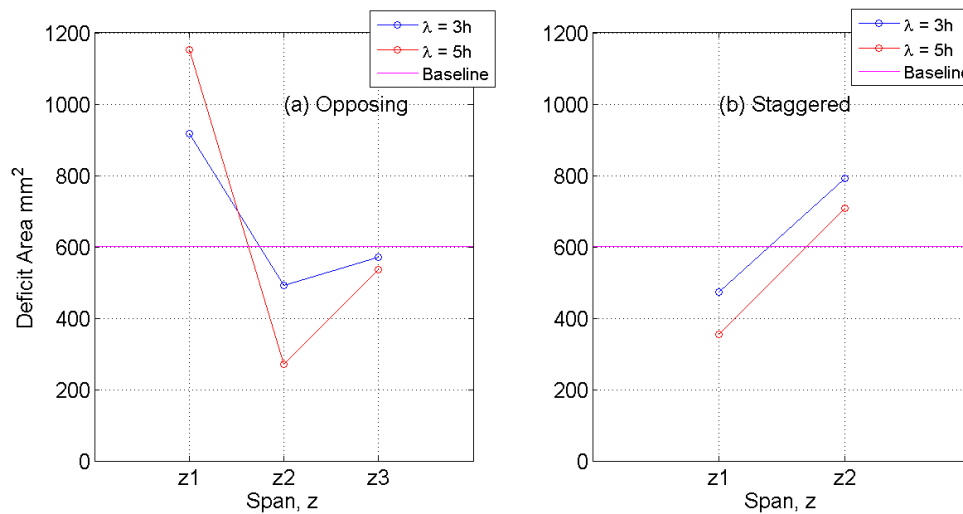


Figure 5.77: Wake areas over all λ 's and spanwise locations for spanwise modulated transverse (a)opposing and (b) staggered actuation at $U_\infty = 5$ m/s

The wake sizes of the tested spanwise actuation configurations at the various spanwise imaged location in a spatial actuation cycle at $U_\infty = 5$ m/s are shown in Fig 5.78. The general trends in wake deficit area over the imaged spanwise locations are:

- Compared to the baseline un-actuated flow, the wake size at ' $z1$ ' is much higher, due to

the lift-up of the shear layers at this location. The stronger the spanwise jets at the point of convergence (stagnation point), the stronger the lift-up and correspondingly the higher the wake size.

- The wake size at ' z_2 ' is reduced compared to the baseline, due to push-down on the shear layers caused by the downward flow at this location. This is independent of the electrode spacing λ and hence is almost the same over the tested spanwise actuation configurations.

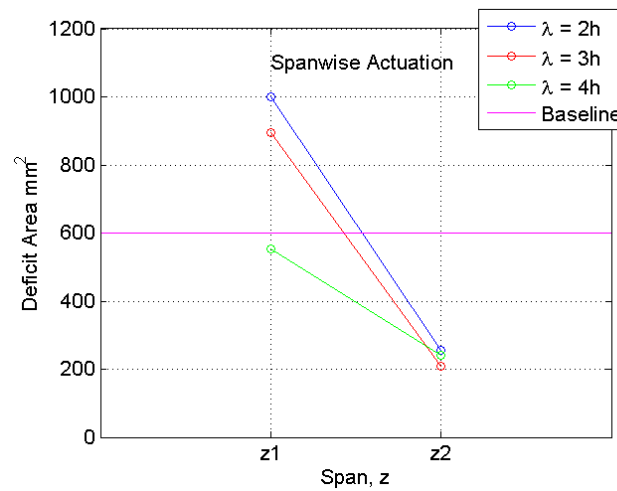


Figure 5.78: Wake sizes over all λ 's and spanwise locations for spanwise actuation at $U_\infty = 5$ m/s. 'B' indicates baseline flow

Chapter 6

Conclusions and Recommendations

6.1 Conclusions

To reiterate, the broad objective of the research and experiments undertaken and described here was to overcome the problem of tonal acoustic noise emission from bluff bodies in flows due to regular, periodic Karman vortex shedding by suppressing/attenuating the shedding using spanwise modulated plasma actuation. For this purpose a suitably designed D-shaped bluff body was chosen as the experimental model to approximate commonly encountered objects in flows while maintaining experimental simplicity.

The usability of polycarbonate Makrolon as a suitable dielectric material for plasma actuators was confirmed. Makrolon sheets 3mm thick were used to construct the plasma actuators using electrodes made of Copper tape, and were seen to give rise to a uniform and steady plasma discharge even at high voltages across them. The plasma actuators were operated at 40 kV and 1250 Hz input for all the tests conducted. At these operating conditions, a peak induced jet of around 4.5 m/s close to the surface and over a distance of upto at least 15 mm downstream from the exposed-encapsulated electrode interface was measured in quiescent conditions.

Time-resolved two component particle image velocimetry (2C-PIV) was the flow measurement technique of choice, due to the high spatial and temporal resolution of the imaged wake velocity fields it yields. To take into account the fact that the expected flow behaviour across the span was expected to be different at different positions in a spatial cycle of actuation, the flow at multiple spanwise planes was imaged and measured. Additionally, transverse planes were also imaged for representative configurations in each actuation mode to study the flow behaviour across the span. The range of flow free-stream speeds over the model for which each of the actuation modes, configurations and imaged planes were tested was from 5m/s to 20m/s. The flow over the model for each case was untripped and laminar till separation at the trailing edge, and the presence of vortex shedding and its various associated parameters for the baseline un-actuated flow was confirmed and calculated for the sake of flow characterisation.

Three different spanwise modulated actuation modes were devised and named based on the direction of forcing with respect to the flow and the electrode layout over the upper and lower

trailing edge surfaces of the model:

1. Transverse Opposing Actuation
2. Transverse Staggered Actuation
3. Spanwise Actuation

These modes were devised based on insights gathered from literature pertaining to two- and three dimensional shedding control and applications of plasma actuators to aerodynamic flow control. For each of these modes, multiple 'configurations' were tested based on the spatial interval over which the actuation scheme was repeated over the model span. To have a benchmark to compare the spanwise modulated actuated results with, transverse actuation that was uniform over the span and similar to what was implemented by Nati [27] was also tested. It was however seen that due to the strong electric fields at the plasma actuators on the upper and lower sides, the individual regions of plasma generated from both sides overlapped at around the region of the center of the model base. In the region of overlap, the electric fields from both sides cancelled out and the plasma ions ceased to be accelerated. Due to this, the effective forcing was lowered. Hence, it can be concluded that the experimental model was not optimised (i.e. the trailing edge height too small) for the high electric fields involved in the transverse-forcing plasma actuation.

The results for all the actuated modes indicate regions of wide wakes with shear layers spread apart and narrow wakes with shear layers drawn inwards alternating along the span. This can be attributed to the generation of streamwise vorticity that was spatially steady and temporally stable for all the modes; the exact mechanism for this creation was however different for the different actuation modes. Additionally, correlation analysis of the velocities at different spanwise positions when considering the transverse planes at the shear layer for all the tested modes indicates a breakdown of the spanwise coherence of the shedding. Likewise, the actuation flow mechanism by which this breakdown was effected is different for the different actuation modes

For the spanwise modulated transverse mode, the actuation was responsible for the creation of strong streamwise vorticity due to the presence of alternating regions along the span of forcing and no-forcing. The aligned transverse forcing from the upper and lower sides gave rise to spanwise flows that mutually reinforced each other, hence the generated streamwise vorticity was strong. Some transverse vorticity was also generated. The actuation-generated vorticity was at the expense of the baseline spanwise vorticity of the shear layers, thus weakening the latter to a large extent. The strong streamwise vorticity created gave rise to alternating regions of large and small wakes along the span that broke up the spanwise coherence of the shed Karman vortex rolls.

For spanwise modulated staggered actuation, however it is expected that the spanwise induced flows due to the anti-aligned transverse forcing from the upper and lower sides weaken each other and hence the streamwise vorticity generated can be expected to be quite weak. The success of this mechanism in vortex shedding suppression rested however on the asymmetry between the interacting shear layers on both sides due to the anti-aligned nature of the actuation over these surfaces.

For the spanwise forcing actuation scheme, the *direct* creation of streamwise vorticity due to the forcing perpendicular to the inflow was expected, as seen in [20] where spanwise forcing DBD plasma actuators were used to generate a counter-rotating vortex array. However, the modulation of the interacting shear layers across the span on both sides due to the alternating common-flow up and flow-down of the generated streamwise vorticity was responsible for the breakdown of the spanwise coherence of the shed vortex rollers across the span.

Significant reduction in the energies of the first two POD modes are seen for the actuation modes at 11 m/s, which then rise to near baseline flow levels at 14 m/s. The upper limit of actuation effectiveness is hence between 11 and 14 m/s. This is an improvement compared to the upper limit of actuator effectiveness in vortex suppression seen in the case of spanwise uniform transverse actuation seen in Nati [27]. The cross-correlations of the velocity time signals across the span, when the transverse shear layer planes are imaged, also indicate a breakdown of spanwise coherence till a free stream of between 11 m/s and 14 m/s. Due to the complex nature of the induced flow mechanisms, it is not appropriate to compare the various actuation modes or the configurations with each other in terms of shedding suppression performance, due to the statistical nature of the comparison criteria such as POD modal energies or spanwise velocity cross-correlations. It does suffice, however, to conclude that spanwise modulated actuation has increased the upper limit of actuation effectiveness due to the three-dimensional mechanism of the vortex suppression.

6.2 Recommendations

As with most scientific and engineering research topics, new insights were obtained in the process of the research that were not expected at the beginning of the work. These insights, however are valuable in bringing to light certain assumptions that may have been made or design factors not taken into account. They provide a valuable learning experience that enables the researchers involved to improve their methodology and approach for future projects, and also open new avenues for future research. The recommendations for future work presented here are a combination of insights that were gained during the course of the current research and relevant expansions of the scope of research tackled in this work to extend the limits of actuation effectiveness:

1. *Experimental Model Optimisation:* As mentioned earlier, the high electric fields generated by the plasma actuator electrodes on the upper and lower surfaces of the trailing edge for spanwise uniform transverse actuation and spanwise modulated transverse opposing actuation give rise to large regions of plasma on both sides that overlap with each other. In the region of overlap, the electric fields will cancel out and the plasma ions from either side will cease to be accelerated. This represents a loss of effective forcing and is undesirable. This can be prevented by using a model with a higher trailing edge thickness or using lower V_{pp} input signal to the actuator (but this option will lead to lesser induced forcing, hence is less preferred). It can hence be expected that the performance of the above mentioned actuation modes can be improved by suitably improving the design of the experimental model to prevent the overlap of the electric fields from both sides.
2. *Pressure Measurements:* As seen in Fig 2.8 the base pressure over a bluff body with vortex shedding fluctuates as the shedding phase changes, causing vortices in the near wake to leave pressure reading 'footprints'. It is this strongly harmonic behaviour of the base pressure fluctuations that is responsible for the emission of tonal acoustic noise. Spanwise velocity signal cross-correlation was chosen as the means of confirming the breakdown of the spanwise coherence of the shed Karman vortex rolls. From the point of view of tonal noise elimination, which was chosen as the broad overlying objective of this Thesis, it is also highly relevant to place arrays of microphones along the upper and lower trailing edges and the base-centerline in order to measure the pressure fluctuations at these points along the span. The pressure time signals from these sensors could be analysed for correlation just as was done with the velocity signals here. Loss of correlation between them would

then indicate random fluctuations and the elimination of tonal acoustic noise, as desired. Such an experimental campaign could also measure the fluctuations in the drag force on the experimental model, which is also a highly undesirable phenomenon.

3. *Moving towards testing of practical objects:* As mentioned in the scope of the research that was undertaken (Sec 1.2) the flow over the model to be tested was low speed (≈ 20 m/s) un-tripped, hence laminar throughout. However in order to extend the testing closer to the ideal model of a truncated trailing edge airfoil or bluff bodies in high speeds such as aircraft landing gear that suffer from unwanted noise generation due to vortex shedding, the flow could be tripped and the boundary layer over the experimental model before separation allowed to transition to turbulence. A turbulent boundary layer is a more energetic boundary layer than a laminar boundary layer, hence stronger plasma actuators would be required in order to deflect the inflow or induce flows and circulation to the same degree as in laminar flows. This can be arranged, however, if the experimental model is optimised to ensure that electric field overlap does not take place (see point 1). Also of interest is the introduction of an adverse pressure gradient, such as is seen on streamlined practical surfaces such as those of truncated airfoils. A tapered of the trailing edge region could do just that, while keeping the model design simple. It can be expected that the flow physics behind such bodies is more complicated than those of simple bluff bodies, based on the results of experiments on vortex shedding conducted on the wake of airfoils, such as in [41], [12], etc.
4. *More extensive Wake PIV Measurements:* As was mentioned earlier, the wake centerline ($y = 0$) transverse $x - z$ planes were not measured for spanwise modulated transverse staggered and spanwise actuation modes, due to experimental time constraints. This meant that lesser data was available for proposing an actuation mechanism for these cases. Additionally, the lack of streamwise $y - z$ plane imaging due to the difficulties associated with
 - (a) out of plane motion of seed particles in the flow, since the flow will go through the imaged plane, and
 - (b) the camera and laser setup

prevents one from acquiring the complete picture of the flow in the wake that can be gathered using two-component PIV. Indeed, the formation of streamwise vorticity can best be confirmed through streamwise $y - z$ plane flow measurements using PIV, rather than through indirect means as was done in this work. The first step to thoroughly understanding the flow physics is to carry out more extensive wake imaging and measurement over two-dimensional multiple planes.

5. *Investigation of Pulsed Actuation:* Nati [27] also investigated the effect of pulsed actuation on vortex shedding through his transverse forcing spanwise uniform plasma actuation system. He found that an effect equivalent to that of steady actuation was obtained only when the pulsing frequency was raised to 3 to 5 times the shedding frequency (i.e. for $St \approx 0.6 - 1$). Thomas et al [37] and Jukes and Choi [19] conducted experiments exploring the effect of steady and pulsed plasma actuation in vortex shedding suppression and on the wake properties and profiles behind a cylinder. It was found in both these investigations that for pulsed actuation, the actuation frequency f corresponding to $St_D = fD/U_{inf} = 1$ with a duty cycle of 25% was found the most effective. Hence, the frequency of actuation should match that of the separated wake region (U_{inf}/D) for optimum pulsed control. In the light of these works, it is of interest to implement spanwise modulated plasma ac-

tuation with a pulsed input signal. If successful, the power savings from reducing both actuator surface area (spanwise modulated when compared to spanwise uniform electrode layout) and actuator firing time (pulsed when compared to steady) could be considerable and improve the desirability of plasma actuation in the field of vortex shedding control.

Bibliography

- [1] A. Artana, J. D'Adama, L. Leger, E. Moreau, and G. Touchard. Flow control with electrohydrodynamic actuators. *AIAA*, 40(9):1773–1778, 2002.
- [2] N. Benard, J. Jolibois, E. Moreau, R. Sosa, G. Artana, and G. Touchard. Aerodynamic plasma actuators: A directional micro-jet device. *Thin Solid Films*, 516:6660–6667, 2008.
- [3] A. Chatterjee. An introduction to the proper orthogonal decomposition. *Current Science*, 78(7), April 2000.
- [4] H. Choi, W.-P. Jeon, and J. Kim. Control of flow over a bluff body. *Annual Review of Fluid Mechanics*, 40:113–139, 2008.
- [5] C. Chyu, J.-C. Lin, J. Sheridian, and D. Rockwell. Karman vortex formation from a cylinder: Role of phase-locked kelvin-helmholz vortices. *Physics of Fluids*, 7:2288–2290, 1995.
- [6] T. C. Corke, C. L. Enloe, and S. P. Wilkinson. Dielectric barrier discharge plasma actuators for flow control. *Annual Review of Fluid Mechanics*, 42:505–529, 2010.
- [7] T. C. Corke, M. L. Post, and D. M. Orlov. Sdbd plasma enhanced aerodynamics: concepts, optimization and applications. *Progress in Aerospace Sciences*, 43:193–217, 2007.
- [8] P. J. Deshpande and S.D. Sharma. Spanwise vortex dislocation in the wake of segmented blunt trailing edge. *Journal of Fluids and Structures*, April 2012.
- [9] T. Do, L. Chen, and J. Tu. Numerical study of the effect of trailing edge bluntness on highly turbulent hydrofoil flow. *ANZIAM*, 47:822–839, 2007.
- [10] S. S. Dol, G. A. Kopp, and R. J. Martinuzzi. The suppression of periodic vortex shedding from a rotating circular cylinder. *Journal of Wind Engineering and Industrial Aerodynamics*, 96:1164–1184, 2008.
- [11] M. van Dyke. *An Album of Fluid Motion*. The Parabolic Press, 1988.
- [12] M. El-Gammal and H. Hangan. Three-dimensional wake dynamics of a blunt and divergent trailing edge airfoil. *Experiments in Fluids*, 44:705–717, 2008.
- [13] M. Forte, J. Jolibois, J. Pons, E. Moreau, G. Touchard, and M. Cazalens. Optimization of a dielectric barrier discharge actuator by stationary and non-stationary measurements of the induced ow velocity: application to airow control. *Experiments in Fluids*, 43:917–928, 2007.
- [14] J. H. Gerrard. The mechanics of the formation region of vortices behind bluff bodies. *Journal of Fluid Mechanics*, 25:401–413, 1966.

- [15] O. M. Griffin. A note on bluff body vortex formation. *Journal of Fluid Mechanics*, 284:217–224, 1995.
- [16] M. Hennevelt. Streak control within a turbulent boundary layer using streamwise arrays of plasma actuators. Master thesis, Delft University of Technology, 2012.
- [17] J.O. Hinze. *Turbulence*. McGraw-Hill classic textbook reissue series. McGraw-Hill, 1975.
- [18] Metals JOM: The Member Journal of the Minerals and Materials Society (TMS). Launching a new era in roller coasters, May 2002.
- [19] T. Jukes and K.-S. Choi. Active control of a cylinder wake using surface plasma. In *IUTAM Symposium on Unsteady Separated Flows and Their Control*, volume 14 of *IUTAM Bookseries*, pages 539–550. Springer, 2009.
- [20] T. N. Jukes and K.-S. Choi. Dielectric-barrier-discharge vortex generators: characterisation and optimisation for ow separation control. *Experiments in Fluids*, 52:329–345, 2011.
- [21] J. Kim and H. Choi. Distributed forcing of flow over a circular cylinder. *Physics of Fluids*, 17(033103), 2005.
- [22] J. Kim, S. Hahn, J. Kim, D.-K. Lee, J. Choi, W.-P. Jeon, and H. Choi. Active control of turbulent flow over a model vehicle for drag reduction. *Journal of Turbulence*, 5(019), 2004.
- [23] M. Kotsonis and S. Ghaemi. Forcing mechanisms of dielectric barrier discharge plasma actuators at carrier frequency of 625 hz. *Journal of Applied Physics*, 110(113301), 2011.
- [24] C. Lin and H. Hsieh. Convection velocity of vortex structures in the near wake of circular cylinder. *Journal of Engineering Mechanics*, October 2003.
- [25] A. Melling. Tracer particles and seeding for particle image velocimetry. *Measurement Science and Technology*, 8:1406–1416, 1997.
- [26] E. Moreau. Airov control by non-thermal plasma actuators. *Journal of Physics D: Applied Physics*, 40:605–636, 2007.
- [27] G. Nati. Suppression of vortex shedding from a truncated trailing edge by plasma actuation. Master thesis, Delft University of Technology, 2011.
- [28] M. Pastoor, L. Henning, B. R. Noack, R. King, and G. Tadmor. Feedback shear layer control for blu body drag reduction. *Journal of Fluid Mechanics*, 608:161–196, 2008.
- [29] M. S. Petrusma and S. L. Gai. Base pressure recovery for segmented trailing edge aerofoils. In *11th Australasian Fluid Mechanics Conference*, University of Tasmania, Hobart, Australia, December 1992.
- [30] M. Raffel, C. Willert, S. Wereley, and J. Kompenhans. *Particle Image Velocimetry, A Practical Guide*. Springer, second edition, 2007.
- [31] A. Roshko. On the drag and shedding frequency of two dimensional bluff bodies. Technical Note 3169, National Advisory Committee for Aeronautics, 1954.
- [32] F. Scarano. *Experimental Methods (notes)*. Delft University of Technology, 2006.
- [33] H. Schlichting. *Boundary-Layer Theory*. McGraw Hill, New York, 7th edition, 1979.
- [34] K.J. Standish and C.P. van Dam. Aerodynamic analysis of blunt trailing edge airfoils. *Journal of Solar Energy Engineering*, 125:479–487, 2003.

-
- [35] Y. Sung, W. Kim, M. G. Mungal, and M. A. Capelli. Aerodynamics modification of flow over bluff objects by plasma actuation. *Experiments in Fluids*, 41:479–486, 2006.
- [36] F. O. Thomas, T. C. Corke, M. Iqbal, A. Kozlov, and D. Schatzman. Optimization of dielectric barrier discharge plasma actuators for active aerodynamic flow control. *AIAA Journal*, 47(9), 2009.
- [37] F. O. Thomas, A. Kozlov, and T. C. Corke. Plasma actuators for cylinder flow control and noise reduction. *AIAA Journal*, 46(8), 2008.
- [38] N. Tombazis and P. W. Bearman. A study of three-dimensional aspects of vortex shedding from a blu body with a mild geometric disturbance. *Journal of Fluid Mechanics*, 330:85–112, 1997.
- [39] C. H. K. Williamson. Vortex dynamics in the cylinder wake. *Annual Reviews in Fluid Mechanics*, 28:477–539, 1996.
- [40] J.-Z. Wu, H.-Y. Ma, and M.-D. Zhou. *Vorticity and Vortex Dynamics*. Springer-Verlag, 2006.
- [41] Q. Zhang, S. W. Lee, and P. M. Ligrani. Effects of surface roughness and freestream turbulence on the wake turbulence structure of a symmetric airfoil. *Physics of Fluids*, 16(6), 2004.

Appendix A

Flow of Experiments

The extensive scope of the work that was undertaken during the current thesis warranted a systematic and sequential approach in tackling the problem at hand. The work involved the design and use of plasma actuation in three dimensional vortex shedding control from a flat plate bluff body. Briefly, the chronological sequence of studies and experiments carried out towards achieving the aforementioned target are follows:

1. *Literature Survey*: In order to get an understanding of the problem at hand as well as to acquire an overview of the work carried out by others in the past in the field of bluff body vortex shedding control, a Literature Survey was carried out. The following aspects were tackled in the study:
 - (a) The physics behind vortex shedding
 - (b) A review of some relevant vortex shedding suppression studies reported in literature;
 - (c) An overview of Dielectric Barrier Discharge Plasma Actuators
 - (d) A review of some relevant applications of Plasma Actuators in aerodynamic flow control.
2. A *Dielectric parametric experimental study* was then carried out on simple, planar plasma actuators (shown in Fig. D.1). The aims of this experimental campaign were focused towards familiarisation and understanding the behaviour of plasma actuators in general, as well specifically those constructed on the dielectric Makrolon that was selected in this work. This campaign is described in detail in Sec. 4.1. Briefly put, its aims were:
 - (a) Optimisation of electrical parameters: to arrive at the optimum combination of input signal voltage and frequency to achieve maximum forcing.
 - (b) Measuring the induced wind speed and its streamwise evolution for a simple plasma actuator constructed on Makrolon.
 - (c) To experiment with dielectric sheet thickness, electrode material and other configurations, and to build up a hands-on familiarity and confidence concerning the construction and use of plasma actuators, the High Voltage Amplifier and its controlling software, the laboratory settings and instruments, and the discharge characteristics of the plasma actuators in general.

-
3. The *Design phase*: In this phase, the actuation and experimental details for the vortex shedding related experiments to be carried out are listed, considered and implemented. The salient aspects were:
 - (a) Based on the results of the Dielectric parametric study, the optimum electric input parameters were arrived at, along with the appropriate physical parameters such as dielectric sheet thickness and electrode material for the plasma actuators to be used.
 - (b) The design considerations for an experimental model were listed, based on which the model was designed and fabricated. This is described in App. C.
 - (c) A selection of published and past scientific and experimental works that were deemed important and relevant to the current study during the literature study phase are listed. Based on these works, the spanwise-modulated (three dimensional) plasma actuation schemes to be implemented in this work are devised. A listing of these works, along with the rationale behind the design of these actuation schemes is described in App. D. The important terms 'mode' and 'configuration' pertaining to the actuation schemes are also explained there.
 4. A *preliminary low speed PIV campaign* was carried out. Though the results from this campaign will not be listed in this report, it was an important step nevertheless, for a variety of reasons:
 - (a) A large number of electrode layout schemes (or 'configurations') for each of the actuation 'modes' were tested over a larger range of free-stream velocity conditions in a low speed wind tunnel. Based on the results, the configurations that show encouraging results are picked out while those that do not are discarded from experimental consideration for the future.
 - (b) An idea of the flow physics involved for each actuation mode, as well as the approximate upper free-stream limit for significant actuation benefit was obtained. Based on these insights, future, a more rigorous and detailed PIV experimental campaign was planned.
 - (c) Familiarity and competency was built up with constructing the electrode layouts for spanwise modulated actuation, the use of wind tunnel laboratory facilities, PIV and its various aspects like the laser and optical system, seeding, controlling software, etc as well as data analysis methods like Proper Orthogonal Decomposition and other data processing techniques.
 5. Some *Hot Wire Anemometry* was carried out to obtain shedding spectra at multiple locations of interest in the wake for certain spanwise modulated transverse actuation configurations in conditions both within and outside the defined scope of the work. These wake locations were ascertained based on the preliminary PIV Campaign. The results of this campaign will not be shown here, as it was carried out primarily to obtain a personal deeper understanding of the flow physics involved in terms of the time-varying shedding at various locations along the span. The results of the HWA analysis were primarily to confirm the presence of vortex shedding using spectral analysis of the velocity signal, as well as study the effect of different input signal frequencies and voltage amplitudes, and the boundary layer state (laminar or tripped) on the shedding Strouhal number.
 6. The *time resolved PIV campaign*. The bulk of the results presented in the report were obtained from this campaign. The results of the various studies and experiments conducted

previously were used to define the experimental details for this campaign, such as the actuation modes and configurations to be tested, spanwise and transverse wake planes to be imaged, etc. The details of this campaign are described extensively in Sec 4.4.

7. *Data processing and analysis* of the large amounts of time-resolved data obtained from 2C-PIV over all the modes, configurations, imaged planes and flow conditions was carried out. The raw data, when analysed and processed using the various techniques explained in Chap. 3 presented a wealth of results in terms of instantaneous vortical structures, statistical flow fields, power spectra and flow modes obtained from Proper Orthogonal Decomposition of the velocity fields. In terms of the understanding gathered of the flow physics of the various actuated cases, this was the most significant step of the whole process.

Appendix B

Overview of Flow Facilities

The experiments were carried out at two different low speed Wind Tunnels at the Aerodynamics building of the Aerospace Engineering faculty at TU Delft, based on their availability - the W-tunnel and the M-tunnel. These tunnels were the venues of the Low Speed and High Speed PIV campaigns respectively.

The W-Tunnel is an open jet low speed Wind Tunnel with a plenum inlet with dimensions $L \times W \times H$ of $2.0 \times 1.5 \times 2.0 \text{ m}^3$ and square exit of size $0.4\text{m} \times 0.4\text{m}$. Air is sucked into the plenum by a 16.5 kW DC motor driven centrifugal fan. The maximum velocity is about 35 m/s and can be regulated by setting the revolutions per minute of the centrifugal fan. Depending on the flow velocity, the minimum achievable turbulence level can be in the order of 0.5%. The air flows from the inlet into a diffuser where it is decelerated, from where it flows into a settling chamber. After this, the flow is accelerated in a contraction nozzle and enters the test section. In the test section, only the central part of area $0.32 \times 0.32 \text{ m}^2$ can be considered to have uniform flow; the measurements of free stream velocity are carried out based on a pitot tube placed in this part.

The M-tunnel is a low-speed wind tunnel that can be operated as either an open jet or closed jet tunnel. In the experiments for this thesis, it was operated as an open jet tunnel, for which the maximum attainable wind speed is 35 m/s. The shape and structure of this tunnel is quite similar to the W-Tunnel. The tunnel exit area at the test section is square and $0.4\text{m} \times 0.4\text{m}$ and due to the large contraction ratio the turbulence level of the flow in the test section is low.

Appendix C

Wind Tunnel Model Design Procedure

In order to test the effectiveness of the various Plasma Actuator configurations on Vortex Shedding in the Wind Tunnel a suitable experimental model was designed based on a variety of considerations. Before going into the details regarding the design considerations, the larger goal of the current experimental campaign must be kept in mind - the control of vortex shedding from practical non-streamlined (bluff) objects and/or streamlined objects with truncated trailing edges. The problem of tonal acoustic noise caused by the periodic shedding induced pressure fluctuations on the base of such objects was discussed earlier in Sec. 1.1. Airfoils with truncated trailing edges, encountered commonly in Wind Turbines for example, are among bodies in flow that suffer from the adverse of vortex shedding. In order to represent such objects a flat plate bluff body was chosen. This is undoubtedly a simplification of the problem complexity at hand. The advantages of this simplification include:

- fixed flow separation locations at the upper and lower trailing edges;
- no external tripping, hence laminar flow everywhere over the model;
- zero pressure gradient applied to the flow across its length.

After the geometry of the model was decided, the following considerations were kept in mind while designing and manufacturing it. They will be discussed in detail in the sections that follow.

- Plexiglass (Polycarbonate Makrolon) was the material of choice for the model, due to the light weight and ease of manufacturing.
- The desired boundary layer characteristics for flow over the model, and the occurrence of vortex shedding;
- To obtain results that can be compared with earlier experimental studies using Plasma Actuators in Vortex Shedding Control carried out in similar experimental facilities by Nati [27];
- To enable arranging and easily varying the plasma actuator electrode spanwise configurations and the PIV imaging planes during the experiments, etc.

C.1 Laminar Boundary Layer

The boundary layer over a body in a flow is the slower-moving layer of fluid that is closest to it that is created due to the no-slip condition at the body surface. Viscosity and vorticity effects are significant in this layer. Boundary layers can be either laminar or turbulent. To avoid the difficulties associated with adverse pressure gradients of the flow over streamlined bodies, a flat plate model was chosen. The added advantage of a flat plate is the fact that exact analytical solutions are known for the boundary layer flow. Over a flat plate in a flow of U_∞ , the boundary layer starts off as laminar, and then naturally develops into a turbulent one at a particular critical distance x_{cr} downstream of the leading edge, depending on the flow speed. The critical Reynolds number Re_{cr} over a flat plate is:

$$Re_x = \frac{U_\infty x}{\nu} \quad (\text{C.1a})$$

$$Re_{cr} = \frac{U_\infty x_{cr}}{\nu} = 5 \times 10^5 \quad (\text{C.1b})$$

where ν is the kinematic viscosity of air, equal to $1.5 \times 10^{-5} \text{m}^2/\text{s}$. It is desired to have laminar boundary layers everywhere over the plate. Taking into account that the maximum testing flow speed will be around 20 m/s, the corresponding critical transition length is 0.375m from Eq. C.1b. Hence, two requirements were imposed on the experimental model related to the Laminarity of the boundary layer:

- A streamwise length of less than 0.375m
- A rounded leading edge to prevent separation at that location and enable laminar boundary layers to develop.

Various boundary-layer characteristic parameters over the flat plate model can be defined: the boundary layer thickness, displacement and momentum thickness δ, δ^* and θ respectively. Practically, the boundary layer thickness δ_{99} is the transverse distance from plate to height where the local flow is 99% as fast as the free stream U_∞ , while the displacement and momentum thickness follow from the conservation of mass and momentum respectively. A detailed explanation of these quantities can be found in Schlichting [33].

$$\delta^* = \int_0^\infty \left(1 - \frac{u}{U_\infty}\right) dy \quad (\text{C.2a})$$

$$\theta = \int_0^\infty \frac{u}{U_\infty} \left(1 - \frac{u}{U_\infty}\right) dy \quad (\text{C.2b})$$

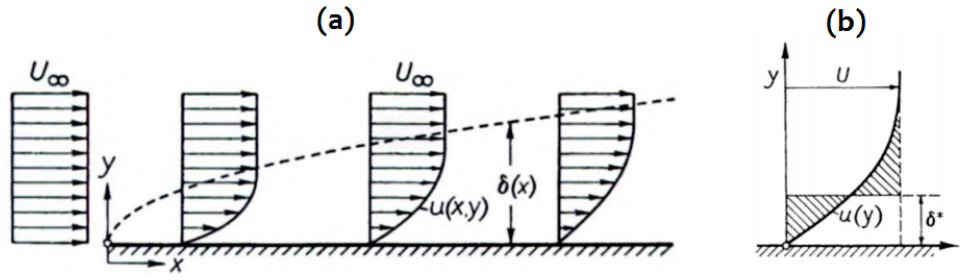


Figure C.1: Diagram showing the (a) development of the boundary layer over a plate plate and the various terms associated with it and (b) the displacement thickness. Taken from [33]

For flow over a flat plate, an exact analytical solution for the development of the boundary layer was given by Blasius in 1908 based on the streamwise location on the plate x and the Reynolds number at that location Re_x . Additionally, a shape factor H is used in determining the nature of the boundary layer flow. In general, the higher its value, the stronger the adverse pressure gradient. Conventionally, $H = 2.59$ is typical of laminar flows, while $H = 1.3 - 1.4$ is typical of turbulent flows.

$$\delta_{99} = \frac{5x}{\sqrt{Re_x}} \quad (C.3a)$$

$$\delta^* = \frac{1.721x}{\sqrt{Re_x}} \quad (C.3b)$$

$$\theta = \frac{0.664x}{\sqrt{Re_x}} \quad (C.3c)$$

$$H = \frac{\delta^*}{\theta} \quad (C.3d)$$

The models streamwise length was set to 0.3m which satisfies the boundary layer transition streamwise length constraint. A semi-ellipse leading edge nose was designed, in order for the model to maintain some similarity to an airfoil, and to prevent leading edge separation. This streamwise length, at a free stream speed of 5m/s would give rise to a boundary layer height of 4.74mm from Eq. C.3b.

An additional parameter, the Trailing Edge bluntness parameter B was used to quantitatively assess if vortex shedding could take place from a bluff body. Do et al [9] report in their work on numerical simulation of vortex shedding from a blunt trailing edge from a hydrofoil that a minimum B value of 0.45 is required for shedding. Other published values of this critical B value in literature are 0.5 and 0.48 (Brooks and Hodgeson, 1981).

$$B = \frac{h}{\delta^*} \quad (C.4)$$

In the present work, the case of flow at $U_\infty = 5$ m/s was considered for calculating the B for the experimental model, because this was the lowest free stream tested at and would hence give rise

to the highest flat plate boundary layer δ^* . The δ^* at this speed calculated from Eq. C.3c was 1.82 mm. The streamwise Reynolds number Re_x that was used in this calculation was based on the length of $x = 0.3\text{m}$ and was found to be 125,000 using Eq. C.1b. Using a critical B value of 0.45, an additional constraint was imposed on the design of the experimental model:

- The required trailing edge height h to endure that vortex shedding will exist is 0.82mm from Eq. C.4.

The following table lists the various model characteristic parameters at the lower and upper free stream velocities that the tests will be carried out (5m/s and 20m/s) calculated using the Laminar boundary layer flat plate equations C.3:

Parameter	$U_\infty = 5 \text{ m/s}$	$U_\infty = 20 \text{ m/s}$
Re_h	4000	16000
Re_x	100,000	400,000
δ_{99}	4.74 mm	2.37 mm
δ^*	1.63 mm	0.816 mm
θ	0.63 mm	0.314 mm
H	2.59	2.59

Table C.1: Model characteristic values at the lower and upper tested $U'_\infty s$

C.2 Physical and Similarity Considerations

The experimental model must be compatible with the experimental facilities available. It was decided that the low speed W-Tunnel and M-Tunnel will be used for carrying out the Wind Tunnel Experimental runs, see App. B. Their test section areas are 40cm \times 40 cm. In order to place the model in such a test section, the spanwise width of the model must equal the dimension of the test section, namely 40 cm. The model would also then have a base span wide enough to allow two-dimensional flow conditions to be measured at its center.

Vortex suppression using spanwise uniform plasma actuation was implemented by Nati [27] in the Wind Tunnels of TU Delft on a flat plate bluff body with a blunt Trailing Edge. It was desired to compare the results of the various configurations of spanwise modulated plasma actuation implemented in this Thesis with those obtained by Nati. Hence, the wind tunnel experimental model was designed similar to that of the Nati. The height of the blunt trailing edge of the current experimental model was set to 12mm, which is far above the minimum required height for vortex shedding to be present according to the trailing edge bluntness constraint (0.82 mm). Once the streamwise, spanwise and transverse lengths of the model have been decided, the design was made, and is shown in Fig C.2. Two M5 screw holes were drilled into the sides of the model so that it can be clamped to the side walls of the test sections of the low speed wind tunnels and held in place during testing.

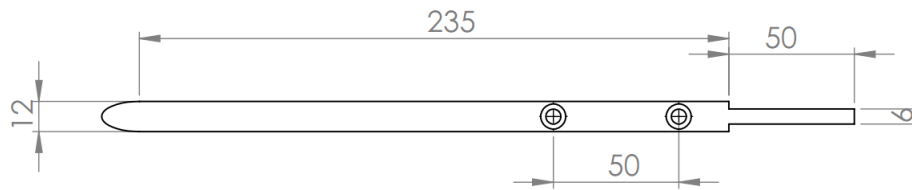


Figure C.2: Experimental model, side view, showing the tapered section near the trailing edge where the movable end fixture was fitted. All dimensions in mm

C.3 Trailing Edge Flexibility

A 3mm thick Makrolon layer was the dielectric material used for the actuators used in the tests conducted. The features and advantages of this material and thickness are mentioned in Sec. 4.1.1. To summarise, the salient advantages are:

- Ability to withstand high electric fields without undergoing breakdown or deterioration.
- Uniform, stable, non-filamentary plasma discharge.

To implement actuators with a 3mm Makrolon layer as the dielectric at the Trailing Edge, a separate end fixture made of Makrolon with its arms 3mm thick was designed that could be fitted on to the end of the main experimental model in a smooth, tight manner. It is shown in Fig. C.3. As can be seen from Fig C.2, the blunt trailing end face of the model is 6mm in height; with the end fixture attached, 3mm is added on either side so that the combined trailing edge height is 12mm as designed. The end fixture is designed so that when it is mated with the model, the resulting body has a smooth, unbroken surface on its upper and lower surfaces.

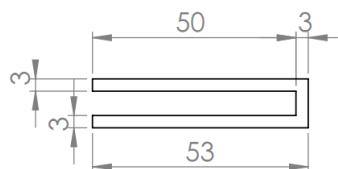


Figure C.3: Side view, trailing edge fixture for the experimental model. All dimensions in mm

Actuators configured to give spanwise-distributed (modulated) forcing in either the streamwise or spanwise direction can be constructed with the exposed electrodes laid out on the upper and lower surfaces of the end fixture and the covered electrode either on the blunt end face or upper and lower surfaces on the tapered section of the model body at appropriate positions along the span close to the trailing edge. This way, when the end fixture is mated with the body, the 3mm Makrolon dielectric layer is present between the exposed and covered electrodes as dielectric as desired. The precise electrode arrangements will be described in App. D. In addition, the movable nature of the end fixture makes it convenient to image streamwise-transverse ($x - y$) planes at different spanwise locations by just shifting the fixture along the span with respect to the flat plate model while carrying out PIV; this way the positions of the laser sheet, imaging camera or

clamping arrangement to the wind tunnel test section do not have to be disturbed. This greatly facilitates varying the actuator configurations and imaging different transverse planes along the span, thus making it easier to carry out the experiments.

Appendix D

Design and Implementation of Plasma Actuator Configurations

This section will describe the various plasma actuation arrangements that will be tested over the course of the various experimental campaigns, along with the rationale that went into their design.

D.1 A Background

Even within the restricted realm of active open loop flow control using plasma actuators, the number of ways of implementing three-dimensional vortex shedding control for a bluff body can be quite extensive due to the large number of possible ways in which the actuator electrodes can be arranged to give the desired direction and mechanism of forcing. Indeed, this versatility of plasma actuators is one of the qualities that makes it a highly desired flow control device. From the preliminary literature study of flow control techniques that was carried out, however, certain studies were found to be highly relevant from a conceptual and experimental point of view. The insights from these were used to devise the various actuation modes and configurations that will be described in the sections that follow. It must be stressed that these studies were not blindly followed; rather their insights were considered from the point of view of flow and actuator physics, and their main ideas combined and implemented into workable models while taking the available experimental constraints into account. Also, differences between these works and the relevant corresponding actuation configuration implemented in this work will be analysed and discussed from an experimental and flow-physics point of view.

Spanwise Modulated Transverse Actuation

For devising spanwise modulated transverse actuation, three studies were found to be highly relevant from a conceptual and experimental point of view. These are listed below, along with their insights and differences from the configurations that were implemented in this work:

1. Spanwise uniform plasma actuation for vortex shedding control by Nati [27]. The transverse actuation configuration was found the most successful of all tested configurations, and hence most relevant to the present study. The mechanism of spanwise uniform transverse actuation is described in detail in Sections 2.3.2 and 5.3.1 and is based on the use of transverse induced flows from both the upper and lower trailing edge surfaces along the model base to give rise to a streamwise jet. A configuration very similar in principle to the one devised by Nati was implemented in this study to realise spanwise uniform transverse actuation, for the sake of comparison with the spanwise modulated actuation cases. As mentioned earlier, one of the aims of the study was to extend the range of success of Nati's spanwise uniform transverse configuration in vortex shedding control with spanwise modulated actuation. The study by Nati was a good starting point conceptually and experimentally in the search for configurations where the actuation along the span would be modulated so that three-dimensional vortex shedding control could be carried out.
2. Distributed forcing on cylinders and D-shaped bluff bodies, [21] and [22]. These methods are reviewed in Sec. 2.2.2. In this active control technique, blowing and suction are applied alternately in a sinusoidal manner along the span and steady in time at the separation locations of cylinder and bluff body. It was found that at the appropriate spatial wavelength of actuation, vortex shedding is eliminated through the break-up of the two-dimensionality of the vortex shedding. Both in-phase and out-of-phase actuation configurations (considering actuation profiles over the upper and lower surfaces) were applied, and it was seen that the in-phase was the most successful. While significant differences exist between the setup used in these works and those available and implemented in this work, the idea of alternating the actuation over the upper and lower surfaces at the trailing edge to have in-phase (simulated by transverse 'opposing') and out of phase (simulated by transverse 'staggered') actuation was nevertheless gained. Some of the above mentioned differences are briefly listed, along with the corresponding experimental approximations that were applied to adapt to the present work using plasma actuators:
 - Suction cannot be implemented using plasma actuators; hence the spanwise locations with suction were replaced with regions of no-actuation.
 - Spatially varying actuation cannot be implemented from a plasma actuator, hence the sinusoidal 'blowing' regions in distributed forcing were replaced with regions of constant plasma actuation.
 - The (distributed) forcing was carried out with a forcing angle with respect to the free stream. However, with plasma actuators the actuation was fixed in the transverse direction, as was done by Nati [27] albeit in a spanwise uniform manner.
3. The use of segmented trailing edges in vortex shedding control, by Petrusma et al [29], and Deshpande et al [8]. The passive flow control implemented through the use of segmented trailing edges in these works could be modelled to a crude degree (in principle) by active control through spanwise modulated plasma actuation in a way that the underlying principle - the creation of spatially fixed and temporally steady streamwise vorticity to weaken the Karman spanwise vorticity, could be achieved. Indeed, spanwise modulated transverse actuation, both opposing and staggered, does give rise to the above mentioned streamwise vorticity due to the three-dimensionality of the electrode placement (see Figs. 5.42(c) and 5.58(c)) that is able to break the two-dimensionality of the shed Karman vortex rolls as desired, to varying degrees of success. The exact actuation-induced flows and vorticity is different however, for these two cases, as shall be seen in Sections 5.5.1 and 5.6.1.

Spanwise Actuation

While devising spanwise actuation configurations, the following studies were found to be relevant and useful from a conceptual and experimental point of view:

- The use of DBD plasma actuators as vortex generators (VG's) in separation control by Jukes and Choi [20]. In this work, electrodes were arranged to induce forcing perpendicular to the flow. Spanwise wall jets are generated that interact with the oncoming laminar boundary layer to create a spatially fixed and temporally steady streamwise vortex array. The mechanism by which incoming laminar fluid is pushed and lifted up by the plasma induced flow to generate circulation was found very insightful in making clear the flow physics that one could expect when plasma actuation is done perpendicular to the inflow in the current experimental setup. Significant differences were expected, however, between the experiment of Jukes and Choi and that of the spanwise actuation configurations implemented in this work. Despite the streamwise length of the actuators in the experiment of Jukes and Choi being roughly the same as those implemented here, in the former the induced flows were allowed to convect undisturbed downstream to develop into streamwise vortices. In the present case, however, the desired location for their placement is such that the downstream end of the plasma actuators is at the trailing edge of the model. Hence, the induced flow will not be allowed to develop downstream due to the flow separation into shear layers at this location. Furthermore, the mechanism of the creation of streamwise vorticity is different in the spanwise actuation configuration implemented here - it is through the lift-up of the spanwise opposing flows, unlike that in Jukes and Choi where the electrodes were spaced appropriately to prevent the lift-up of the spanwise jets..
- The creation of a directional micro jet device in undisturbed conditions by Benard [2]. This was carried out by using opposing plasma-induced streams from plasma actuators to create a jet that could be oriented based on the difference in inputs to the actuators. The idea of using plasma actuators in the current work to create an array of streamwise-oriented opposing spanwise forcing actuators that give rise to a lift up jet was similar to that behind Benard's jet. This jet is responsible for the actuation mechanism present in the current work and the interaction of the various flow phenomena here such as the separating shear layers, strong spanwise vorticity, creation of streamwise vorticity, etc.
- The use of Streak control within a turbulent boundary layer using streamwise arrays of plasma actuators by Hennevelt [16]. The actuation scheme in this work is very similar to that which was implemented in the current work for spanwise actuation, but with the aim of the actuation rather different. Nevertheless, the results regarding the working principle of the actuator array and the effect of the alternate flow-up (created by the converging spanwise flows) and flow down (created due to the 'charging' of the spanwise flows by the ambient air above the exposed electrodes) on the incoming flow were found to be quite insightful and revealing, despite the inflow being turbulent instead of laminar as in the current work.

D.2 Spanwise Uniform Transverse Actuation

Electrode Layout

The electrode layout for this actuation mode was quite straightforward to implement due to its spanwise uniform nature. Two lengths of adhesive copper tape of length comparable to the span of the experimental model and width 2.5 cm was cut and affixed on the upper and lower surfaces of the end fixture. The length of the segments lie *along* the trailing edge of the fixture. These segments on the upper and lower surface are aligned and connected to the signal output terminal of the HVA to form the exposed electrode of the actuation scheme. Similarly, a length of adhesive copper tape with length similar to that of the exposed electrode segments and width 6 mm is affixed over the blunt base of the flat plate experimental model and connected to the ground terminal of the HVA. When the end fixture is mated with the model, this electrode forms the encapsulated electrode of the actuation scheme.

Induced Forcing

This actuation mode can more accurately be termed a spanwise uniform transverse opposing actuation mode, as it is based on the generation of opposing transverse jets all along the span from the upper and lower trailing edge surfaces that converge close to the center of the model base and give rise to a streamwise jet that manipulates the shear layers and near wake flow to suppress or attenuate the vortex shedding. The flow and actuator physics involved in this is reviewed in detail in Secs. 2.3.2 and 5.3.1.

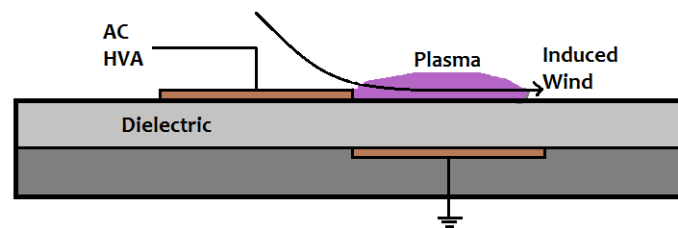


Figure D.1: Schematic of a typical planar plasma actuator

The induced jet from a plasma actuator is 'born' close to the interface between the exposed and encapsulated electrodes and directed along the width of the latter). The extent of the jet is determined by the extent of the plasma region. Since the plasma acts as a source of momentum to the surrounding air (and not a source of mass flow itself like a conventional blowing fan), the induced jet is 'charged' by the air above the exposed electrode. Hence, it is the encapsulated electrode determines the direction of the forcing, with the exposed electrode acting just a source of electrons. In the actuation mode considered, due to the perpendicularity of the exposed and encapsulated electrode segments, the induced wind is directed from the upper and lower trailing edges towards the model base center in the transverse direction close to the wall, while the charging region is above the exposed electrode segments on either side. The zone of plasma on either side is as shown in Fig. D.2(b).

The region of plasma formation for a typical plasma actuator is above the covered electrode (Fig. D.1). For the actuation scheme currently considered, in any $x - y$ plane along the span of an exposed electrode segment on a side (upper or lower), the plasma zone began from the corresponding sharp trailing edge and spread along the blunt face of the model. The same is true of the plasma generated due to the corresponding exposed electrode on the other side. As mentioned earlier, the 3mm thick Makrolon in between the exposed and encapsulated electrodes was able to withstand the strong electric fields generated by the high amplitude input signal (40 kV) used. Stronger the electric field, the farther the plasma can expand and longer the distance over which the ions are accelerated [26]. Consequently, the plasma generated due to the exposed electrodes on either side cross the transverse mid-point of the model trailing base and overlap. This is shown in Fig. D.2(b). The electric fields generated by the exposed-encapsulated electrode combination on either side are similar in magnitude and sign due to the identical actuation input and geometry of the combination. An analysis of the electric field generated by the present electrode layout and actuation conditions is given in App. F.1. In the region of overlap, the electric fields will cancel out and the ions will cease to be accelerated. This represents a loss of effective forcing and is undesirable. One can conclude that the geometry of the model (the trailing edge height h) is not optimised for the actuation taking place. This is reflected in the results in Sec. 5.3.2.

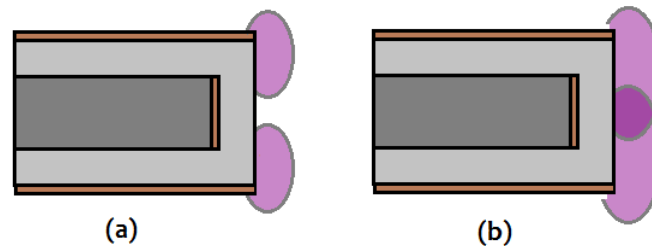


Figure D.2: Zones of plasma due to the exposed-encapsulated electrode combinations on either side showing (a) Ideal non-overlapping and (b) overlapping zones

Imaged Spanwise Planes

Due to the spanwise uniform actuator layout, it is expected that the flow behaviour under the influence of actuation is similar all along the span of the actuator, like the baseline flow that is being modified. Hence, only one spanwise $x - y$ plane was chosen for PIV imaging and measurement located close to the middle of the actuator span (to avoid actuation end effects). Similarly, to study the flow along the span as was done for the other actuated cases mentioned in the following sections (in order to study the spanwise coherence of the shed Karman vortices, for example) one $y - z$ plane was imaged at a transverse location corresponding to the upper shear layer, $y = 0.5h + 2$ mm.

D.3 Spanwise Modulated Transverse Opposing Actuation

Electrode Layout

The following steps were involved in the implementation of spanwise modulated transverse opposing actuation with a configuration of spatial wavelength λ . The resulting arrangement in the $y - z$ plane at the model bluff base is shown in Fig.D.3.

- Segments of adhesive copper tape were cut with (spanwise) width $\lambda/2$ and (streamwise) length of 25 mm. These comprised the exposed electrode(s) of the actuation scheme. These segments were arranged and affixed in an alternating manner on the upper and lower surfaces of the end fixture with
 - one spanwise edge *along* the trailing edge of the end fixture;
 - the electrode segments on both the surfaces lined up so that when they were projected on any $x - z$ plane they coincided;
 - the spanwise distance between corresponding streamwise edges of any two adjacent exposed electrode segments on both surfaces equal to λ ;
 - A thin strip of copper tape was laid out on both the upper and lower end fixture surfaces to connect the respective separate individual exposed electrode segments. These thin strips from both sides were then jointly connected together to the high-voltage output of the High Voltage Amplifier (HVA).
- A long segment of copper tape was affixed to cover the flat plate model's blunt base. This segment formed the encapsulated electrode when the trailing edge end fixture is mated with the bluff end of the flat plate model:
 - The width of this segment was equal to the transverse height of the flat plate model bluff base (6mm) and its length nearly equal to the span of the model.
 - The ground end of the HVA was connected to the electrode to be encapsulated.

Induced Forcing

The plasma zones generated by the exposed electrodes at the upper and lower trailing edge surfaces at the spanwise position at the middle of the exposed electrode segments ($z3$) are quite similar to that of spanwise uniform transverse actuation seen in App. D.3. However, with spanwise modulated transverse actuation, the three-dimensionality in the electrode layout, namely the presence of alternating regions of exposed electrode and no-electrodes prevents the actuation from being as ineffective. At the $z1$ spanwise location within a spatial actuation cycle, there are no exposed electrodes present on either side, hence one can expect that no plasma will be formed. At the $z2$ location, which lies at the spanwise interface of regions with and without exposed electrodes, edge effects would be present, making it difficult to predict the plasma formation mechanism. The actuation here can be characterised by the fact that at the locations where exposed electrodes are present on both sides the transverse flows induced from either side are opposite and converging, hence this actuation mode is labelled the 'transverse opposing' mode.

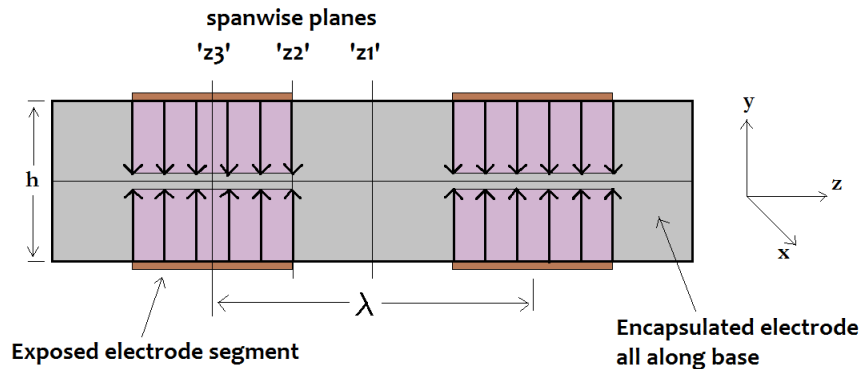


Figure D.3: Schematic showing the electrodes, induced forcing and imaged $x - y$ planes in the spanwise modulated transverse opposing actuation mode

Imaged Spanwise Planes

Since the aim of the spanwise modulated actuation was to break up the inherent two-dimensionality of the Von-Karman vortex rolls in the near wake, it was expected that the wake would differ along a spanwise wavelength of actuation. Based on the electrode configuration, it was decided to laser-illuminate three spanwise $x - y$ and two transverse $x - z$ planes for PIV time-resolved measurements in order to have as good a picture of the flow field of the near wake as can be obtained through as few imaging planes as possible. The $x - y$ planes imaged were chosen close to the middle of the span of the model to avoid end-effects associated with the wind tunnel walls. To change the $x - y$ plane being imaged, the movable trailing edge end-fixturing was moved along the spanwise direction by $\lambda/2$ without the other experimental components being disturbed so that the salient spanwise locations could be illuminated by the laser and captured. These are listed below and shown in Fig D.3.

- Spanwise $x - y$ planes in one actuation spatial cycle:
 1. The middle of a spanwise location without any exposed electrode on either side; $z = z_1$
 2. The spanwise location at the interface between the regions having exposed electrode and no-electrode on the upper and lower sides, displaced by $\lambda/2$ along the span from z_1 ; $z = z_2$
 3. The middle of a spanwise location with exposed electrodes on either sides, and displaced by $\lambda/2$ along the span from z_2 ; $z = z_3$
- Transverse $x - z$ planes:
 1. The wake centerline, $y = 0$
 2. The shear layer plane, $y = 0.5h + 2$ mm. A transverse height of $y = 0.5h$ at the trailing edge upper surface would have been ideal, but the laser plane was lifted by 2mm from the surface to avoid the reflections from the surface.

D.4 Spanwise Modulated Transverse Staggered Actuation

Electrode Layout

The following steps were involved in the implementation of spanwise modulated transverse staggered actuation with a configuration of spatial wavelength λ . The resulting arrangement in the $y - z$ plane at the model bluff base is shown in Fig.D.4.

- Segments of adhesive copper tape were cut with (spanwise) width $\lambda/2$ and (streamwise) length of 25 mm. These comprised the exposed electrode(s) of the actuation scheme. These segments were arranged and affixed in an alternating manner on the upper and lower surfaces of the end fixture with
 - one spanwise edge *along* the trailing edge of the end fixture;
 - the electrode segments on both the surfaces anti-aligned so that when they were projected on any $x - z$ plane they did not coincide - there was no overlap or gap between the projected areas. This staggered arrangement of the exposed electrode segments on the upper and lower sides is responsible for the name of this actuation mode.
 - the spanwise distance between corresponding streamwise edges of any two adjacent exposed electrode segments on both surfaces equal to λ .
 - A thin strip of copper tape was laid out on both the upper and lower end fixture surfaces to connect the respective separate individual exposed electrode segments. These thin strips from both sides were then jointly connected together to the high-voltage output of the High Voltage Amplifier (HVA).
- A long segment of copper tape was affixed to cover the flat plate model's blunt base. This segment formed the encapsulated electrode when the trailing edge end fixture is mated with the bluff end of the flat plate model:
 - The width of this segment was equal to the transverse height of the flat plate model bluff base (6mm) and its length equal to the span of the model, 400mm.
 - The ground end of the HVA was connected to the electrode to be encapsulated.

Induced Forcing

The induced winds in the spanwise modulated transverse staggered actuation case are shown in Fig. D.4. As before, the plasma zone for one exposed electrode segment on a side in any $x - y$ plane along its span started from the sharp trailing edge on its side and extended along the blunt model base in the transverse direction, close to the wall. However, unlike in the transverse opposing actuation case, there was no plasma generated from the other side at the same spanwise locations due to the staggered placement of the exposed electrode segments on the upper and lower trailing edge surfaces. Hence, the plasma zone from one exposed electrode segment could spread across the blunt base without any overlap. An analysis of the electric field generated by the present electrode layout (at spanwise location ' $z3'$ ') and actuation conditions is given in App. F.2. The induced wind from an exposed-encapsulated electrode combination starts from the sharp trailing edge on the side considered, is directed along the transverse direction towards the base center and close to the base surface.

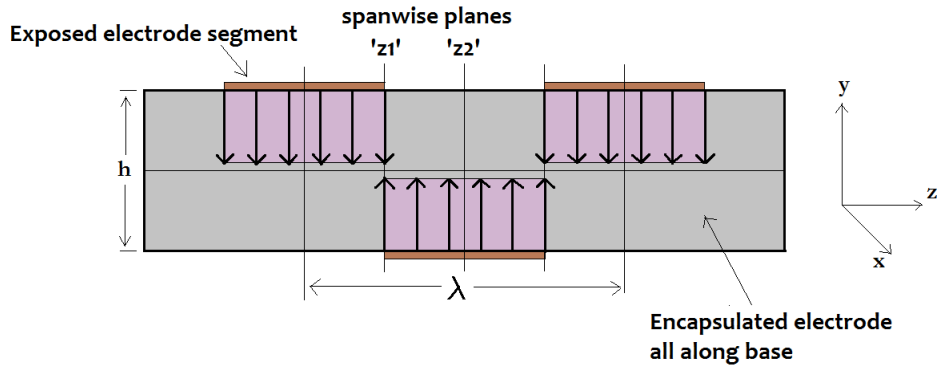


Figure D.4: Schematic showing the electrodes, induced forcing and imaged $x - y$ planes in the spanwise modulated transverse staggered actuation mode

Imaged Spanwise Planes

Based on the electrode configuration, it was decided to laser-illuminate two spanwise $x - y$ and one transverse $x - z$ plane for PIV time-resolved measurements. The $x - y$ planes imaged were chosen close to the middle of the span of the model to avoid end-effects associated with the wind tunnel walls. These are listed below and shown in Fig D.3.

- Spanwise $x - y$ planes in one actuation spatial cycle:
 1. The spanwise location at the interface between the regions having exposed electrode and no-electrode on the upper and lower sides; $z = z1$.
 2. The middle of a spanwise location without exposed electrode on one side and an exposed electrode on the other, displaced by $\lambda/2$ along the span from $z1$.
- Transverse $x - z$ planes:
 1. The shear layer plane, $y = 0.5h + 2$ mm. A transverse height of $y = 0.5h$ at the trailing edge upper surface would have been ideal, but the laser plane was lifted by 2mm from the surface to avoid the reflections from the surface.

D.5 Spanwise Actuation

Electrode Layout

The following steps were involved in the implementation of spanwise actuation with a configuration of spatial wavelength λ . The resulting arrangement in the $y - z$ plane at the model bluff base is shown in Fig.D.5.

- Segments of adhesive copper tape were cut with (spanwise) width 5mm and (streamwise) length of 25 mm. These comprised the exposed electrode(s) of the actuation scheme.

These segments were arranged and affixed in an alternating manner on the upper and lower surfaces of the end fixture with

- one spanwise edge parallel to and 3mm upstream of the trailing edge;
- the electrode segments on both the surfaces lined up so that when they were projected on any $x - z$ plane they coincided;
- the spanwise distance between corresponding streamwise edges of any two adjacent exposed electrode segments on both surfaces equal to λ .
- A thin strip of copper tape was laid out on both the upper and lower end fixture surfaces to connect the respective separate individual exposed electrode segments. These thin strips from both sides were then jointly connected together to the high-voltage output of the High Voltage Amplifier (HVA).
- Segments of adhesive copper tape were cut with (spanwise) width $(\lambda - 5)$ mm and (streamwise) length of 25 mm. These segments comprised the encapsulated electrode when the trailing edge end fixture is mated with the bluff end of the flat plate model. These segments were arranged and affixed in an regular manner on the upper and lower surfaces of the flat plate experimental model such that:
 - the electrode segments on both these surfaces lined up so that when they were projected on any $x - z$ plane they coincided;
 - each segment lay at a spanwise position exactly between two exposed electrode segments; when the exposed electrode segments are projected on the $x - z$ plane of the electrode segments to be encapsulated on any surface, they did not coincide - there was no overlap or gap between the projected areas.
 - one spanwise edge along the trailing edge of the flat plate model;
 - A thin strip of copper tape was laid out on both the upper and lower flat plate model surfaces close to the trailing edge to connect the respective separate individual electrode segments to be encapsulated. These thin strips from both sides were then jointly connected together to the ground terminal of the High Voltage Amplifier (HVA).

Induced Forcing

The induced winds for a spanwise actuation layout are shown in Fig. D.5. In this case, the plasma zone from one exposed electrode extends from its streamwise edges along the spanwise direction on both sides. In general for a plasma actuator the extent of the plasma zone depends on the strength of the electric field. For the strong electric field used in these experiments, it is likely that the zone of plasma on a surface (upper or lower) on either spanwise sides of an exposed electrode segment will spread, encounter and overlap with the plasma zones from the exposed electrode segments adjacent to the one considered on either side. Since the ions are accelerated till the edge of the plasma zone away from the exposed electrode, in the cases with overlap of plasma the induced spanwise flows from the exposed electrode segment towards either side will encounter the opposing flow from the adjacent exposed electrode. A local stagnation region will be created around the middle of the spanwise extent of an encapsulated electrode segment and a lift-up will be created. Concomitantly, a flow down will take place over the exposed electrode segments to main momentum balance - this 'depression' is what 'charges' the plasma induced spanwise flows on either side of an exposed electrode segment.

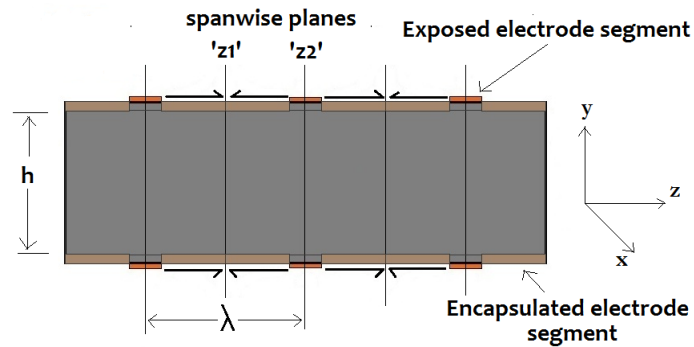


Figure D.5: Schematic showing the exposed and covered electrode placement on the upper and lower trailing edge end fixture surfaces and flat plate model surfaces, induced forcing and imaged $x - y$ planes in the spanwise actuation mode

Spanwise Planes

Based on the electrode configuration, it was decided to laser-illuminate two spanwise $x - y$ and one transverse $x - z$ plane for PIV time-resolved measurements. The $x - y$ planes imaged were chosen close to the middle of the span of the model to avoid end-effects associated with the wind tunnel walls. These are listed below and shown in Fig D.5.

- Spanwise $x - y$ planes in one actuation spatial cycle:
 1. the middle of a spanwise location over an encapsulated electrode; $z = z_1$;
 2. the middle of a spanwise location over a covered electrode, and displaced by $\lambda/2$ along the span from z_1 ; $z = z_2$;
- Transverse $x - z$ planes:
 1. The shear layer plane, $y = 0.5h + 2$ mm. A transverse height of $y = 0.5h$ at the trailing edge upper surface would have been ideal, but the laser plane was lifted by 2mm from the surface to avoid the reflections from the surface.

Appendix E

Time Resolved PIV Experimental Matrix

This section lists the various imaging 'runs' that were carried out during the time-resolved PIV Campaign. Some points to note while reviewing the tables that follow:

1. The 'Mode' column is the actuation scheme that was tested. The numbers 1, 2, 3, 4 and 5 used stand for the following:
 - 1 - Baseline (un-actuated) flow
 - 2 - Spanwise uniform transverse actuation
 - 3 - Spanwise modulated transverse opposing actuation
 - 4 - Spanwise modulated transverse staggered actuation
 - 5 - Spanwise actuation
2. The column 'Location' refers to the location of the imaged plane.
3. The column 'Rec' is the recording mode, which was Double-frame (DF) in all the cases.
4. The experimental parameters and their units are as follows:
 - U_∞ - Free stream, m/s
 - V_{pp} - Actuation input signal peak to peak amplitude, kV
 - f_{AC} - Actuation input signal frequency, Hz
 - Δt - Time separation between image-pairs, μs
 - f_{PIV} - PIV frequency of image-pair acquisition, Hz
 - FOV - Field of view, mm^2

Mode	Config.	Imaged Plane	Location	U_∞	V_{pp}	f_{AC}	Δt	Rec.	f_{PIV}	Images	FOV
1	n.a.	$x - y$	n.a.	5	40	1250	150	DF	3000	2816	50×50
				8			95				
				11			68				
				14			53				
2	n.a.	$x - y$	n.a.	5	40	1250	150	DF	3000	2816	50×50
				8			95				
				11			68				
				14			53				
3	$\lambda = 3h$	$x - y$	$z = z1$	5	40	1250	150	DF	3000	2816	50×50
				8			95				
				11			68				
				14			53				
3	$\lambda = 3h$	$x - y$	$z = z2$	5	40	1250	150	DF	3000	2816	50×50
				8			95				
				11			68				
				14			53				
3	$\lambda = 3h$	$x - y$	$z = z3$	5	40	1250	150	DF	3000	2816	50×50
				8			95				
				11			68				
				14			53				
3	$\lambda = 3h$	$x - y$	$z = z1$	5	40	1250	150	DF	3000	2816	50×50
				8			95				
				11			68				
				14			53				
4	$\lambda = 3h$	$x - y$	$z = z2$	5	40	1250	150	DF	3000	2816	50×50
				8			95				
				11			68				
				14			53				

Mode	Config.	Imaged Plane	Location	U_∞	V_{pp}	f_{AC}	Δt	Rec.	f_{PIV}	Images	FOV
4	$\lambda = 5h$	$x - y$	$z = z1$	5	40	1250	150	DF	3000	2816	50×50
				8			95				
				11			68				
				14			53				
4	$\lambda = 5h$	$x - y$	$z = z2$	17	40	1250	44	DF	3000	2816	50×50
				5			150				
				8			95				
				11			68				
4	$\lambda = 5h$	$x - y$	$z = z3$	14	40	1250	53	DF	3000	2816	50×50
				17			44				
				5			150				
				8			95				
4	$\lambda = 5h$	$x - y$	$z = z1$	11	40	1250	68	DF	3000	2816	50×50
				14			53				
				17			44				
				5			150				
4	$\lambda = 5h$	$x - y$	$z = z2$	8	40	1250	95	DF	3000	2816	50×50
				11			68				
				14			53				
				17			44				
4	$\lambda = 5h$	$x - y$	$z = z2$	5	40	1250	150	DF	3000	2816	50×50
				8			95				
				11			68				
				14			53				
5	$\lambda = 2h$	$x - y$	$z = z1$	17	40	1250	44	DF	3000	2816	50×50
				5			150				
				8			95				
				11			68				
5	$\lambda = 2h$	$x - y$	$z = z2$	14	40	1250	53	DF	3000	2816	50×50
				17			44				
				5			150				
				8			95				

Mode	Config.	Imaged Plane	Location	U_{∞}	V_{pp}	f_{AC}	Δt	Rec.	f_{PIV}	Images	FOV
5	$\lambda = 3h$	$x - y$	$z = z1$	5	40	1250	150	DF	3000	2816	50×50
				8			95				
				11			68				
				14			53				
5	$\lambda = 3h$	$x - y$	$z = z2$	5	40	1250	150	DF	3000	2816	50×50
				8			95				
				11			68				
				14			53				
5	$\lambda = 4h$	$x - y$	$z = z1$	5	40	1250	150	DF	3000	2816	50×50
				8			95				
				11			68				
				14			53				
5	$\lambda = 4h$	$x - y$	$z = z2$	5	40	1250	150	DF	3000	2816	50×50
				8			95				
				11			68				
				14			53				
1	n.a.	$x - z$	$y = 0$	5	40	1250	150	DF	3000	2816	50×50
				8			95				
				11			68				
				14			53				
1	n.a.	$x - z$	$y = USL$	5	40	1250	150	DF	3000	2816	50×50
				8			95				
				11			68				
				14			53				
2	n.a.	$x - z$	$y = USL$	5	40	1250	150	DF	3000	2816	50×50
				8			95				
				11			68				
				14			53				

Mode	Config.	Imaged Plane	Location	U_∞	V_{pp}	f_{AC}	Δt	Rec.	f_{PIV}	Images	FOV
3	$\lambda = 3h$	$x - z$	$y = 0$	5	40	1250	150	DF	3000	2816	50×50
				8			95				
				11			68				
				14			53				
				17			44				
3	$\lambda = 3h$	$x - z$	$y = USL$	5	40	1250	150	DF	3000	2816	50×50
				8			95				
				11			68				
				14			53				
				17			44				
4	$\lambda = 3h.$	$x - z$	$y = USL$	5	40	1250	150	DF	3000	2816	50×50
				8			95				
				11			68				
				14			53				
				17			44				
5	$\lambda = 2h.$	$x - z$	$y = USL$	5	40	1250	150	DF	3000	2816	100×100
				8			95				
				11			68				
				14			53				
				17			44				
5	$\lambda = 4h.$	$x - z$	$y = USL$	5	40	1250	150	DF	3000	2816	100×100
				8			95				
				11			68				
				14			53				
				17			44				
1 (BL)	n.a.	$x - y$	$y = USL$	5	40	1250	150	DF	3000	500	50×50
				8			95				
				11			68				
				14			53				
				17			44				

Appendix F

Electric Field Analysis

This section contains the electric field for the various actuation cases determined by solving the electrostatic Poisson equation for the electric potential ϕ for the appropriate respective geometries:

$$-\Delta(\epsilon\Delta\phi) = \rho \quad (\text{F.1})$$

where ϵ is the dielectric coefficient of the material between the exposed and covered electrodes (in the present cases, Makrolon with $\epsilon \simeq 3$) and ρ is the space charge density. The equation is solved here by setting ρ to 0, an approximation that takes into account the low space charge density of the ionised plasma region. The equation to be solved now reduces to the Laplace equation for the electric potential. The input for the electric potential is chosen to be the maximum voltage used during the experiment. It should be noted that this is the maximum value reached during an actuation cycle and not an averaged value. The various boundary conditions are:

1. Air side: $\Delta(\epsilon_A\Delta\phi) = 0$ $\epsilon_A = 1.0$
2. Dielectric material: $\Delta(\epsilon_D\Delta\phi) = 0$ $\epsilon_A = 3$
3. Exposed electrode: Connected to HVA high voltage input $\phi = V_{pp}/2 = 20kV$
4. Covered electrode: Connected to HVA ground terminal $\phi = 0$
5. Outer boundaries of calculation domain: $\frac{\partial\phi}{\partial n} = 0$

F.1 Transverse Opposing Actuation

The (two-dimensional) electrode geometry considered here for calculating the electric field is at a spanwise position of $'z3'$. The layout of the electrodes is shown in Fig. F.1, with the thickness of the electrodes greatly exaggerated for ease of locating them.

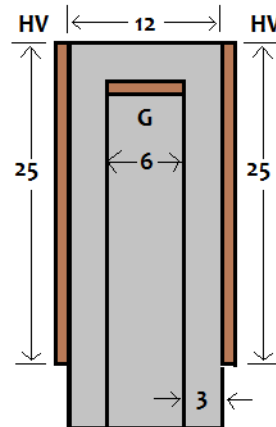


Figure F.1: Transverse Opposing electrode layout used for determining electric field and potential

The electric potential and electric field strengths are shown in Fig F.2. The strongest electric field is found at the tips of the electrodes closest to each other and the strength of the electric field decays when moving away from away from the exposed electrode. It is clear that electric fields of opposite signs are generated at both the ends. At the location where they overlap, around the middle of the model base, the electric field strength goes to zero, which indicates cancellation. As mentioned earlier, the plasma ions are not accelerated in this region due to the electric field cancellation, and this represents a loss of effective forcing that can be delivered by the plasma actuation layout.

Another point to be noted is that the exposed electrodes were arranged all the way to the trailing edge. If the exposed electrodes had stopped short, ending instead at the streamwise location of the covered electrode, it can be expected that the electric field generated would be stronger, due to the shorter distance between the tips of the electrodes.

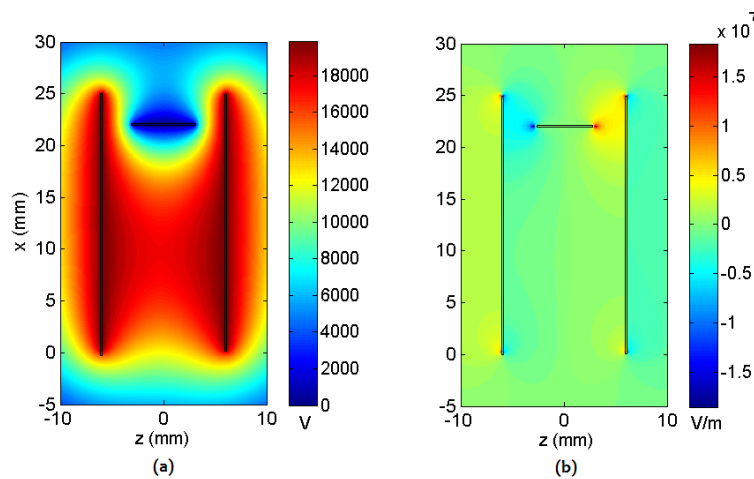


Figure F.2: Electric (a) potential and (b)field for transverse opposing actuation

Fig F.3(a) shows the magnitude of the electric field, in an image that covers a larger area of the flow field around the base. As can be seen, the field strength is the same at both the ends of the covered electrode (but opposite in sign). Also of interest is the fact that the majority of the areas with the largest electric fields lie *inside* the experimental model, and not in the region of fluid flow. However, the observation of Nati [27], that the actual effective area of electric field on the surrounding air has increased by a quadrant compared to the case of a planar plasma actuator such as in Fig D.1, is still valid, and on both the sides. Based on the electric field being responsible for the electric wind this indicates a more efficient flow acceleration due an increased effective area.

Fig F.3(b) shows the contours of electric field magnitude for 1×10^6 V/m and 2×10^6 V/m. These values, based on Artana's analysis mentioned in Sec 3.1.2, are the salient electric field strengths that delimit areas of electrostatic effect on the tracer particles. The areas where the field strength is 2×10^6 V/m or higher are enclosed by the brown contour lines, and are the regions of significant electrostatic effect on the flow tracer particles. The majority of these regions, however lie within the area of the model; the regions that are outside in the flow are found mainly at the extremities of the exposed electrodes on the upper and lower sides. Since the FOV's in the $x - y$ plane that were imaged lay mainly just downstream of the model base, the overlap between the FOV's and the regions in the flow with $E \geq 2 \times 10^6$ V/m was minimal. Also, one must take into account that the field was calculated using the maximum value $V_{pp}/2 = 20kV$ which was reached only twice during every actuation cycle and not an averaged value.

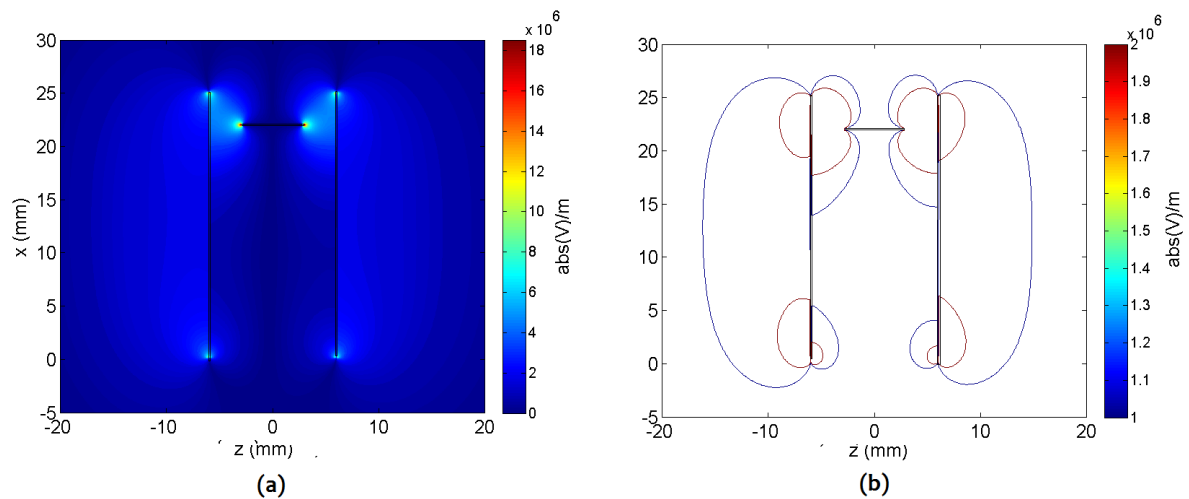


Figure F.3: (a) Electric field magnitude and (b) contours of electric field magnitude for 1×10^6 V/m and 2×10^6 V/m for transverse opposing actuation. The peak electric field is 1.866×10^7 V/m, occurring at the ends of the covered electrode

F.2 Transverse Staggered Actuation

The (two-dimensional) electrode geometry considered here for calculating the electric field is at a spanwise position of z' . The layout of the electrodes is shown in Fig. F.4, with the thickness

of the electrodes greatly exaggerated for ease of locating them.

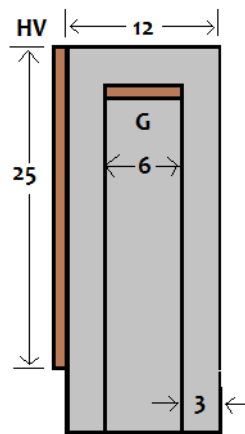


Figure F.4: Transverse Staggered electrode layout used for determining electric field and potential

The electric potential and electric field strengths are shown in Fig F.5. As before the strongest electric field is found at the tips of the electrodes closest to each other and the strength of the electric field decays when moving away from the exposed electrode. Unlike in the case of transverse opposing actuation, however, there is no electric field overlap.

As with transverse opposing actuation, the exposed electrodes were arranged all the way to the trailing edge. If the exposed electrodes had stopped short, ending instead at the streamwise location of the covered electrode, it can be expected that the electric field generated would be stronger, due to the shorter distance between the tips of the electrodes.

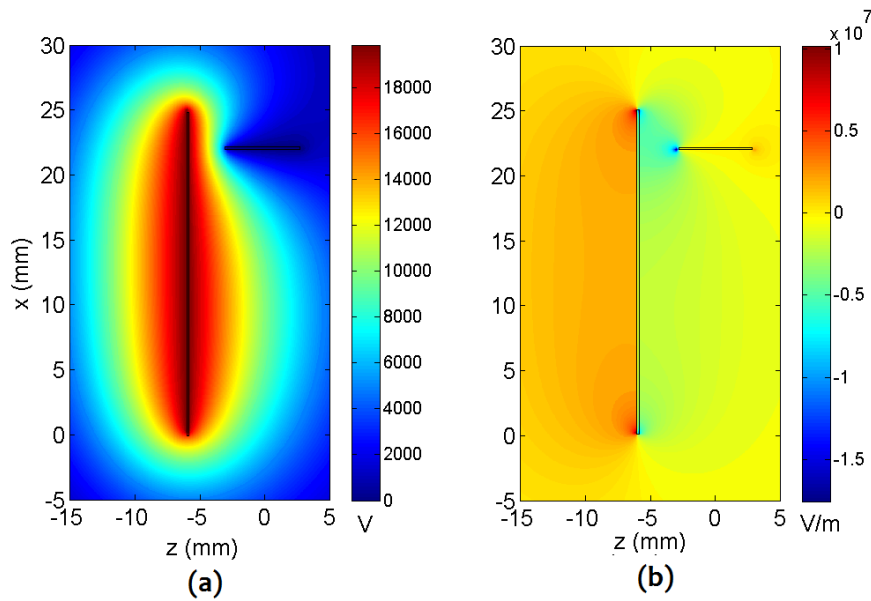


Figure F.5: Electric (a) potential and (b) field for transverse opposing actuation

Fig F.6(a) shows the magnitude of the electric field, in an image that covers a larger area of the flow field around the base. The majority of the areas with the largest electric fields lie inside the experimental model, and not in the region of fluid flow. However, the observation of Nati [27], that the actual effective area of electric field on the surrounding air has increased by a quadrant compared to the case of a planar plasma actuator such as in Fig D.1, is still valid. Based on the electric field being responsible for the electric wind this indicates a more efficient flow acceleration due an increased effective area.

Fig F.6(b) shows the contours of electric field magnitude for 1×10^6 V/m and 2×10^6 V/m. The areas where the field strength is 2×10^6 V/m or higher are enclosed by the brown contour lines, and are the regions of significant electrostatic effect on the flow tracer particles. The majority of these regions lie within the area of the model; the regions that are outside in the flow are found mainly at the extremities of the exposed electrodes on the upper and lower sides. Since the FOV's in the $x - y$ plane that were imaged lay mainly just downstream of the model base, the overlap between the FOV's and the regions in the flow with $E \geq 2 \times 10^6$ V/m was minimal. Also, one must take into account that the field was calculated using the maximum value $V_{pp}/2 = 20kV$ which was reached only twice during every actuation cycle and not an averaged value.

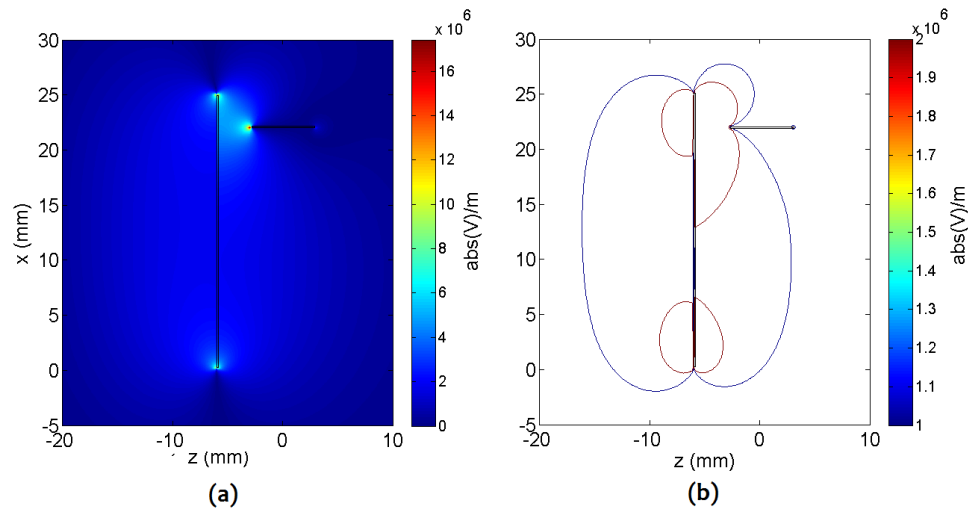


Figure F.6: (a) Electric field magnitude and (b) contours of electric field magnitude for 1×10^6 V/m and 2×10^6 V/m for transverse staggered actuation. The peak electric field is 1.755×10^7 V/m, occurring at the end of the covered electrode closest to the exposed electrode

F.3 Planar Actuator Configurations

In this section, the electric field generated by the 'corner actuator' will be compared with those of planar actuator configurations. In this exercise, planar configurations with and without overlap between the exposed and covered electrodes are considered, Fig F.7. The overlap would be found if the corner actuator covered electrode would be rotated perpendicular to itself and aligned with the exposed electrode. The no-overlap case represents a typical planar plasma actuator. The objective of this exercise is to better understand the effect of the perpendicularity between the electrodes and the net effect it has on the induced flow, which was one of the recommended topics for further research in the work of Nati [27]. Nati suggested that based on the electric field being responsible for the electric wind, the increase in effective area of the electric field exposed to the fluid by a quadrant (Fig F.6) might indicate a more efficient flow acceleration due an increased effective area.

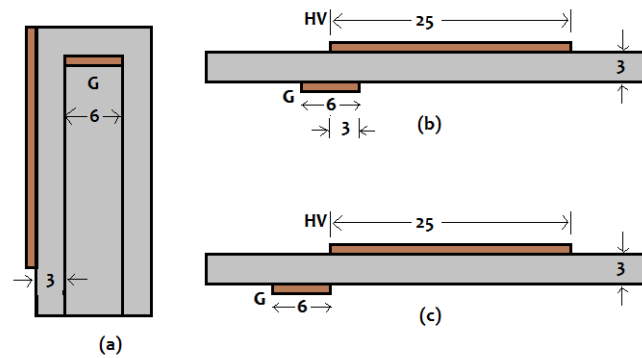


Figure F.7: (a) Corner Actuator; (b) and (c) Planar Actuator configurations with and without overlap between the exposed and covered electrodes

The following figures show the electric field contours from 0 to 2×10^6 V/m in steps of 0.1×10^6 V/m for the corner actuator (Fig. F.8) and the planar actuator configurations with overlap (Fig. F.9) and without overlap (Fig. F.10) between the exposed and covered electrodes respectively. It can be seen that the corner actuator produces the largest region with high electric field. most of this regions lies outside the body, hence is exposed to the flow outside. Hence a large region of plasma induced flow acceleration is found. Comparing the electric field contours of the planar actuators with and without electrode overlap, it is seen that the increased proximity between the extremities of the exposed and covered electrodes for the no-overlap actuator gives rise to a larger area with high electric field. The bulk of this region, however is found within the body. For the planar actuator with overlap, individual regions with electric field are found at the extremities of the exposed and covered electrodes closest to each other, but their greater distance means that these regions do not coalesce. However, the *peak* electric field value for the no-overlap planar actuator is 2.02×10^7 V/m, which is *lower* compared to that of the planar actuator with overlap, 2.12×10^7 V/m. Also a slightly larger region with high electric field is seen for the latter case at the extremity of the exposed electrode away from the covered electrode compared to the no-overlap case, due to the lesser distance of this end from the covered electrode. When comparing the regions of high electric field that is exposed to the flow (outside the body) however, the overlap and no-overlap cases are roughly equal, meaning that the induced forcing on the air would be roughly the same. It is however clear that the forcing of the corner actuator would greatly exceed that of the planar actuators, due to the larger regions of high electric field that are outside the body.

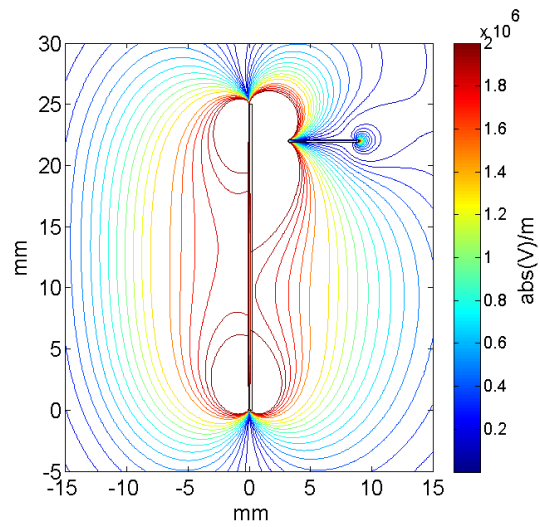


Figure F.8: Electric field contours of the corner actuator

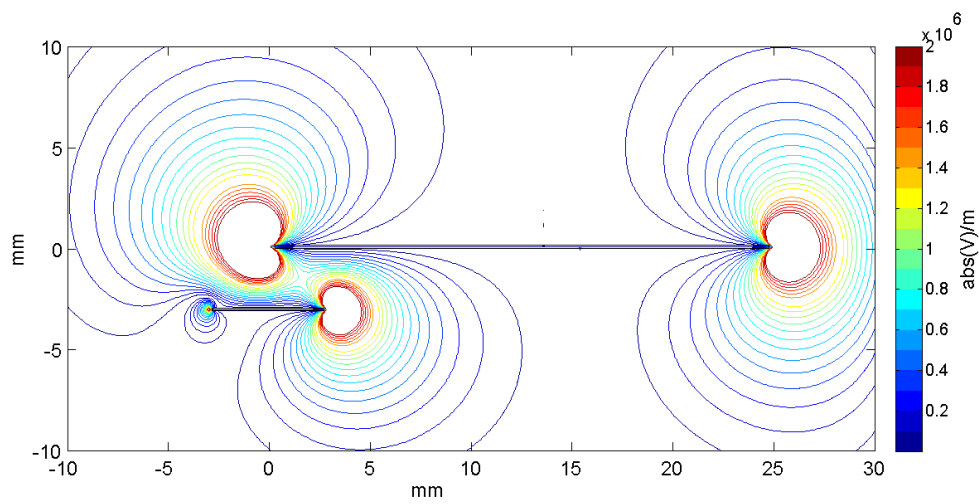


Figure F.9: Electric field contours of a planar actuator with electrode overlap. The peak electric field is 2.12×10^7 V/m at (0,0)

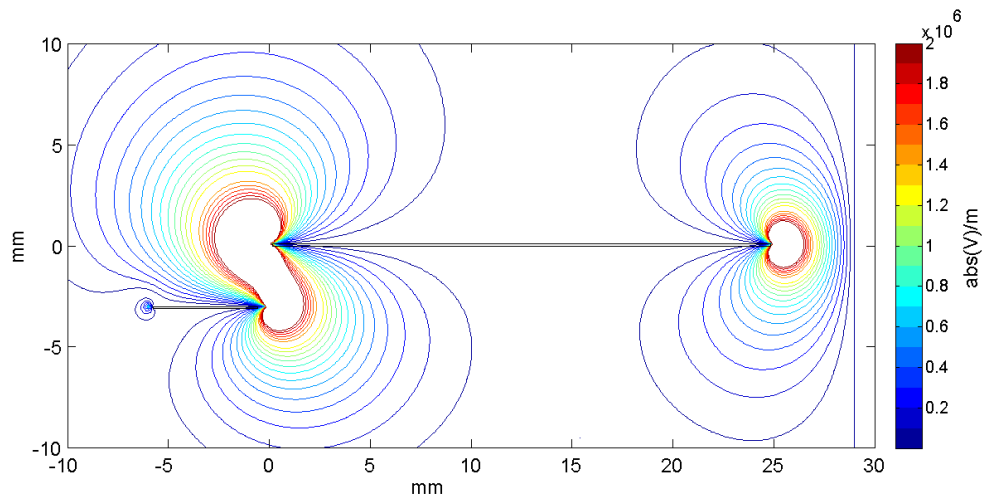


Figure F.10: Electric field contours of a planar actuator without electrode overlap. The peak electric field is 2.02×10^7 V/m at (0,0)

Appendix G

POD Energies over all tested Free Stream Speeds

This section includes the performance in terms of POD modal energies of the three modes tested - spanwise modulated opposing and staggered actuation and spanwise actuation

- over all the configurations tested for each (see Table 4.5)
- over all tested free stream speeds of $U_\infty = 5, 8, 11, 14$ and 17 m/s

It is stressed that *due to the significantly different actuation induced flow mechanisms of these modes, they must not be compared directly solely on the basis of these quantities.* The objective behind showing the various plots together here is to present this information in one place.

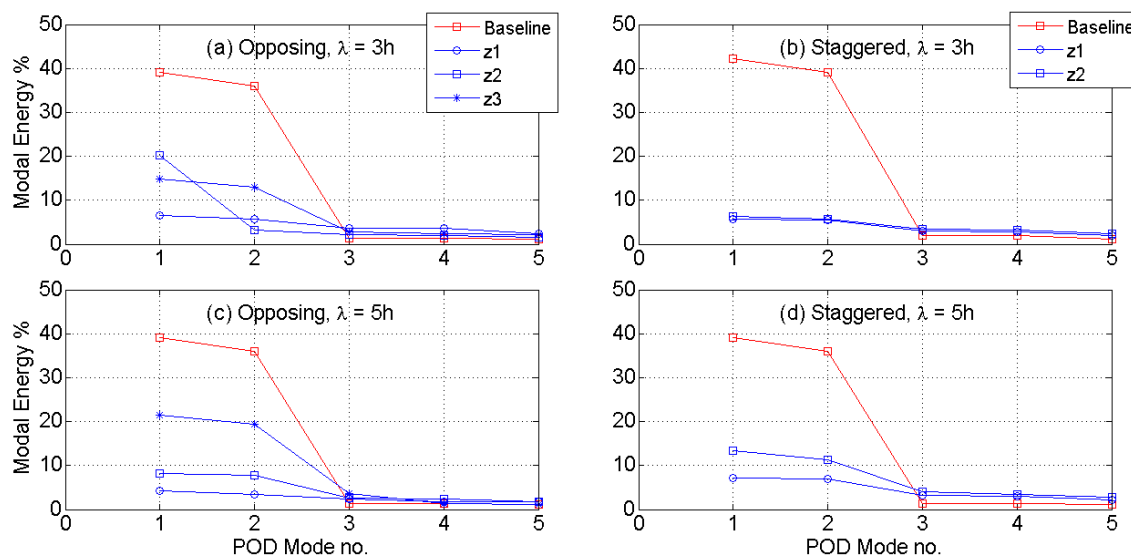


Figure G.1: Individual shares of the Fluctuating KE of the wake $x - y$ plane captured by the first five POD modes for $\lambda^* = 3$ and 5 configurations over all imaged spanwise locations for spanwise modulated transverse (a), (c) opposing and (b), (d) staggered actuation modes at $U_\infty = 5$ m/s. The Baseline flow values are also shown as reference in each

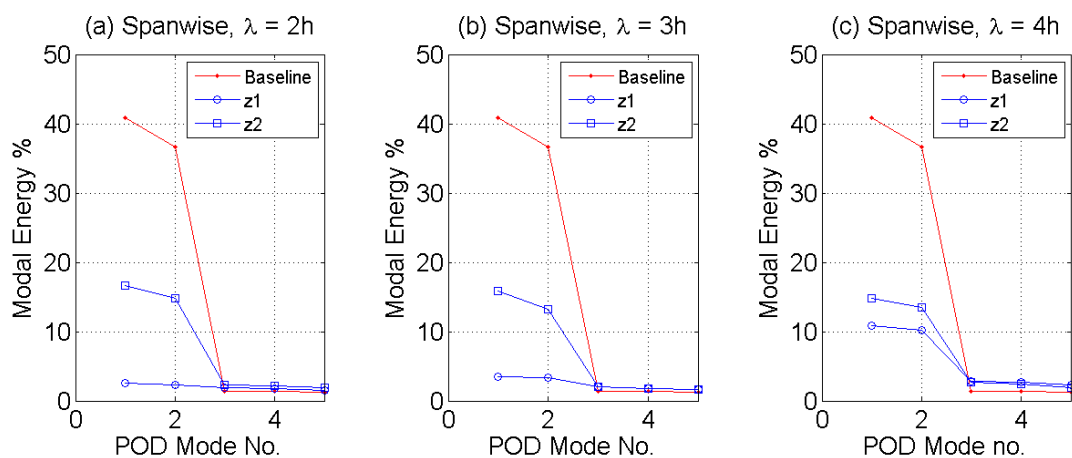


Figure G.2: Individual shares of the Fluctuating KE of the wake $x - y$ plane captured by the first five POD modes for spanwise actuation configurations $\lambda^* = 2, 3$ and 4 over all imaged planes at $U_\infty = 5$ m/s. The reference baseline flow value is also shown

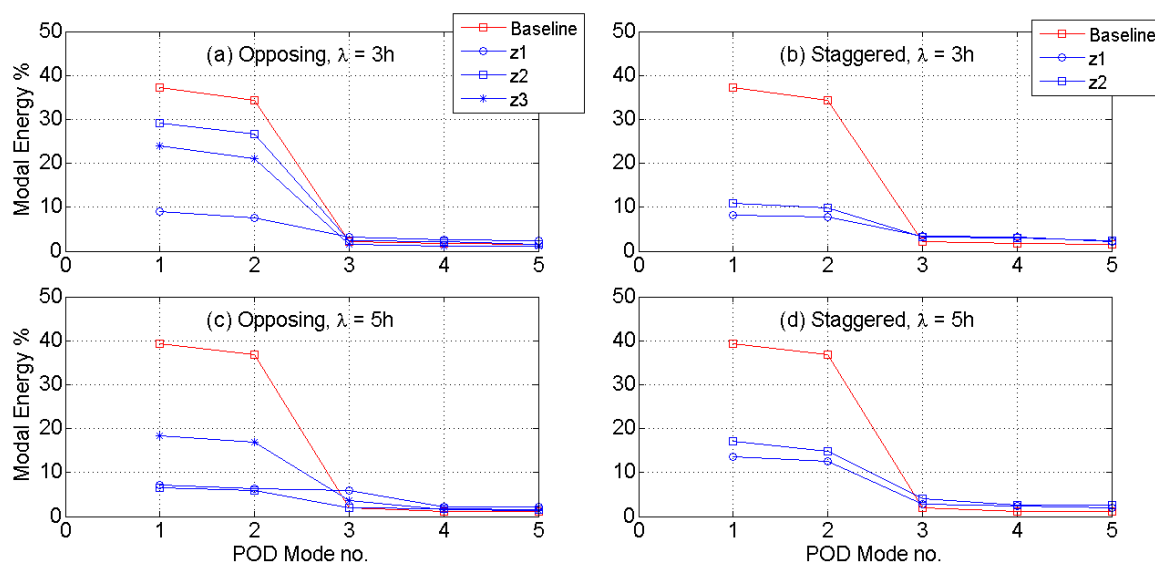


Figure G.3: Individual shares of the Fluctuating KE of the wake $x - y$ plane captured by the first five POD modes for $\lambda^* = 3$ and 5 configurations over all imaged spanwise locations for spanwise modulated transverse (a), (c) opposing and (b), (d) staggered actuation modes at $U_\infty = 8$ m/s. The Baseline flow values are also shown as reference in each

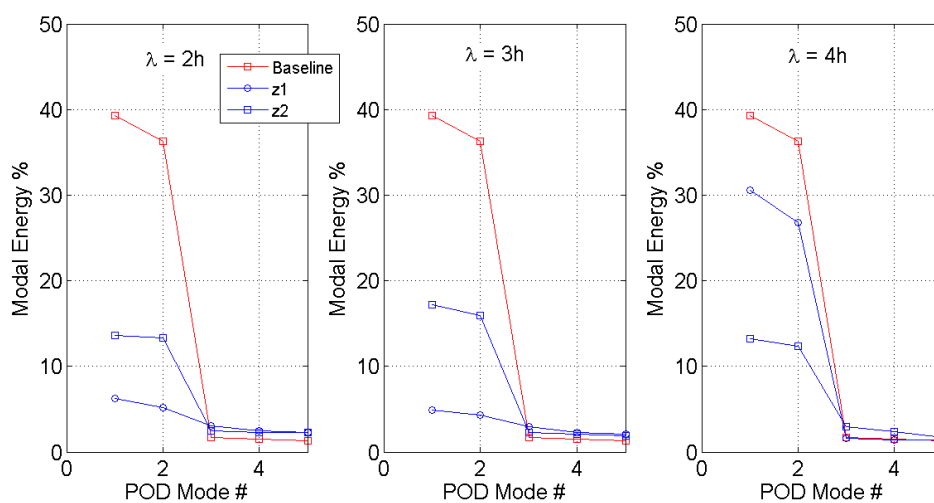


Figure G.4: Individual shares of the Fluctuating KE of the wake $x - y$ plane captured by the first five POD modes for spanwise actuation configurations $\lambda^* = 2, 3$ and 4 over all imaged planes at $U_\infty = 8$ m/s. The Baseline flow values are also shown as reference in each

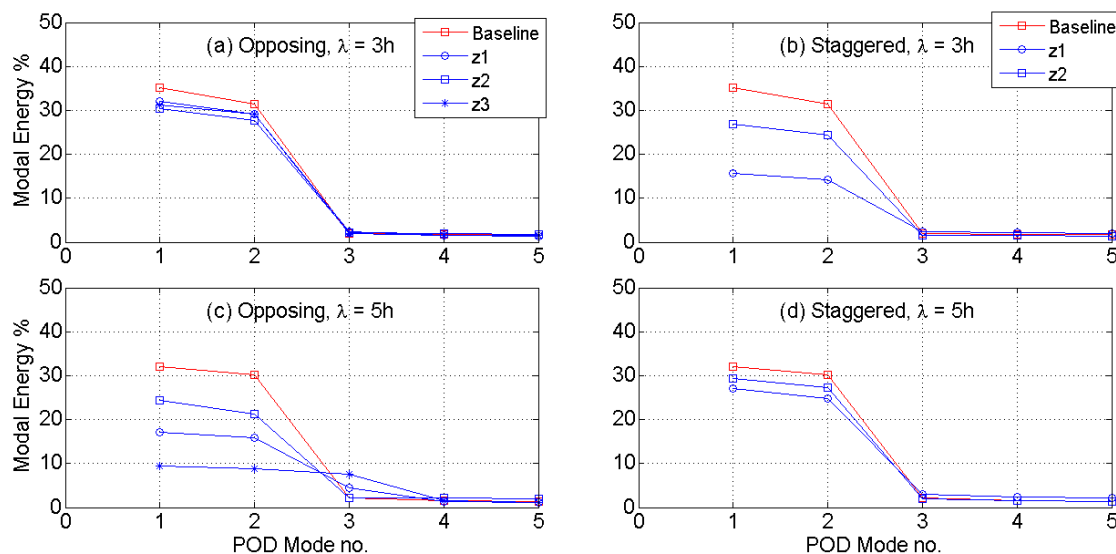


Figure G.5: Individual shares of the Fluctuating KE of the wake $x - y$ plane captured by the first five POD modes for $\lambda^* = 3$ and 5 configurations over all imaged spanwise locations for spanwise modulated transverse (a), (c) opposing and (b), (d) staggered actuation modes at $U_\infty = 11$ m/s. The Baseline flow values are also shown as reference in each

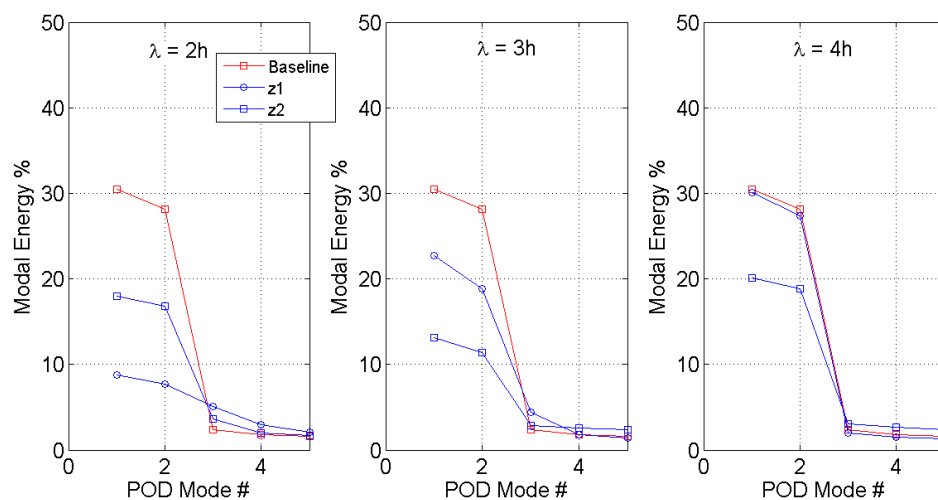


Figure G.6: Individual shares of the Fluctuating KE of the wake $x - y$ plane captured by the first five POD modes for spanwise actuation configurations $\lambda^* = 2, 3$ and 4 over all imaged planes at $U_\infty = 11$ m/s. The Baseline flow values are also shown as reference in each

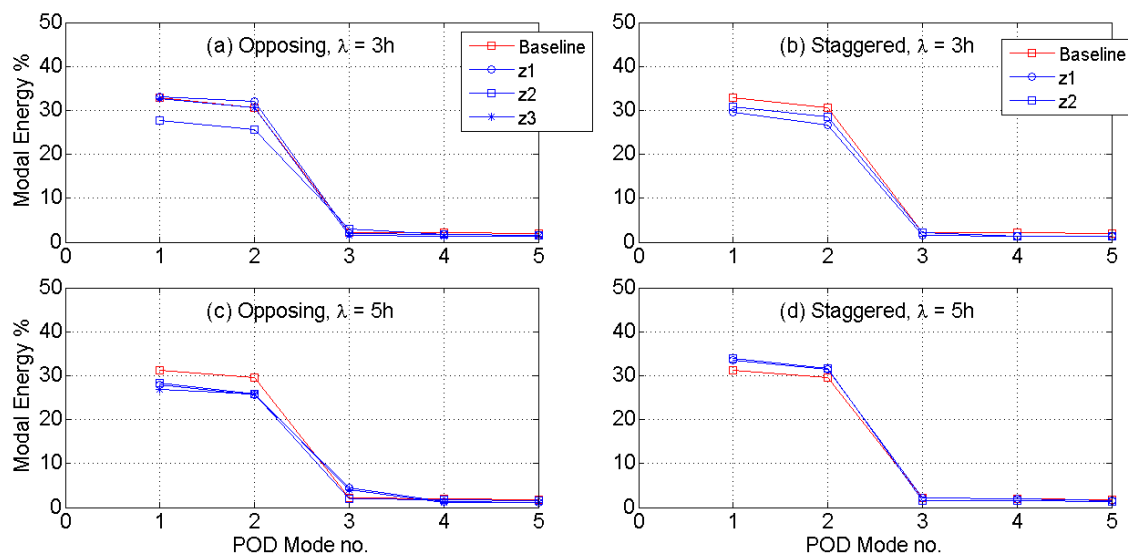


Figure G.7: Individual shares of the Fluctuating KE of the wake $x - y$ plane captured by the first five POD modes for $\lambda^* = 3$ and 5 configurations over all imaged spanwise locations for spanwise modulated transverse (a), (c) opposing and (b), (d) staggered actuation modes at $U_\infty = 14$ m/s. The Baseline flow values are also shown as reference in each

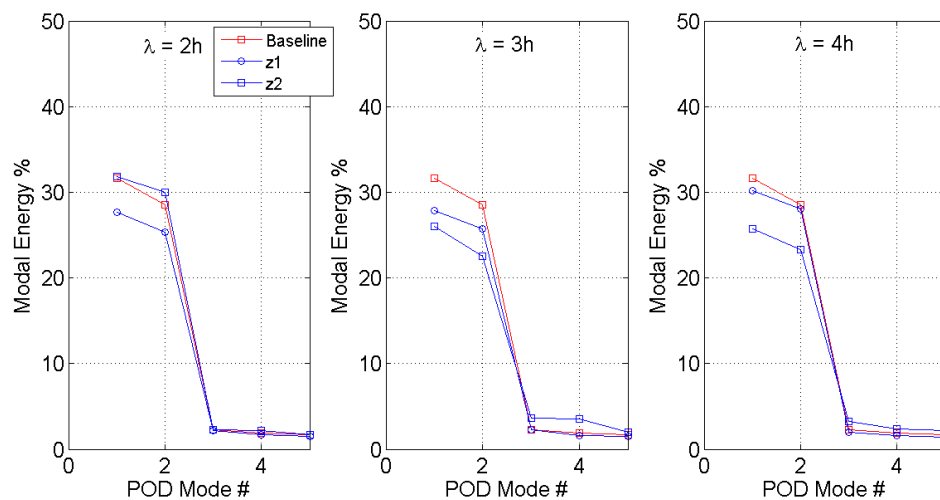


Figure G.8: Individual shares of the Fluctuating KE of the wake $x - y$ plane captured by the first five POD modes for spanwise actuation configurations $\lambda^* = 2, 3$ and 4 over all imaged planes at $U_\infty = 14$ m/s. The Baseline flow values are also shown as reference in each

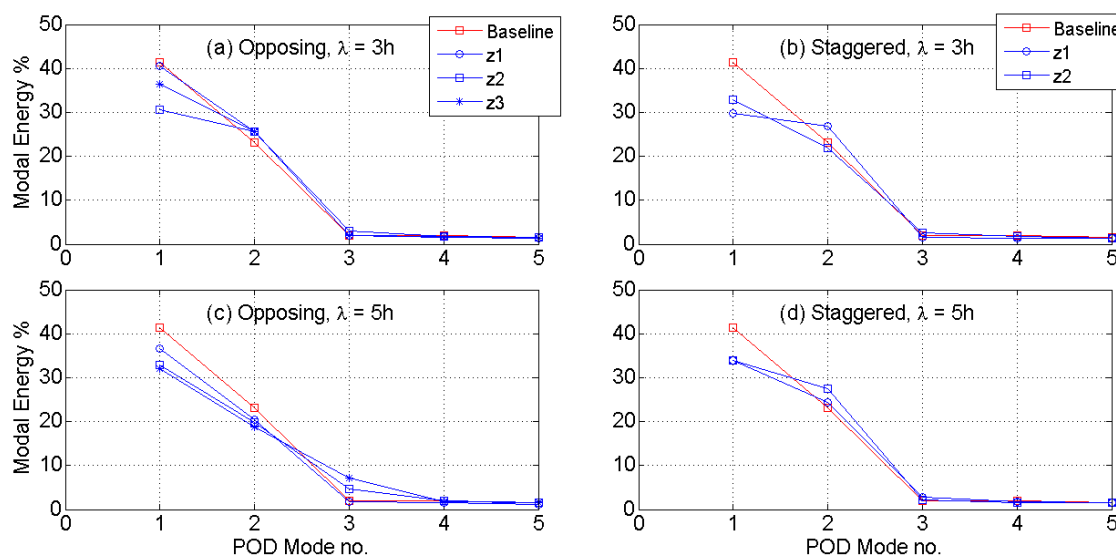


Figure G.9: Individual shares of the Fluctuating KE of the wake $x - y$ plane captured by the first five POD modes for $\lambda^* = 3$ and 5 configurations over all imaged spanwise locations for spanwise modulated transverse (a), (c) opposing and (b), (d) staggered actuation modes at $U_\infty = 17$ m/s. The Baseline flow values are also shown as reference in each

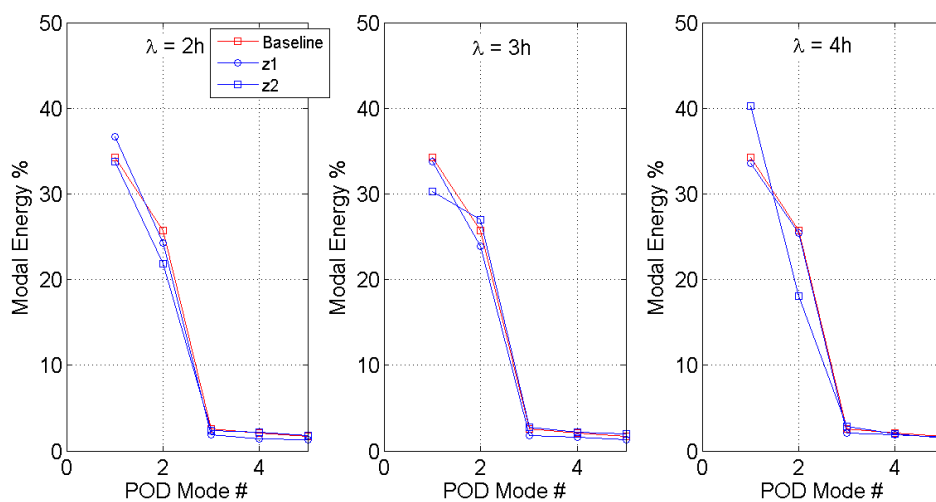


Figure G.10: Individual shares of the Fluctuating KE of the wake $x - y$ plane captured by the first five POD modes for spanwise actuation configurations $\lambda^* = 2, 3$ and 4 over all imaged planes at $U_\infty = 17$ m/s. The Baseline flow values are also shown as reference in each

Appendix H

Spanwise Correlation for all Modes and Configurations over all tested $U'_{\infty}s$

This section presents the correlation of the streamwise velocity signals across the span in the shear layer transverse $x - z$ plane (at $y = 0.5h + 2\text{mm}$) for all the spanwise modulated actuated configurations that had their spanwise plane flow fields imaged (see Table 4.5 for an overview). General observations and conclusions regarding the spanwise coherence of the shed Karman vortex rolls will be made based on the correlation results. The following are the aspects that one must keep in mind while reviewing the predominantly graphical results presented here:

1. The left hand side of the figures show the mean streamwise velocity flow field non-dimensionalised by the free stream in the imaged flow (u/U_{∞}). The trailing edge of the body is at $x = 0$ in these images. The spanwise positions of the $x - y$ planes imaged for each of the spanwise modulated actuated cases will be indicated in these figures too.
2. The right hand side shows multiple lines co-plotted. Each of these lines shows the correlation coefficients between the streamwise velocity time signal at the reference point whose streamwise position is fixed and the streamwise velocity time signal at other points along the span at the same streamwise position, plotted against the spanwise positions of the other points. The spanwise position of the reference point differs for each actuation mode (will be mentioned in the subsequent sections) but is generally at around mid-span of the imaged FOV.
3. The time period of the velocity signals here is over the PIV imaging period of 0.98 sec and with 2816 points collected at a frequency of 3000 Hz (See Table 4.4 for a summary of the experimental parameters).
4. All the length scales are non-dimensionalised - the streamwise distances by h the trailing edge height of the model (12 mm) and the spanwise distances by λ , the spanwise spatial 'wavelength' of actuation over which the electrode layout repeats itself.

H.1 Baseline flow cases

The correlation of the streamwise velocity signals across the span in the shear layer transverse $x - z$ plane for the baseline flow cases at all the tested free stream velocities $U_\infty = 5, 8, 11, 14$ and 17m/s will be shown here. This is done so that the spanwise correlation of the velocity signals for the actuated cases in the subsequent sections can be compared with that of the baseline flow cases shown here at the same free stream velocity.

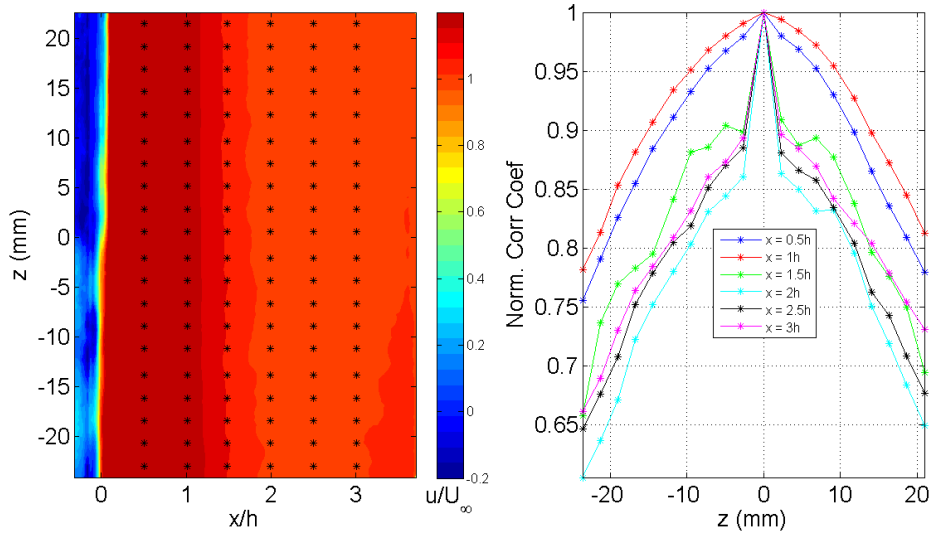


Figure H.1: Spanwise velocity-correlations for baseline flow at $U_\infty = 5\text{ m/s}$

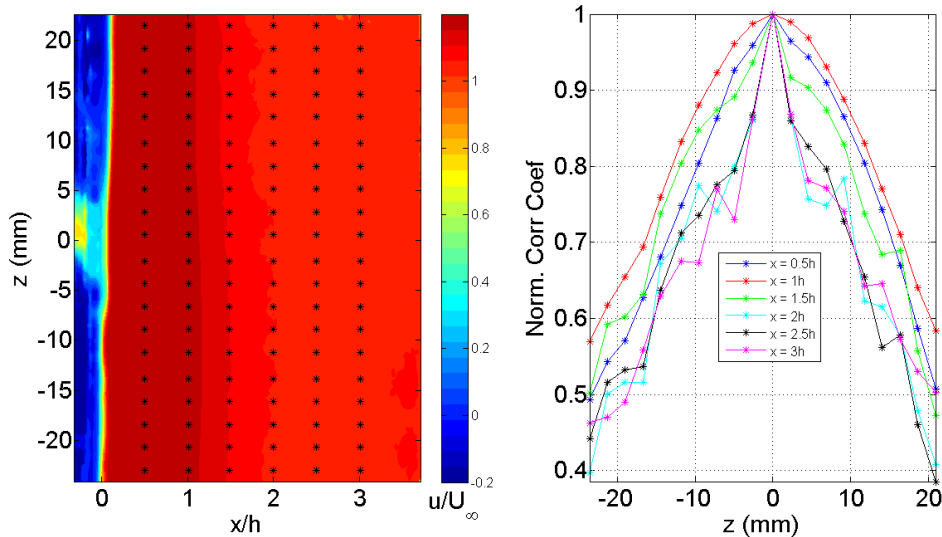


Figure H.2: Spanwise velocity-correlations for baseline flow at $U_\infty = 8\text{ m/s}$

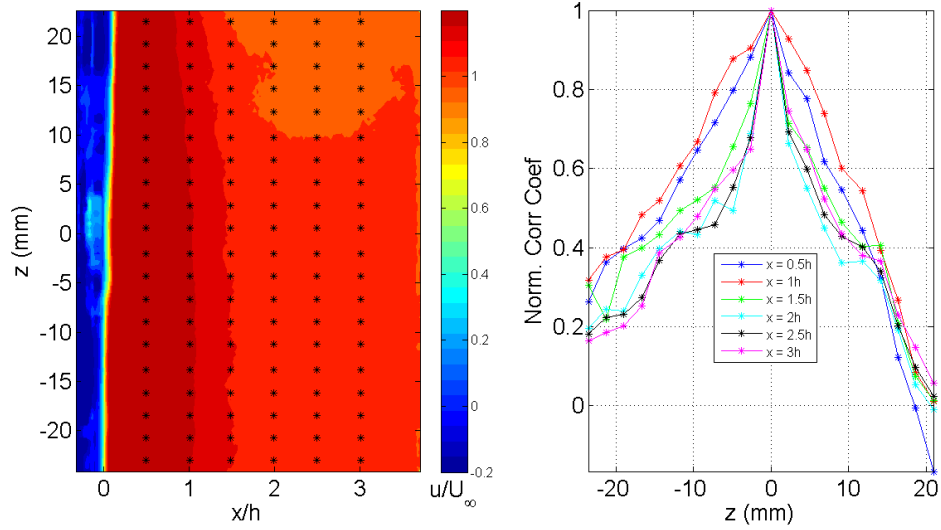


Figure H.3: Spanwise velocity-correlations for baseline flow at $U_\infty = 11$ m/s

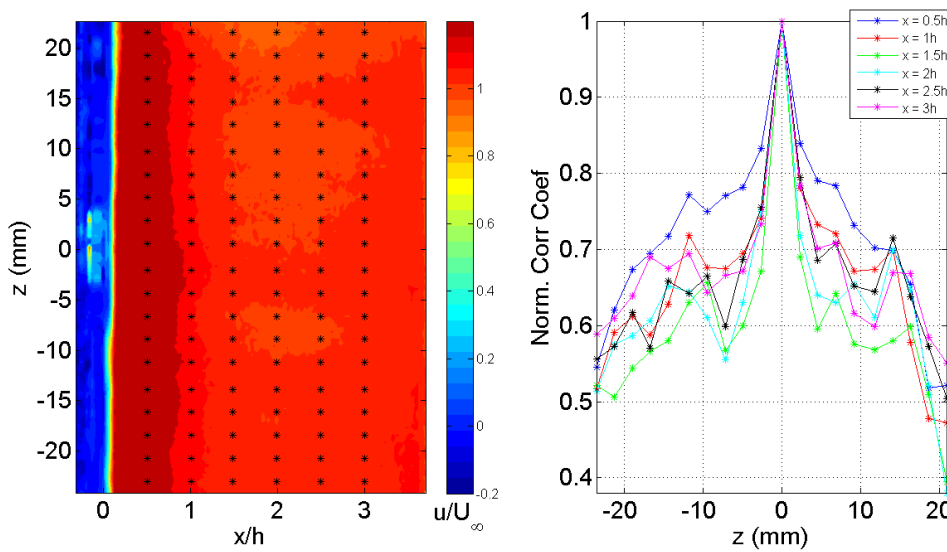


Figure H.4: Spanwise velocity-correlations for baseline flow at $U_\infty = 14$ m/s

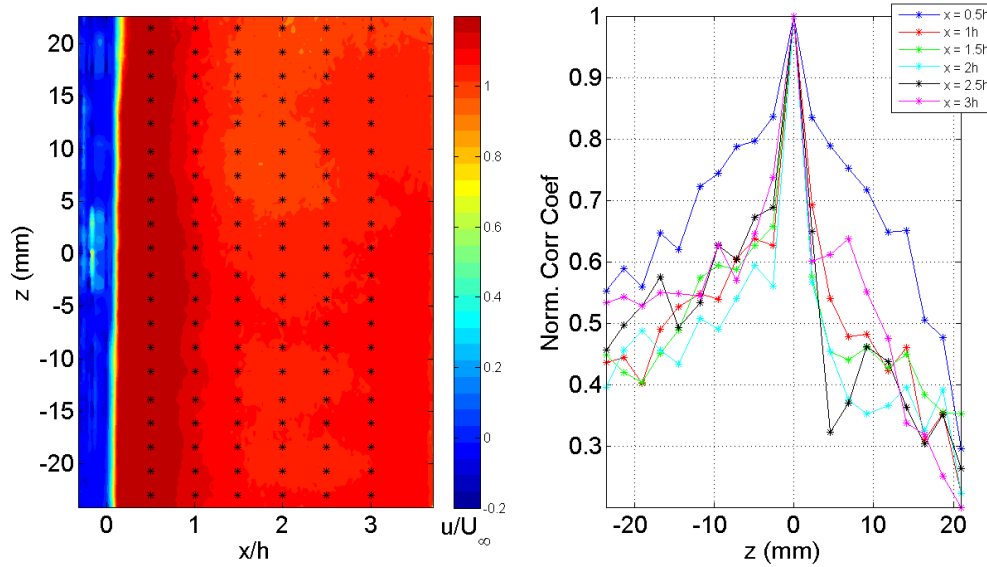


Figure H.5: Spanwise velocity-correlations for baseline flow at $U_\infty = 17$ m/s

H.2 Spanwise Modulated Transverse Opposing Actuation

The shear layer $x - z$ plane was imaged for spanwise modulated transverse opposing actuation for $\lambda_* = 3$. The ' z_2 ' spanwise position was taken as the reference position ($z = 0$) at which the velocity signal was found with respect to which all the other velocity signals along the spans at the various streamwise positions were correlated. The following are the observations that one can make from the figures:

1. The unique flow features associated with the different spanwise positions (for example, the lift-up that brings the low velocity fluid from the inner wake towards the outer flow at ' z_1 ') get less distinct as the U_∞ increases. This can be associated with the decreased effect of the fixed-power input actuation in deflecting the flow as the inflow momentum increases.
2. The correlation coefficients across the span are seen to rise as the U_∞ increases. In a similar manner as the previous observation, this can be associated with the decreased effect of the fixed-power input actuation in breaking the spanwise coherence of the shed Karman rolls.
3. Near baseline level correlation is regained by the shed Karman vortex rolls at $U_\infty = 11$ m/s, indicating that the upper limit of the effectiveness of the present actuation mode and configuration is around 11 m/s. However, this does not mean that the shedding is not attenuated at this speed. For this, the POD modal energies at the various spanwise positions would serve as a useful indicator (Sec. G).

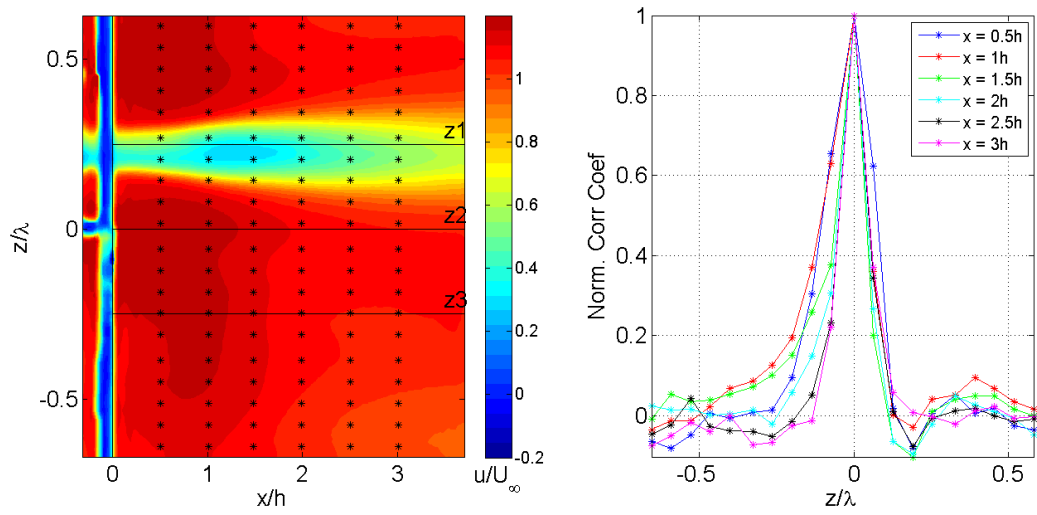


Figure H.6: Spanwise velocity-correlations for transverse opposing actuated flow at $U_\infty = 5$ m/s

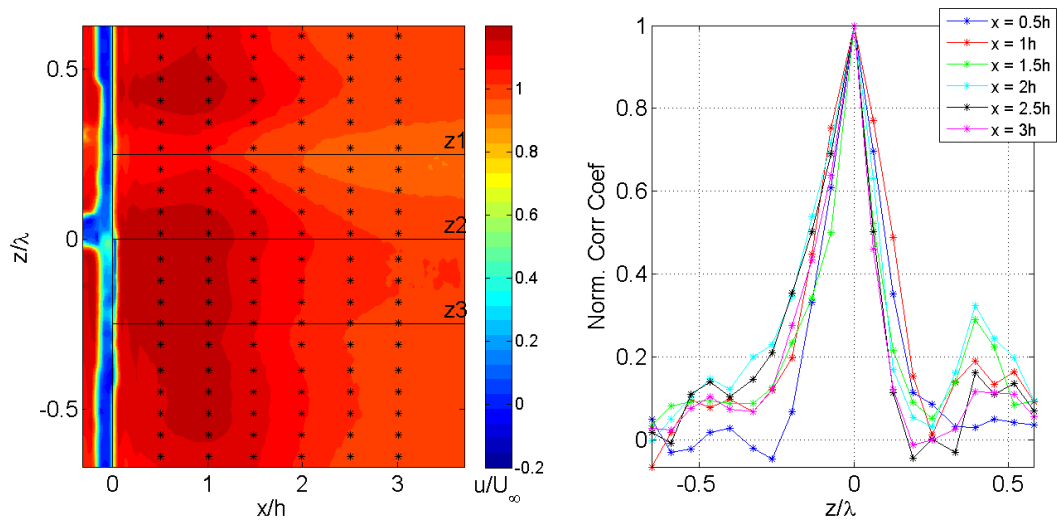


Figure H.7: Spanwise velocity-correlations for transverse opposing actuated flow at $U_\infty = 8$ m/s

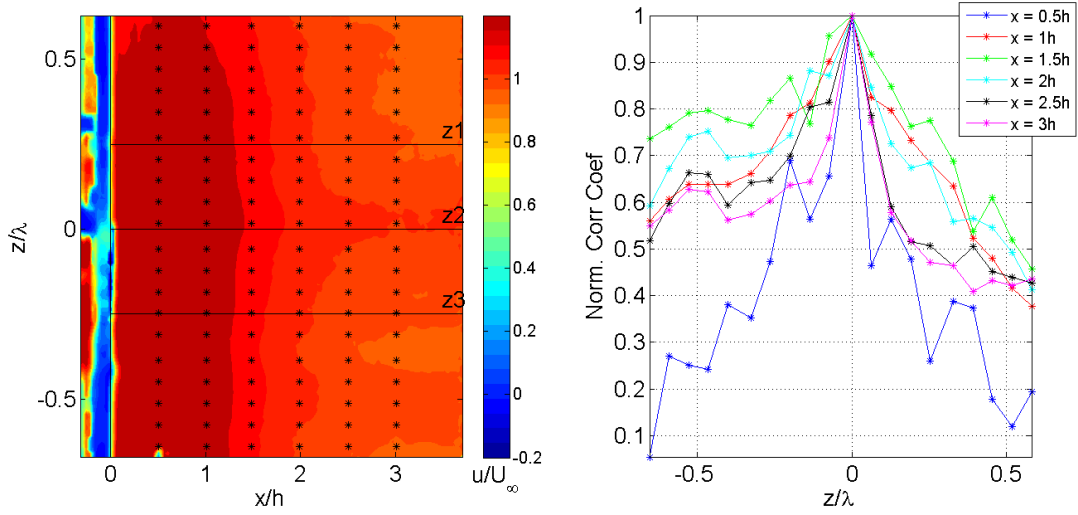


Figure H.8: Spanwise velocity-correlations for transverse opposing actuated flow at $U_\infty = 11$ m/s

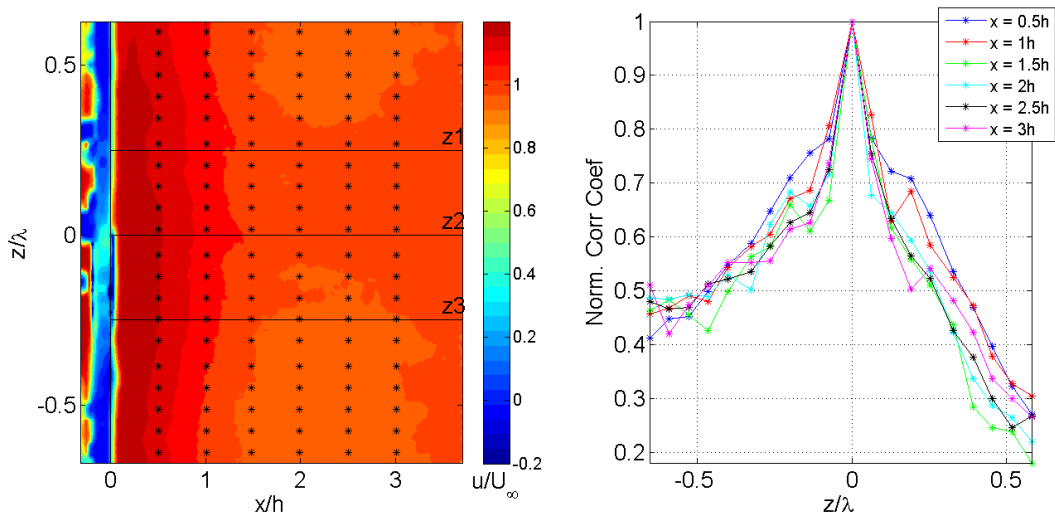


Figure H.9: Spanwise velocity-correlations for transverse opposing actuated flow at $U_\infty = 14$ m/s

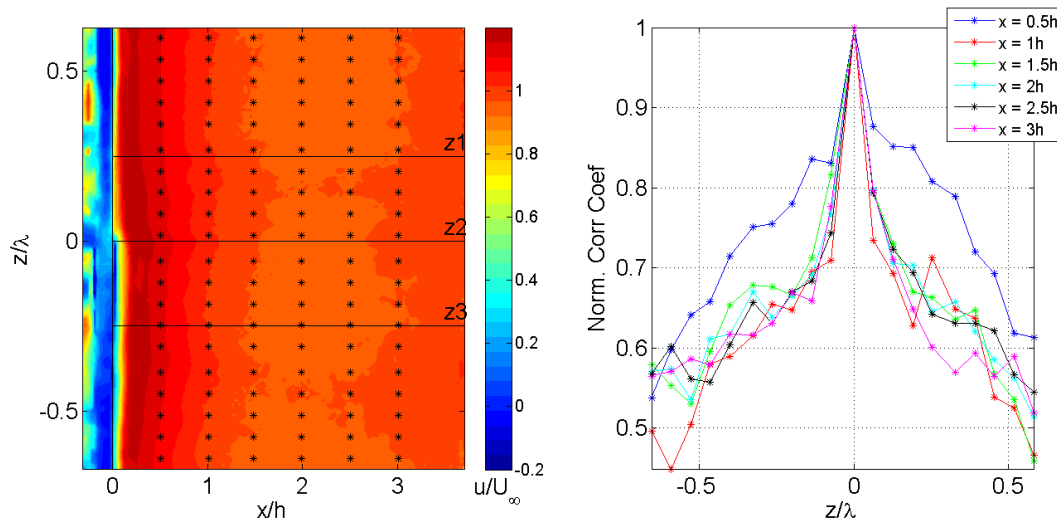


Figure H.10: Spanwise velocity-correlations for transverse opposing actuated flow at $U_\infty = 17$ m/s

H.3 Spanwise Modulated Transverse Staggered Actuation

The shear layer $x - z$ plane was imaged for spanwise modulated staggered opposing actuation for $\lambda^* = 3$. The ' $z1$ ' spanwise position was taken as the reference position ($z = 0$) at which the velocity signal was found with respect to which all the other velocity signals along the spans at the various streamwise positions were correlated. As for the previous actuation mode, the following are the observations that one can make from the figures:

1. The unique flow features associated with the different spanwise positions get less distinct as the U_∞ increases.
2. The correlation coefficients across the span are seen to rise as the U_∞ increases.
3. The spanwise correlation levels rise at $U_\infty = 11$ m/s. However, significant attenuation in the spanwise coherence persists at even the higher tested free stream velocities.

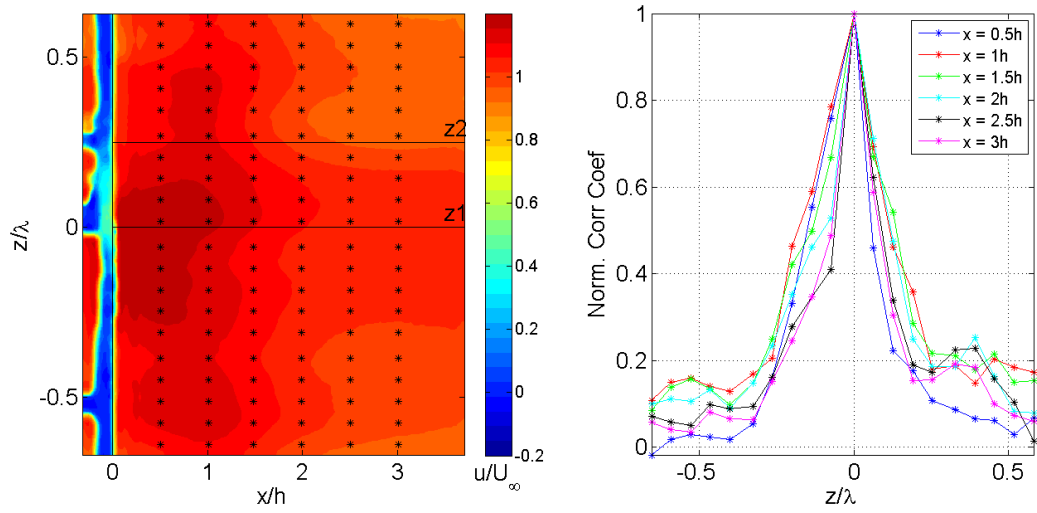


Figure H.11: Spanwise velocity-correlations for transverse staggered actuated flow at $U_\infty = 5$ m/s

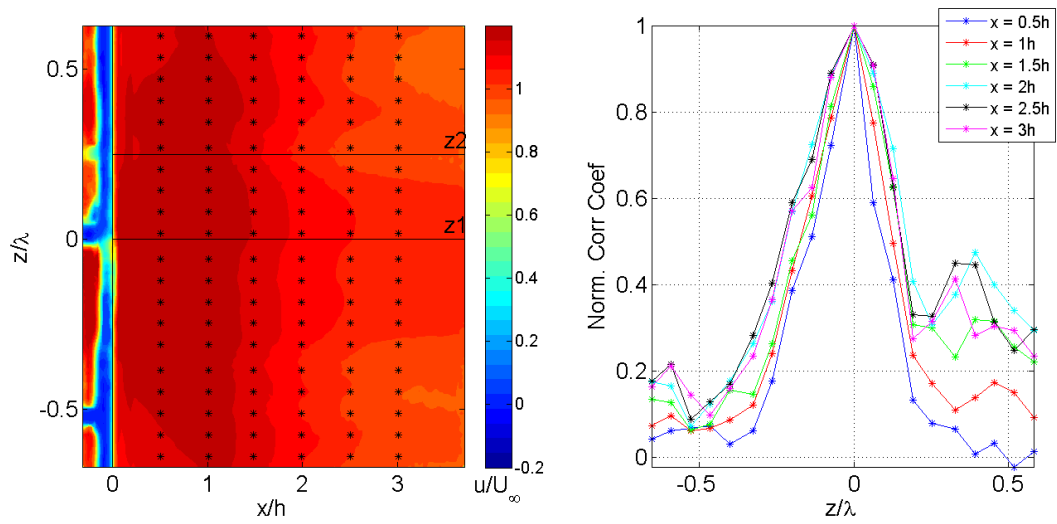


Figure H.12: Spanwise velocity-correlations for transverse staggered actuated flow at $U_\infty = 8$ m/s

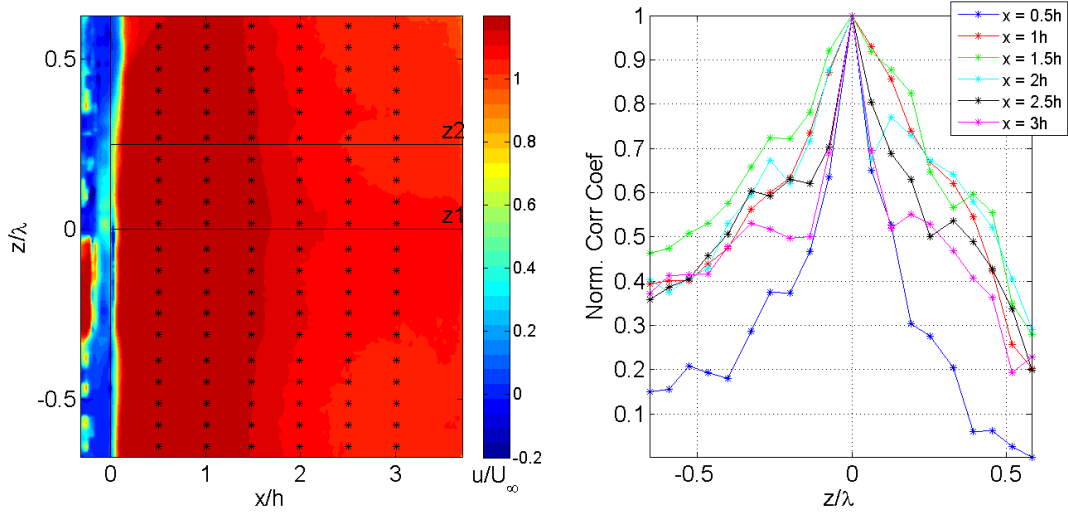


Figure H.13: Spanwise velocity-correlations for transverse staggered actuated flow at $U_\infty = 11$ m/s

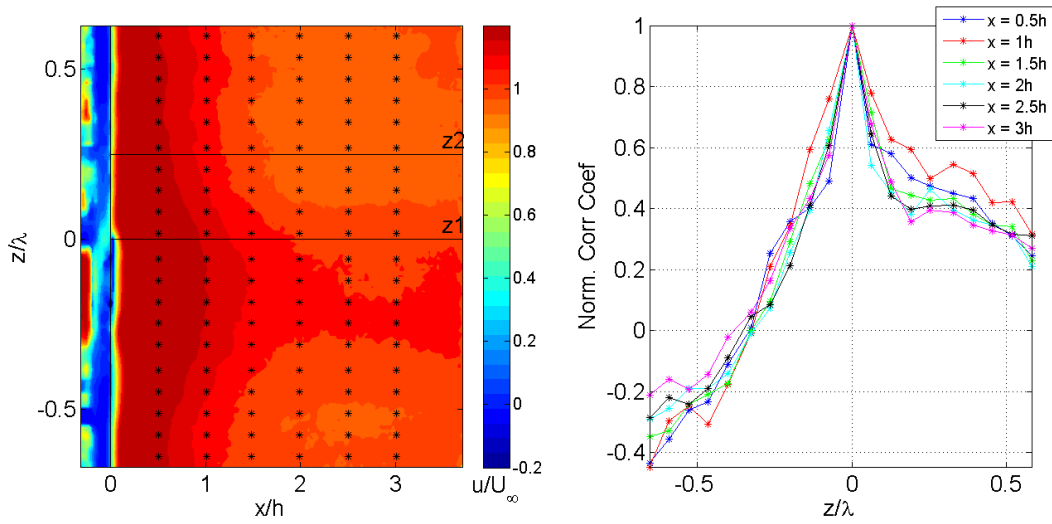


Figure H.14: Spanwise velocity-correlations for transverse staggered actuated flow at $U_\infty = 14$ m/s

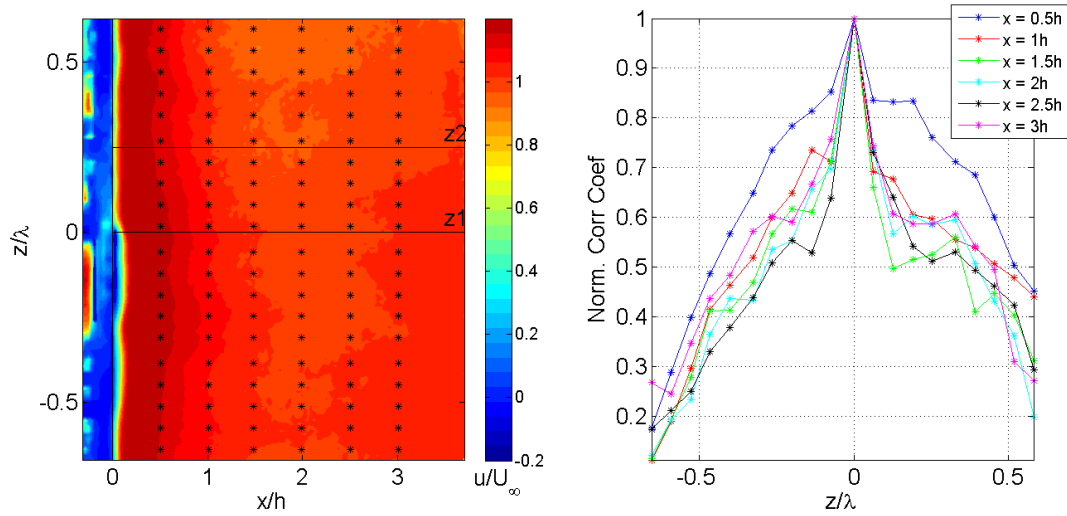


Figure H.15: Spanwise velocity-correlations for transverse staggered actuated flow at $U_\infty = 17$ m/s

H.4 Spanwise Actuation

The shear layer $x-z$ plane was imaged for spanwise actuation for $\lambda^* = 2$ and 4. The ' $z1$ ' spanwise position was taken as the reference position ($z = 0$) at which the velocity signal was found with respect to which all the other velocity signals along the spans at the various streamwise positions were correlated. The plots will be presented in a sequence first for the $\lambda^* = 2$ configuration over all tested U_∞ 's, then for the $\lambda^* = 4$ configuration. As for the previous actuation mode, the following are the observations that one can make from the figures:

1. The unique flow features associated with the different spanwise positions get less distinct as the U_∞ increases. It is also clear from the mean flow features and the correlation values that the $\lambda^* = 2$ configuration has a greater effect on the flow than the $\lambda^* = 4$ configuration. The reason for this is explained in Sec. 5.7.
2. The correlation coefficients across the span are seen to rise as the U_∞ increases.
3. For the $\lambda^* = 2$ configuration the spanwise correlation levels rise at $U_\infty = 11$ m/s. However, significant attenuation in the spanwise coherence persists at even the higher tested free stream velocities, indicating the high degree of success of this actuation mode. The results for the $\lambda^* = 4$ configuration, however indicate a weaker effect of the actuation on the spanwise coherence of the flow.

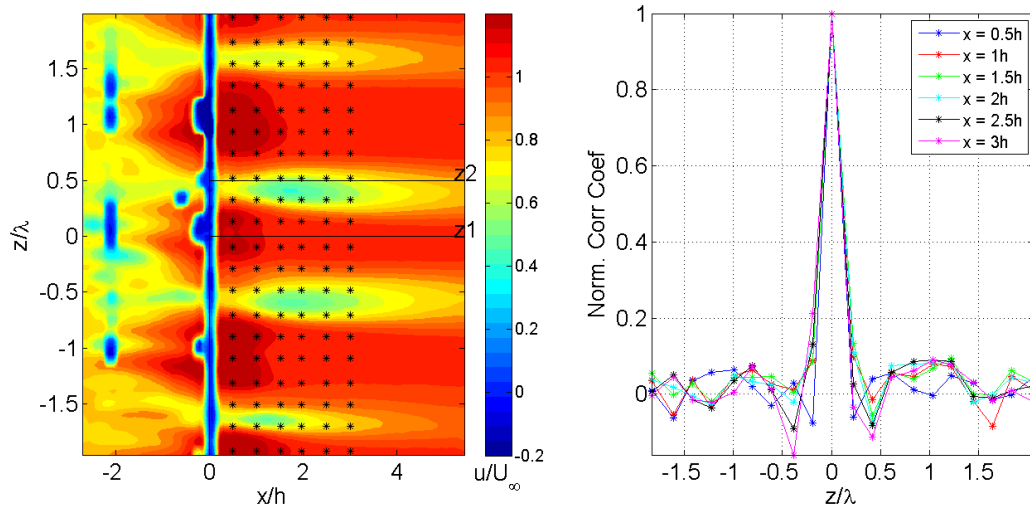


Figure H.16: Spanwise velocity-correlations for spanwise actuated flow for $\lambda^* = 2$ at $U_\infty = 5$ m/s

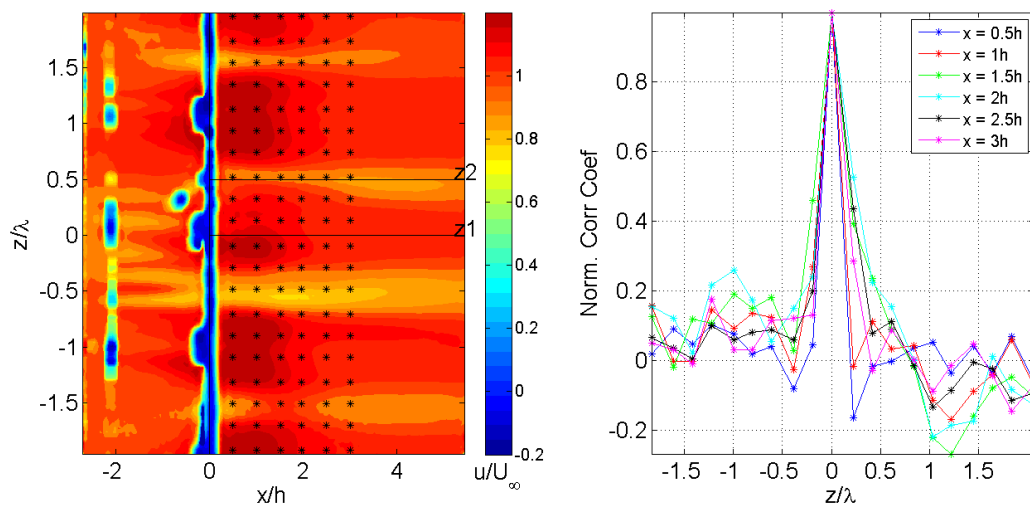


Figure H.17: Spanwise velocity-correlations for spanwise actuated flow for $\lambda^* = 2$ at $U_\infty = 8$ m/s

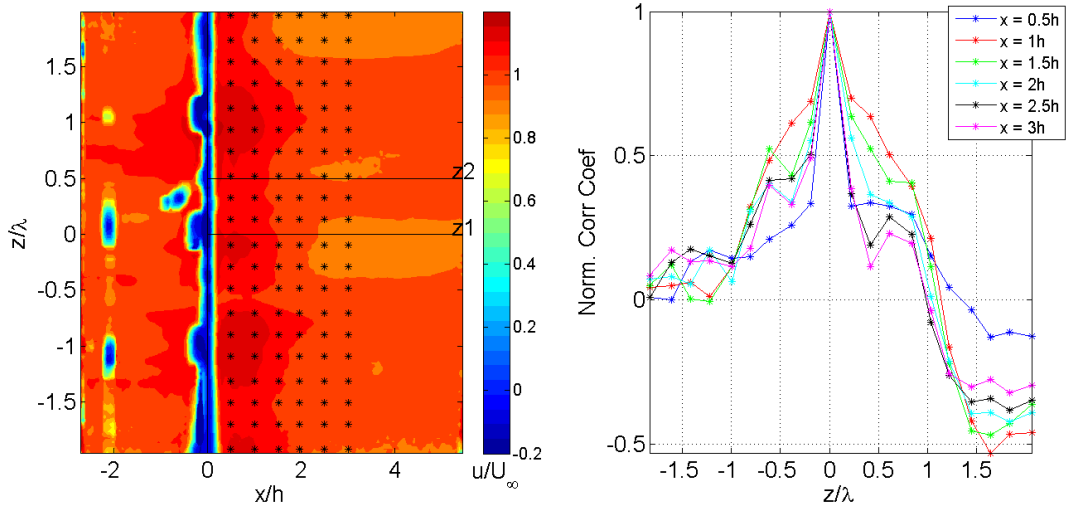


Figure H.18: Spanwise velocity-correlations for spanwise actuated flow for $\lambda^* = 2$ at $U_\infty = 11$ m/s

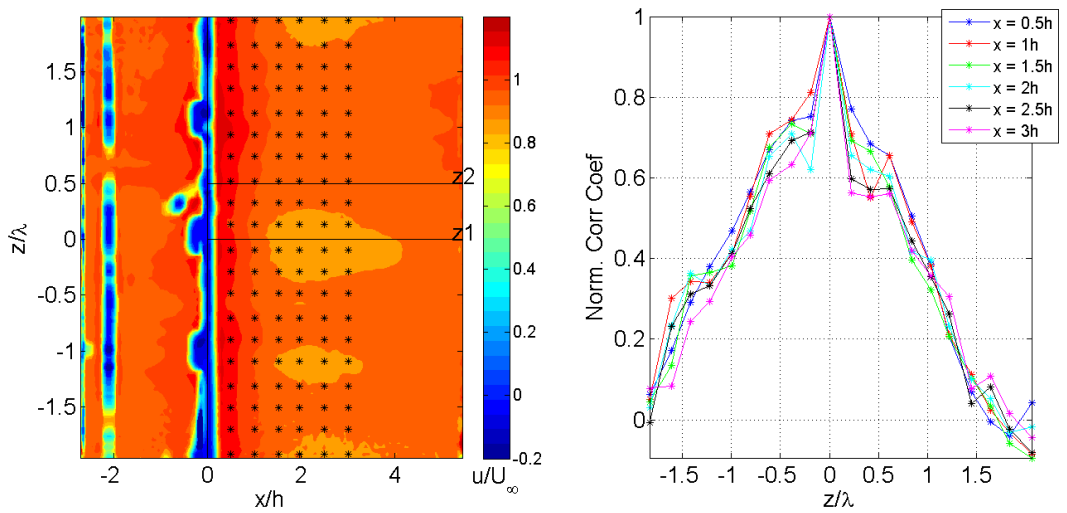


Figure H.19: Spanwise velocity-correlations for spanwise actuated flow for $\lambda^* = 2$ at $U_\infty = 14$ m/s

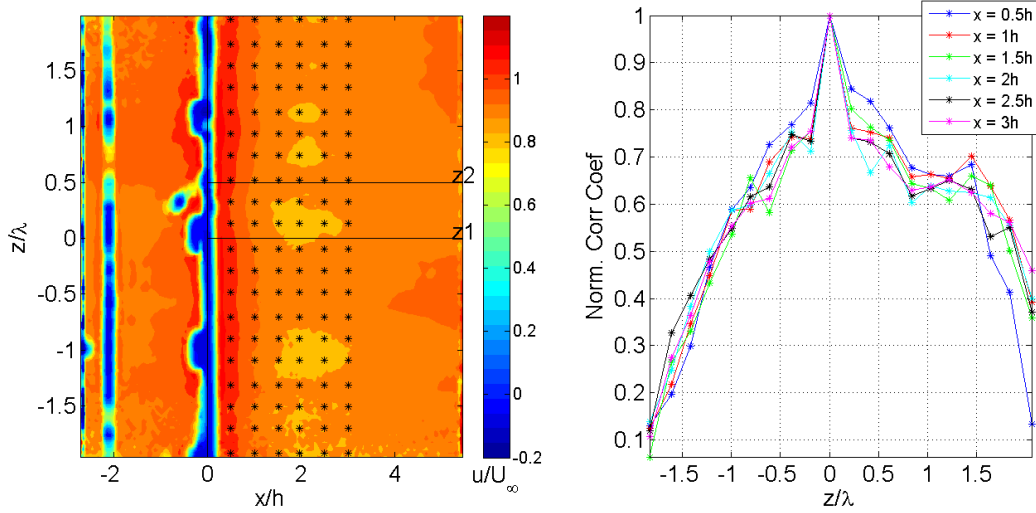


Figure H.20: Spanwise velocity-correlations for spanwise actuated flow for $\lambda^* = 2$ at $U_\infty = 17$ m/s

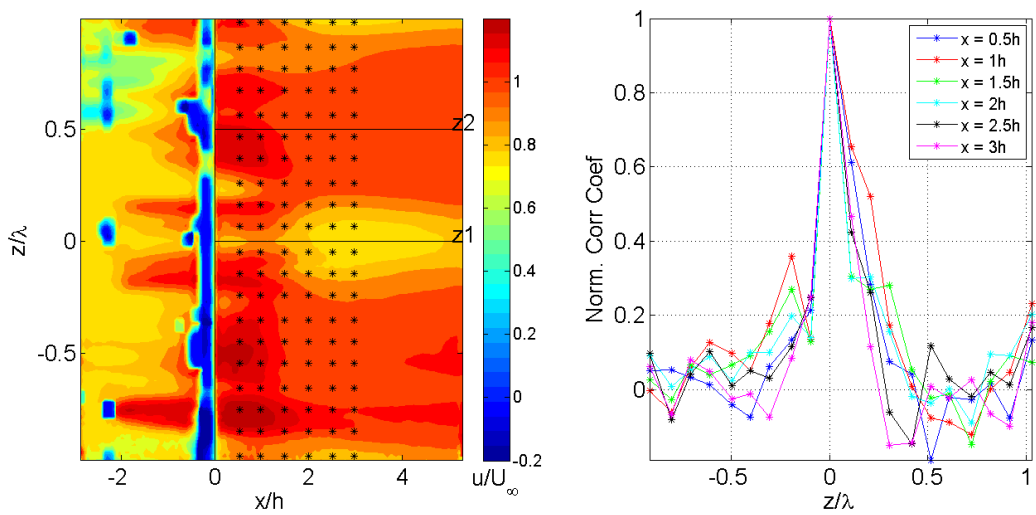


Figure H.21: Spanwise velocity-correlations for spanwise actuated flow for $\lambda^* = 4$ at $U_\infty = 5$ m/s

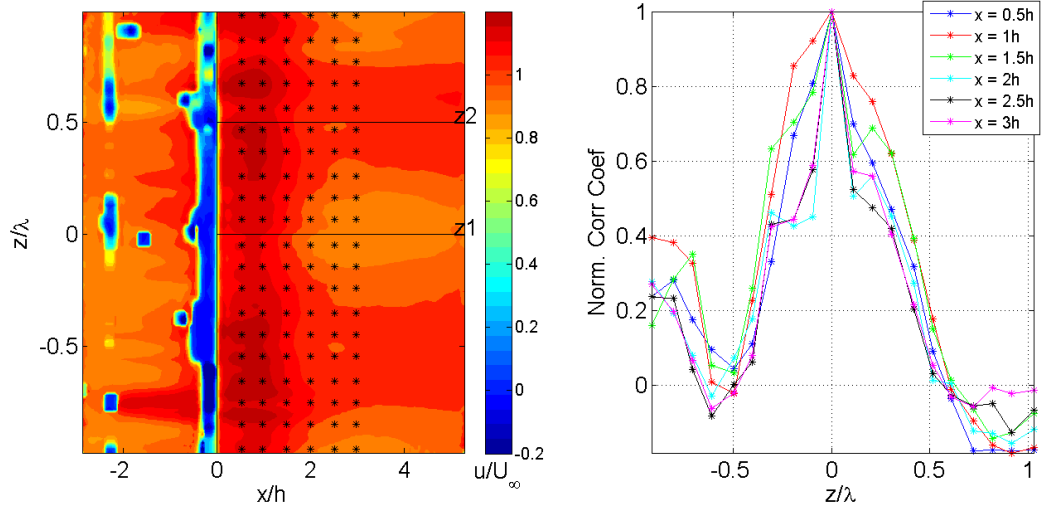


Figure H.22: Spanwise velocity-correlations for spanwise actuated flow for $\lambda^* = 4$ at $U_\infty = 8$ m/s

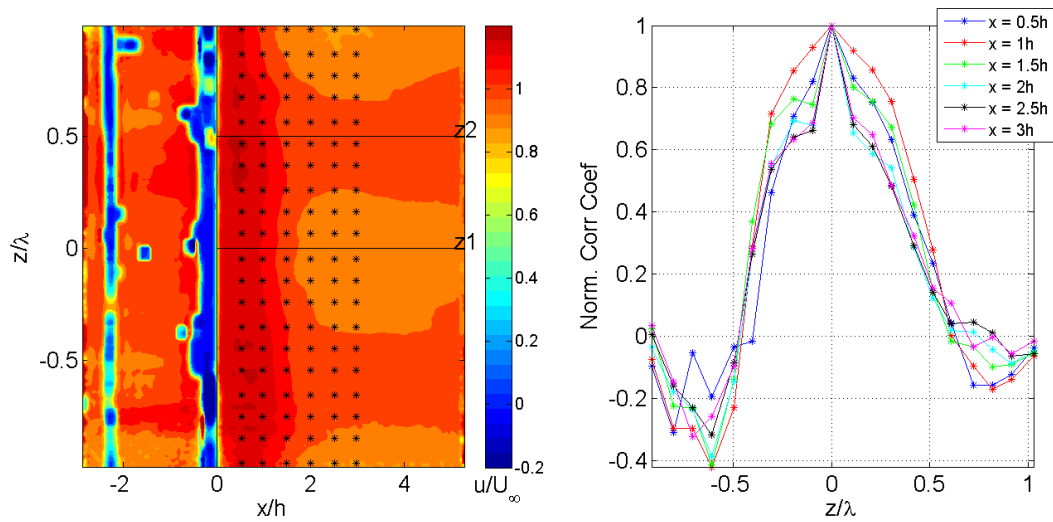


Figure H.23: Spanwise velocity-correlations for spanwise actuated flow for $\lambda^* = 4$ at $U_\infty = 11$ m/s

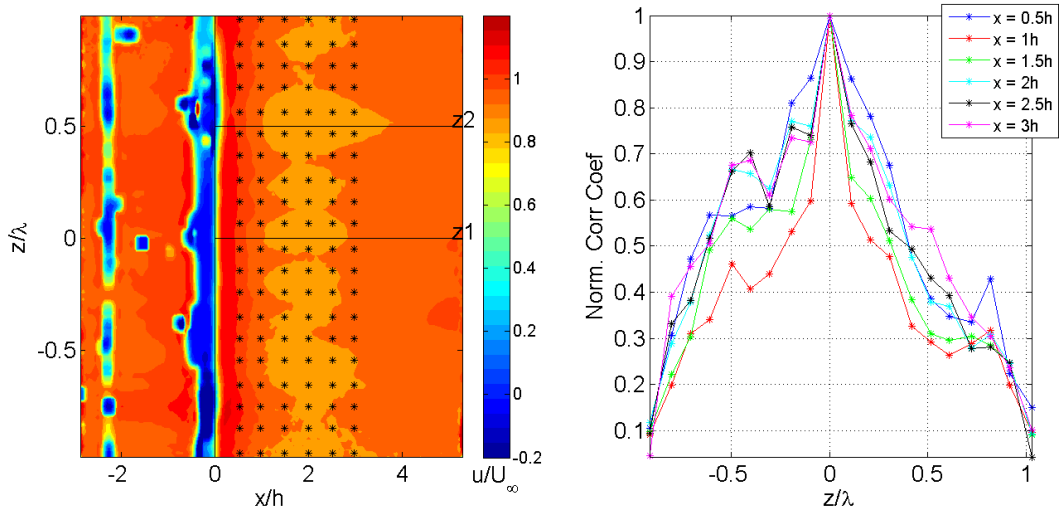


Figure H.24: Spanwise velocity-correlations for spanwise actuated flow for $\lambda^* = 4$ at $U_\infty = 14$ m/s

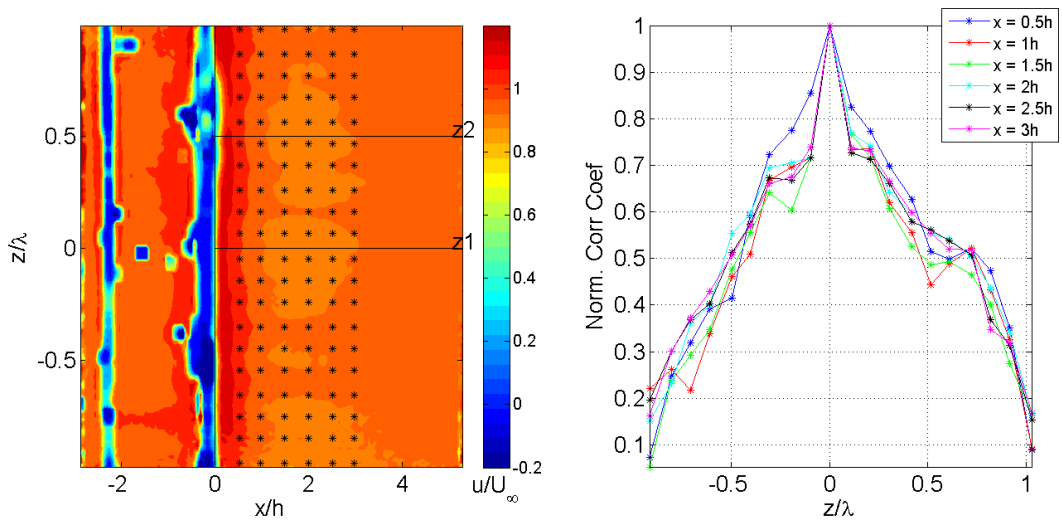


Figure H.25: Spanwise velocity-correlations for spanwise actuated flow for $\lambda^* = 4$ at $U_\infty = 17$ m/s